Ultrafast Plasmonic and Real-time Label-free Polymerase Chain Reaction for Point-of-care Diagnostics

Padideh Mohammadyousef

Department of Electrical & Computer Engineering

McGill University

Montreal, Canada

December 2020

A thesis submitted to McGill University in partial fulfillment of the requirements for the PhD degree of Electrical Engineering.

© Padideh Mohammadyousef 2020

Abstract

In response to the need of the world's medical community for accurate and immediate identification of infectious diseases, many researchers have focused on adapting the gold-standard molecular diagnostic method, polymerase chain reaction (PCR), to point-of-care (POC) applications. Despite all advances in microfluidic PCR as an alternative to bulky, slow, and power-intensive conventional thermocyclers, a simple-to-operate/fabricate PCR device is still lacking.

In this thesis, we introduce a miniature plasmonic PCR thermocycler in which fast DNA amplification is derived from efficient photothermal heating of suspended gold nanorods (AuNRs) inside PCR reaction by a small-scale vertical-cavity surface-emitting laser (VCSEL). Using this method, we demonstrate 30 cycle-assay time of sub-ten-minute for successful Chlamydia Trachomatis DNA amplification in 20 µL total PCR sample volume containing 2.5 nM AuNRs. Furthermore, we report an ultrasensitive real-time amplicon detection strategy which is based on cycle-by-cycle monitoring 260 nm absorption of PCR reaction. This was accomplished by irradiating PCR sample with a UV LED and collecting the transmitted optical power by a photodetector. UV absorption dependency on nucleotides' structural degree of freedom gives rise to distinctive features in the shape of UV amplification curves for PCR results determination (success/fail) and amplicon quantification with a high detection sensitivity of one DNA copy. This is the first demonstration of a compact plasmonic thermocycler combined with a real-time fluorophore-free quantitative amplicon detection system. The small footprint of the proposed PCR device stems from hardware miniaturization while abundant sample volume facilitates highly sensitive detection and fluid-handling required for on-field sample analysis. This simple, portable, and rapid PCR device is the first proof-of-concept demonstration of combining plasmonic DNA amplification and UV detection towards POC molecular diagnostics. More importantly, the realtime detection method is universal and purely optical solely dependent on standard PCR reagent (nucleotides) circumventing the need for the complicated and costly design of target-specific probes.

Résumé

Face au besoin du corps médical de méthodes d'identification précises et immédiates des maladies infectieuses, de nombreux chercheurs se sont concentrés sur l'adaptation de la méthode de diagnostic moléculaire de référence, la réaction de polymérisation en chaîne (Polymerase Chain Reaction en anglais, PCR) et ses applications cliniques directes (applications au point de service ou point-of-care en anglais, POC). Même si les dernières avancées permettent une PCR microfluidique moins encombrante, moins lente et moins consommatrice d'énergie qu'un thermocycleur conventionnel, un dispositif de PCR plus simple d'utilisation et de fabrication reste nécessaire.

Dans cette thèse, nous présentons un thermocycleur PCR plasmonique miniature dans lequel l'amplification rapide de l'ADN découle d'un chauffage photothermique efficace de nanorods d'or (AuNRs) en suspension, au sein d'une réaction PCR, par une diode laser à cavité verticale et émission de surface (vertical cavity surface emitting laser ou VCSEL) de petite échelle. En utilisant cette méthode, nous démontrons une durée de test inférieure à dix minutes, pour un test de 30 cycles, et une amplification réussie de l'ADN de Chlamydia Trachomatis dans un volume total d'échantillon de PCR de 20 µL contenant 2.5 nM d'AuNRs. Par ailleurs, nous développons une stratégie de détection d'amplicon en temps réel ultra-sensible basée sur une surveillance cycle par cycle de la réaction PCR d'absorption à 260 nm. Ceci a pu être réalisé en irradiant un échantillon de PCR à l'aide d'une LED UV et en collectant la puissance optique transmise avec un photodétecteur. La détermination des résultats de la PCR (succès/échec) ainsi que la quantification de l'amplicon, avec une haute sensibilité de détection, dépendent alors de l'absorption d'UV, absorption directement liée au degré de liberté structurelle des nucléotides donnant lieu à des caractéristiques distinctes sous la forme de courbe d'amplification UV. C'est ainsi la première mise au point d'un thermocycleur plasmonique compact combiné à un système de détection d'amplicon quantitatif sans fluorophore en temps réel. La petite taille du dispositif de PCR proposé vient de la miniaturisation du matériel, tandis qu'un volume d'échantillon abondant facilite une détection hautement sensible et la manipulation des fluides nécessaires pour l'analyse des échantillons sur le terrain. Ce dispositif simple, portable et rapide de PCR est une première démonstration de validation de concept combinant l'amplification de l'ADN plasmonique et la détection UV envers

le diagnostic moléculaire POC. De surcroit, cette méthode de détection en temps réel est universelle et purement optique et donc uniquement dépendante du réactif PCR standard (nucléotides), évitant la nécessité d'une conception complexe et coûteuse de sondes ciblespécifiques.

Acknowledgements

First and foremost, I would like to express my profound and sincere gratitude to my supervisor, Prof. Andrew G. Kirk, for introducing me to this exciting field of science, providing me invaluable guidance throughout this research, and teaching me how to think like a Ph.D. His patience, kindness, and constant support throughout these years helped me to enjoy learning and doing research under his supervision.

I would also like to thank Dr. Mark Trifiro for his continuous guidance and encouragement. He generously gave his time to offer me invaluable comments towards improving my work.

I thank Dr. Miltiadis Paliouras for sharing his knowledge and suggestions that impacted this research project considerably. Our discussions improved my understanding of the material substantially.

I also extend my gratitude to my committee members, Prof. Odile Liboiron-Ladouceur and Prof. Sara Mahshid. They provided constructive criticism which helped me develop a broader perspective to my thesis.

I wish to express my love and gratitude to my parents. My parents raised me to believe that I could achieve anything I set my mind to. Finally, to my husband, thank you for being my best friend. This chapter of my life would have not been possible without your love and support.

Statement of Originality

The work done in this thesis includes the following original contributions which have been submitted in the form of journal papers, published in conference papers, as well as a provisional US patent.

1. Journal papers:

- **J1**) P. Mohammadyousef, S. S. Lee, and A. G. Kirk, "Optical DNA amplification and detection in PCR assay at point-of-care: A literature review", submitted to Royal Society of Chemistry, Analyst, Dec. 2020.
- **J2**) P. Mohammadyousef, M. Paliouras, M. A. Trifiro, and A. G. Kirk, "Plasmonic and real-time label-free PCR for point-of-care diagnostics", submitted to Royal Society of Chemistry, Analyst, Dec. 2020.

Conference Papers:

- **C1**) P. Mohammadyousef, G. Uchehara, M. Paliouras, M. A. Trifiro, and A. G. Kirk, "Ultrafast VCSEL-based plasmonic polymerase chain reaction with real-time label-free amplicon detection for point-of-care diagnostics", Proc. SPIE BiOS, Feb. 2020.
- C2) P. Mohammadyousef, M. Paliouras, M. A. Trifiro, and A. G. Kirk, "Ultrafast plasmonic and real-time label-free polymerase chain reaction", Proc. SPIE BiOS, Feb. 2020.
- C3) P. Mohammadyousef, M. Paliouras, M. A. Trifiro, and A. G. Kirk, "A Novel Portable Fluorophore-free Photonic qPCR for Point-of-Care Applications", OSA Biophotonics Congress-Biomedical Optics, April 2020.
- C4*) P. Mohammadyousef, M. Paliouras, M. A. Trifiro, and A. G. Kirk, "Model-based Analysis for Real-time label-free Ultraviolet Quantification of Ultrafast Plasmonic Polymerase Chain Reaction", IEEE EMBC conference, July 2020.

^{*}This conference paper is in preparation for journal submission.

- **C5**) M. Tran, M. Paliouras, P. Mohammadyousef, M. Trifiro, and A. G. Kirk, "Real-time fluorophore-free optical monitoring of ultrafast DNA amplification for qPCR", 2nd European Biosensor Symposium 2019, EBS2019, Feb. 2019.
- **C6**) G. Uchehara, A. G. Kirk, M. A. Trifiro, M. Paliouras, and P. Mohammadyousef, "Real time label-free monitoring of plasmonic polymerase chain reaction products", Proc. SPIE Nano-, Bio-, Info-Tech Sensors, March 2019.
- 2. **Patent**: M. A. Trifiro, N. Tran, M. Paliouras, A. G. Kirk, S. S. Lee, and P. Mohammadyousef, "Ultraviolet quantitative label-free detection of DNA amplification", US provisional patent No. 62/779,132 filed in Dec. 2018.

Collaboration and author contributions

The information in brackets indicates the relevant journal and conference papers.

- P. Mohammadyousef:
 - a. i) Designed and tested the real-time plasmonic PCR device, ii) performed the experiments, iii) discussed the results, iv) developed the numerical model, and v) wrote the manuscripts [J1, J2, and C1-4].
 - b. Edited the manuscripts [C5 and C6].
- A. G. Kirk:
 - a. i) Discussed the results, ii) edited the manuscripts, and iii) coordinated the project.
 All the works done in this thesis and all the publications were under his supervision [J1, J2, and C1-6].
 - b. Wrote the manuscript [C5].
- M. A. Trifiro and M. Paliouras: i) Provided lab testing equipment to perform PCR related experiments, ii) contributed to the design of PCR experiments, iii) discussed the results, and iv) edited the manuscripts [J2 and C1-6].
- G. Uchehara:
 - a. Discussed the results and edited the manuscript [C1].
 - b. i) Designed and tested the real-time plasmonic PCR device, ii) performed the experiments, iii) discussed the results, and iv) wrote the manuscripts [C6].
- M. Tran: i) Designed and tested the real-time plasmonic PCR device, ii) performed the experiments, iii) discussed the results [C5].
- S. S. Lee: Edited the manuscript [**J1**].
- Dr. David Liu: helped in microscope operation and taking TEM images of PCR samples at the facility for Electron Microscopy Research of McGill University [J2 and C1].
- This work was supported by the financial assistance of an operating grant from Genome Canada/Genome Quebec (DIG-Phase 1- 9516) [J2 and C1-6].

Contents

| Chapt | er 1 | | |
|---------|----------|--|----------|
| Introdu | uction . | | <i>'</i> |
| 1.1 | Pro | blem statement | 1 |
| 1.2 | Sign | nificance of the work | 4 |
| 1.3 | Res | earch aims | 4 |
| 1.4 | Res | earch objectives | |
| 1.5 | The | esis outline | |
| Chapte | er 2 | | |
| Literat | ure re | view | 8 |
| 2.1 | Intr | oduction | 8 |
| 2.2 | A b | rief history of PCR development towards photonic PCR | 8 |
| 2.3 | Opt | ical amplification | 14 |
| 2. | 3.1 | Broadband IR-mediated PCR (Optical intrinsic heating) | 16 |
| 2. | 3.2 | Laser-assisted nanodroplet PCR (Optical intrinsic heating) | 19 |
| 2. | 3.3 | NanoPCR | 28 |
| | 2.3.3 | 1 Nanomaterial-assisted PCR | 28 |
| | 2.3.3 | 2 Optical nanoPCR (Optical extrinsic heating) | 30 |
| 2.4 | Opt | ical detection | 39 |
| 2. | 4.1 | Absorbance detection | 43 |
| 2. | 4.2 | Fluorescence detection | 44 |
| | 2.4.2 | .1 Fluorescent reporter molecules | 44 |
| | 2.4.2 | 2 Fluorescent nanoparticles | 49 |
| 2. | 4.3 | Plasmonic-based detection | 51 |
| | 2.4.3 | .1 Surface plasmon resonance (SPR) sensor | 51 |
| | 2.4.3 | 2 Surface-enhanced fluorescence (SEF) | 55 |
| | 2.4.3 | 3 Surface-enhanced Raman scattering (SERS) | 56 |
| | 2.4.3 | .4 Plasmon coupling sensor (Colorimetric assay) | 58 |
| 2 | 1 1 | Ontical ways guide has ad dataction | 61 |

| 2.4.5 | 5 Chemiluminescence detection | 63 |
|----------|--|-----|
| 2.5 | Conclusions and perspectives | 64 |
| Chapter | 3 | |
| VCSEL- | pased plasmonic thermocycler | 66 |
| 3.1 | Introduction | 66 |
| 3.2 | Study Design | 67 |
| 3.2. | Plasmonic PCR sample preparation | 67 |
| 3.2.2 | 2 Laser selection | 69 |
| 3.2.3 | 3 VCSEL-to-tube coupling efficiency | 72 |
| 3.2.4 | 4 Instrument design | 74 |
| 3.3 | Principle of operation | 75 |
| 3.4 | Experimental results and discussion | 77 |
| 3.4. | DNA amplification in VCSEL-based plasmonic thermocycler | 77 |
| 3.4.2 | 2 Study of AuNR robustness in plasmonic PCR reaction | 79 |
| 3.4. | Plasmonic PCR protocol optimization | 83 |
| 3.5 | Summary | 87 |
| Chapter | 4 | |
| Real-tim | e label-free PCR product detection | 88 |
| 4.1 | Introduction | 88 |
| 4.2 | Study Design | 88 |
| 4.3 | Principle of operation | 91 |
| 4.4 | Experimental results and discussion | 93 |
| 4.4. | 1 UV absorption and exposure limit of PCR reaction | 93 |
| 4.4.2 | Real-time UV monitoring of PCR kinetics | 94 |
| 4.4. | PCR results classification based on UV curves shape analysis | 96 |
| 4.4.4 | 4 Real-time amplicon quantification | 98 |
| 4.4. | 5 Limit of detection for dNTPs concentration | 102 |
| 4.4.0 | Analysis of increasing UV transmission in negative control | 104 |
| 4.4. | 7 Comparison of UV system and qPCR limit of detection | 106 |
| 4.5 | Summary | 108 |

| Chapte | r 5 | |
|---------|---|--------|
| Model-k | pased analysis of real-time UV detection | 110 |
| 5.1 | Introduction | 110 |
| 5.2 | Model description | 111 |
| 5.3 | Model calibration with experimental UV detection results | 115 |
| 5.4 | Results and discussion | 118 |
| 5.4 | .1 Analysis of model parameters on PCR efficiency | 118 |
| 5.4 | .2 Minimum detectable threshold cycle | 121 |
| 5.5 | Summary | 124 |
| Chapte | r 6 | |
| Conclus | sion | 125 |
| 6.1 | Thesis Summary | 125 |
| 6.2 | Applications and implications of the POC-ideal real-time label-free VCSEL | -based |
| plasn | nonic thermocycler | 128 |
| 6.3 | Future work and potential improvements | 130 |

List of Figures

| Figure 2.1 Classification of optical thermocyclers based on intrinsic and extrinsic optical heating of PCR reaction |
|---|
| Figure 2.2 (a) Layout of infrared PUC19 amplification and fluorescence detection on glass microchip. (b) Temperature profile and real-time fluorescence measurement 304 bp PUC19 amplification. Reprinted from Ref. [72], Copyright (2012), with permission from American Chemical Society. Schematic of (c) Polyester-toner (PeT) microchip with a PCR chamber and a dummy chamber for temperature measurement and (d) IR heating and forced air cooling setup for PeT microchip. Reprinted from Ref. [9], Copyright (2015), with permission from Elsevier 17 |
| Figure 2.3 (a) Droplet array loaded in mineral oil using home-built contact printing system. (b) Laser-assisted heating of droplet with 200 µm beam size at FWHM. Reprinted from Ref. [85] with permission from the Royal Society of Chemistry. (c) Schematic description of laser-irradiated nanodroplets dispersed in mineral oil for PCR on a microscope stage. (d) Droplets of phosphate-buffered saline containing single MDA-MB-231 breast cancer cells (1) and lysis buffer (2) are optically combined to perform cell lysis (3), and PCR reagents droplet (4) will be coalesced with lysed droplet (5) <i>via</i> laser beam manipulation for amplification (6). Reprinted from Ref. [87], Copyright (2012), with permission from Springer Nature |
| Figure 2.4 (a) COMSOL 3D geometry to obtain time-dependent temperature cooling of droplet centered in mineral oil. (b) 2D and (c) 3D plot of time-dependent thermal cooling of droplet with varying diameter (D) |
| Figure 2.5 (a) COMSOL geometry used for time-dependent heat-transfer analysis of 5×5 droplet array. (b) close-up view of model geometry for 5×5 droplet array |
| Figure 2.6 Time-dependent cooling from denaturation to annealing stage for aforementioned droplet PCR studies using single droplet COMSOL model |
| Figure 2.7 (a) Schematic of 2-layer Au film optical cavity for maximum photon absorption by cavity medium (PCR solution). (b) Optical setup with a PCR chamber and reference/thermocouple chamber positioned at lens focal length. (c) Heating and cooling rate dependence on Au films' separation distance. (d) Thermocycling curve for PCR and reference chamber. Reprinted from Ref. [15], Copyright (2015), with permission from Wiley-VCH |
| Figure 2.8 Classification of ontical PCR product detection 39 |

| Figure 2.9 (a) UV amplification curve obtained from real-time UV monitoring of plasmonical amplified <i>C. Trachomatis</i> DNA with varying starting copy numbers (10 ⁵ -10). (b) Gel image samples with varying initial DNA concentrations amplified in plasmonic thermocycler [143] ² | | |
|--|--|--|
| Figure 2.10 Jablonski diagram explaining the occurrence of fluorescence and phosphorescence. | | |
| Figure 2.11 Overview of the system design of real-time continuous flow PCR assay introduced by Hatch <i>et al.</i> Reprinted from Ref. [167] with permission from the Royal Society of Chemistry 48 | | |
| Figure 2.12 (a) Schematic illustration of PCR products amplified by modified forward and reverse primers and their detection on LFA strips through interaction with two different antibodies and two different sizes of streptavidin-modified QDs. Images of test strips and their intensity analysis by smartphone application for detection of (b) femA and (c) mecA genes with different concentrations by using 625 nm and 525 nm labeled-QDs, respectively. Reprinted from Ref. [142], Copyright (2019), with permission from Elsevier | | |
| Figure 2.13 (a) Functionalized FO-SPR sensor and AuNPs with forward and reverse primers, respectively and generation of amplicons on FO-SPR sensor. (b) Real-time measurement of SPR wavelength shift for varying DNA template concentration and plot of threshold cycles against logarithm of DNA concertation. Reprinted from Ref. [21], Copyright (2011), with permission from Wiley-VCH. (c) Schematic representation of FO-PCR-MA for multiplex detection. (d) First order derivative of FO-SPR signal vs. temperature for resolving target-specific melting points. Reprinted from Ref. [22] with permission from the Royal Society of Chemistry | | |
| Figure 2.14 (a) Schematic of closed SERS primer in the absence of target DNA. (b) Hybridization of target DNA to its complementary sequence in SERS probe setting free the dye labeled ssDNA parts of SERS primer to get adsorbed on negatively charged AgNPs. (c) SERS spectra for positive control (green), no template control (dark blue), negative PCR sample (red), and blank (light blue). (d) Discrimination of PCR results based on average SERS signal peak at 1632cm-1 for three positive, negative, and no DNA template controls. Reprinted from Ref. [147], Copyright (2011), with permission from American Chemical Society. | | |
| Figure 2.15 (a) Conceptual overview of colorimetric amplicon detection based on AuNPs protection against salt-induced aggregation due to the presence of target ssDNA; however, in the absence of target, salt-induced aggregation of AuNPs leads to a visible color change from ruby-red to blue-purple. (b) The change in absorption spectra of AuNPs with varying concentrations of target (emetic B. cereus). (c) The absorbance ratio of PCR sample at 650 nm to 520 nm wavelength is plotted against different emetic B. cereus concentrations. Adapted from Ref. [148], Copyright (2017), with permission from Elsevier | | |

| Figure 3.1 Comparison between EEDL-tube and VCSEL-tube distance for optimum beam coupling |
|---|
| Figure 3.2 Thermal images of VCSEL-based plasmonic thermocycler showing different system components' temperature close to (a) denaturation and (b) annealing stage |
| Figure 3.3 Zemax non-sequential model for VCSEL-based plasmonic thermocycler to maximize coupling efficiency |
| Figure 3.4 Optical simulation for VCSEL-to-tube beam coupling. (a) Calculated coupling efficiency for different VCSEL-tube separation distances based on Zemax optical model. Optical configuration and ray-tracing diagram for VCSEL-tube separation of (b) 3 mm and (c) 10 mm.74 |
| Figure 3.5 Design layout of VCSEL-based plasmonic thermocycler |
| Figure 3.6 (a) Schematic of the VCSEL-based plasmonic thermocycler using suspended AuNRs as a light-to-heat converting medium and (b) conceptual illustration of VCSEL status during thermocycling. |
| Figure 3.7 (a) An example of temperature profile of 30 thermocycles for successful DNA amplification. (b) Heating and cooling rates obtained from the temperature profile showing the average values (solid lines) with standard deviations (dashed lines) |
| Figure 3.8 Gel electrophoresis image of PCR results. Band intensities obtained from conventional and plasmonic thermocyclers show comparable PCR efficiencies, and negative controls indicate a contamination-free master mix and validity of results. |
| Figure 3.9 Normalized absorption spectra of plasmonic positive PCR reaction before and after PCR with (a) Klentaq, (b) KAPA2G, and (c) Phusion Polymerases. (d) Gel image for plasmonic and conventional DNA amplification using different polymerases, and the results on gel image demonstrate similar amplicon yield |
| Figure 3.10 An example of close up TEM images captured from AuNRs from (a) pre-PCR and (b) post-PCR samples demonstrating unaltered AuNRs size and morphology |
| Figure 3.11 Calculated AuNRs' normalized perimeter densities for (a) Pre-PCR positive, (b) Post-PCR positive, (c) Pre-PCR negative, and (d) Post-PCR negative controls. Average of normalized (e) Pre-PCR and (f) post-PCR densities |

| Figure 3.12 (a) Comparison of PCR yield using different AuNRs concentration in conventional thermocycler. The results reveal that AuNRs concentration can be increased up to 29 nM for faster DNA amplification without compromising PCR yield. (b) The gel image shows the impact of different PCR parameters on amplification efficiency. PCR failed for ta less than 5 s (lane 2 and 3). Successful PCR was obtained with CR of 4.1 °C (lane 4). However, further increase in CR inhibits PCR (lane 5 and 6), and amplicon generation only occurs by lowering TA (lane 7) 84 |
|---|
| Figure 3.13 COMSOL simulation to obtain time-dependent cooling temperature profiles of the different lines defined in (a) the model geometry of 20 µL water placed in a 0.2 mL PCR plastic tube. (b) The bar graph shows the impact of increased heat transfer coefficient (h0) on temperature difference between line A and B (thermal lag) |
| Figure 3.14 Comparison of PCR yield on gel image for different (a) TA and (b) TD |
| Figure 4.1 Schematic of the VCSEL-based plasmonic thermocycler and real-time UV detection system |
| Figure 4.2 Optical simulation for UV detection system. Optical configuration and ray tracing diagram for (a) no-lens system and (c) 2-lens system. Detector viewer for (b) no-lens and (d) 2-lens UV detection system |
| Figure 4.3 Pyrimidines and purines with one and two heterocyclic rings respectively [209] 91 |
| Figure 4.4 (a) Optical density for different dNTPs: adenine (A), thymine (T), guanine (G), and cytosine (C). (b) Change in UV absorbance based on conformational freedom of dNTPs [210].92 |
| Figure 4.5 Schematic illustration of dNTPs consumption as PCR cycles proceed, and thereby cycle-by-cycle drop in A ₂₆₀ . [dNTP] denotes dNTPs concentration |
| Figure 4.6 Conceptual illustration of the status of VCSEL and UV LED during plasmonic thermocycling |
| Figure 4.7 (a) Absorption spectra of different PCR reagents with the same concentration as in positive PCR. (b) Absorption spectra of positive PCR reaction before and after plasmonic thermocycling exhibits 260 nm absorption drop as a result of dNTPs conversion to dsDNAs. (c) Gel image of positive PCR samples exposed to 1 mW UV LED irradiation for different UV exposure time durations of 20-320 s and 50-80 s, and their impact on amplicon yield. 70 s UV exposure time shows less amplicon generation/faint band |

| Figure 4.8 The measured UV optical power at photodetector (discrete triangles) is plotted agains cycles to generate UV amplification curve. 4 different curves (dashed lines) were least square fitted to experimental values to show 4 phases of PCR kinetics |
|--|
| Figure 4.9 (a) UV amplification curves for positive and negative controls. (b) Min-max normalized UV amplification curves for different samples were generated by fitting curves (solid lines) to experimental UV transmission (discrete data points). All amplification curves follow a 2 nd degree exponential function throughout 40 cycles except successful PCR (black) with sigmoidal increase at threshold cycle (Ct). |
| Figure 4.10 (a) Comparison of percentage increase in UV transmission from cycle 1 to Ct (=27) and cycle 27 to 40 for different controls. (b) The gel image confirms the validity of UV results to differentiate successful and failed PCR |
| Figure 4.11 The rectangular blue and orange bars represent calculated P40/PCt and PCt/P1 for 20 different plasmonic positive PCR samples. The first 10 samples are failed PCR tests with PCt2P40×P1 (green bars) greater than 1.15, whereas PCt2P40×P1 is less than or equal to 1.15 for successful PCR tests. |
| Figure 4.12 Distribution of different DNA copy numbers in 20 μ L sample for (a) λ =3.5 and (b) λ =35 |
| Figure 4.13 (a,b) Original UV curves and (c,d) min-max normalized UV amplification curves for positive PCR samples with initial DNA copy numbers ranging from 105-100. The Ct shifts right to higher cycles with decreasing target concentration. (e) UV standard curve established between obtained Ct values and log of DNA copy number for real-time amplicon quantification. (f) Ge electrophoresis image of plasmonically amplified samples with different DNA starting concentrations. |
| Figure 4.14 UV standard curve showing mean and S.D of obtained threshold cycles 102 |
| Figure 4.15 (a) UV absorption spectra and (b) UV transmission of solutions containing differen dNTPs concentration obtained from spectrophotometer and 2-lens UV detection system respectively. |
| Figure 4.16 (a) Min-max normalized UV optical power from plasmonic thermocycling of each PCR ingredient separately. Only the sample with Klentaq polymerase (S3, red) showed increasing UV transmission throughout 40 cycles. (b) Comparison of percentage change in UV optical power from first to last cycle for different plasmonic solutions containing one PCR ingredient 105 |

| Figure 4.17 Comparison of normalized UV and fluorescent amplification curves using (a) 105, (b) 104, (c) 103, (d) 102, and (e) 10 initial DNA copy numbers |
|---|
| Figure 5.1 Least square fitted TModel (solid lines) to TExperimental (plus signs) to quantify unknown parameters for (a) 105 to 100 and (b) 10 to zero initial DNA copy number |
| Figure 5.2 (a) DNA and (b) polymerase thermal damage impact on amplificon generation 119 |
| Figure 5.3 (a) DNA and (b) polymerase UV damage impact on amplificon generation 120 |
| Figure 5.4 Amplification profiles for different ta |
| Figure 5.5 The plot of (a) dNTPs, (b) Taq polymerase, and (c) dsDNA concentrations vs. PCR cycles calculated by the model for the initial DNA copy number of 105 |
| Figure 5.6 The plot of model UV absorption for (a) dNTPs, (b) Taq polymerase, and (c) both Taq and dNTPs as well as (d) UV transmission vs. PCR cycles for the initial DNA copy number of 105 |
| Figure 5.7 dNTPs concentration changes throughout 40 PCR cycles for 105 DNA copy numbers. |
| Figure 6.1 Schematic illustration of NA analysis steps carried out in (a) current laboratories and (b) POC format. Reprinted from Ref. [235], Copyright (2017), with permission from American Chemical Society. |

List of Tables

| Table 2.1 Photothermal efficiency in photonic PCR devices using broadband IR lamp |
|--|
| Table 2.2 Comparison of droplet-based PCR devices in terms of their speed and photothermal efficiency |
| Table 2.3 Comparison between heating and cooling time durations for different droplet PCR devices |
| Table 2.4 Photonic nanomaterial-assisted PCR devices with their calculated photothermal efficiency |
| Table 2.5 Comparison of optical detection methods used in PCR assay and their POC adaptability. |
| Table 2.6 Representative examples of various optical detection methods used for PCR product detection |
| Table 3.1 Positive PCR protocol for different polymerases |
| Table 3.2 Negative Controls with Taq polymerase |
| Table 3.3 Positive PCR protocol with Taq polymerase for 2.5-29 nM AuNRs concentration 68 |
| Table 3.4 Summary of VCSEL-based plasmonic thermocycler characteristics |
| Table 3.5 Mean, median, and mode of AuNRs perimeters data set for pre- and post-PCR samples 83 |
| Table 4.1 Mean and standard deviation of the obtained threshold cycles for different DNA starting copy numbers |
| Table 4.2 Comparison of threshold cycles obtained from UV and fluorescence detection 106 |
| Table 5.1 Model constant parameters |

| | | ٠ | ٠ |
|---|----|---|---|
| X | V1 | 1 | 1 |
| | | | |

| Table 5.2 Model cycle-dependent variables. | 113 |
|---|-----|
| Table 5.3 Known parameters for model calibration. | 115 |
| Table 5.4 Unknown parameters for model calibration. | 116 |
| Table 5.5 Experiments for quantifying unknown parameters | 116 |
| Table 5.6 Quantified unknown parameters by least square fitting TModel to TExperimental | 117 |

List of Abbreviations

PCR Polymerase chain reaction

NAAT Nucleic acid amplification test

NA Nucleic acid analysis

POC Point-of-care

qPCR Quantitative/real-time polymerase chain reaction RT-PCR Reverse transcription polymerase chain reaction

aPCR Asymmetric polymerase chain reaction

LAMP Loop-mediated isothermal amplification

SPE Solid-phase extraction
HRM High-resolution melting
CE Capillary electrophoresis

bp Base pairs

DNA Deoxyribonucleic Acid

dsDNA Double stranded deoxyribonucleic Acid ssDNA Single stranded deoxyribonucleic Acid mtDNA Mitochondrial deoxyribonucleic Acid

PNA Peptide nucleic acid

dNTPs Deoxynucleotide triphosphates

A Adenine
G Guanine
C Cytosine
T Thymine

ddH₂O Double distilled water

WHO World health organization COVID-19 Coronavirus disease 2019

MERS Middle east respiratory syndrome SARS Severe acute respiratory syndrome

HPV Human papilloma virus

LASER Light amplification by stimulated emission of radiation

VCSEL Vertical-cavity surface-emitting laser

LED Light emitting diode
PMT Photomultiplier tube

EM Electromagnetic
CW Continuous wave

IR Infrared

NIR Near-Infrared UV Ultraviolet

OPL Optical path length

EFL Effective focal length

LOD Limit of detection

RI Refractive index

DCX Double-convex

FFT Fast Fourier transform SNR Signal-to-noise ratio SD Standard deviation

RRI Relative reflected intensity

LFA Lateral flow assay

NP Nanoparticle

NR Nanorod

AuNP Gold nanoparticle

AgNP Silver nanoparticle

AuNR Gold Nanorod

AuNS Gold nanosphere

AuBP Gold bipyramid nanoparticle

AuNF Gold dendritic nanoforest

SEF Surface-enhanced fluorescence

SERS Surface-enhanced Raman spectroscopy/scattering

SP Surface plasmon

SPR Surface plasmon resonance

LSPR Localized surface plasmon resonance

SPP Surface plasmon polariton

FO Fiber Optic

FO-SPR Fiber optic surface plasmon resonance

FO-PCR-MA Fiber optic polymerase chain reaction melting assay

NC Nanocluster

QD Quantum dot

UCNP Up-converting nanoparticleMWCNT Multi wall carbon nanotube

PEG PEGylation

FRET Fluorescent resonance energy transfer

SA/V Surface-to-volume ratio

SA Streptavidin
Dig Digoxigenin

FEP Fluorinated ethylene propylene

PAA Porous Anodic Alumina

PMMA Poly(methyl methacrylate)

PDMS Polydimethylsiloxane

CHAPTER 1

Introduction

1.1 Problem statement

Point-of-care (POC) testing refers to analytical testing activities provided outside the clinical laboratory and performed by non-laboratory personnel near the site of the patient to provide instant availability of results. This facilitates quick medical decisions and enhances healthcare outcomes. POC testing devices should be easy-to-operate, portable, and handheld electronics or molecular collection tools. It is expected that faster and more accurate POC diagnostic tests will play a significant role in expanding health care in low- and middle-income countries where diagnostic challenges exist due to poor clinical laboratory infrastructures, lack of skilled technicians, and cost constraints [1, 2]. Therefore, many studies have focused on adapting different diagnostic tests such as polymerase chain reaction (PCR) platforms to POC settings.

The current global pandemic of Coronavirus disease 2019 has alerted us once again to the importance of POC diagnostics testing to provide timely and sensitive pathogen detection. PCR is a technology specifically designed for sensitive and specific nucleic acid sequence quantification and has always been in the center of attention to be adapted for POC applications. The high sensitivity and specificity of PCR assays originate from enzymatic amplification of specific sequences of low-abundance target nucleic acids *via* repetitive thermal cycling. In a standard PCR, 15-100 µL PCR sample [3] undergoes sequential three PCR steps at different set temperatures (denaturation: 94-98 °C, annealing: 45-55 °C, and elongation: 72 °C) in a device called thermocycler [4]. Conventional Peltier-based thermocyclers are mainly confined to laboratories owing to their lack of speed, large dimensions, and high-power requirements. Thus, many academic and industrial groups have made a great deal of effort to adapt PCR assay to POC platform in which short turnaround time, easy portability, assay simplicity, and low power consumption are requisite features particularly in resource-limited settings or during mass testing. These advances towards a POC-suitable PCR assay can be categorized in two groups: microfluidic

and photonic PCR. Microfluidic PCRs offer sub-minute amplification timescale by reducing sample and device thermal mass and increasing surface-to-volume ratio (SA/V) up to 20 mm²μL¹¹ [5-7]. However, one major hurdle restricting the practicality of microfluidic PCR for POC testing is their intrinsic size often referred as macro-to-micro interface [8]. This originates from the fact that reagents are available and pipetted in μL-mL volumes while in the microfluidic device, the reaction occurs within the microchambers with pL-nL capacity or in the form of nanodroplets. From POC diagnostic standpoint, liquid-handling for these miniature-sized PCR assays require highly precise pipetting skill, and this will be challenging for their on-site application by untrained non-laboratory users. Therefore, in order to eliminate operational errors and difficulties in sample preparation, microfluidic fluid handling should move towards an automated assay. Other challenges with microfluidics such as sensitivity loss due to shortened optical path length (OPL), recovery of nL-pL sample for post-PCR manipulation or analysis (*e.g.*, sequencing or cloning), and fabrication of microchips and micropipettes have led researchers to investigate more cost-efficient and easy-to-fabricate/operate PCR assays.

In the first generation of photonic PCR thermocyclers, a large broadband IR source (halogen or tungsten lamp) of at least 50 W was used to irradiate small sample volume of 2, 0.28, 0.16 µL to achieve heating rate of 10.1, 13.4, 65 °C.s⁻¹, respectively by making use of the natural optical absorbance of the sample [9-11]. Plasmonic PCR on the contrary exploits the very high optical absorbance of metallic nanoparticles (suspended in the sample) or thin films (embedded in the heating chamber walls) and enables heating rates of up to 72.7 °C.s⁻¹ for larger sample volumes of 25 µL with significantly reduced optical power (2 W) [12-15]. Although plasmonic thermocyclers have shortened time per PCR cycle down to few seconds (≤20 s.Cycle⁻¹), their portability and scalability due to employment of large laser diodes still need to be improved for POC testing adaptation. LEDs have been proposed to reduce the cost and size of plasmonic thermocyclers; however, due to broad spectral power distribution and high-divergence beam, high-power LEDs (>3 W) with the addition of focusing lenses are necessary to obtain photothermal efficiency comparable to laser-based plasmonic thermocyclers [14-16].

For a complete analytical POC diagnostic device, real-time amplicon quantification should be incorporated into these thermocyclers. One of the first steps towards a POC-suitable quantitative PCR (qPCR) assay was traditional fluorimeters integration into microfluidic thermocyclers

through their miniaturization and conversion to on-chip mode [17, 18]. However, this leads to shortened OPL and consequently degrades the detection sensitivity. Furthermore, other challenges associated with the fluorescence detection method such as costly and laborious labeling process, limited shelf life of fluorescent dyes, and loss of detection sensitivity due to intensity-dependent photobleaching event make this detection method less practical for POC applications. Surface plasmon resonance (SPR) sensors are another promising real-time detection strategy. Since the detection mechanism in SPR sensor is based on monitoring spectral shift in resonance wavelength, bulky spectrophotometers are part of detection system [19-23]. Hence, despite its high detection sensitivity owing to near-field surface interactions sensing mechanism, SPR biosensor has not advanced beyond proof-of-concept laboratory demonstration due to the size of spectrophotometers, high sensor chips/instrumentation cost, labor-intensive target-specific surface functionalization, and short shelf life.

In response to these challenges, this thesis is focused on developing a rapid, compacted, and robust plasmonic thermocycler combined with a real-time label-free amplicon detection method ideal for POC testing. In this thesis, the previously proposed laser induced-plasmonic thermocyclers are miniaturized by replacing large laser diode with vertical cavity surface emitting laser (VCSEL). Owing to the compact form factor of VCSELs and their low beam divergence as well as circular beam characteristics, by placing a VCSEL in proximity to the bottom of the PCR tube, maximum light coupling efficiency is obtained. This leads to uniform and efficient photothermal heating of PCR reaction in a simple optical setup without adding any optical components (e.g., optical fibers or lenses). Real-time amplicon quantification was accomplished by monitoring UV absorption of PCR reaction at the elongation stage of every PCR cycle. The plot of UV transmission against cycles (UV amplification curve) serves as a fingerprint to identify PCR results (success/fail) and quantify target DNA concentration. Finally, a mathematical model for DNA quantification was calibrated using experimental results from real-time UV transmission measurements of plasmonic PCR thermocycling. The effect of different PCR parameters on template amplification was investigated using the calibrated model. We have used Zemax optical design, COMSOL Multiphysics, and MATLAB software for the simulations presented in this thesis.

1.2 Significance of the work

The key contributions of this thesis towards the advancement of a POC-ideal PCR device are:

- Introduction of VCSEL-based plasmonic thermocycler to enhance POC adaptability of plasmonic PCR devices.
- 2. Development of an optical model to maximize VCSEL-to-tube beam coupling efficiency.
- Experimental investigation of optimal plasmonic PCR condition including set temperatures, hold-times, cooling rate, and AuNRs concentration to maximize amplicon yield.

The previously demonstrated real-time UV monitoring of plasmonic PCR method by Tran *et al.* [24] was significantly advanced by:

- Undertaking rigorous measurements of the UV absorption of all PCR components by UVvis spectroscopy and UV detection system to understand their impact on amplicon UV monitoring.
- 5. Development of an optical model for UV detection system to improve signal-to-noise ratio and subsequently the detection sensitivity.
- 6. Classification of PCR results based on the shape of UV curves *via* testing various positive and negative controls.
- 7. Measuring the quality of experimental results (repeatability) both for PCR results classification and amplicon quantification technique based on UV threshold cycles.
- 8. Numerical model analysis of UV transmission data to study the impact of different PCR conditions (*e.g.*, PCR hold-times and UV exposure time duration) on PCR overall efficiency.

1.3 Research aims

- 1. Development of VCSEL-based plasmonic PCR thermocycler for *Chlamydia Trachomatis* DNA amplification: An attempt towards PCR-based point-of-care testing.
- 2. Integrating real-time UV detection of amplicons in plasmonic PCR thermocycler.

1.4 Research objectives

The main objectives of this thesis are:

- 1. Designing the VCSEL-based plasmonic thermal cycler for high temperature stability, beam coupling efficiency, photothermal efficiency, and PCR efficiency.
- 2. Optimizing plasmonic PCR condition and AuNRs concentration for fast thermocycling and maximum amplicon yield.
- 3. Investigating system reliability for different PCR polymerases to validate our methodology.
- 4. Advancement of UV monitoring system by:
 - a. Improving signal-to-noise ratio and subsequently detection sensitivity.
 - b. Testing the system performance by using PCR positive and various negative controls.
 - c. Measuring the detection sensitivity (limit of detection) of the system.
 - d. Quantifying maximum and minimum detectable dNTPs concentration
- Measurement of the repeatability of plasmonic DNA amplification and amplicon quantification.
- 6. Numerical model analysis of UV transmission data to study PCR controlling parameters for optimal efficiency.

1.5 Thesis outline

The content of this thesis has been published in the aforementioned journal and conference papers. The following demonstrates the structure of this thesis, and the reference to the publications is presented in brackets for each chapter.

- Chapter 2: reviews
 - The fundamental principles of polymerase chain reaction (PCR).
 - Modern optical thermocyclers used in PCR assay. These optical thermocyclers are compared in terms of their speed, practicality for POC testing, and light-to-heat conversion efficiency [J1].

 Optical biosensing methods used to date for qualitative and quantitative analysis of PCR products. The focus is to study and compare these optical DNA detection strategies with respect to their sensitivity and POC compatibility [J1].

• Chapter 3 [**J2**, **C1**, & **C3**]: presents

- The principle of plasmonic DNA amplification.
- The design and development of VCSEL-based plasmonic thermocycler with high temperature stability and ramping rate.
- Zemax optical model to optimize VCSEL-tube separation distance for maximum beam coupling efficiency.
- o Successful DNA amplification in VCSEL-based plasmonic thermocycler.
- The comparison between conventional thermocycler and VCSEL-based plasmonic thermocycler in terms of amplicon yield.
- The experiments to test system reliability and performance under different conditions (*e.g.*, different controls and polymerases).
- The study of AuNRs robustness in plasmonic PCR reaction using spectroscopy, electron microscopy, and MATLAB image processing toolbox.
- o Plasmonic PCR protocol optimization to enhance heating and cooling rate.
- Heat transfer model to prove the presence of thermal lag in the system and subsequently to determine the limit of cooling rate enhancement.

• Chapter 4 [**J2**, **C2**, & **C3**]: presents

- o The principle of real-time UV monitoring of PCR-amplified target DNA.
- The design and development of real-time UV monitoring system for PCR product detection.
- o Development of Zemax optical model for UV detection.
- Investigation of safe UV exposure limit without compromising PCR yield.
- o Demonstration of PCR kinetics in UV amplification curve.
- Analysis of UV transmission data to classify PCR results (fail/success).
- o Quantification of amplicon limit of detection (LOD) in the UV system.
- Analysis of each PCR ingredients' impact on UV amplification curve.
- Quantification of detectable dNTPs concentration range by our UV detection system.

- o Measurement of the repeatability of UV experiments.
- The comparison between UV- and fluorescence-based detection of amplicons in terms of their LOD.

• Chapter 5 [C4]: includes

- o A brief explanation of the mathematical model presented by Booth et al.
- o The model calibration based on experimental UV amplification curves.
- The study of different PCR conditions impact on overall efficiency using the calibrated model.

• Chapter 6:

- o Summarizes the major work.
- o Presents the applications of the proposed work.
- o Provides recommendations for future research directions.

CHAPTER 2

Literature review

2.1 Introduction

Timely and accurate pathogen detection is essential to maximize patient safety, prevent disease transmission, and reduce health care costs. Control over target abundance during sample collection is challenging; thus, many pathogen detection strategies such as widely used and commercialized lateral flow assay fail to detect low-abundance nucleic acids. Nucleic acid amplification techniques such as polymerase chain reaction (PCR) provide detectable target concentration via enzymatic amplification. However, its practicality for POC testing is limited due to its size, assay time, and power consumption as well as skilled labor requirements. Consequently, a great deal of effort has been made to introduce a rapid portable and automated PCR device suitable for POC applications via optical or electrochemical means. Although, electrochemical methods are advantageous in certain applications, optical strategies are considered to have more multiplex capabilities, less costper-test, as well as less intervention in PCR reaction due to absence of electrodes. Conventional optical biosensing systems used for qualitative and quantitative analysis of PCR products such as UV-visible spectroscopy do not meet POC requirements. Therefore, miniaturization of traditional optical detection systems and novel optical biosensors are also considered. This chapter highlights the recent advances in optical amplification and detection of nucleic acids in PCR assay for their integration in POC settings. In particular, we describe advantages and shortcomings associated with different photonic approaches used in PCR-based DNA amplification and detection and compare these methodologies in terms of their sensitivity, simplicity, and practicality for POC applications.

2.2 A brief history of PCR development towards photonic PCR

The importance of identification and detection of pathogenic disease has been proven throughout history. Infectious diseases such as smallpox and the 1918 influenza pandemic with a global death

toll of over 300 million and 50 million respectively remain a dire warning for public health and safety [25-27]. The availability of vaccines and antibiotics since the mid-twentieth century have eradicated two major infections (smallpox and rinderpest) and protected global health against many infectious diseases [28, 29]. In 2015, the World Health Organization (WHO) reported that 17.1 million lives were saved thanks to the measles vaccines since 2000. Despite all the immunization and enhanced public health measures, the appearance of new pandemic viral infections has always been a threat, and many entering human population by host switching such as the emergence of severe acute respiratory syndrome coronavirus 2 (SARS-CoV-2) in December 2019 [30]. Hence, accurate and timely diagnostic tests are a fundamental need for determination of correct antibiotic to prevent antibiotic resistance and control the spread of life-threatening infectious diseases [31]. Conventional microbiological techniques such as traditional culture and serological methods suffer from low sensitivity, long turnaround time, and false negative results for patients receiving antibiotic therapy [32, 33]. Thus, the world's medical community has directed their attention to DNA/protein-based techniques, namely, nucleic acid amplification test (NAAT) for rapid and sensitive detection of pathogens in various fields from food industry, water and environment, forensic science to clinical applications [34, 35]. NAAT, also known as Polymerase Chain Reaction (PCR), was invented by Kary B. Mullis in 1985 [36]. PCR employs thermo-stable polymerase to generate millions of copies of specific segment of deoxyribonucleic acid (DNA) by thermocycling five core ingredients (DNA target sequence, thermostable polymerase, buffer, forward/reverse primers, and nitrogenous bases) typically through three sequential steps (denaturation, annealing and elongation) at different discrete temperatures. The set temperatures are around 94-98, 45-55, and 72 °C to allow separation of target DNA duplexes, hybridization of two primer sequences to complementary upstream and downstream of the specific region of denatured DNAs, and extension of annealed primers by incorporating four types of nucleotides (adenine (A), thymine (T), guanine (G), and cytosine (C)), respectively. These set temperatures are dependent on length of double stranded DNA (dsDNA), DNA sequence, and polymerase type. Melting temperature increases for longer DNA and more G-C bonded base pairs (bp) present in dsDNA. In fact, melting temperature is an indicator for scientists to reveal the base content of DNA [37]. Optimization of PCR temperatures governs PCR efficiency. As a case in point, polymerase inactivation and formation of primer dimers are the result of high melting temperature and suboptimal annealing temperature [38, 39]. Additionally, PCR efficiency is

dependent on other features such as PCR protocol (number of cycles and hold-times at each PCR step), DNA template structure and sequence, occurrence of undesired molecular interference, and reagents concentration [40]. The three-step thermal cycling is considered one PCR cycle, and normally a complete PCR process consists of 30 to 40 cycles carried out continuously in a device called thermocycler. In conventional PCR machines/thermocyclers, the 15-100 µL sample is placed in a thin walled polypropylene tube in contact with thermally conductive metal/solid-state Peltier blocks, and temperature regulation is carried out by thermoelectric energy conversion and heat conduction through metal blocks, PCR chamber, and finally PCR reaction. Therefore, power requirement, amplification time, and ramping rate depend on thermal properties and mass of metal blocks. Typically, Peltier-based PCR thermocyclers require approximately an hour and up to 1000 W electrical power to complete 30 to 40 PCR cycles due to large thermal mass and poor heat transfer between metal blocks and plastic tube. An example of such system is LightCycler® 1536 from Roche Molecular Systems, Inc. with heating and cooling rate of 4.8 and 2 °C/s, amplification time of 50 min, 55 kg weight, and power consumption of 1500 VA. Consequently, conventional PCR machines are confined to medical laboratories, and despite their high sensitivity and specificity, these machines are not accessible, cost-efficient, and fast enough to be deployed for point-of-care (POC) testing in resource-limited settings or during mass testing. Rapid therapeutic turnaround time is an important factor to decrease mortality rate and control the spread of disease. As a case in point, even with high sensitivity of one parasite.µL⁻¹, PCR is ineffective for malaria detection in endemic areas due to slow PCR process resulting in the death of one child every 2 min [41, 42]. Another example is the current situation in many countries struggling to keep up with the high demand for COVID-19 testing exceeding laboratory testing capacity.

It is reported that PCR assay is the most reliable and accurate test for detection of COVID-19; however, due to high cost (\$125/test) and slow turnaround time (at least 2-4 days), fast and inexpensive antibody-based testing kits are more popular [43]. False negative results have higher chances of occurrence in antibody tests than PCR [44]. This will jeopardize not only the health of test takers due to delayed treatment but also public health, as self-isolation is neglected, and the risk of unknowingly transmitting the virus to others is heightened. Consequently, both academic and industrial groups have focused on adapting PCR assay to POC diagnostics by minimizing time span between sample preparation and test results as well as reducing the PCR devices footprint while maintaining sensitivity. Factors such as optimal surface-to-volume ratio (SA/V), thermal

properties/mass of heating material/reaction vessel, and effective contact between heat source and reaction chamber can be tailored to improve heat transfer and shorten reaction time. The first step in PCR development was to increase SA/V and lower reaction volume for rapid heat transfer. As a result, the plastic PCR tube was replaced with at least five times higher SA/V glass or plastic capillary tube. Witter et al. took the second step by eliminating heavy metal blocks and directing hot and cold air onto glass capillaries [45]. Their method reduced the size of thermocyclers as well as amplification time; one PCR cycle only in 1 s. This was shortly employed in commercial PCR devices outpacing the Peltier-based heating/cooling instruments. Later, the same group used hot and cold water baths to thermocycle 1 to 5 µL PCR sample in 0.4 –2 s using a stepper motor to mechanically rotate the sample between water baths at denaturation and annealing temperatures [46]. The temperature was measured by a fine wire thermocouple in a parallel/control tube. In this method, rapid thermocycling is achieved by maintaining 1 liter of water at 95 °C and 74 °C with the use of electric hot plates. Although, these PCR instruments are an excellent diagnostic tool in medical laboratories, their size, speed, and power requirement do not meet the ASSURED (Affordable, Sensitive, Specific, User-friendly, Rapid and Robust, Equipment-free, and deliverable to users) criteria required for POC applications [47]. For example, PCR thermocycling with hot and cold water requires unnecessary heating of 1 liter of water at 95 °C and 74 °C for thermocycling 1 µL sample volume. Furthermore, water baths are made in 4.5 quart stainless steel dressing jars which results in not much reduction in hardware size compared to benchtop PCR machines.

Microchip PCRs possess all the POC testing requirements owing to both sample size and equipment miniaturization. The enhancement of SA/V from 8 mm²μL¹¹ for capillary tubes to 10, 17.5, and 20 mm²μL¹¹ for on-chip PCRs provides faster heat transfer, reduces the length of assay time and sample/reagents consumption without compromising the PCR specificity and sensitivity [7]. One of the commonly used material in micro-PCR chips is silicon due to its well-established fabrication technology, ease of mass production, resistance to high temperature, and superior thermal conductivity [48]. Recently, a disposable silicon-based micro-qPCR chip was introduced by Bajo et al. which integrates electrical heating, resistance thermometry, and label-free electrochemical amplicon sensing [49]. Silicon microchips were also used for real-time fluorescence-based PCR with improved sensitivity for the detection of pathogen genomes of both

viruses and bacteria compared to standard PCR system [50]. The well-developed silicon industry allows facile fabrication of thousands of consistently sized nanoscale reaction wells by etching silicon substrate to enable precise sample partitioning for digital PCR. The advantage of digital signal (high and low) detection is simpler instrumentation, as the optical sensor needs to only detect the difference between a positive and negative partition. The ratio of positive to negative partitions can then be related to the number of DNA copy numbers in the sample, using Poisson statistics. Although digital PCR enables sensitive and absolute target quantification, the commercially available digital PCR instruments have multi-step PCR process using multiple devices apart from PCR thermocycler such as automated chip loader and chip reader [51]. Consequently, for the use of digital PCR in field testing, the workflow should be more automated and carried out in a single device. Moreover, silicon-based micro-PCR chip has its own complications. For instance, bare silicon inhibits PCR, the opacity of silicon degrades optical detection, high thermal conductivity of silicon requires proper thermal isolation, and combination of micro-PCR and micro capillary electrophoresis is not feasible due to high electrical conductivity of silicon [48].

Microfluidic PCR systems are categorized into two groups of time and space domain PCR [6, 52-54]. Time domain or static chamber PCR is attributed to microfabricated PCR device resembles to traditional thermocyclers in which the sample is stationary, and contact/noncontact methods are used to regulate the reaction temperature. In time domain PCR with contact heating, resistive heaters and miniaturized Peltier-based ceramic blocks were employed for temperature regulation [55]. One main problem with contact heating resistors fabrication is the complicated and highly required precision in thin film metals deposition and patterning as well as sample placement to be in contact with heaters. Although, static microchip PCRs reduced amplification time and power consumption by lowering sample size and heat capacity of total PCR system, these systems are still slow and power-intensive due to thermal inertia as a result of unnecessary heating of resistive film heaters and metal heating blocks. To overcome these limitations, many groups explored noncontact sample heating via hot air stream, induction heating, infrared (IR), and microwave radiation benefiting from strong IR absorption of water and water molecules rotation in response to applied electric field [56-58]. Another solution to reduce thermal mass of PCR device is using a space domain configuration in which the sample flows through microchannels/zones at three different PCR temperatures. In flow-through/space domain PCR sample moves in capillary tube

(off chip) [59], serpentine microchannel (on chip) [60], and radial/circular channel design (on/off chip) [61] using syringe pump [62], centrifugal force [63], capillary force [64], magnetic force [65] to direct PCR solutions to different zone temperatures. In serpentine flow-through PCR, the interaction of biomolecules with chamber walls due to continuous and repetitive travel of sample solution leads to lower sensitivity and PCR yield. During the design procedure of serpentine flow-through PCR, the number of cycles is configured on microchip; hence, after chip fabrication, amplification time and cycle number cannot be altered. However, the problems with flow-through PCR were solved in circular flow-through PCR in which not only sample travels shorter distance, but also the number of cycles can be adjusted [66, 67].

Although, literature is rife with advancement in microfluidic PCRs, the adaptation of micro devices to macro-environment (macro-to-micro interface) encounters with some difficulties which is often neglected in research studies. The idea of sample and equipment miniaturization was built upon faster PCR devices suitable for POC application; however, the practicality of these devices for on field sample analysis is controversial. Microchambers are designed for nanolitre and picolitre sample volume, whereas typical reagents volume is in the order of microlitres. This becomes more critical when a microfluidic device is introduced as a POC device in which sample loading and fluid handling can be performed by non-laboratory personnel.

In light of the challenges associated with contact heating methods and microfluidic PCRs, photonic PCR pioneered by Landers group became popular among researchers to introduce faster and more POC compatible PCR devices [68]. Light to heat conversion eliminates the need for a heat transfer medium with good thermal contact. In these systems, electromagnetic (EM) radiation is absorbed by the target medium (*i.e.*, PCR reaction) directly, and thereby this reduces thermal mass by eliminating unnecessary heating of microchamber, vessel, or PCR tube, consequently increasing heating rate. The absence of heat transfer medium also increases cooling rate, as the heat is only removed from sample, *e.g.*, not from Peltier blocks. Other factors controlling heating and cooling rate in photonic PCR devices are the spectral power distribution of the light source, focusing power of optical elements, sample volume, SA/V of PCR chamber, PCR chamber material, nanoparticles (NPs) concentration in nanoPCR devices, and type of sealant. It should be noted that photonic thermocyclers facilitate rapid enzymatic amplification of low abundant target/nucleic acid in sample; however, in order to quantify amplicons and subsequently learn PCR results, a detection

strategy should be integrated into these thermocyclers for a complete analytical PCR assay. Therefore, some groups tried to adapt conventional optical detection systems for POC applications through miniaturization (*e.g.*, capillary electrophoresis and fluorescence detection), while others investigated novel optical methodologies such as nanoengineered optical probes. These detection paradigms are integrated into conventional, microfluidic, or optical thermocyclers for a complete PCR-based diagnostic device. Thus, the combination of PCR thermocyclers with these optical biosensors makes them powerful and sensitive diagnostic tools since the common problem of low target concentration in test sample is resolved by their amplification in PCR assay.

In this chapter, we categorize optical methodologies used in PCR assay in two groups. First, photonic thermocyclers having been developed to date for fast target amplification are presented and compared in terms of their speed, practicality for POC testing, and light-to-heat conversion efficiency. In the second half of this chapter, optical strategies used for PCR product detection are described with emphasis on the challenges within their fabrication, target detection, and their translation to POC platforms. Lastly, sensitivity or limit of detection (LOD), the most critical performance parameter in diagnostic test, is listed and compared for each work.

2.3 Optical amplification

IR-mediated and laser-assisted heating of PCR solution can be categorized in two groups: i) optical intrinsic and extrinsic heating (Figure 2.1). In the former category, PCR solution is irradiated by a broadband IR light source benefiting from intrinsic optical absorption property of the most copious PCR ingredient, water. Since water has high absorption in IR region (2.66, 2.78, and 6.2-8.5 μm), upon exposure to IR light, the optical energy is absorbed through intramolecular vibrational transitions, and this excitation energy is converted to heat. In the second category (extrinsic heating), the absorption property of PCR reaction is enhanced with the addition of an extrinsic element, *i.e.*, noble metal NPs or thin noble metal film. Hence, with laser irradiation at their plasmon wavelength, these NPs act as nanoheaters inside PCR reaction. Consequently, for the light-assisted PCR thermocyclers proposed to date, light sources such as tungsten filament/halogen lamp, LED, and laser diode were used, and their output optical power was directed on a PCR capillary tube, microchip, or conventional plastic tube. Researchers employed different optical components such as lenses or gold-coated mirror to focus and reflect stray radiation back on to PCR sample. In some studies, the visible radiation of broadband IR light source is blocked by

long-pass IR filter to eliminate visible wavelength interference with PCR components and allow accurate fluorescence measurements in real-time PCR. Cooling in photonic PCR devices is carried out by natural or forced convection either by chilled or at room temperature air. In case of droplet-based microfluidics (water-in-oil emulsions), PCR reaction droplets are cooled by the dispersed phase of water-in-oil emulsions through natural convection. Temperature is measured *via* inserting a thermocouple into PCR chamber or a dummy chamber close to PCR chamber which is filled up with PCR buffer and receives the same amount of optical power as PCR solution. However, insertion of any type of contact sensing probe inside PCR reaction requires surface passivation to avoid PCR inhibition. This will add to system complexity and fabrication cost. As a result, some studies utilized non-contact temperature reading methods such as detecting IR thermal radiation or adding temperature sensitive dyes into PCR reaction for laser induced fluorescence thermometry [69]. In order to prevent sample evaporation and bubble formation, PCR fluid is mostly sealed by mineral oil, epoxy glue, Teflon septa, PCR sealing tape, acrylic adhesive, or silica gel. A closed-loop temperature control system is also typically included.

The non-contact nature of photonic PCR devices and the ability to control fluids motion by light circumvent the need for complicated fabrication of heaters (*e.g.*, thermoelectric heater/cooler and resistive heaters), fluidic circuitry components (*e.g.*, pumps and valves). Furthermore, light source can be placed far from PCR chamber or outside the microchip which allows fabrication of simpler devices and even disposable PCR sample containers. In other words, PCR microchips are only the housing of sample without integrated pumps, valves, and heaters; thus, the fabrication cost is significantly reduced, and microchips can be disposed after each PCR experiment to preclude the necessity of cleaning, drying, and repassivation of PCR chamber after each run and to prevent run-to-run cross contamination.

| | Optical thermocyclers | | | | | | | | | | |
|--|-------------------------------|--------------------------|--------------------------|----------|--------------------|--|--|--|--|--|--|
| | Intrinsic h | eating | Extrinsic heating | | | | | | | | |
| | IR-mediated | Nanodroplet | Plasmonic | | | | | | | | |
| Light Source | IR lamp ¹ | Laser diode ² | LED ³ | Laser di | VCSEL ⁵ | | | | | | |
| Cooling | NC, CA, & Fan | Oil Cooling | Fan | | | | | | | | |
| Thermometry | Non-contact (IR) & Contact | Fluorescence | Contact Non-contact (IR) | | | | | | | | |
| Sample volume | 160 nL-10 μL | 10 nL-30 nL | 5 μL-25 μL | | | | | | | | |
| $^{1}P_{o}$: 50 W & 100 W NC: Natural convection $^{2}P_{o}$: 0.02 W-1 W, λ_{p} : 1460 nm & 1480 nm CA: Compressed Air $^{3}P_{o}$: 3.5 W, 3.8 W, & 20W, λ_{p} : 447.5 nm & 850 nm $^{4}P_{o}$: 2 W & 2.7 W, λ_{p} : 532 nm & 808 nm $^{5}P_{o}$: 2 W, λ_{p} : 808 nm | | | | | | | | | | | |

Figure 2.1 Classification of optical thermocyclers based on intrinsic and extrinsic optical heating of PCR reaction.

2.3.1 Broadband IR-mediated PCR (Optical intrinsic heating)

One of the first optical ultrafast temperature cycling was proposed by Landers and coworkers in which a 50 W tungsten filament lamp irradiated a 160 nL PCR sample placed in a fused-silica capillary [11]. Since the lamp radiation wavelength (0.35-3 µm) overlaps with water intramolecular vibrational wavelengths in IR range (≈3 μm and 6.2-8.5 μm) with high absorption coefficient of approximately 10⁴-10⁶ cm⁻¹ [70], the optical power of lamp is absorbed and increases the amplitude of molecular vibration and consequently the water temperature. Moreover, the capillary made of fused-silica is highly absorptive in IR region leading to better photon-to-heat conversion. The capillary vessel provides high SA/V, and compressed air at 20 °C was used to maximize the cooling rate. Since shorter wavelength of light (<600 nm) are detrimental to DNA, to avoid photolysis a long pass filter was used between the PCR capillary and light source. This IR-mediated PCR system was able to amplify 500 bp λ -bacteriophage DNA with heating and cooling rates of 30 and 15 times faster than conventional thermocyclers. Later, the same group used polymeric/glass microdevices with convective fan, non-contact temperature reading method (IR pyrometer), and gold coated parabolic mirror to focus scattered light on sample to achieve faster thermocycling and avoid contact-based temperature sensor (thermocouple) PCR inhibition [71]. Other groups utilized the idea of IR-mediated PCR on microchips to obtain faster thermocycling by reducing sample size [9, 72]. Figure 2.2 demonstrates two different setups used for IR heating of sample in microchips and the resulting PCR temperature profile. Giordano and coworkers focused 50 W tungsten lamp IR radiation via plano-convex lens on 2 mm (W)×5.5 mm

(L)×150 mm (H) polyimide microchip containing 1.7 μL PCR reaction [73]. Additionally, similar to previous works, a gold-coated mirror and long pass filter were used to reflect back scattered light on PCR chamber as well as to selectively transmit IR radiation of the light source. In order to measure temperature directly with a type-T thermocouple, polyethylene glycol was added to PCR fluid to avoid polymerase inactivation. Finally, amplification of 500 bp λ -bacteriophage DNA was confirmed *via* capillary electrophoresis. Later, Landers group proposed surface passivated glass microchip performing DNA extraction from whole blood, optical amplification of 380 bp β -globin gene, and microchip electrophoresis with laser induced fluorescence technique [57]. Their method was a breakthrough in photonic PCR by introducing a complete micro-total analysis system from whole blood DNA extraction to identification of amplified DNAs. The simplicity in design of IR-mediated PCR devices encouraged researchers to integrate optical amplification methods with sample preparatory microchips such as solid-phase extraction procedure for DNA purification. This can be seen in Legendre *et al.* work in which solid-phase extraction bed *via* DNA adsorption on silica surface was interfaced with photonic PCR domain on a single microchip [74].

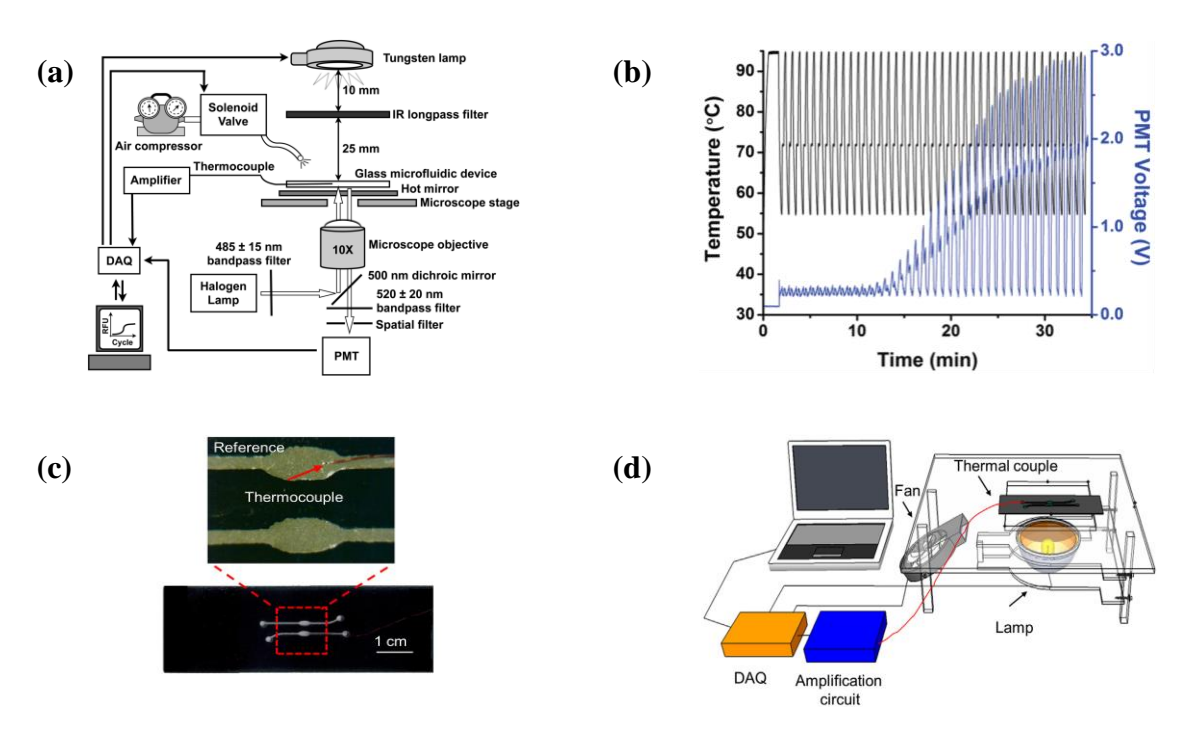


Figure 2.2 (a) Layout of infrared PUC19 amplification and fluorescence detection on glass microchip. (b) Temperature profile and real-time fluorescence measurement 304 bp PUC19 amplification. Reprinted from Ref. [72], Copyright (2012), with permission from American Chemical Society. Schematic of (c) Polyester-toner (PeT) microchip with a PCR chamber and a dummy chamber for temperature measurement and (d) IR heating and forced air cooling setup for PeT microchip. Reprinted from Ref. [9], Copyright (2015), with permission from Elsevier.

For faster thermocycling, the chamber material is required to be transparent and less IR absorptive than water. PMMA or plastic is an example of a suitable material choice which was used for fabrication of IR-mediated oscillatory thermocycler equipped with fan and linear motor to cool and oscillate reaction chamber [75, 76]. Microchip substrates made of silicon are also of interest due to its high thermal conductivity and well-established mass production. Silicon was shown to provide uniform heating throughout the sample, high compatibility with biomolecules, and low-cost fabrication making it an excellent material to be utilized for miniature POC devices [77]. Table 2.1 demonstrates list of photonic PCR devices with broadband IR lamp proposed to date. It is of great importance to compare these optical thermocyclers in terms of their speed and optothermal efficiency. To fulfill this, the thermal energy (Q) needed to increase sample temperature from elongation to denaturation ($\Delta T_{E\to D} = T_D - T_E$) and from annealing to elongation step ($\Delta T_{A\to E} = T_E - T_A$) for one PCR cycle is calculated using heat capacity of water (C) and sample mass (m) in each study.

$$Q_{\text{cvcle}}(j) = mC(\Delta T_{E \to D} + \Delta T_{A \to E})$$
(2.1)

The power ($P_{photothermal}$) required to increase sample temperature in one cycle can be estimated by the ratio of Q_{cycle} and heating duration of one PCR cycle. Heating duration per cycle $(t_{T_E \to T_D} + t_{T_A \to T_E})$ is calculated using the reported heating rate and total temperature increase per cycle $(\Delta T_{E \to D} + \Delta T_{A \to E})$ in each study, and for studies in which heating rate is not provided, the total cycle duration (t_{cycle}) was used to obtain $P_{photothermal}$.

$$P_{\text{photothermal}} = \frac{Q_{\text{cycle}}}{t_{T_E \to T_D} + t_{T_A \to T_E}}$$
(2.2)

The photothermal efficiency $(\eta_{photon \rightarrow heat})$ is obtained by using the ratio of calculated $P_{photothermal}$ to the optical power emanating from the light source (P_{in}) . For studies with unreported heating rate, the calculation of $P_{photothermal}$ with t_{cycle} leads to lower efficiency.

$$\eta_{\text{photon}\to \text{heat}} = \frac{P_{\text{photothermal}}}{P_{\text{in}}}$$
(2.3)

Table 2.1 Photothermal efficiency in photonic PCR devices using broadband IR lamp.

| Ref. | Lamp type | $P_{in}(W)$ | Cooling Method | PCR chamber | V(µL) | $t_{cycle}(\mathbf{s})$ | Heating rate(°C/s) | Cooling rate(°C/s) | Q _{cycle} (j) | P photothermal (mW) | %onphoton→heat |
|------|-----------|-------------|----------------|---|-------|-------------------------|--------------------|--------------------|------------------------|---------------------|----------------|
| [68] | Т | NS | CA | Glass microchambers | 5 | 17±0.4 | 10 | 20 | 0.83 | 208.97 | NA |
| [11] | Т | 50 | CA | Glass capillary tube | 0.16 | 38.4 | 65 | 20 | 0.02 | 43.5 | 0.087 |
| [73] | Т | 50 | NC | Polyimide microchip | 1.7 | 16 | 10 | 10 | 0.18 | 71.04 | 0.142 |
| [57] | NS | NS | NC | Passivated glass microchamber | 5 | 25.71 | NS | NS | 0.71 | 27.64 | NA |
| [77] | Н | 100 | Fan | Silicon microreactor | 7 | 81.6 | 4 | 4 | 1.17 | 117.03 | 0.117 |
| [78] | Т | 50 | Fan | Glass microchip | 0.28 | 24.4 | 13.4 | 6.4 | 0.04 | 5.50 | 0.011 |
| [74] | Т | 50 | Fan | Glass microchip | 0.33 | 32 | NS | NS | 0.05 | 1.42 | 0.003 |
| [71] | Т | 50 | Fan | Glass microchambers | 0.55 | 37.6 | NS | NS | 0.06 | 1.65 | 0.003 |
| [72] | Т | 50 | CA | Glass microchamber | 10 | <60 | NS | NS | 1.67 | 27.86 | 0.056 |
| [79] | Т | 50 | CA | Glass microchamber | 2 | NS | NS | NS | 0.33 | NA | NA |
| [9] | Т | 50 | Fan | PeT microchip | 2 | 70 | 10.1 ±0.7 | 12± 0.9 | 0.23 | 84.53 | 0.169 |
| [75] | NS | 100 | Fan | PMMA-based chamber within oscillatory reactor | 10 | 100 | 1.73 | 1.26 | 1.55 | 72.30 | 0.072 |

T: Tungsten, H: Halogen, NS: Not Specified, CA: Compressed Air, NC: Natural Convection, NA: Not Applicable.

2.3.2 Laser-assisted nanodroplet PCR (Optical intrinsic heating)

Lasers produce collimated beam with low divergence and narrow spectral bandwidth compared to broadband IR light sources. These intrinsic characteristics of lasers have motivated many groups to replace IR light sources with lasers in optical thermocyclers. The superiority of lasers was mainly revealed in microfluidic PCR devices in which more focused light beam is desired for small sample volume [80]. Moreover, the output optical power of lasers is concentrated at one specific

wavelength (monochromatic beam) which targets absorption wavelength maximum of PCR solution/water leading to higher photothermal efficiency. This contrasts with IR lamps having their power distributed over a broad IR spectrum, and only the small wavelength range overlapping with water absorption peak wavelengths contributes to photothermal effect. As a case in point, Pak developed a laser-mediated PCR using a 1450 nm laser diode with 580 mW power collimated on a PMMA-based microchip loaded with 820 nL PCR reaction, and their device was able to amplify 500 bp λ -bacteriophage DNA in 10 min [81]. The manipulation of light in microfluidics to control flow rates, flow direction, mixing, and separating chemicals obviates the need of classical microfluidic components such as microvalves or external pumps. By incorporating this capability of light in fluidic circuitry, new generation of valve-less and pump-less PCR microfluidics were introduced as droplet-based PCR. Discrete nanoliter or picolitre volume of PCR reaction in the form of droplet is pipetted in an immiscible liquid (oil) providing high SA/V for rapid heat transfer. The size and shape of droplets depend on the viscosity of immiscible phase, hydrophilicity of channel surface, and channel geometry [82]. Two fundamental forces govern droplets motion in oil phase: thermal Maragoni effect and convection current. Surface Marangoni flow is induced by surface temperature and tension gradient between two fluids which applies a net force on droplet leading to mass transfer or motion [83]. The temperature difference between water droplet and oil phase originates from oil weaker absorption in IR region compared to water and nonuniform heating of water-in-oil emulsions. Also, the photothermal heating of oil generates convective current in oil phase which is used to control droplets motion. The velocity of droplets in oil is dependent on droplets size and oil viscosity, i.e., smaller droplets move faster in oil bath with lower viscosity. Deceleration and immobilization of droplets can be controlled by reducing laser power and as a result lowering the amount of heat generated in oil. The oil's viscous drag force decreases droplets velocity to be finally settled and immobilized.

Terazono *et al.* demonstrated a real-time droplet-based PCR in which 10-30 nL PCR droplets were placed on a glass plate using glass micropipettes. The plate was covered with mineral oil at a constant annealing temperature (60 °C) [84]. The IR heating and real-time detection were executed with a 1 W laser (λ_0 =1.48 µm) and a mercury lamp, respectively, and they were both focused on PCR droplets through an objective lens. During amplification, an inverted microscope was used to detect spatial distribution of the droplet's fluorescence emission containing SYBR Green I. Laser-assisted amplification and detection was completed in 3.5 min for 50 cycles.

In the absence of temperature sensor in droplet microfluidic, a relationship between laser irradiation power and temperature of droplet is established, so that temperature is regulated by laser power modulation. To obtain this relationship, first, the temperature of droplets is calibrated based on the fluorescence quenching of a temperature sensitive fluorescence dye (e.g., rhodamine B) as a result of applying heat to droplets. Next, the fluorescence intensity response to the temperature variation as a result of applying heat via laser irradiation is recorded. Finally, using the emission intensity-temperature and emission intensity-laser power relations, the relationship between irradiation power and temperature can be estimated. Results from this work indicated that with laser power of 0.9 W the heating rate can reach up to 33.6 °C/s. This method of laser powertemperature calibration necessitates formation of uniform-sized droplets since the laser power adjustment for specific heating rate is only valid for particular size of droplet which in this work is droplets with 20-30 μ m diameter. Droplets with higher diameter (D > 20-30 μ m) will be slow in reaching the denaturation stage, and smaller droplets often evaporate. Therefore, droplets are often placed on a dish by using a micropipette equipped with a linear actuator to control their motion and create uniform-sized droplets (Figure 2.3.a and Figure 2.3.c) [85]. Other works utilized lower laser power (30 mW and 50 mW) at 1.46 µm with disposable plastic substrate and micropipettes to amplify PCR droplets of 20 to 100 nL dispersed into oil phase [85, 86]. Their method was able to replicate 187 bp eukaryotic 18S rRNA gene in 370 s for 40 PCR cycles. The selection of laser wavelength favors a strong absorption band in liquid water while plastic and oil have weak absorption at that wavelength. Similar to the Terazono study, other droplet-based PCR studies use real-time fluorescence detection method via microscope imaging of droplet arrays. In study conducted by Hettiarachchi et al., light-assisted droplet-based PCR was used to perform cell lysis and amplification of 133 bp eukaryotic 18S rRNA gene via reverse-transcription polymerase chain reactions (RT-PCR) in less than 15 min. MDA-MB-231 breast cancer cells, lysis buffer, PCR reagents were positioned as three separate droplets on Petri dish surface, and by directing or defocusing laser beam at a target droplet, the target droplet is moved towards or away from other droplets for droplets combination, separation, and heating (Figure 2.3.d) [87].

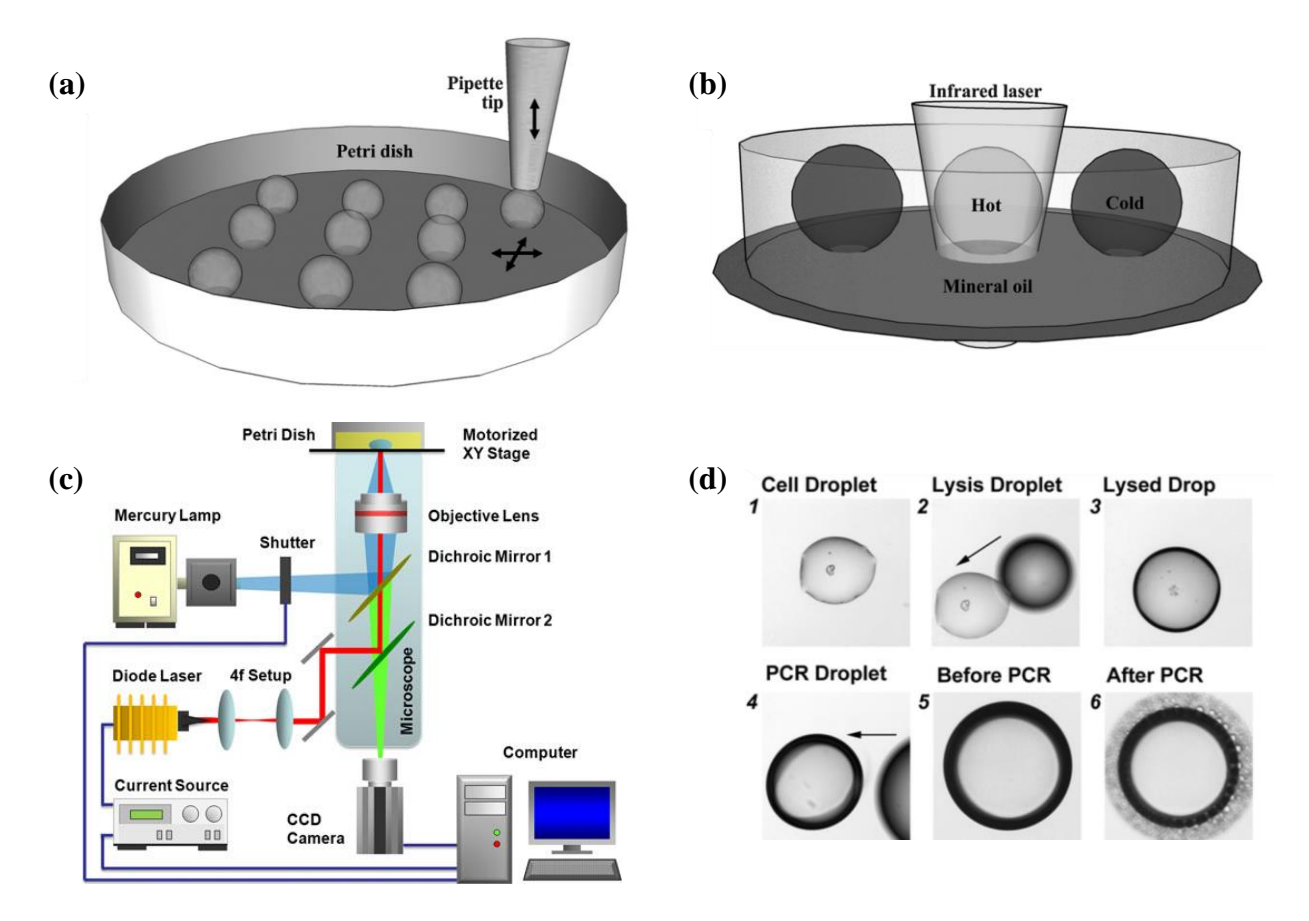


Figure 2.3 (a) Droplet array loaded in mineral oil using home-built contact printing system. (b) Laser-assisted heating of droplet with 200 μm beam size at FWHM. Reprinted from Ref. [85] with permission from the Royal Society of Chemistry. (c) Schematic description of laser-irradiated nanodroplets dispersed in mineral oil for PCR on a microscope stage. (d) Droplets of phosphate-buffered saline containing single MDA-MB-231 breast cancer cells (1) and lysis buffer (2) are optically combined to perform cell lysis (3), and PCR reagents droplet (4) will be coalesced with lysed droplet (5) *via* laser beam manipulation for amplification (6). Reprinted from Ref. [87], Copyright (2012), with permission from Springer Nature.

One of the challenges with PCR droplet-in-oil emulsion is the precise optical alignment of laser and microscope on droplets with diameter of hundreds of micrometers to achieve optimal light to heat conversion and sensitive detection. Suboptimal alignment between laser and droplet leads to temperature rise in the surrounding medium such as plastic substrate/polystyrene Petri dish which undergoes temperature-dependent deformation around denaturation temperature (T_D). Moreover, the dispersed sample in oil is difficult to recover for post-PCR manipulations or detection particularly for on-site sample analysis. Also, as discussed earlier, droplets are not immobile upon laser irradiation, and they move with different velocities leading to cross-contamination between samples. The more challenging aspect is to control the movement of cell droplet towards the PCR reagents droplet with the help of laser beam for a complete PCR from cell lysis to amplicon

generation. Lastly, temperature-laser power calibration starts with relating fluorescence intensity to temperature and later relating laser power to fluorescence intensity and temperature. This calibration method depends on the droplet size, type of laser, and microchip design. Hence, the relationship between laser power and temperature is unique for different droplet microfluidic, and its calibration process is considered labor-intensive and more liable to operational errors. Various laser-assisted droplet-based microfluidics presented since 2008 is demonstrated in Table 2.2. The photon-to-heat conversion efficiency ($\eta_{photon\rightarrow heat}$) for each study can be calculated using Druett equation [88]. Assuming only conductive heat loss, for a perfect sphere at temperature T_1 suspended in fluid at temperature T_0 , the energy per second (P_{sphere}) required to maintain sphere's temperature constant at T_1 , can be calculated as follows:

$$P_{\text{sphere}} = 2\pi k (T_1 - T_0) D \tag{2.4}$$

Where k is the thermal conductivity of fluid, and D is the diameter of the suspended sphere. For the case of droplet-based PCR, the required power (P_{sphere}) to keep droplet with diameter D at denaturation temperature ($T_D = 90\text{-}95$ °C) while suspended in mineral oil with thermal conductivity of $0.15 \frac{W}{mK}$ at annealing temperature ($T_A = 55\text{-}60$ °C) can be calculated as is shown in Table 2.2. Analogous to photothermal efficiency ($\eta_{photon \to heat}$) stated for optical PCR devices with broadband IR light source, the ratio of P_{sphere} to laser power (P_{in}) gives the efficiency of photon-to-heat conversion ($\eta_{photon \to heat}$) in droplet PCR assay.

$$\eta_{\text{photon}\to \text{heat}} = \frac{P_{\text{sphere}}}{P_{\text{in}}}$$
(2.5)

As is shown in Table 2.2, the maximum $\eta_{photon \to heat}$ is 0.44 indicating the most efficient optical droplet-based PCR presented to date.

Table 2.2 Comparison of droplet-based PCR devices in terms of their speed and photothermal efficiency.

| Ref. | P _{in} (mW) | Light source | λ(nm) | D(µm) | $\mathrm{T_D/T_A}{=}\mathrm{T_E}$ | V(nL) | $\mathfrak{t}_{\operatorname{cycle}}(\mathbf{s})$ | $P_{\rm sphere}(mW)$ | %¶photon⊸heat |
|------|----------------------|--------------|-------|---------|-----------------------------------|-------|---|----------------------|---------------|
| [84] | 1000 | LD | 1480 | 200-300 | 90-95/60 | 10-30 | 4.2 | 0.66-0.99 | 0.07-0.1 |
| [85] | 25-50 | LD | 1460 | 300 | 95/60 | 12 | 9 | 9.9 | 19.8-39.6 |
| [86] | 30 | LD | 1460 | 300-400 | 93/58 | 30 | 9.25 | 9.9-13.2 | 33-44 |
| [87] | 20-40 | LD | 1460 | 200 | 95/55 | NS | 14 | 7.54 | 18.8-37.7 |

LD: Laser Diode, NS: Not Specified.

Furthermore, using the total amplification time and number of cycles presented in each study, we can obtain the time per cycle (t_{cycle}); however, heating and cooling rates are lacking in these studies. Therefore, here, we modeled these droplets with the same diameters stated in each work by COMSOL Multiphysics simulation software to obtain time transient thermal cooling of droplets. In this model, COMSOL module for heat transfer in solids and fluids was used to derive time dependent thermal cooling of a droplet with dimeter D at denaturation temperature (T_D =90 °C) dispersed in mineral oil at constant annealing temperature (T_A =60 °C). Next, water-in-oil emulsion is placed in a polystyrene Petri dish with 2 mm thickness. The size of Petri dish is similar to conventional disposable Petri dish available in market (100 mm×15 mm). Figure 2.4 shows our COMSOL model geometry and time-dependent cooling temperature profile for droplets with different sizes. For the sake of better visibility of droplet in Figure 2.4.a, the droplet diameter is set at 2 mm.

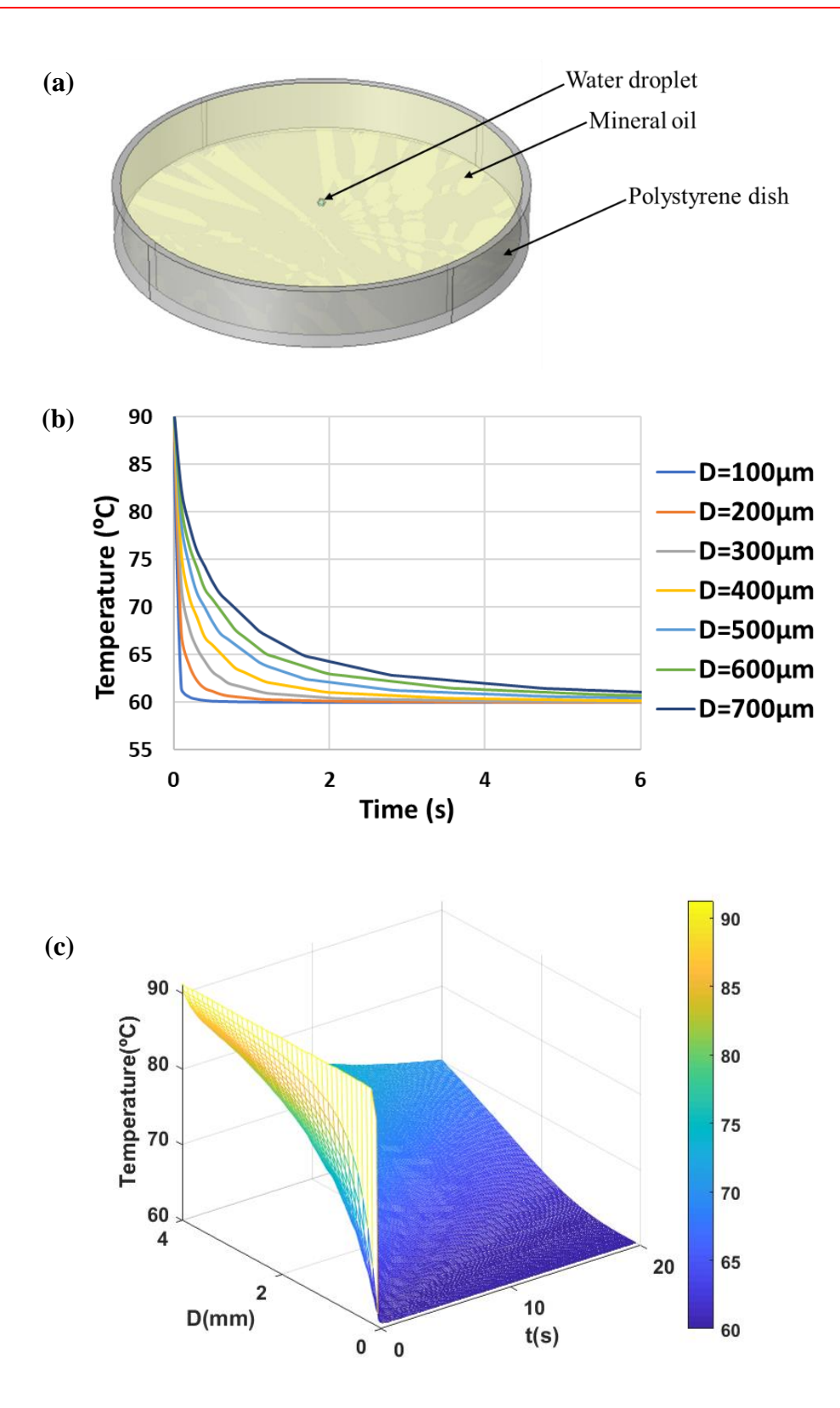


Figure 2.4 (a) COMSOL 3D geometry to obtain time-dependent temperature cooling of droplet centered in mineral oil. (b) 2D and (c) 3D plot of time-dependent thermal cooling of droplet with varying diameter (D).

The simulation presented above was based on the analysis of a single droplet in the center of an oil bath. However, in droplet-based PCR, droplet arrays are placed in the oil bath. It is expected that the relation between D and cooling time (t) will follow the single droplet analysis. In order to confirm this, a droplet array of 5×5 at pitches of 2 mm with 400 µm diameter is placed in the same COMSOL model (Figure 2.5), and time-dependent thermal cooling for the droplets is studied. The results demonstrate that the central droplet in 5×5 droplet array has the same cooling rate as a single droplet in oil; furthermore, the droplets on outer side of the array cool as fast as the central droplet. Hence, heating and cooling time durations per cycle for each study are calculated based on single droplet model.

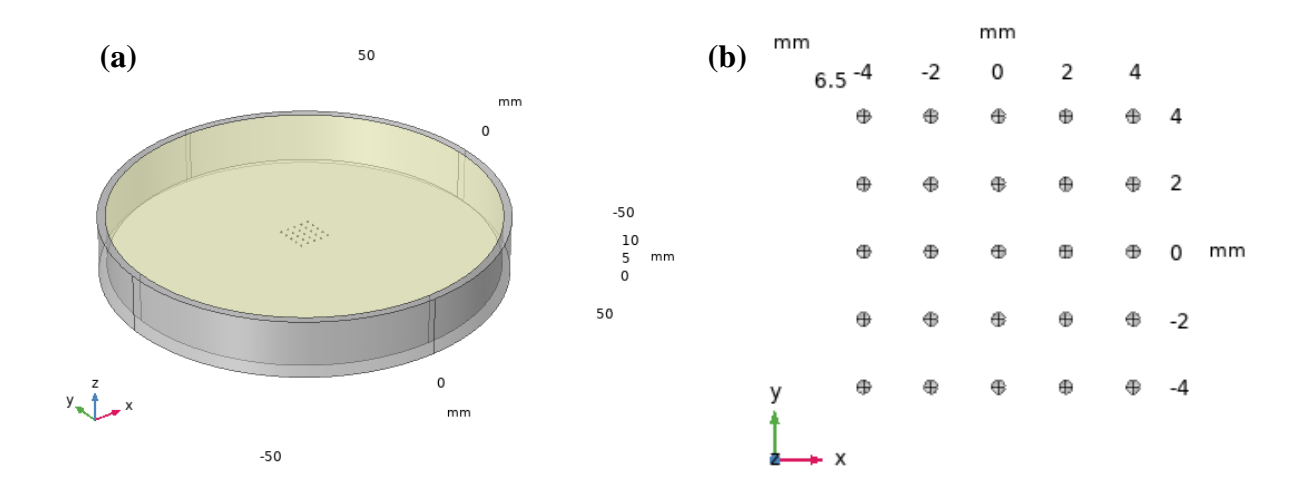


Figure 2.5 (a) COMSOL geometry used for time-dependent heat-transfer analysis of 5×5 droplet array. (b) close-up view of model geometry for 5×5 droplet array.

Using single droplet model, the droplet diameter and oil temperature used in each study was implemented to the model to obtain time duration between denaturation and annealing step $(t_{T_D \to T_A})$ in that study (Figure 2.6). Consequently, by subtracting cooling time duration from total cycle time (t_{cycle}) , the heating time duration $(t_{T_A \to T_D})$ can be calculated for each study (Table 2.3). Smaller $t_{T_A \to T_D}$ is the result of finer optical alignment and better beam focusing on PCR droplet.

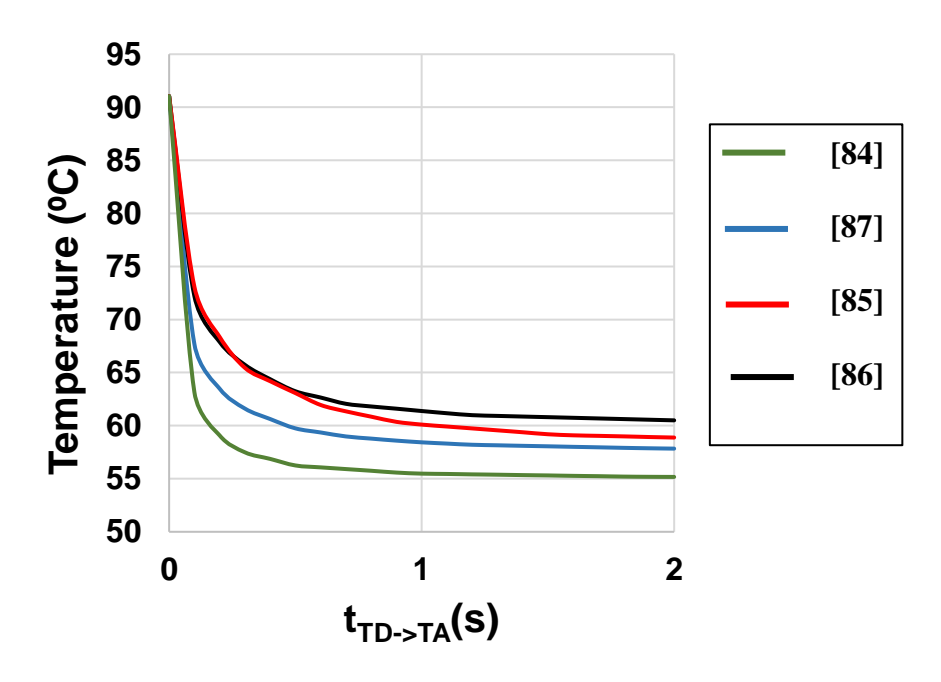


Figure 2.6 Time-dependent cooling from denaturation to annealing stage for aforementioned droplet PCR studies using single droplet COMSOL model.

Table 2.3 Comparison between heating and cooling time durations for different droplet PCR devices.

| Ref. | $t_{T_D 	o T_A}$ (S) | $\mathbf{t}_{\mathrm{T_A} ightarrow \mathrm{T_D}} \left(\mathbf{s} \right)$ | DNA target/Initial DNA copy number | dq# | Polymerase Type | Cell lysis |
|------|----------------------|---|---|-------------|---|------------|
| [84] | 0.5 | 3.7 | Bacillus subtilis DNA/1, 10, and 1000 | 72 | KOD plus polymerase | |
| [85] | 1.2 | 7.8 | Eukaryotic 18S rRNA gene/8000 | 187 | Taqman Fast Universal PCR Master Mix | |
| [86] | 1.8 | 7.45 | Eukaryotic 18S rRNA gene/120- 160 | 187 | Taqman Fast Universal PCR Master Mix | |
| [87] | 0.7 | 13.3 | Eukaryotic 18S rRNA gene; BRCA1 gene /NS | 133 /255 | PerfeCTa SYBR Green FastMix | • |

NS: Not specified.

2.3.3 NanoPCR

2.3.3.1 Nanomaterial-assisted PCR

Researchers have been investigating methods to overcome PCR obstacles governing PCR efficiency; for instance, many articles reported unsuccessful attempts to amplify DNA with high GC content and high melting temperature [89]. The most practiced methods are reagent concentration (primers, polymerase, DNA, and magnesium ions) and PCR protocols (temperatures, hold-times, and cycle numbers) optimization, enzyme modification, as well as designing touchdown and nested PCR strategies [90]. Alternatively, the implementation of PCR additives such as betaine [91, 92], tetramethyl-ammonium chloride [93], formamide [94], and glycerol [95], was another approach to enhance PCR efficiency by focusing on complete DNA denaturation and stability. The second group of additives is nanomaterials which the span of their application varies from cell lysis, PCR specificity/efficiency/selectivity enhancement, to lowering limit of detection in qPCR. Due to their superior electrical, optical, mechanic, magnetic, and structural properties, nanomaterials such as gold/silver nanoparticles (AuNPs and AgNPs) [96, 97], carbon nanotubes (CNTs) [98], quantum dots (QDs) [99], graphene oxide (GO), reduced graphene oxide (rGO) [100], titanium oxide nanoparticles (TiO₂NPs) [101], and other metallic nanomaterials and nanocomposites [102] have been extensively used in PCR assay. All nanomaterials provide high SA/V and easy tunability in their physical dimensions which give rise to their high thermal conductivity and activation of particular optical, electrical, or chemical properties. In addition, since each nanomaterial has unique features, their utilisation is applicationdependent. For instance, AuNPs are popular for their stability and biocompatibility, and facile surface modification, CNTs for their mechanical strength, and GO for their fluorescence quenching ability, hydrophilic quality, and easy covalent functionalization [103].

Nanomaterial-assisted PCR also known as nanoPCR, was initially introduced as an approach to enhance thermal conductivity of nanofluids (dispersion of nanomaterials in base fluid) due to heat transfer property of nanomaterials. After numerous developments in microfluidic PCR, researchers remarked that addition of nanomaterials inside PCR reaction accelerates the rate of amplification in conventional PCR platforms precluding the necessity of sample and equipment miniaturization to improve heat transfer and consequently shorten amplification time. NanoPCR enables rapid temperature ramping while maintaining the conventional PCR sample volume (20-25 µL) which

makes on-site sample loading and analysis with much more convenience, and it also facilitates sample retrieval and post-PCR manipulations. A greater sample volume provides higher optical path length (OPL) which favors optical detection strategies since light undergoes more absorption and scattering events. The presence of nanomaterials inside the PCR reaction revealed other advantages such as higher amplification efficiency and lower off-target priming. Li et al. studied the impact of 0.4 nM citrated-stabilized AuNPs on 283 bp λ -bacteriophage DNA amplification for 35 cycles [104]. Their results showed that the presence of AuNPs not only increases PCR yield without any loss in specificity but also allows amplification at suboptimal annealing temperatures as low as 25 °C to 40 °C which eliminates the need for touch-down PCR process and decreases the formation of primer dimers. However, there is an optimal range for AuNPs concentration, as higher concentrations (~1 nM) inhibit PCR. Moreover, it was reported that suspension of 0.7 nM of AuNPs with 13 nm diameter in PCR reaction reduced the amplification time by half and enhanced the sensitivity in real-time amplicon detection more than 10⁴ fold using LightCycler PCR machine (Roche Diagnostic Systems, Penzberg, Germany) [105]. The reason for the enhanced PCR yield and thermocycling rate is associated with high thermal capacity and conductivity of AuNPs which increase the heat conductivity of nanofluids on whole significantly [106, 107]. Others found that the presence of AuNPs improves the stability of nanofluids compared to microfluids due to stochastic motion (Brownian motion) of nanosized particles [108, 109]. Complementary to what Li et al. reported, other studies hypothesized that AuNPs only increase the amplification efficiency of shorter DNA templates than longer extended products, and the effective concertation of polymerase particularly Taq and Tfl is lowered due to surface interaction between AuNPs and polymerase [110]. In order to compensate formation of polymerase-conjugated AuNPs, bovine serum albumin (BSA) as a polymerase displacer on the surface of AuNPs and higher amount of polymerase can be used. Later, Mandal et al. demonstrated that higher PCR yield originated from both heat-transfer enhancement and strong surface interaction of AuNPs with Taq polymerase [111]. UV-visible spectroscopy of gold colloid with Taq, primer, and DNA showed 8 nm, 2 nm, and zero redshift in the plasmon wavelength of AuNPs indicating AuNPs higher affinity to Taq polymerase. Also, by circular dichroism, it was reported that the melting temperature of AuNPs-Tag complex was increased by 8 °C in comparison with pure Tag. This implies that adsorption of Taq on surface of AuNPs make polymerase molecules more active at normal extension temperature between 68 to 72 °C even during the final cycles of PCR leading to higher PCR yield.

The interaction between AuNPs is enzyme-specific, and for each type of polymerase, AuNPs' optimal concentration should be obtained [112]. The nature of AuNPs interaction with PCR ingredients is not fully understood; some studies observed that the affinity between Pfu DNA polymerase and AuNPs originates from electrostatic interaction and Au–NH₂ bond [113], while other studies indicate the PCR output enhancement is owing to formation of AuNPs-DNA clusters [114]. On the contrary, Haber *et al.* reported that addition of AuNPs did not enrich the efficiency and specificity of their PCR assay using different type of DNA templates [115].

In conclusion, nanomaterial-assisted DNA amplification within traditional thermocyclers has the potential to enhance sensitivity, specify, and thermocycling speed. It has been hypothesized that two mechanisms govern this enhancement effect: (1) thermal physical property of nanomaterials and (2) their high reactivity to PCR ingredients. However, to achieve this enhancement effect both in DNA amplification and detection, the concentration of nanomaterial, polymerase, and DNA as well as PCR condition (*e.g.*, PCR stage temperatures) should be optimized particularly for qPCR assay [115]. Finding the optimal nanomaterial concentration based on the type and concentration of DNA and polymerase is the key; otherwise, excess nanomaterial concentration inhibits PCR process, and lowering nanomaterial concentration have no impact on PCR yield [116]. The aforementioned advancements in nanoPCR were accomplished without utilizing optical feature of nanomaterials. Inclusion of nanomaterials inside biological reaction mixture and benefiting from their optical and photothermal properties founded a new research area to develop novel therapeutic and diagnostic modalities. Photonic PCR has already been a fully fledged active research domain, and by incorporating nanomaterials, it has been upgraded to a faster, more sensitive, and more suitable tool for POC applications.

2.3.3.2 Optical nanoPCR (Optical extrinsic heating)

In optical intrinsic heating, photothermal efficiency and subsequently heating rate are restricted to water optical absorption, power of light source at water absorption peak wavelength, and focusing power of optical elements. As an alternative, metallic NPs can be used in PCR reaction to increase optical absorption by several orders of magnitude (optical extrinsic heating), and consequently higher photothermal efficiency can be obtained. Moreover, the photothermal efficiency is further enhanced due to employment of lower power light sources, *i.e.*, lasers. The enhanced optical properties of subwavelength-sized conductive NPs arise when an oscillating electromagnetic (EM)

field excites the free electrons in conduction band coherently. The electron cloud deviates from its original location, and an effective restorative force owing to curved surface of particles oscillates the electron clouds with respect to ionic stationary core of NP in an electromechanical manner [117]. This oscillation leads to accumulation of charges (dipoles) on the surface of NPs. This dipole oscillations are the result of both incident EM field and restorative force [118]. If the resonance oscillation on the surface of NPs and the frequency of EM waves are in phase, an enhanced local field named as localised surface plasmon resonance (LSPR) is generated inside and outside of NPs. Mie's solution to Maxwell's equation for an EM wave interacted with spherical particle together with proper boundary conditions reveals a series of normal modes/multipole oscillation in the extinction cross section ($C_{\text{ext}} = C_{\text{abs}} + C_{\text{sca}}$) of NPs. Using a dipole approximation, the C_{ext} can be calculated as follows for a homogenous metallic sphere smaller than 20 nm [119]:

$$C_{\text{ext}}(w) = 9 \frac{w}{c} \varepsilon_{\text{m}}^{\frac{3}{2}} V \frac{\varepsilon_2(w)}{[\varepsilon_1(w) + 2\varepsilon_{\text{m}}(w)]^2 + \varepsilon_2(w)^2}$$
(2.6)

Where ε_m is dielectric constant of surrounding medium, $\varepsilon_1(w)+i\varepsilon_2(w)$ is the wavelength-dependent complex dielectric function of the bulk metal, V is the volume of the spherical NP, w is the angular frequency of incident EM wave, and c is the speed of light in vacuum. The real and imaginary parts of dielectric function determine the SPR position and its bandwidth, respectively. The resonance condition is met when the denominator of equation (2.6) is zero. For most noble metal NPs, the imaginary part of their dielectric constant is small leaving to the only condition of $\varepsilon_1(w)$ =-2 $\varepsilon_m(w)$ for the SPR to occur.

The coefficient of $\varepsilon_m(w)$ in the denominator of equation (2.8), often referred to as geometry-dependent factor (κ), is dependent on the shape of NP. Equation (2.7) shows that how κ factor governs the ratio between the spectral shift in resonance wavelength maximum ($\Delta\lambda_{LSPR}$) and refractive index (RI) change in surrounding medium (Δn_m) [120]:

$$\frac{\Delta \lambda_{\rm LSPR}}{\Delta n_{\rm m}} \propto \sqrt{\kappa} \tag{2.7}$$

This explains why NPs with greater κ factor exhibit more spectral shift due to RI changes in their surrounding, *i.e.*, NPs with greater κ factor provide higher detection sensitivity. The value of κ is

equal to 2 and 3 for small spherical and ellipsoid NPs, respectively, and it can increase up to 20 for gold nanorods (AuNRs) with high aspect ratio (AR) which explains the great interest in the application of nanorods and nanostarts in biosensing [120].

Moreover, equation (2.8) shows how absorption spectrum of NPs varies with the change in the size of NPs. In fact, more calculations on Mie theory show that C_{sca} and C_{abs} are proportional to the sixth and third power of NP radius, respectively. The larger the NP becomes (>20 nm), EM wave polarizes NPs inhomogeneously and generates higher order modes which redshift the plasmon band and broaden the absorption bandwidth. Jain *et al.* studied size normalized optical properties of AuNPs, and the results in their study showed that AuNRs with high AR have higher absorption (C_{abs}) and scattering coefficient (C_{sca}) compared to nanoshells and nanospheres [121]. Furthermore, the effective radius of AuNRs (r_{eff}) is an important factor which should be tailored based on the application. r_{eff} can be derived from NR volume (V) [122]:

$$r_{\text{eff}} = \left(\frac{3V}{4\pi}\right)^{1/3}$$
 (2.8)

AuNRs having small r_{eff} are more photoabsorbing and suitable for photothermal destruction of cancer cells, while AuNRs with larger r_{eff} have higher scattering coefficient and are mostly used in imaging applications. Another advantage associated with AuNRs is their facile resonance tunability by changing their geometry. By increasing the length of nanorods, the longitudinal and transverse modes are redshifted to higher wavelengths in NIR range which favors in vivo imaging and therapeutic applications due to high tissue transmittivity and low hemoglobin absorption in NIR range [123]. The wavelength maximum of suspended AuNRs in aqueous solution can be modulated by varying their aspect ratio (AR) using the following equation [124]:

$$\lambda_{\text{max}}(\text{nm}) = 95\text{AR} + 420$$
 (2.9)

Where λ_{max} is the wavelength maximum in nanometer unit. Moreover, SPR band intensity and wavelength depend on the metal type. For instance, SPR band for copper, silver, and gold nanosphere is located in visible region, whereas other metals have weak and broad SPR band in UV region [125, 126]. Consequently, spectral properties of noble metal NPs are determined by their size, shape, material, dielectric function of surrounding medium, and the particle separation

distance. As an alternative to LSPR, surface plasmon polaritons (SPPs) also offers enhanced optical properties upon light illumination on a planar thin metal film at specific angle. In contrast to LSPR with direct light excitation, phase-matching techniques such as using prism or grating couplers should be implemented to induce SPPs. EM field decreases exponentially as it propagates away from thin metal film into dielectric layer. The decay length of LSPRs (~10 nm) is typically much shorter than SPPs (~200 nm).

Addition of AuNPs inside PCR solution enhances optical absorption coefficient and subsequently light-to-heat conversion efficiency. This absorption enhancement can be tailored by changing AuNPs concertation allowing to obtain higher photothermal efficiency with smaller sample volume. This is in contrast to intrinsic heating in which photothermal efficiency is restricted to water absorption coefficient and fixed OPL. For instance, the molar extinction coefficient of AuNRs (Nanopartz, Loveland, CO) used in PCR plasmonic thermocycler were $9.8\times10^8~\text{M}^{-1}\text{cm}^{-1}$ at their plasmonic wavelength (808 nm) [12]. Considering AuNRs negligible scattering coefficient at 808 nm, their absorption coefficient per cm OPL and per molar concentration (C_{abs}=C_{ext}-C_{sca}) is approximately 10⁶ times higher than pure water at its absorption wavelength maximum (3 µm) targeted by broad band IR lamps discussed in the previous section. Thus, laserinduced heating of AuNPs (optical extrinsic heating) leads to higher photothermal efficiency and subsequently offers faster thermocyclers in comparison with intrinsic heating method. The first demonstration of plasmonic thermocyclers is the study conducted by Roche et al. in 2012 [127]. They added citrate capped gold nanospheres of 60 nm diameter with final concentration of 4.4 pM to 25 µL PCR reaction. A continuous wave 532 nm laser with 2.7 W optical power excited suspended gold nanospheres in PCR solution. Laser-induced excitation of AuNPs alters electron distribution in AuNPs conduction band and increases the electrons temperature to thousands of degrees Kelvin owing to minute electron heat capacity. Electrons deexcitation occurs via electronelectron scattering within 500 fs to reach to an equilibrium fermi electron distribution [128]. The new fermi electron distribution thermalizes by electron-phonon coupling within the gold nanospheres lattice in 2-5 ps [129]. It is then the phonon-phonon interaction with the surrounding medium which dissipates energy of the resonance of the oscillating dipole in the form of heat to the water shell around the AuNPs. The relaxation time (τ) for energy dissipation of excited AuNPs in aqueous solution can be estimated by [130]:

$$\tau = 0.64 r(nm)^2 \tag{2.10}$$

Where r is the radius of NP in nanometer unit, and for the case of AuNRs, r_{eff} should be used. The heat-transfer time (τ) is independent of initial temperature of AuNPs and aggregation events since heat-transfer coefficient, heat-transfer effective area, mass, and other optothermal properties of aqueous AuNPs suspension remain constant during deexcitation [131]. Therefore, a relaxation time of around 108 ps is expected from AuNPs with 13 nm radius suspended in PCR solution to reach thermal equilibrium. The AuNPs relaxation with a fixed laser power under a steady state condition gives rise to temperature increase with respect to ambient temperature (T-T_{ambient}) in aqueous solution which can be calculated by [13, 132]:

$$T-T_{ambient} = P \frac{\varepsilon_{abs}}{\varepsilon_{scat}} \left(\frac{1-10^{-A_{\lambda}}}{hS} \right) \eta$$
 (2.11)

Where P is the laser power, ε_{abs} is the molar absorption coefficient, ε_{scat} is the molar scattering coefficient, A_{λ} is the absorbance at wavelength of laser radiation, η is the AuNPs photothermal efficiency, h is the heat transfer coefficient, and S is the cross-sectional area perpendicular to conduction. Based on Beer-Lambert law, A_{λ} can be calculated as follows:

$$A_{\lambda} = \varepsilon_{\text{ext}} \times c \times \text{OPL}$$
 (2.12)

Where ε_{ext} is the molar extinction coefficient of solute (AuNPs), c is the concentration of solute (AuNPs), and OPL is the optical path length for propagating laser beam. This photothermal temperature increase together with a cooling fan was used in Roche *et al.*'s study to thermocycle PCR reaction for 30 cycles in less than 10 min. Moreover, they reported that by using BSA in plasmonic PCR solution, polymerase inactivation due to formation of AuNP and polymerase adduct was prevented, and it allowed using higher AuNPs concentration up to 6.6 pM for faster temperature ramping. Further improvements in their plasmonic thermocycler resulted in manipulation of AuNRs with AR of 4.1 with plasmon wavelength of 808 nm [12]. The AuNRs were pegylated to avoid polymerase adsorption on AuNRs and obviate the need for BSA. In contrast to their previous work, a non-contact temperature reading (IR thermopile) was utilised to avoid contamination and PCR inhibition, and the laser wavelength selection (808 nm) offered the flexibility of combining their plasmonic thermocycler with typical fluorescence measurements in

visible region. Their modified plasmonic thermocycler with increased AuNRs concentration between 10 to 50 nM was able to perform cell lysis and amplification of 25 µL PCR reaction containing human glucokinase gene (1 ng-50 ng) under one minute using KAPA2G fast polymerase enzyme. This plasmonic thermocycler was combined with real-time detection method deploying spectral shift in plasmon wavelength of AuNRs owing to RI change of surrounding medium as a result of amplicon generation. In other studies, this plasmon-driven ultrafast PCR was used with modifications on the plasmonic amplification hardware together with a different real-time detection method [133, 134].

As an alternative to AuNRs, thin Au film embedded in PCR chamber wall was used as plasmonic medium in the study conducted by Son et al. [135]. The 4 mm diameter PCR wells were formed in PMMA sheet, and a 120 nm thick Au film was deposited on the PMMA sheet. Furthermore, in contrast to previous plasmonic thermocyclers, they replaced expensive laser diodes with more cost-effective light source, LED (wavelength of 447.5 nm and optical power of 890 mW). A planoconvex lens with 16 mm focal length was used on LED to focus light beam on 10 µL PCR sample located in PCR wells. Their photonic thermocycler was able to complete 30 PCR cycles in 5 min with heating and cooling rate of 12.7 and 6.6 °C/s, respectively for 98 bp λ-bacteriophage DNA amplification. In this optical design, since efficient light-to-heat conversion is limited to a thin layer of PCR reaction in contact with Au film, utilisation of smaller sample volume provides more efficient photothermal effect and uniform heating. Therefore, Son et al. upgraded their Au film based-photonic PCR for a better temperature uniformity throughout sample (Figure 2.7) [15]. An optical cavity was made of two parallel Au films deposited on PMMA substrate, and the Au film thicknesses were optimized for maximum photon absorption and heat distribution across the sample. The optical cavity provides light confinement between the two Au films, so that most of the trapped photons will be eventually absorbed by the cavity medium, PCR solution. Temperature reading was carried out by a thermocouple placed in a reference chamber adjacent to PCR chamber. The LED distance from reference and PCR chamber were adjusted such that i) the chambers are located at beam waist for maximum beam delivery, and ii) equal optical power is absorbed by both chambers for accurate temperature reading. The height of the optical cavity governs the amplification speed and PCR efficiency; a cavity with 200, 400, and 750 µm height was shown to provide a total amplification time of 6.8, 9.3, and 14.7 min for 40 cycles,

respectively. However, amplicon yield decreases with smaller cavity height and faster thermocycling.

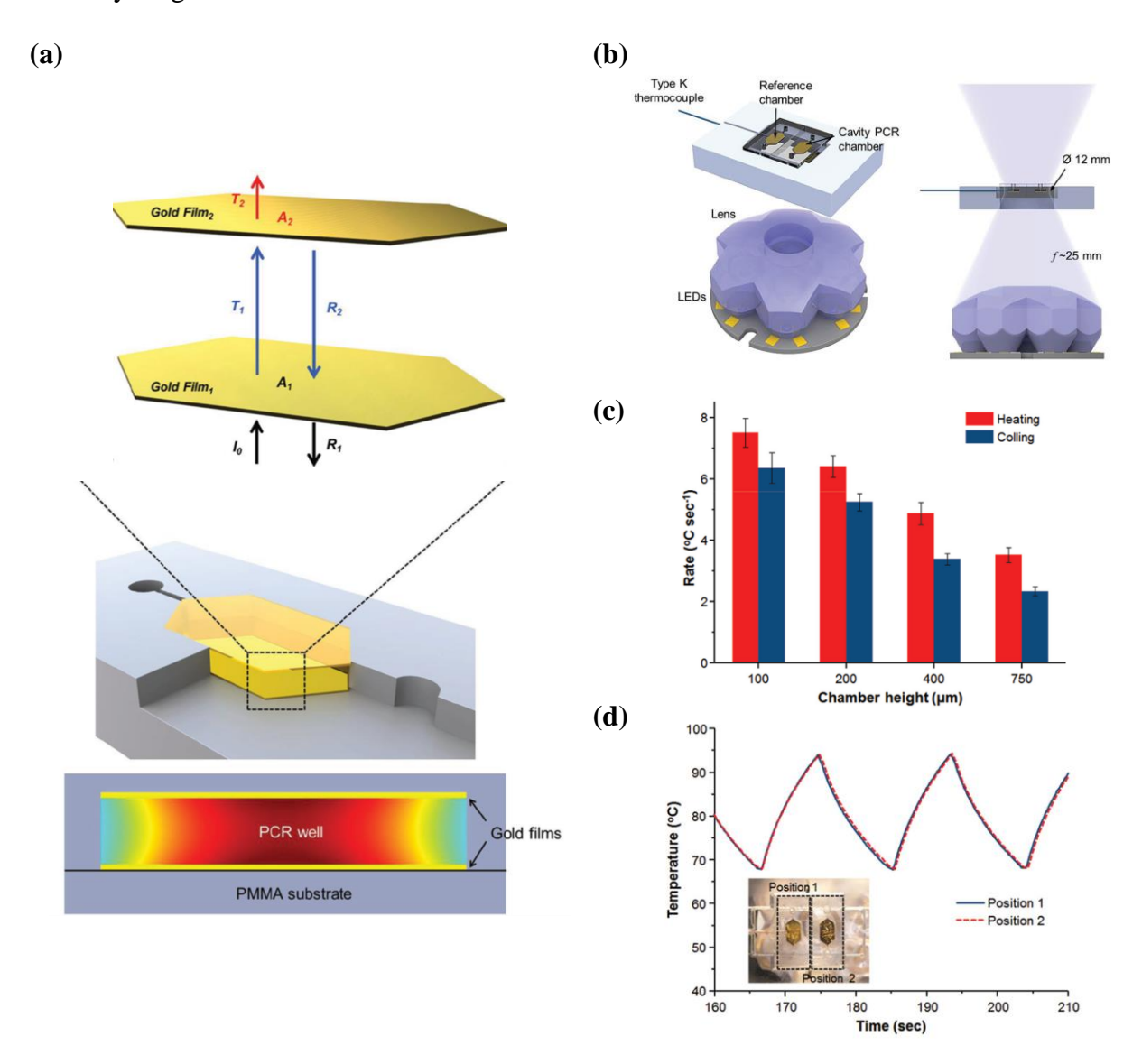


Figure 2.7 (a) Schematic of 2-layer Au film optical cavity for maximum photon absorption by cavity medium (PCR solution). (b) Optical setup with a PCR chamber and reference/thermocouple chamber positioned at lens focal length. (c) Heating and cooling rate dependence on Au films' separation distance. (d) Thermocycling curve for PCR and reference chamber. Reprinted from Ref. [15], Copyright (2015), with permission from Wiley-VCH.

An Example of an alternative AuNP morphology used in plasmonic PCR can be found in Lee *et al.* study in which suspended PEGylated silica coated gold bipyramid NPs (PEG-Si-AuBPs) in test solution offer numerous advantages over gold nanospheres and AuNRs [16]. First, the silica shell makes AuBPs more thermally stable and acts as a spacer to increase the particle—chromophore distance to avoid photobleaching in qPCR. Second, it has been reported that AuBPs demonstrate

fluorescence emission enhancement by factor of 1.4 in comparison with gold nanosphere owing to strong electric field near their sharp edges [136], and lastly, their plasmon band (846 nm) are far from the excitation and emission wavelength of widely used fluorescence dyes. In their plasmonic amplification strategy, the PCR sample contained PEG-Si-AuBPs with 18.3 optical density, fast KAPA2G polymerase, M13mp18 DNA template, and SYBR Green I dye for real-time detection. An IR-LED and a fan were placed above and below the PCR tube to carry out 40 cycles of plasmonic amplification and detection in less than 8 min.

Other researchers have explored various nanomaterials to introduce novel rapid and energy-efficient thermocyclers. Li *et al.* incorporated iron oxide nanoclusters (Fe₃O₄ NCs) with high temperature stability, magnetization, and absorption at 808 and 1064 nm wavelength inside 10 µL PCR sample [137]. The optical properties of Fe₃O₄ NCs together with an 808 nm laser diode with 460 mW power was utilized to amplify defective mitochondrial DNA (mtDNA) mtDNA from skin fibroblasts in 7 min for 30 cycles. Temperature regulation was measured by a K-type thermocouple, and to capture mtDNA from 500 cells µL⁻¹, they benefited from magnetic properties of NCs@gelatin with the presence of carbodiimide hydrochloride/N-hydroxysulfosuccinimide on amine-functionalized sequence-specific mtDNA probe. Finally, real-time fluorescence (Sybr Green) detection with a 450 nm laser diode and CMOS camera detector was employed, and the lowest detectable mtDNA concentration was 50 pg.

Although, many other optical PCR devices were proposed, they could not compete with plasmonic PCRs in terms of shortened assay time, higher PCR/photon-to-heat conversion efficiency, as well as simplicity in sample preparation and device fabrication. An example of such optical non-plasmonic PCR systems is the microfluidic chip designed by Liu's group. The microchip consists of a PMMA layer for PCR reaction, a second PMMA layer located below PCR chamber for conducting oil, and a 100 µm copper layer sandwiched between PCR and oil chamber [138]. The oil chamber is a square shape spiral channel connected to an oil tank through peristaltic pump. Multi-walled carbon nanotubes (MWNTs) with 4 mg/ml concentration were suspended in oil, so that upon 850 nm LED illumination (20 W), the MWNTs generate heat inside oil flowing through spiral channel beneath the copper layer. Consequently, owing to high thermal conductivity of copper, the heat is transferred to PCR chamber layer. The pump draws the cold oil back to tank, and the photothermal effect in tank reheats the oil for the following PCR cycle. Using pulse width

modulation on LED's and pump's voltage signal, the LED's optical power and oil flow rate is controlled to regulate the PCR reaction's temperature. This light-assisted microfluidic device completed 30 cycles of human papillomavirus (HPV) gene amplification (amplicon size: 140 bp) in 50 min comparable to conventional thermocyclers.

In Table 2.4, a more detailed overview of the discussed articles is listed. The photothermal efficiency ($\eta_{photon \to heat}$) of each plasmonic thermocycler was calculated using the same approach used in broadband IR-mediated PCR thermocyclers (equation (2.1)-(2.3)). For studies in which heating rate was not reported, the $\eta_{photon \to heat}$ is not calculated.

Table 2.4 Photonic nanomaterial-assisted PCR devices with their calculated photothermal efficiency.

| Ref. | Light source | Pin | λ (nm) | Nanomaterial Type | [Nanomaterial] ¹ | $V(\mu L)$ | $\mathfrak{t}_{\mathrm{cycle}}(\mathrm{s})$ | Heating/Cooling rate (°C/s) | Q _{cycle} (j) | P(mW) | %nphoton→heat |
|-------|------------------|------|--------|--------------------------------|-----------------------------|------------|---|--------------------------------|------------------------|-------|---------------|
| [127] | LD | 2.7 | 532 | AuNS | 6.6 pM | 25 | 20 | 7.62 /3.33 | 4.08 | 0.80 | 29.5 |
| [135] | LED | 3.5 | 447.5 | Au film ³ | NA | 5 | 10 | 12.79/6.6 | 0.73 | 0.27 | 7.65 |
| [15] | LED ² | 20 | 447.5 | Au film ⁴ | NA | 10 | 22.5 | 3.5/2.35 | 1.09 | 0.15 | 0.73 |
| [137] | LD | 0.46 | 808 | Fe ₃ O ₄ | 2500 p.p.m | 10 | 15 | NS/NS | 1.55 | NS | NS |
| [16] | LED | 3.8 | 850 | AuBP | 18.3 OD | 10 | 11.25 | 14.12/9.4 | 0.98 | 0.59 | 15.5 |
| [138] | LED | 20 | 850 | MWNT | 4 mg/ml | 20 | 100 | 1.5/2 | 2.93 | 0.13 | 0.63 |
| [139] | Halogen Lamp | 250 | NA | AuNF | NS | 25 | 45 | NS/NS | 3.87 | NS | NS |

LD: Laser diode, AuNS: Au-nanosphere, AuBP: Au-bipyramid nanoparticle, MWNT: Multiwalled carbon nanotube, AuNF: Au-dendritic nanoforest, NA: Not applicable, NS: Not specified, ¹Nanomaterial concentration, ²7 LEDs of 3 W, ³120 nm thick Au film, ⁴10 nm thick top and 120 nm thick bottom Au film.

2.4 Optical detection

Optical detection of amplicons relies on converting the change in PCR ingredient concentration (measurand) as a result of DNA replication to a change in one of the characteristics of light wave (intensity, wavelength, phase, or polarization) as an optical output. The optical output measurement is performed either without sample displacement (*in situ*) or by sample withdrawal from PCR chamber (*ex situ*). The classification of different PCR product detection methods is shown in Figure 2.8. *In situ* detection offers significant advantages over *ex situ* detection, as post-PCR sample preparation steps specific to each detection method (*e.g.*, gel electrophoresis, SPR, or SERS) are eliminated. Thus, the assay format is simplified, and it requires less user intervention making it ideal for POC applications. Furthermore, sample contamination due to sample carryover and subsequently false PCR results are minimized.

Real-time optical detection of amplicons is performed on stationary sample (*in situ*) during PCR process. In real-time detection, amplicon concentration is correlated to an optical signal on a cycle-by-cycle basis, and quantification is achieved by tracing optical response variations for different initial DNA concentrations. Since the detection occurs after every cycle, it allows for the measurement of reaction kinetics. On the other hand, end-point PCR refers to optical detection of amplicons after amplification or other preparatory steps (*e.g.*, sample purification, labeling, incubation, and/or heating) on stationary or displaced PCR sample. This is in contrast to real-time PCR in which optical biosensors are present in reaction from the beginning of PCR. For successful integration of PCR assay to POC testing, minimal user intervention during operation is necessary to avoid user error, contamination, and subsequently false results. Thus, *in situ* real-time PCR devices are considered more user-friendly and simple detection platforms.

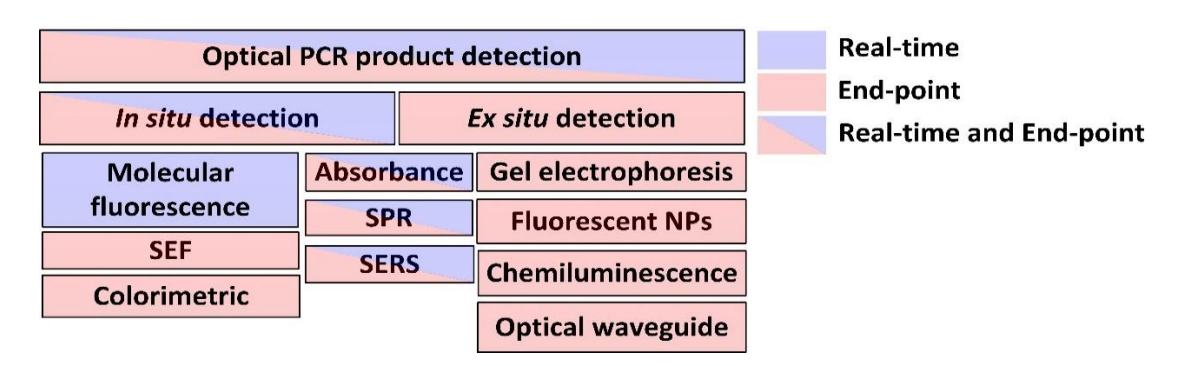


Figure 2.8 Classification of optical PCR product detection.

Optical detection methods have advantages over other sensing methods such as electrochemical assay since optical signal is less influenced by variations in temperature, pH, and ionic concentration which are the potential problems in electrochemical detection of analytes by electrodes [140]. Another advantage of optical detection is its multiplex detection capability. Optical multiplexing is mainly realized through two approaches: spatial and spectral multiplexing. Spatial multiplexing is pixel/area-based quantification in which multiple targets are spatially separated into different PCR wells, chambers, or pots, and the pixel intensity values of commercial CCD or CMOS image sensors are correlated to different target locations [86, 141]. In the second approach, multiple targets are spectrally separated by using unique identifiers or labels such as different colored dyes [17] or different sized nanoprobes (e.g., quantum dots) [142], and their detection is achieved often by employing multiple optical filters and detectors specific to the wavelength of each identifier. Therefore, this increases the cost and size of the detection system making it less practical for POC testing. One proposed solution to lessen the number of optical components in spectral multiplexing is to modulate the light source for each label at specific frequency, and through demodulation of total signal on one detector, the presence of different targets is revealed [79].

A summary of various optical detection techniques used in PCR assay is presented in Table 2.5, and they are compared in terms of their POC compatibility. In some studies, PCR was used as a signal-enhancing approach *via* target amplification for sensitive and reliable detection of low-abundance nucleic acids, while others were specifically focusing on a simple field-applicable detection platform integrated in a portable PCR thermocycler.

In the following section of this chapter, the principles of the aforementioned optical detection strategies are discussed. We presented studies contributing to the advancement of each optical detection technique in PCR assay towards their integration for POC applications. In Table 2.6, representative examples of these studies are gathered, and the critical performance parameter of a diagnostic test, limit of detection (LOD), for each study is presented for better comparison.

Table 2.5 Comparison of optical detection methods used in PCR assay and their POC adaptability.

| ogy | ndpoint | ction | xing | POC co | ycler | |
|---------------------------|---------------------|-----------------|--------------|--|---|--------------|
| Technology | Real-time/ Endpoint | Data collection | Multiplexing | Benefits | Challenges | Thermocycler |
| Absorption | R/E | N | F* | Simple instrumentation | Sensitivity loss for M ¹ | P/T |
| Molecular fluorescence | R | N | • | High sensitivity | -Costly - Sensitivity loss for M ¹ -Low sensitivity for MUX ² -High background | P/T/M |
| Fluorescent NPs | Е | N | • | -Low background -Cost-effective -High sensitivity -High spectral MUX | -Long detection time -Target-specific probe ³ | Т |
| SPR | R/E | N | • | | -Costly | P/T |
| SEF | Е | N | F | Low background | -Post-processing steps -Long detection time | Т |
| SERS | R/E | С | • | Low background | -Surface regeneration step -Target-specific probe ^{3,4} | T/M |
| Colorimetric | Е | С | F* | -No light sources -No detector ⁵ -Cost-effective | -Low sensitivity -Long detection time - Sensitivity loss for M ¹ | Т |
| Optical waveguide | Е | N | F* | -Miniature -High sensitivity | -Complex fabrication design - Surface regeneration step - Target-specific probe ³ -Costly ⁶ | Т |
| Chemiluminescence | Е | N | F | -No light sources -Low background | -Low sensitivity -Long detection time -Sensitivity loss for M ¹ -Sensitive photodetector | Т |

R: Real-time, E: Endpoint, N: Numerical (quantitative), C: Categorical (qualitative), F: Feasible, *Only spatial multiplexing, MUX: Multiplexing, P: Plasmonic, T: Traditional, M: Microfluidic, ¹Due to shortened OPL, ²Due to small Stokes shift & overlap of emission peaks, ³Requires target specific probe even for qualitative detection, ⁴Valid for SEF and SERS, ⁵For lower LOD spectroscopy is used, ⁶Requires tunable laser which is bulky and expensive.

Table 2.6 Representative examples of various optical detection methods used for PCR product detection.

| Ref. | Optical detection method | Target DNA | LOD | Optical biosensor | Detection |
|-------|--------------------------|----------------------------------|-------------------------------------|---|-----------|
| [143] | Absorption | C. Trachomatis | 10 ⁴ DNA copies/20 μL | Label-free | R |
| [144] | Fluorescence | E. coli O157:H7 | 10 DNA copies/μL | FAM probe | R |
| [17] | Fluorescence+CE | Bacteriophage phiX174 RF1 | 50 DNA copies/25 μL | FAM probe | R |
| [20] | SPR | Human genomic DNA | 0.2 ng/μL | Au substrate-thiolated primers | R |
| [145] | SPR imaging | BCR/ABL fusion gene | 10.29 nM | Au arrays chip-thiolated oligo probe | R |
| [22] | FO-PCR-MA | Mycobacterium bovis | 0.4 μΜ | FO sensor/AuNPs-oligo probes | R |
| [21] | FO-SPR | Anti-IgE aptamer ¹ | 0.1 fg/μL | FO sensor/AuNPs-thiolated primers | R |
| [146] | SEF | Recombinant plasmids | 100 fmol | Au surface-PNA probe + Cy5- labeled primers | Е |
| [147] | SERS | FemA gene ² | 1 nM ⁴ | Dyed SERS primers+AgNPs | Е |
| [148] | Colorimetric | Emetic B.cereus | 92 CFU/mL (naked eye) | Unmodified AuNPs | Е |
| [149] | Colorimetric | HIV | 1.2 copies/μL (naked eye) | AuNP-oligo | Е |
| [150] | Colorimetric | Bacillus anthracis | 10 pg (naked eye) | AuNP-oligo | Е |
| [142] | QD-based LFA | MRSA | 10 ³ copies/ml | QD-SA | Е |
| [151] | QD-based LFA | S. aureus ³ | 3 CFU/mL | QD-SA | Е |
| [152] | UCNP-based LFA | HIV I virus | 10 ³ pathogen particles | UCNPs-anti-Dig | Е |
| [153] | Interferometry | apoE gene polymorphisms | 10 pM-10 μM | Au deposited PAA layer chip- thiolated DNA probe | Е |
| [154] | Chemiluminescence | HPRT1 gene | 137 DNA copies/50 μL | SA-HRP+Chemiluminogenic substrate | Е |

CE: Capillary electrophoresis, FO-PCR-MA: Fiber optic PCR melting assay, FO: Fiber optic, SPR: Surface plasmon resonance, SEF: Surface-enhanced fluorescence, SERS: Surface-enhanced Raman scattering, QD: Quantum dot, UCNP: Up-converting nanoparticles, MRSA: Methicillin resistant Staphylococcus aureus, HPRT1: Hypoxanthine hosphoribosyltransferase-1, SA: Streptavidin, Dig: Digoxigenin, PAA: Porous anodic alumina, HRP: Horseradish peroxidase, R: Real-time, E: Endpoint, ¹Anti-immunoglobulin E (IgE) aptamer, ²of Staphylococcus epidermidis, ³Staphylococcus aureus, ⁴By using 1 nM of SERS primer.

2.4.1 Absorbance detection

UV-visible absorption spectroscopy is a well-established optical method in which light attenuation at different wavelengths is measured and correlated to the presence of absorbing species/analytes with unique internal energy level distribution responsible for wavelength-dependent light absorption. Hence, based on Beer-Lambert law (equation (2.12)), UV-visible spectroscopy of a solution at a fixed OPL reveals absorption peaks which can be used to identify the composition and concentration of the absorbing media. Since proteins and nucleic acids are strong UV absorbers, absorption-based detection in PCR assay is a promising technique for their quantitative detection. This technique is mostly used as an end-point spectral measurement of PCR products by bulky spectrometers. Recently, Tran et al. demonstrated an in situ real-time PCR product detection method based on measuring the transmitted 260 nm light from a UV LED through PCR reaction at every PCR cycle [24, 143]. Since free nucleotides are strong UV absorbers, their consumption to extend new dsDNAs during elongation stage of PCR leads to a cycle-to-cycle increase in UV transmission signal (Figure 2.9.a). Using this method, a LOD of 10⁴ DNA copies per 20 µL PCR reaction was achieved. It is noteworthy that incorporating this detection method in microfluidic devices is challenging due to reduction in sample size and subsequently the OPL, and this will directly influence the detection sensitivity according to Beer-Lambert law. Also, in absorption detection, PCR chamber material should be selected such that it is transparent to the probe wavelength to minimize signal loss. This makes absorption measurements less practical for Peltier-based thermocyclers where PCR chambers are typically surrounded by a heating block.

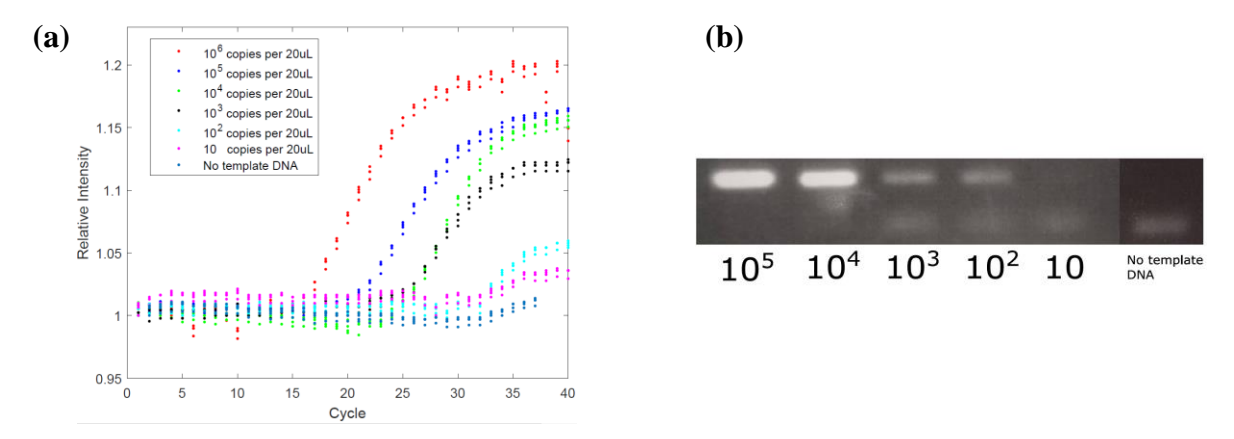


Figure 2.9 (a) UV amplification curve obtained from real-time UV monitoring of plasmonically amplified *C. Trachomatis* DNA with varying starting copy numbers (10⁵-10). (b) Gel image of samples with varying initial DNA concentrations amplified in plasmonic thermocycler [143].

2.4.2 Fluorescence detection

2.4.2.1 Fluorescent reporter molecules

Fluorescence analysis of PCR product is the most common optical detection method which owes its high sensitivity and selectivity to advances in molecular fluorescent labeling techniques such as FRET probes, molecular beacons, and scorpion primers. In this method, the intensity of the fluorescence signal acquired by exciting a fluorescent dye or probe at every cycle is correlated to newly generated dsDNAs. The most common fluorescence formats are i) sequence-independent fluorescent dyes (intercalating dyes) and ii) sequence-specific probes, and the format selection depends on the required specificity in detection. Using the former fluorescence format, fluorescence emission occurs when intercalators insert between base pairs of dsDNA (e.g., SYBR Green I); however, for the sequence-specific probes such as hydrolysis probes (TaqMan), the fluorescence emission occurs when the fluorescence reporter and quencher are separated by $5^{'} \rightarrow 3^{'}$ of exonuclease activity of Taq polymerase for target DNA extension [155]. Intercalators are costefficient; however, they bind to any generated dsDNA resulting in false positive signal from formation of primer-dimers. Also, their addition between dsDNA base pairs perturbs DNA structure and stability [156]. On the contrary, sequence specific probes target the sequence of interest in DNA templates and allow simultaneous detection of multiple targets within a single reaction, but their proper design to unfold (e.g., molecular beacons and scorpion primers) and hybridize (e.g., Taqman) upon target presence make them costly compared to intercalators [157]. Fluorescence emission is induced by broad band sources (e.g., arc mercury lamp) [158, 159], laser diodes [160, 161], and mostly LEDs [162, 163] owing to their long lifetime, low energy consumption and low cost. Optical components such as filters and lenses are used particularly with broad band light source and LED to selectively pass the desired excitation wavelength and lower the beam divergence. The detection of fluorescence signal is accomplished by instruments such as photodetectors, pixelated detectors for array-based systems, spectrofluorometers, and fluorescence microscopes/scanners. The fluorescence detection sensitivity is restricted by three phenomena: i) background signal (autofluorescence and unbound/non-specifically bound probes), ii) Stokes shift enabling the separation of target fluorescence signal from Rayleigh-scattered excitation light and other fluorescent probes, and iii) fluorescence lifetime in excited states depending on excitation light intensity and exposure time (photobleaching) [164]. Thus, emission filters are needed to

detect the desired wavelength and exclude background fluorescence or optical signals generated by other fluorescent probes. The fluorescence emission is a three-step process which is depicted in Figure 2.10: i) fluorophore molecule absorbs the energy of incident photons (hv_{ex}) to populate excited singlet electronic states within femtosecond time scale, ii) the non-radiative decay of excited molecule in the form of vibrations or heat within picoseconds, and iii) radiative decay of excited molecule to ground state within nanoseconds ($hv_{em} < hv_{ex}$). Since the non-radiative decay occurs several orders of magnitude faster than fluorescent transition, there is always a competition between the two processes to deexcite the fluorophore molecule. Quantum yield is a measure of efficiency of fluorescent transition to all other non-fluorescent transitions [165]:

$$\eta_{Q} = \frac{k_{f}}{k_{f} + k_{nf}} \tag{2.13}$$

Where k_f is the rate constant for fluorescence decay, and k_{nr} is the rate constant for non-fluorescent transitions, *i.e.*, internal conversion, non-radiative relaxation, quenching, intersystem crossing, and phosphorescence. The quantum yield can also be expressed as the ratio of absorbed photons to the emitted photons through fluorescence, and its value never exceeds unity. Finally, the fluorescence optical power at detection sight can be estimated as follows:

$$P_{out} = P_{in} \eta_O \eta_A \eta_Q \tag{2.14}$$

Where P_{in} is the incident optical power from light source, η_{O} is the efficiency of optical system to selectively detect emitted optical power from the target fluorophore and exclude optical power from light source, and η_{A} is the absorbance (A_{λ}) calculated by Beer-Lambert law (equation (2.12)). Since PCR kinetics have 4 phases of baseline, exponential, linear, and plateau, the plot of P_{out} against cycles (amplification curve) have the same 4 phase-sigmoidal behaviour as PCR kinetics. The crossing point at which the exponential generation of amplicons exceeds the background signal is referred as threshold cycle which is linearly inversely proportional to the logarithm of starting DNA concentration. Hence, the absolute quantification of the template concentration is achieved by comparing the threshold cycle of the target's amplification curve with the threshold cycles of the standard/calibration curve generated from amplification is based on the amplification concentrations (calibrator). On the other hand, relative quantification is based on the amplification

of internal reference genes (*e.g.*, 18s rRNA, GAPDH, or beta-actin) and is expressed as a ratio of the threshold cycle of the target to the reference gene. By far, fluorescence detection is the most widely and commonly used method for real-time nucleic acid analysis which is considered a gold standard technique after traditional endpoint detection method, gel electrophoresis.

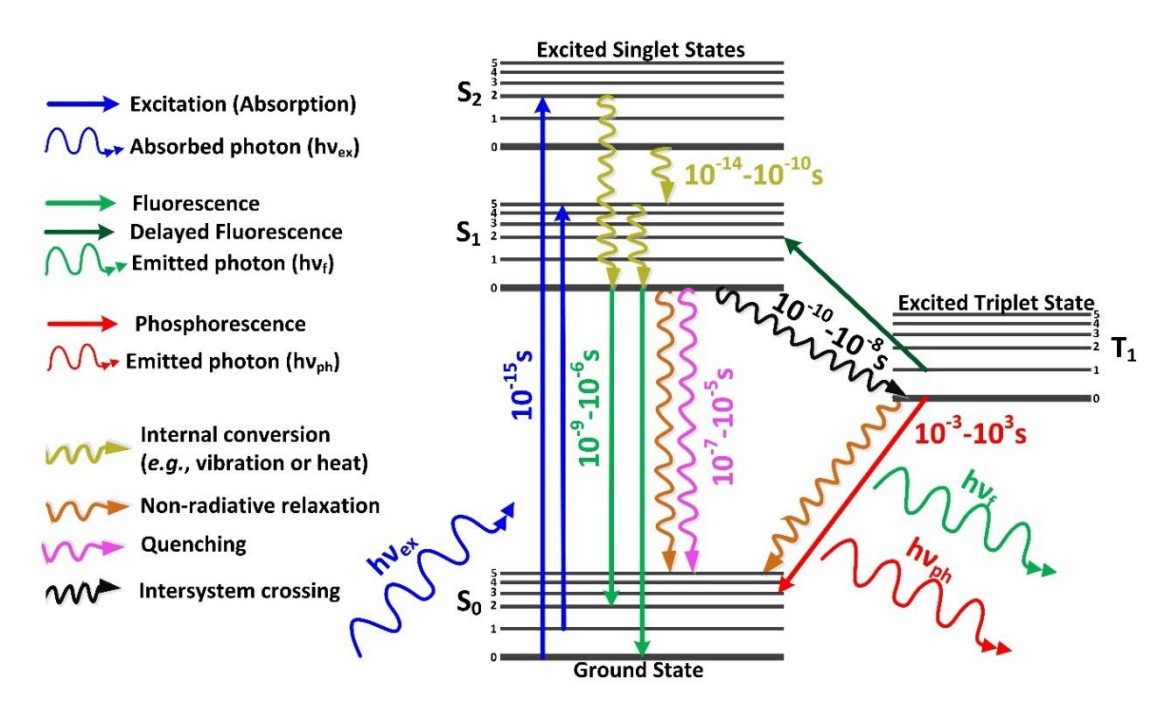


Figure 2.10 Jablonski diagram explaining the occurrence of fluorescence and phosphorescence.

Today, recent advances in fluorescence detection are centered around its integration into PCR microdevices. For instance, fluorescent PCR combined with capillary electrophoresis (CE) separation was performed on a microfluidic chip for single and multiple color fluorescence detection with average run time of approximately 1 h [17, 160]. The study presented by Easley *et al.* demonstrates one of the most advanced qPCR-CE microchips capable of executing DNA purification through solid-phase extraction (SPE) from whole blood, DNA amplification, microchip electrophoresis, and laser-induced fluorescence detection in less than 30 min [166]. One major challenge with qPCR-CE microfluidics is that at each PCR cycle, an aliquot of the sample undergoing amplification should be withdrawn for CE analysis and amplicon quantitation without perturbing the PCR kinetics. Moreover, in order to avoid the injection of unextended and denatured amplicons to CE channel, the PCR process should be suspended during elongation stage of every cycle, and the PCR reactor is maintained at elongation temperature during sample transfer. Finally, for qPCR-CE microchip design, PCR reactor should be positioned far enough from CE separation

channel, so that the heat generated in PCR chamber does not disturb CE analysis. Hence, PCR suspension and sample migration from PCR reactor to CE channel at every cycle lengthen the assay time.

Microfluidic qPCR that excludes CE has led to much simpler and less time-consuming assay. Carballo et al. presented a disposable thermoplastic continuous flow PCR chip with an optical fluorescence detection system equipped with 490 nm LED and optical power meter to measure fluorescence emission of FAM probes [144]. Another example of real-time continuous flow PCR assay was proposed by Hatch et al. via incorporating 0.1-10 µL PCR droplets passing through 40 wraps of fluorinated ethylene propylene (FEP) tubing to perform 40 thermal cycles by using thin film resistive heaters (Figure 2.11) [167]. To carry out multiplex real-time detection, the excitation light of a blue LED couples into 37 silica optical fibres, and each optical fiber is connected to a wrapped FEP tubing for every cycle fluorescence measurement. On the other side of the detection system, the emitted fluorescence signal from droplets at every cycle goes through another set of fibers (emission fibers) to be finally incident on a 64-channel multi-anode PMT. In this work, some factors should be carefully observed to be able to successfully amplify and detect targets. For example, in order to preserve the droplets sequence in tubing, the droplet diameter must be larger than the inner dimeter of the tubing. Also, the optical alignment and coupling angle of fibers to tubing should be carefully designed. In flow-through qPCR, the assay time depends on the length and diameter of channels as well as sample flow rate. This means that after system fabrication, the assay time can no longer be altered. Another challenge is that the sensitivity of detection can be easily degraded by cross-contamination and loss of reagents due to their adsorption to flow channel surfaces. However, these complications were alleviated in Zhu et al. work in which a disposable cost-efficient static microfluidic chip made of polydimethylsiloxane (PDMS) was coupled with an on-chip qualitative fluorescent detection [18].

A strategy towards a more compact, inexpensive, and yet simple qPCR device is to reduce the number of optical elements and detectors by using color-blind fluorescence detection. In color-blind method proposed by Schrell *et al.*, fluorescence emission from each individual fluorophore is encoded by pulsing the excitation laser at different rates, and the total emitted fluorescence signal is collected on one single detector [79]. Consequently, the contribution of each fluorophore's emission intensity is determined by demodulating the photodetector signal using

series of fast Fourier transform (FFT). Since an IR-mediated heating thermocycler was used in Schrell's study, the modulation frequencies were selected such that the temperature-dependent IR lamp pulses do not contaminate the probe laser modulation frequencies. One advantage of colorblind fluorescence detection method is that the required optical setup for detection of each individual dye such as dichroic mirror, bandpass filter, and detector is omitted leading to a less populated and costly optical detection system.

Generally, fluorescence detection is considered as a powerful tool for sensitive and selective detection of various biomolecules and cells due to substantially available fluorophores and advanced labeling techniques; however, some challenges has limited its practicality for a fully automated and cost-effective POC device. For instance, the labeling procedure is a laborious step needs to be performed by skilled technicians from fluid handling to incubating, mixing, and washing. Moreover, fluorophore dyes are expensive and have short shelf life. Also, factors such as pH level of solution, high background noise induced by overlap of emission peaks of multiple targets, and autofluorescence impact fluorescence assay performance. Hence, label-free detection techniques discussed in the following section are extensively investigated to overcome these challenges.

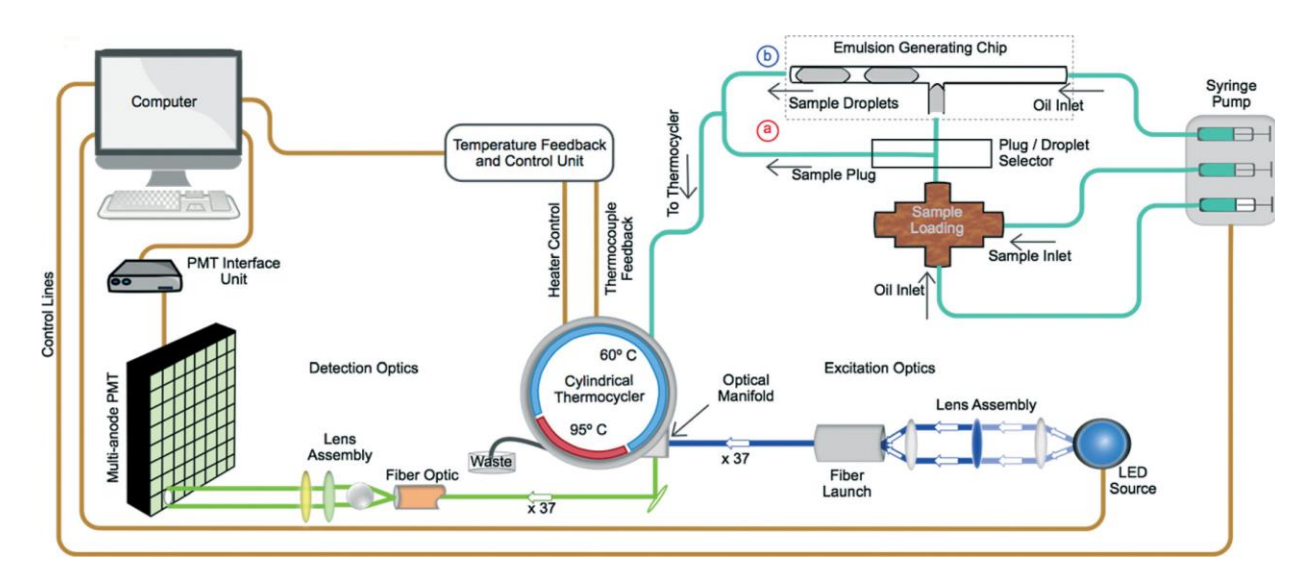


Figure 2.11 Overview of the system design of real-time continuous flow PCR assay introduced by Hatch *et al.* Reprinted from Ref. [167] with permission from the Royal Society of Chemistry.

2.4.2.2 Fluorescent nanoparticles

Quantum dots with their size range of 1-10 nm are semiconductor nanocrystals that offer size-tunable absorption and emission cross-sections [168]. These luminescent inorganic nanoparticles can be excited by UV to blue-green light source (*i.e.*, broad excitation spectrum), while mostly emitting from green to IR region with narrow and symmetric emission spectra. Contrary to organic fluorescent dyes with a relatively small Stokes shift between their excitation and emission peaks, QDs offer larger Stokes shift especially by exciting at shorter wavelength (UV light) and significantly larger extinction coefficient (>2×10⁶ cm⁻¹M⁻¹) [169, 170]. This improves detection sensitivity by reducing background signal. Moreover, QDs exhibit higher photostability and higher resistance to biological degradation in comparison with organic dyes or fluorescent proteins. The fluorescence lifetime of QDs is approximately 10 times more than the organic dyes (QDs:10-100 ns vs. organic dyes: 1-10 ns). Also, QDs have typically multi-exponential decay dynamics in contrast to mono-exponential decay of organic dyes [171]. These characteristics make QD-based biosensing a powerful tool for fluorescence multiplexing.

QDs are widely employed in lateral flow assay (LFA) for nucleic acid endpoint detection. The PCR-amplified amplicons labeled at both ends with biotin and digoxigenin (Dig) are captured by QDs- streptavidin (QD-SA) conjugates and anti-Dig antibody on LFA strip [151]. As a result, upon UV light exposure, the fluorescence emission of QDs leads to qualitative detection of target DNA.

QD-based LFA was further enhanced for multiplex quantitative amplicon detection [142]. After amplifying two different genes with labeled primers, PCR products are immobilized and captured on test strips by two different sized QD-SA conjugates and two types of antibodies (Figure 2.12.a). The excitation light of a 455 nm LED goes through a filter and dichroic mirror to be finally incident on QD-labeled PCR complex, and the fluorescence intensity is captured by the camera of a smartphone after passing through a planoconvex lens and gelatin filter. Next, the concentration of targets is quantified by analyzing the pixel intensity of captured images from test strips using a mobile app (Figure 2.12.b and Figure 2.12.c). All the optical components are assembled into an optical module which accommodates test strips and a smartphone. Replacing costly fluorescent readers by smartphone camera reduces the overall cost of system making this methodology more applicable for POC testing.

QD-based LFA is a low-cost and practical analytical tool for POC testing; however, it should be pointed out that LFA is an endpoint detection method, and after DNA amplification, the detection time needed for PCR products to flow through strips and interact with labelling agents is at least 10-15 min.

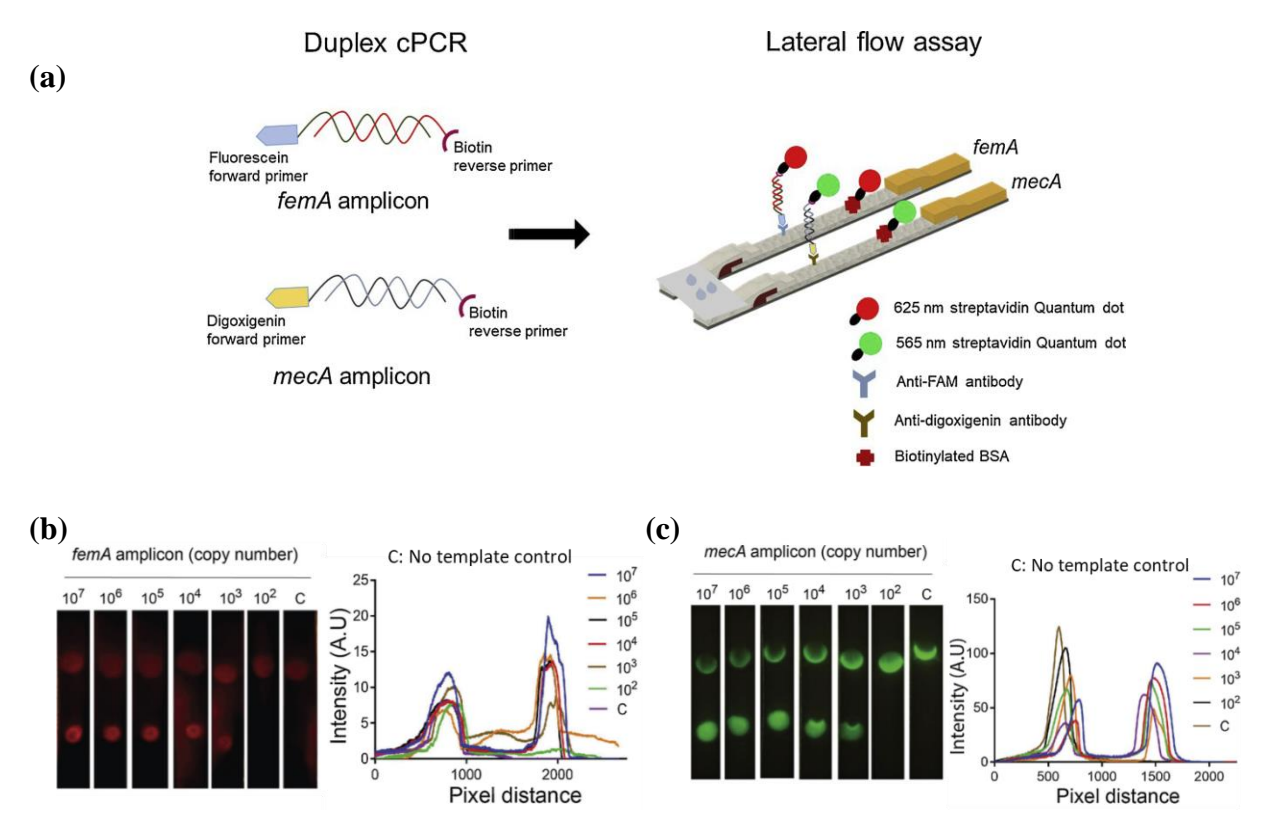


Figure 2.12 (a) Schematic illustration of PCR products amplified by modified forward and reverse primers and their detection on LFA strips through interaction with two different antibodies and two different sizes of streptavidin-modified QDs. Images of test strips and their intensity analysis by smartphone application for detection of (b) femA and (c) mecA genes with different concentrations by using 625 nm and 525 nm labeled-QDs, respectively. Reprinted from Ref. [142], Copyright (2019), with permission from Elsevier.

Another generation of fluorophores are up-converting nanoparticles (UCNPs) which convert low energy photons in NIR range to high energy photons in visible range (anti-Stokes shift) *via* multiple absorption events or non-linear energy transfer process. Similar to QDs, UCNPs have narrow emission bands in visible region making them applicable in multiplex FRET-based target sensing for imaging and biodetection assays [168]. Other advantages of UCNPs are high SNR due to absence of high background noise generated by biological media autofluorescence, no photobleaching, and the possibility of using IR excitation light since biomolecules are transparent or have minimal absorption in IR wavelength region. UCNPs are available in different colors, and

their incorporation on LFA strips with an NIR or IR laser diode and a PMT makes them a powerful endpoint detection tool for viral and bacterial pathogens.

Similar to QDs, UCNPs on LFA strips was used for PCR product detection. Chen *et al.* developed a POC-suitable polycarbonate microfluidic cassette able to perform cell lysis, nucleic acid isolation, PCR, and target labeling, and detection [152]. Liquid buffers and dry reagents were stored in storage pouches, and on-chip pumps and valves controlled the reaction flow for mixing, solid-phase extraction, thermocycling, and detection steps. A 980 nm light source was used to excite up-converting phosphor particles-dsDNA complex, and the emission intensity in visible region (450 nm) was collected to measure the fluorescence intensity for semi-quantitative amplicon detection.

2.4.3 Plasmonic-based detection

2.4.3.1 Surface plasmon resonance (SPR) sensor

SPR sensor is considered as a label-free detection strategy which translates RI change at its metal-dielectric interface to light wave characteristics. Biorecognition elements such as antibodies or aptamers are immobilized on the surface of thin metal film, and in the presence of target analyte, analyte molecules bind to molecular recognition ligands. This will result in RI change of SPR sensor's surrounding medium (dielectric medium) and subsequently a change in propagation constant of surface plasmon; thus, light coupling condition with the surface plasmon will be altered in the form of change in coupling angle, coupling wavelength, phase, intensity, and polarization [172]. For the case of LSPR, no special coupling instrument (*e.g.*, grating coupler or prism) is needed to excite resonant oscillation of electrons in conduction band. Therefore, after direct light coupling, plasmonic NPs act as a transducer capable of converting local RI change due to binding events to spectral shift in their scattering and extinction spectra measured by spectroscopy. For an ideal spherical nanoparticle with a thin coating film/analyte adsorbed on its surface, the amount of spectral shift can be estimated as follows [173]:

$$\Delta \lambda = s \times \Delta n$$
 (2.15)

$$\Delta n = (n_a - n_s) + [1 - \exp(-D/\delta_d)]$$
 (2.16)

Where s is LSPR sensitivity (nanometers spectral shift per one unit RI change), D is the distance from the center of nanosphere to the surface of adsorbed film, δ_d is the characteristic decay length for localized field, and n_a and n_s are refractive indices of adsorbed film and surrounding medium, respectively. Equation (2.15) is valid for small variations in RI; however, for a significant amount of spectral shift, we have [173]:

$$\Delta \lambda = s_1 \times \Delta n + s_2 \times \Delta n^2 \tag{2.17}$$

Where s_1 and s_2 are sensitivity factors for bulk solution, and Δn can be calculated using equation (2.16).

Roche *et al.* demonstrated a label-free LSPR-based detection method in which the transmitted optical power of a laser diode at 650 nm through a PCR reaction mixture containing AuNRs was monitored [12]. This wavelength was selected due to it being close to the minimum absorption wavelength for these AuNRs (which had transverse and longitudinal resonances at 507 and 808 nm, respectively). They reported a gradual cycle-to-cycle decrease in 650 nm transmission signal for positive PCR reactions which they hypothesized as being indicative of interaction between the generated amplicons and the AuNRs resulting in a red-shift in the absorption spectrum.

Another approach to induce RI change for real-time PCR product detection is to employ functionalized PNA/oligo probes. These probes are immobilized on the surface of AuNPs or Au substrate *via* biotin-streptavidin or thiol—gold interactions. Since these biotinylated or thiolated probes are complementary to specific sequence in DNA template, their hybridization leads to a change in resonance angle, resonance wavelength, or reflected light intensity from the sensor chip. However, in order to make the sequence of interest in amplicons available for probe hybridization, the amplicons need to go though a post-amplification process such as denaturation and buffer addition, *i.e.*, endpoint detection [174]. Thus, other studies advanced SPR/LSPR-based monitoring of binding events in real-time fashion for their better translation into POC applications. This can be found in Heip *et al.* study in which denatured DNAs are captured during amplification (denaturation stage of PCR) by thiolated oligonucleotide primers linked to Au-coated nanostructured biochip [20]. For real-time detection, the relative reflected intensity (RRI) from the surface of biochip was collected at the end of elongation of each PCR cycle by UV–vis spectrophotometer. For successful PCR, significant increase in RRI is observed from early cycles

(cycle 3 and 4), and RRI signal flattens out during last cycles similar to fluorescence signal saturation in plateau phase of qPCR. Amplicon quantification is achieved by the amount of increase in RRI signal. On the contrary, the negative control showed continuous flat RRI signal throughout all cycles.

Fiber optic surface plasmon resonance (FO-SPR) sensing technology is another real-time technique in which suspended AuNPs and a fiber optic (FO) sensor are responsible for SPR signal amplification and detection, respectively [21]. During the annealing stage of PCR, the denatured DNA template is sandwiched between the FO sensor and the AuNPs through hybridization to its complementary thiolated forward and reverse primers immobilized on FO sensor and AuNPs, respectively (Figure 2.13.a). As thermal cycling progresses, the number of AuNPs and PCR products around FO sensor increase, leading to greater redshift in SPR wavelength, and threshold cycle in "SPR shift vs. time" curve is used for DNA template quantification (Figure 2.13.b).

FO-SPR technology is also used in obtaining characteristic melting temperature of the target DNA for real-time multiplex amplification and detection [22, 23]. In fiber optic PCR melting assay (FO-PCR-MA), the amplicons hybridized to FO-SPR sensor and AuNPs at both ends dissociates in the form of ssDNAs during denaturation stage of PCR (Figure 2.13.c). Thus, FO-SPR sensor and AuNPs are no longer bounded to each other, and this change in the mass/density of FO sensor's surrounding medium is expressed as SPR signal shift. The first order derivative of SPR signal with respect to temperature after only few PCR cycles resolves melting point/peak (T_m) unique for each target (Figure 2.13.d).

One main advantage of FO-SPR technology is that its detection threshold is lower than fluorescence-based detection; hence, successful PCR identification is detectable at earlier cycles leading to shorter assay time. Furthermore, in FO-SPR technology, complexities such as DNA labeling and reporters' emission spectra overlap in multiplex detection occurring in fluorescent PCR or high-resolution melting (HRM) is precluded. One of the complications in fluorescence and absorbance detection is that the background interference contaminates the changes in the main signal. However, this is not an issue in LSPR biosensing, since LSPR measurements are sensitive to near-field/near-surface RI changes depending on size of nanoparticle. In addition, SPR sensors can provide much stronger signal intensity compared to absorption and fluorescence detection

method. For instance, it is reported that a single silver nanosphere with 80 nm diameter have a millionfold greater scattering cross-section than a fluorescein molecule [175].

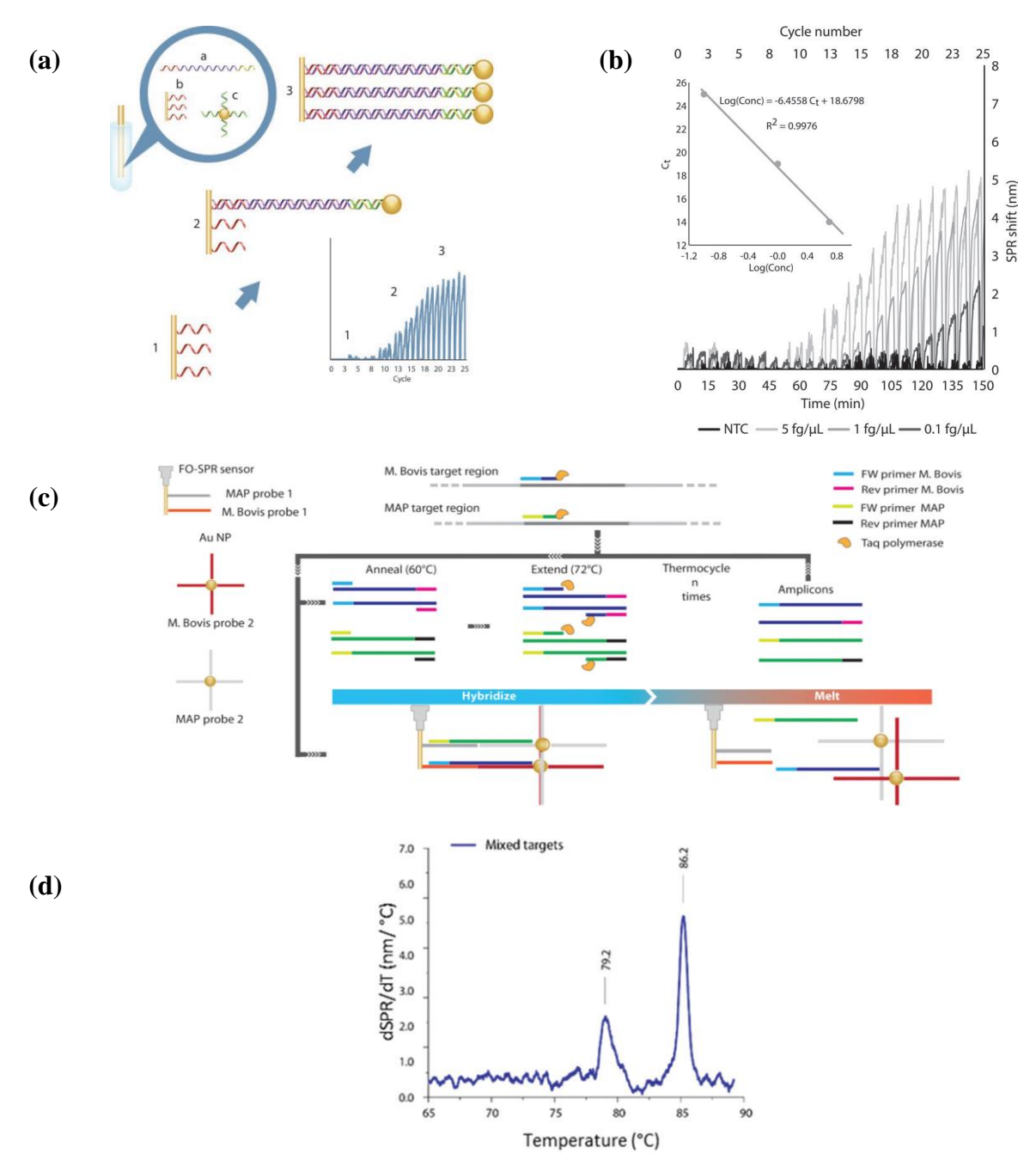


Figure 2.13 (a) Functionalized FO-SPR sensor and AuNPs with forward and reverse primers, respectively and generation of amplicons on FO-SPR sensor. (b) Real-time measurement of SPR wavelength shift for varying DNA template concentration and plot of threshold cycles against logarithm of DNA concertation. Reprinted from Ref. [21], Copyright (2011), with permission from Wiley-VCH. (c) Schematic representation of FO-PCR-MA for multiplex detection. (d) First order derivative of FO-SPR signal vs. temperature for resolving target-specific melting points. Reprinted from Ref. [22] with permission from the Royal Society of Chemistry.

2.4.3.2 Surface-enhanced fluorescence (SEF)

Surface-enhanced fluorescence (SEF), also known as plasmon-enhanced fluorescence, is a fluorescence signal enhancement technique which arises when a fluorophore molecule is in close proximity to a noble metal film or nanoparticle. There are two mechanisms giving rise to SEF phenomenon: i) owing to enhanced electric field around metallic NP, fluorophore molecule gain stronger photon absorption property and ii) non-radiative decay of excited fluorophore molecule couples into SPR of NP [176], and consequently, plasmonic medium radiates light with enhanced intensity through elastic scattering at the same frequency of fluorophore emission. Moreover, this overlap between SPR and molecular absorption/emission spectra not only generates emission intensity enhancement, but also decreases fluorescence lifetime in the excited state leading to photostability improvement [176]. The fluorescence emission intensity enhancement factor varies from 10 for thin metal films [177] to 10^3 for nanoantennas [178] allowing detection of as low as single molecule which is difficult to detect by fluorophore molecules due to their low optical cross section and poor stability [179]. Although, other potential alternatives to SEF were reported such as quantum dots with higher photostability and fluorescence intensity, their cost, toxicity, and irregular blinking in biological environment made them less favorable as biosensors in certain applications [180].

An example of PCR product detection by SEF can be found in the study conducted by of Yao *et al.* in which DNA template was amplified by using fluorophore labeled primers [146]. After amplification, PCR products underwent two separate steps: i) 6 h-purification *via* ethanol precipitation to remove salt, excess primers, and enzyme and ii) 10 min-denaturation process for PCR products conversion to labeled ssDNAs with higher binding affinity. Finally, they were exposed to their complementary DNA probes immobilized on Au surface for hybridization. The surface plasmon spectrometer showed that fluorescence signal increased with higher DNA concentrations, and the reported LOD was 100 fmol and 500 fmol using PNA and DNA probes on Au surface, respectively. Apart from the long post-PCR process, an extra wait time is necessary for PCR product interaction with functionalized Au surface which also follows a surface regeneration step to remove bound analytes and prepare it for the next analysis cycle. This makes SEF method a time-consuming and laborious detection technique less practical for POC testing.

2.4.3.3 Surface-enhanced Raman scattering (SERS)

Surface-enhanced Raman scattering has become a powerful surface spectroscopic technology detecting low concentration of analytes through capturing molecular structure information. This phenomenon happens when a nanostructured metallic substrate is placed in the vicinity of a molecule. The incident EM field on the substrate goes through amplification by SPR excitation, and this concentrated EM field loses or gains energy upon interaction with the adjacent molecule via inelastic/Raman scattering. The inelastically scattered and plasmonically enhanced EM field contains information about the vibrational modes of the interacted molecule which is used as a fingerprint to detect target molecules [146]. In brief, there are two mechanisms contributing to SERS enhancement: i) EM enhancement due to LSPR and ii) chemical enhancement due to charge transfer between molecule and metal atoms. It is reported that SERS enhancement factor can be up to 10^{15} [181, 182]; therefore, one can achieve ultrahigh sensitive detection of a single molecule by using SERS using dense metallic nanostructures [183]. Since SERS spectroscopy measures molecular vibrations, the background environmental signal interference is excluded. Moreover, signal-to-noise-ratio (SNR) can be improved in SERS technology by simply shifting the excitation and Raman scattering wavelength into NIR biological transparency window, so that the background noise produced by complex biological materials is minimized. In addition, PCR-SERS assay offers greater number of DNA target detection in comparison with fluorescence multiplex detection. This is due to the fact that Raman bands of labels are 10-100 times narrower than excitation and emission bands of fluorescent dyes [184]. The other advantage of SERS over realtime fluorescence assay is the absence of multiple excitation wavelengths and filters for multiplex detection. Also, SERS is capable of detecting dye-labeled oligonucleotide probes as low as $7.5 \times 10^{-13} \text{ M}$ which is considerably lower than the reported LOD values in fluorescence-based techniques [185]. Despite all these advantages, SERS-based amplicon detection is an endpoint detection technique which consists of numerous and laborious steps [186]: i) DNA amplification with labeled primers, ii) post-PCR denaturation step, iii) SERS probes addition to labeled ssDNAs for hybridization, iv) ssDNA-SERS complex immobilization on modified magnetic beads, v) washing and discarding magnetic beads, and vi) finally the pure ssDNA-SERS complex addition to SERS reagents (e.g., silver colloidal suspension) for Raman spectroscopic analysis.

One solution to reduce SERS-based detection steps is to use self-hybridized/self-complimentary SERS primers (Figure 2.14.a) [147]. During PCR, the closed primers denature to hybridize to their complementary sequence in DNA target, and their non-complementary region overhangs freely in solution. After PCR process, PCR reaction is added to plasmonic NPs colloid to allow the overhang regions adsorb on NPs (Figure 2.14.b), and thereby, an increase in SERS signal intensity is observed. The SERS signal detected for positive controls is significantly greater than negative controls enabling classification of PCR results (Figure 2.14.c and Figure 2.14.d). Using this method, the total assay time is 2 h, and the detection sensitivity is reliant on PCR efficiency, *i.e.*, for better discrimination between positive and negative control based on SERS spectra, the PCR yield should be more than 50%. The other factor impacting the detection sensitivity is the competition between PCR ingredients to adsorb on the surface of NPs making NPs less available for SERS probes.

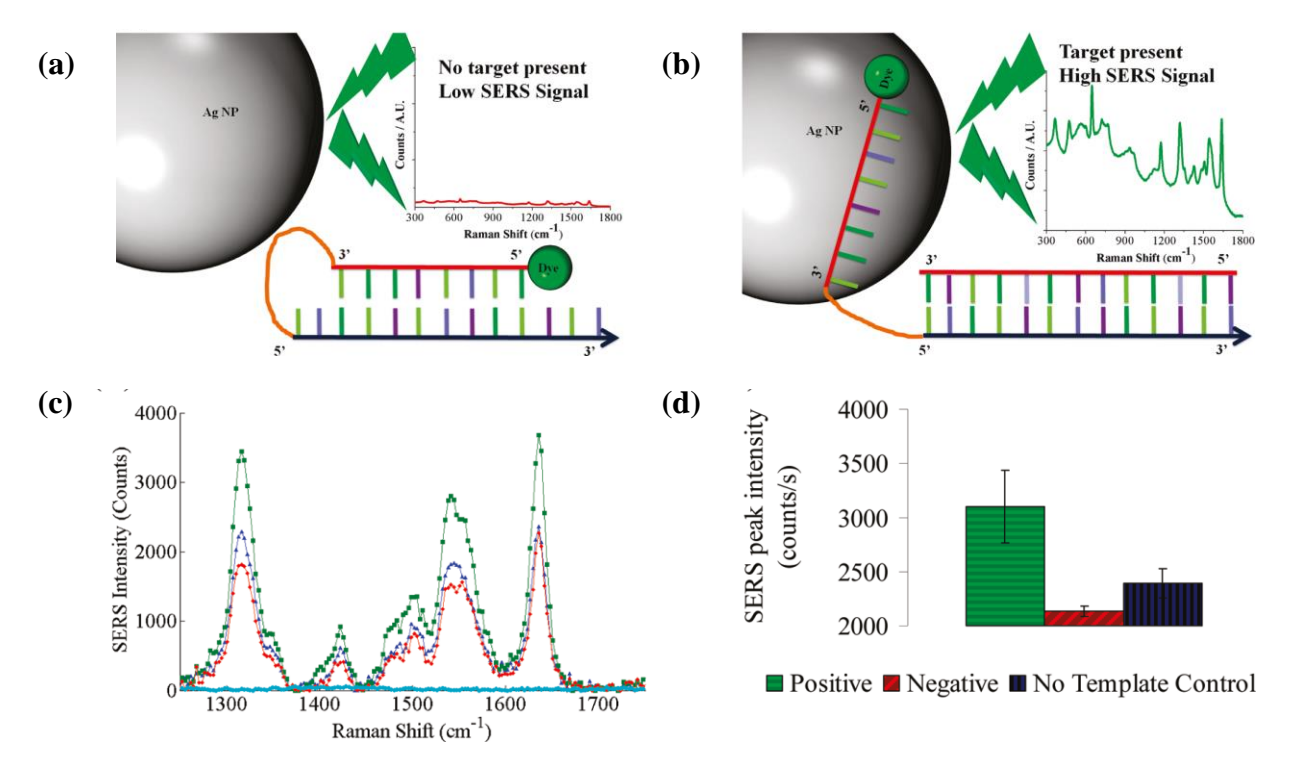


Figure 2.14 (a) Schematic of closed SERS primer in the absence of target DNA. (b) Hybridization of target DNA to its complementary sequence in SERS probe setting free the dye labeled ssDNA parts of SERS primer to get adsorbed on negatively charged AgNPs. (c) SERS spectra for positive control (green), no template control (dark blue), negative PCR sample (red), and blank (light blue). (d) Discrimination of PCR results based on average SERS signal peak at 1632cm⁻¹ for three positive, negative, and no DNA template controls. Reprinted from Ref. [147], Copyright (2011), with permission from American Chemical Society.

A breakthrough in SERS technology was the introduction of multiplexed real-time PCR-SERS assay carried out in a low-cost thermoplastic fluidic chip [187]. By using a dialysis membrane, the PCR chamber was isolated from the AgNPs colloid, and through SERS probe digestion by polymerase during PCR process, the SERS dye is released from the probe and passed through the pores of the dialysis membrane to interact with silver colloid. Thus, the membrane sealing to avoid AgNPs leakage to PCR chamber and pass only SERS dye is critical for proper functioning of this assay. The other challenge with this approach is the temperature dependency of SERS dye diffusion. Moreover, SERS performance is highly temperature dependent making its integration into real-time PCR assay more complicated than fluorescence- and absorption-based detection methods. Considering the inherent multistep process of PCR-SERS assay, costly SERS probe design, and its qualitative amplicon detection, this assay requires more improvements towards its practicality for POC applications.

2.4.3.4 Plasmon coupling sensor (Colorimetric assay)

LSPR is a sensitive optical transducer which translates changes in metallic nanostructure size, morphology, composition, local RI, and distribution/aggregation state into spectral shift in absorption or scattering spectrum. Based on previous discussion in this chapter, the spectral shift due to RI change of metallic NP's surrounding medium is the basis of SPR sensor. On the contrary, in a colorimetric assay, the spectral shift is induced by changes in plasmonic NPs' interparticle distance, size, as well as morphology upon target molecule presence. Accordingly, this spectral shift in optical properties of NPs manifests itself as a color change in plasmonic NPs colloidal solution which allows rapid and sensitive colorimetric target detection by naked eye or cost-efficient optical devices [188]. The plasmonic coupling sensing is one of the methodologies used in colorimetric assay, and plasmon coupling is a phenomenon that can take place when the distance between two NPs is less than few nanometres (lower than the size of NPs); as a result, the electric field of each NP is the superposition of incident light field and the field induced by electric dipole oscillation of the neighboring NP. Jain *et al.* calculated that the plasmon wavelength maximum redshift for two-particle system (coupled particle) with respect to an isolated particle resonance maximum ($\Delta t_{two-particle}$) is proportional to the following fraction [120]:

$$\Delta \lambda_{\text{two-particle}} \propto \varepsilon_{\text{m}} \left(\frac{3}{4(\frac{\text{S}}{\overline{D}} + 1)^{3} - 1} \right)$$
 (2.18)

Where s is the interparticle distance (surface-to-surface), D is the NP diameter, and $\varepsilon_{\rm m}$ is the surrounding medium dielectric constant. It should be noted that particles were assumed to be identical and spherical. From equation (2.18), it is evident that events such as aggregation or target-induced forming cross-linking assembly lead to redshift in resonance wavelength. Therefore, the basis of colorimetric assay is to induce this reduction in interparticle distance upon target molecule presence by various forces, namely, electrostatic interaction, covalent bonding, hydrophobic interaction, and biologically specific interactions [189].

One approach to trigger plasmonic NP aggregation is to use thiolated primers to add a thiol group to the amplicon during the PCR process [190]. After amplification, thiolated amplicons are added to AuNPs colloid, and their cross-linking (covalent bonding) *via* thiol—gold interaction prevents salt-induced aggregation of NPs. Thus, color change is only observable when the target template is absent. Using the cross-linking between primer-functionalized AuNPs and amplicons, Cai *et al.* introduced a one-step and one-pot colorimetric detection eliminating post-PCR processing steps [191].

Additionally, other studies employed AuNP-oligos in an asymmetric PCR (aPCR) [150]. aPCR is a methodology of using unequal primers concentrations in which the strand of DNA template with excess primer amount amplifies in the form of dsDNA, while the other strand accumulates in the form of ssDNA due to depletion of lacking primer. After aPCR completion, the generated ssDNAs will be added to two sets of AuNPs-oligos complementary to different parts of target ssDNA to crosslink and bring AuNPs close to each other.

It should be noted that these colorimetric amplicon detection methods require target-specific probe design even for qualitative testing of sample. This is in contrast to qualitative sample analysis *via* absorption or fluorescence detection in which no probe or intercalators, respectively, are required.

This problem was solved by aPCR-amplified ssDNAs containing a universal tag, *i.e.*, DNA template was amplified with limiting forward primer including a sequence complementary to a universal tag [149]. Thus, oligo probes on the surface of AuNPs are complementary to a portion

of universal tag making the assay universal for any target DNA detection. Another universal colorimetric amplicon detection strategy is to take advantage of target ssDNAs affinity to plasmonic NPs surface *via* electrostatic interaction (non-cross-linking method). As a result, the aPCR-amplfied ssDNAs interact with negatively charged AuNPs through non-covalent and non-specific interaction (Figure 2.15.a). Adsorption of ssDNAs on AuNPs surface leads to more particle stability and protects AuNPs from salt-induced aggregation; hence, no spectral shift and no color change in solution is observed in a positive control. On the other hand, in the absence of target ssDNAs, AuNPs solution undergoes salt-induced color change. Quantification of amplicons is obtained both by spectroscopy (Figure 2.15.b) or by naked-eye color observation (Figure 2.15.c).

One main advantage of colorimetric assay compared to other PCR product detection methods is the assay simplicity and cost-effectiveness due to absence of costly light sources, optical components, and detectors, particularly in non-cross-linking method with the additional advantage of using unfunctionalized plasmonic NPs. However, some considerations should be carefully observed to achieve valid colorimetric analysis. First, oligos/primers immobilized on NPs should have minimal complimentary base pairs to prevent AuNP-primer dimers conjugates aggregation and false positive results. Second, the design of probes is of great importance since detection sensitivity depends on the probe's length. That is, with shorter cross linking oligos, less interparticle distance, and subsequently more spectral shift and higher detection sensitivity is achieved. On the other hand, shorter sequences have higher hybridization tendency at room temperature giving rise to particle aggregation and false positive results. Third, the colorimetric detection sensitivity is also dependent on sample volume and detection/wait time. In other words, through sample miniaturization, the number of particle aggregation events is decreased, and thereby the detection sensitivity is degraded. Also, in order to detect lower target concentration, longer incubation and detection time is needed after mixing amplified products with NPs. Finally, generally in colorimetric assay, the concentration of PCR ingredients especially polymerase and Mg²⁺ is required to be calibrated to prevent steric crowding of reagents molecules on NPs surface.

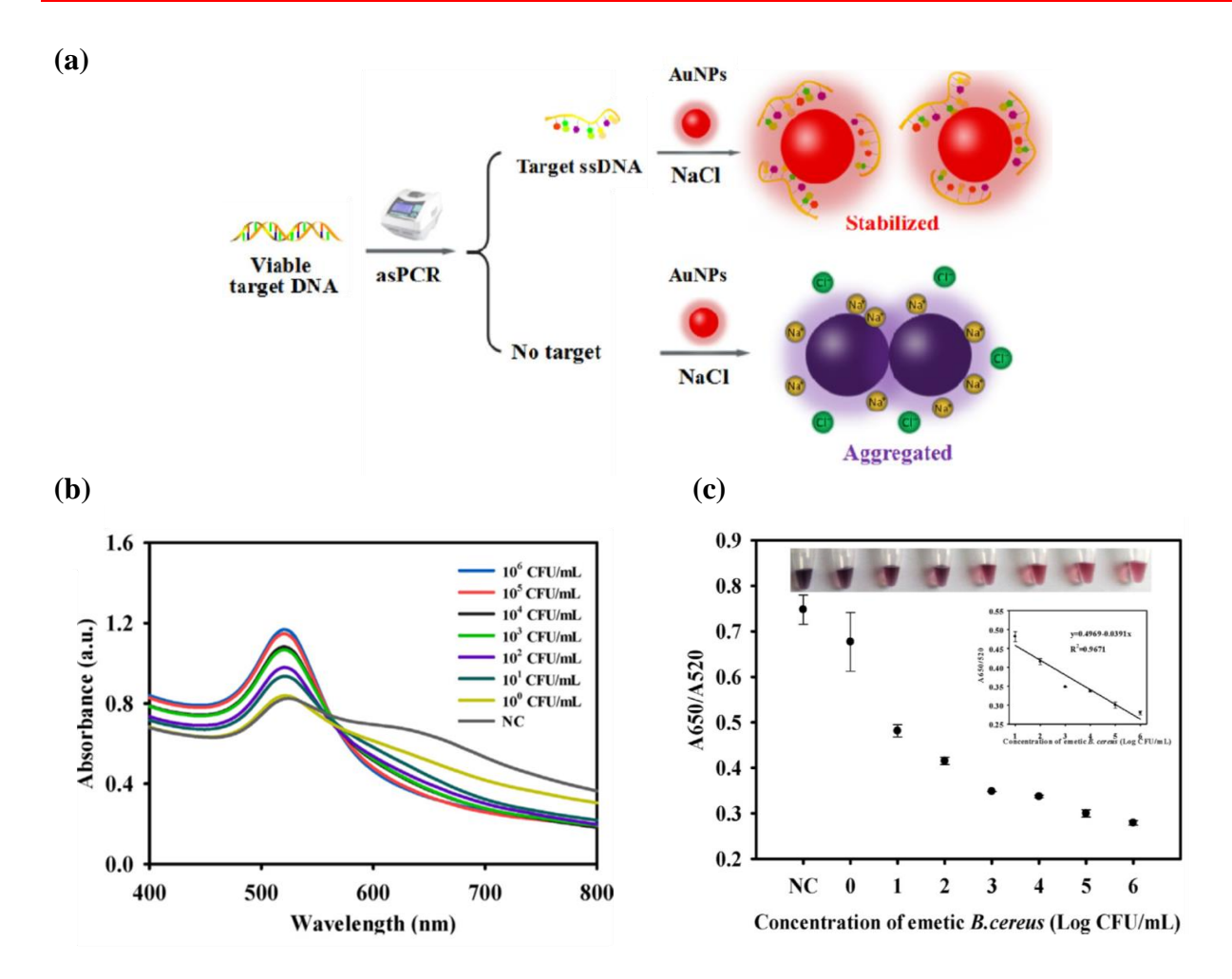


Figure 2.15 (a) Conceptual overview of colorimetric amplicon detection based on AuNPs protection against salt-induced aggregation due to the presence of target ssDNA; however, in the absence of target, salt-induced aggregation of AuNPs leads to a visible color change from ruby-red to blue-purple. (b) The change in absorption spectra of AuNPs with varying concentrations of target (emetic B. cereus). (c) The absorbance ratio of PCR sample at 650 nm to 520 nm wavelength is plotted against different emetic B. cereus concentrations. Adapted from Ref. [148], Copyright (2017), with permission from Elsevier.

2.4.4 Optical waveguide-based detection

Optical waveguide interferometry is a label-free detection of biomolecules in which coherent light undergoes two identical paths: reference and sensing arm. The only difference between the two arms is that the sensing arm is functionalized with a probe to target analyte of interest. The binding events result in RI change and consequently phase shift in the beam propagating along the sensing arm. Equation (2.19) shows how RI change (n) in optical path length (OPL) alters the sensing beam phase (φ) with λ wavelength [192].

$$\varphi = \frac{2\pi \times OPL \times n}{\lambda} \tag{2.19}$$

Once the two split beams are optically combined, the interference pattern is analyzed to detect the presence of binding events. Since interferometric biosensors are highly sensitive, they were used to achieve a PCR-free detection method such as development of four optical channel waveguide by Ymeti *et al.* [193]. Therefore, optical waveguide-based detection coupled with PCR can provide superior detection sensitivity. In the study conducted by Kim *et al.*, the detection of PCR-amplified DNA was achieved by reflectometric interferometry combined with LSPR [153]. In reflectometric interferometry, light from a tungsten halogen lamp (360-2000 nm) is incident on a specially fabricated and functionalized substrate, and the reflected interference from the substrate is captured and analyzed. The substrate was made of deposited AuNPs on a porous anodic alumina (PAA) layer chip which was functionalized by thiolated probe DNA, and upon target DNA hybridization, the plasmonically enhanced relative reflected intensity was increased and fringe wavelength was also redshifted. Consequently, a linear relationship between DNA concentration and relative reflected intensity as well as fringe wavelength shift was observed, and the lowest and highest limit of detection was reported as 10 pM and 10 µM. The upper limit is owing to the saturation of immobilized probes on Au deposited PAA layer chip surface by target DNA.

One of the challenges associated with interferometric biosensors is that the length of arms should be long enough to achieve low detection limit. Furthermore, based on fringe period formula $(\frac{\lambda L}{d})$, the fringe resolution depends on the spacing of two arms (d) and the detector distance from the arms' output (L) [192]. Thus, for a maximum fringe resolution, the two arms should be sufficiently close without field overlapping creating coupled waveguides. Additionally, other critical factors such as required detector pixel pitch, detector distance from waveguide to maximize fringe resolution, and proper channel/arm width to avoid propagation of additional modes are of great importance in design fabrication.

Optical ring resonator also gained attention as a promising amplicon sensor for POC testing due to its fast response and miniature size. A ring resonator, or resonant optical cavity, is an optical waveguide looped back on itself to accumulate and confine light energy by total internal reflection at specific wavelength [194]. Once the analytes bound to the surface of waveguide, the effective

RI in the path of evanescent field of the resonating light changes. Equation (2.20) shows how effective RI (n_{eff}) impacts the resonance wavelength of resonator (λ) [195].

$$m\lambda = 2\pi R n_{eff}$$
 $m=1,2,3,...$ (2.20)

Where R is the radius of ring resonator. The biomolecular binding events manifest themselves as a redshift in resonance wavelength which is used to quantify biomolecule concentration [196]. For instance, a silicon microring resonator functionalized by oligo probes was used for multiplex detection and quantification of aPCR-amplified ssDNAs [197, 198]. For quantification purpose, the plot of resonance wavelength shift against cycles was used to obtain threshold cycle. The threshold cycle in this methodology was defined as the cycle number at which wavelength shift is equal to 40% of its maximum value. Ring resonators gained increasing importance for biosensing due to their high sensitivity and easy on-chip integration. However, ring resonators suffer from side-wall surface roughness leading to larger surface scattering losses, a compromise in the Q-factor, and subsequently limited sensitivity [199]. Furthermore, ring resonators require expensive and bulky tunable lasers which challenge their utilisation for POC testing.

2.4.5 Chemiluminescence detection

Chemiluminescence is a detection technique in which light emission occurs due to analyte binding and its subsequent electrochemical oxidation or reduction creating products in electronically excited states with short decay time [200]. As a result, the deexcitation of these products to ground state emits photons at specific wavelength. One advantage of this technique is the absence of light source, and consequently, the detected signal is not affected by external light scattering, background interference due to luminescent impurities, and source fluctuations [201]. Thus, all the captured photons at detection sight are true signal from a dark chemical reaction [202]. Moreover, since this approach only requires a luminescence reader, the simplification in system design (*i.e.*, no light source) provides a more cost-effective, compact, and simple diagnostic tool for POC testing.

The chemiluminescence detection of PCR products was accomplished in the study conducted by Kalligosfyri *et al.* by performing the following steps [154]: i) denaturation of biotin labeled PCR-amplified dsDNAs, ii) hybridization to target probe, iii) adding streptavidin-horseradish

peroxidase conjugate combined with a chemiluminogenic substrate, iv) 1 min sample incubation, and v) finally the photochemical emission was detected by smartphone camera to obtain an analytical relationship between chemiluminescence intensity and target DNA concentration

One challenge associated with detection of chemiluminescence is the weak light intensity resulting in lower detection sensitivity compared with other detection methods. To overcome this problem, chemiluminescent labels are coupled with plasmonic NPs to obtain signal amplification as a result of chemiluminescence emission peak overlap with the absorption band of plasmonic NP [201]. Another challenge is the need for sensitive detectors to capture low light intensity. Moreover, the features of luminometers to detect chemiluminescence of reactions depend on the kinetic behaviour of labels [203]. That is, transient labels with fast kinetics in orders of seconds require fast response detectors, while enzyme labels have steady-state kinetics in order of minutes or hours.

2.5 Conclusions and perspectives

In this chapter, modern optical strategies used in gold standard molecular diagnostic test, PCR, was summarized. In the first part of this chapter, we focused on the advances in rapid optical thermocyclers for the purpose of delivering high sensitivity and specificity of PCR assay to nearpatient testing by using optical absorption property of one PCR ingredient (water) or PCR additives, i.e., nanomaterials. Furthermore, studies benefited from sample miniaturization and microscale optofluidic techniques for the purpose of shorter assay time and simpler microfluidic designs were presented. In the second part, real-time (in situ) and endpoint (in situ and ex situ) optical detection methods together with their challenges were explained. Some studies improved the portability aspect of traditional optical detection systems such as spectrometers and fluorimeters through miniaturization and their conversion to on-chip detection mode. On the other hand, other studies explored novel detection paradigms by using nanoengineered optical probes (QDs, UCNPs, and plasmonic NPs) with their enhanced optical characteristics to overcome complications associated with conventional organic dyes and detection methods such as shortened OPL and high background. In contrast to optical volumetric detection techniques such as absorbance, fluorescence, interferometry, and chemiluminescence in which the whole bulk sample volume is assessed for target detection, in optical nano-biosensing methods, analyte binding events on nanoprobes' surface are measured, and as a result, noise generated from non-specific molecules interference in bulk sample volume is eliminated. However, nano-biosensors' practicality for onfield applications is limited owing to their high cost, short shelf life, and their surface functionalization requirement with target-specific bioreceptors.

Apart from all complications with the aforementioned optical techniques used in PCR, the main challenge is to propel these proof-of-concept optical demonstrations towards the next generation of POC devices. First, from the manufacturing standpoint, in order to be a commercially available POC instrument, the mass fabrication of thermocyclers and biodetectors should be feasible and cost-effective. This is dependent on advances in optoelectronics industry, device fabrication process, and the required material in design (PDMS, paper, Si, etc). Second, field-testing should be less reliant on the skills of users to perform manual sample preparation and loading. The growing trend towards fully automated molecular diagnostic instrument reduces the dependency of the validity of results on user performance. Third, although multiple target PCR-based amplification and detection are successfully achieved in lab-based platforms, the capability of these new optical approaches for co-amplification and multiplex detection should be investigated for their POC testing integration. Next, the dual aspect of PCR process (amplification and detection) should be carried out in one POC-suitable device; thus, a new route for researchers is to combine these photonic thermocyclers with novel optical detection techniques into one platform since even the most sensitive optical detection method is impractical for on-site testing when target amplification is carried out in a convectional lab-based thermocycler. Additionally, the difficulties related to world-to-chip interface (µL-mL reagents pipetting into nL-pL PCR chambers) and chipto-world interface (user read-out modality) should be minimized in research environments, as these are critical factors dictating the degree of practicality of a device in real world testing condition. Finally, another promising trend is to add a validation layer to improve the accuracy of test results by incorporating multiple detection strategies into one device such as combination of colorimetric assay and FO-SPR technology in one optical detection system. The aforementioned challenges towards a PCR-based POC device open up new objectives for researchers to pursue, and with rapid development in the field of optofluidic, microfluidic, nanomaterial, and analytical methodologies, we expect the emergence of more powerful and POC-ideal PCR devices enabling lab-quality diagnostic results for rapid and accurate medical decisions.

CHAPTER 3

VCSEL-based plasmonic thermocycler

3.1 Introduction

Recent progress in microfluidics and optical systems has made enormous impact in the advancement of nucleic acid amplification and detection. However, commercial and currently reported microfluidic PCR devices have not yet found their utilization in point-of-care (POC) applications. This is due to long amplification time, high power requirement, and bulky size of commercial PCR machines or cost-inefficiency, complex fabrication, and operation of microfluidic chips. In this chapter, we present a compact PCR device in which fast amplification is accomplished by photothermal heating of gold nanorods (AuNRs) evenly dispersed in PCR reaction by a vertical-cavity surface-emitting laser (VCSEL). Although small-scale LEDs have replaced bulky laser diodes in POC diagnostic devices, VCSELs have the additional advantage of low-divergence and focused beam characteristics enabling effective photothermal effect and subsequently faster thermocycling with lower optical power. Furthermore, due to the compact form factor of VCSEL, it can be placed close to the PCR tube for maximum light coupling efficiency as well as uniform heating inside the PCR reaction without the need for any additional optical components. The amplification of 221 bp Chlamydia Trachomatis DNA was accomplished under ten minutes for 30 PCR thermal cycles from 60 to 85 °C. In addition, employing conventional PCR tubes with 20 µL PCR reaction provides ease in sample loading and simplicity in design for POC diagnostics. Abundant sample volume facilitates any post-PCR sample analysis. As it has been reported that larger sample volume favors lower limit of detection in real-time PCR, integration of our system with a quantitative detection method will deliver higher sensitivity in amplicon quantification [204, 205]. The AuNRs appears to be robust in PCR solution after prolonged laser irradiation, which leads to stable temperature regulation and consistent PCR results. In contrast to other plasmonic thermocyclers with embedded plasmonic materials in PCR chamber walls, AuNRs are disposable and more cost-effective precluding the risk of biofouling

and run-to-run cross contamination. Moreover, AuNRs offer a tunable absorption and heating rate by simply varying their concentration in PCR reaction. The proposed thermocycler has the potential to circumvent some of the limitations of current PCR thermocyclers with its simple, low-cost, small footprint, and large sample volume for better adaptability to POC testing.

3.2 Study Design

3.2.1 Plasmonic PCR sample preparation

Poly(enthylene glycol)-modified gold nanorods (PEG-AuNRs) with 50 nM particle concentration were purchased from Nanopartz (Loveland, CO). The forward primer with 5 μM initial concentration were used to amplify 221 bp *C. Trachomatis* DNA Strain LGV III with 4.5×10⁵ stock concentration. Both primers and DNA template were purchased from ATCC (Manassas, VA). Hemo KlenTaq polymerase, Phusion® high-fidelity polymerase, and their buffers were purchased from New England Biolabs (Ipswich, MA), and KAPA2G Fast HotStart was purchased from Kapa Biosystems (Wilmington, MA). 2 mM dNTPs were purchased from ThermoFisher (Waltham, MA). 20 μL plasmonic PCR mixture was prepared by using 1 μL of PEG-AuNRs, 1 μL of DNA template, and 0.6 μL of dNTPs. Primers, polymerase, and buffer volumes follow each polymerase PCR protocol indicated in Table 3.1. The rest of PCR sample volume is made of double distilled water (ddH₂O). The same PCR protocol was used to prepare PCR reaction mixture for conventional PCR machine. The final PCR mixture was loaded in a 0.2 mL thin wall plastic tube, and plasmonic PCR samples were covered with 50 μL mineral oil to avoid water evaporation.

Table 3.1 Positive PCR protocol for different polymerases.

| PCR component | Volume (µL) |
|---------------------------------------|---|
| 5X Taq/Kapa2G/Phusion Reaction Buffer | 4 |
| Taq/Kapa2G/Phusion polymerase | 0.8/0.1/1 |
| dNTPs (2 mM) | 0.6 |
| Forward Primer (5 µM) | 0.6/1 ^{a, b} |
| Reverse Primer (5 μM) | 0.6/1 ^{a, b} |
| DNA (10 ⁴ copies) | 1 |
| PEG-AuNRs (50 nM) | 1 |
| ddH ₂ O | 11.4/11.3 ^a /10.4 ^b |
| Total | 20 |

^{a, b} Reagent volume used for Kapa2G and Phusion, respectively.

The preparation of different negative PCR samples follows Table 3.2. The negative controls are reactions missing one of the PCR ingredients, and as a result no bands are expected on gel image. These negative controls are run along with positive controls to verify the absence of contamination introduced into the master mix or into samples.

Table 3.2 Negative Controls with Taq polymerase.

| PCR component | Volume (μL) | | | | | |
|---------------------------------|-------------|---------------|-------------------|--|--|--|
| 1 CK component | No DNA | No Polymerase | No Forward Primer | | | |
| 5X Taq Reaction Buffer | 4 | 4 | 4 | | | |
| Taq polymerase | 0.8 | 0 | 0.8 | | | |
| dNTPs (2 mM) | 0.6 | 0.6 | 0.6 | | | |
| Forward Primer (5 µM) | 0.6 | 0.6 | 0 | | | |
| Reverse Primer (5 µM) | 0.6 | 0.6 | 0.6 | | | |
| DNA (10 ⁴ copies) | 0 | 1 | 1 | | | |
| PEG-AuNRs (50 nM) | 1 | 1 | 1 | | | |
| d ₂ H ₂ O | 12.4 | 12.2 | 12 | | | |
| Total | 20 | 20 | 20 | | | |

To achieve the different AuNRs concentration (2.5-29 nM), the volume of ddH_2O (11.4 μ L) was reduced and replaced by 50 nM AuNRs stock solution (Table 3.3). After amplification, PCR products along with Invitrogen 1 Kb Plus DNA ladder were separated by 1% agarose gel electrophoresis and visualized by using ethidium bromide under UV light.

Table 3.3 Positive PCR protocol with Taq polymerase for 2.5-29 nM AuNRs concentration.

| AuNRs final concentration in PCR reaction (nM) | PEG-AuNRs stock solution (µL) | ddH2O (µL) | Rest of PCR reagents (µL) |
|---|-------------------------------|---------------|---------------------------|
| 2.5 | 1 | 11.4 | |
| 4 | 1.6 | 10.8 | |
| 6 | 2.4 | 10 | |
| 8 | 3.2 | 9.2 | |
| 10 | 4 | 8.4 | 7.6 |
| 12 | 4.8 | 7.6 | |
| 15 | 6 | 6.4 | |
| 20 | 8 | 4.4 | |
| 29 | 11.6 | 0.8 | |

3.2.2 Laser selection

As was stated in the previous section, the POC practicality of previous laser diode-based plasmonic thermocyclers is limited due to the size of laser diodes and their drivers. Furthermore, edge-emitting diode lasers (EEDLs) have a rectangular cavity producing highly asymmetric elliptical beams with a divergence angle of 50° to 60° in the fast axis and 10° to 12° in the slow axis. Therefore, for properly collimating the output of EEDL complex optical solutions such as cylindrical fast axis collimator lens with high numerical aperture close to the diode facet is required. On the other hand, since VCSELs have optical cavities orthogonal to those of conventional EEDLs, they emit circularly symmetrical and less divergent beams (beam divergence<20°).

To obtain optimum beam coupling into the bottom of the PCR tube, the light source should be placed at a proper distance with respect to laser beam divergence. Using Gaussian beam propagation, we obtained Figure 3.1 demonstrating the relation between beam waist-tube distance (z) and divergence angle (θ) for specific beam width (W(z)). Since 86% of Gaussian beam power is carried within W(z), for maximum laser-to-tube beam coupling and photothermal efficiency, the beam width should be less than the width of the PCR tube (W_{tube}=3 mm). For an EEDL with fast and slow axis divergence of 50° and 10°, the beam width on the fast axis is equal to W_{tube} at beam waist-tube distance of 3.44 mm, while at the same distance, the beam width on the slow axis is equal to 0.6 mm. For a VCSEL with a divergence angle of 20°, the beam width identical to tube width occurs at a waist-tube distance of 8.5 mm (W(8.5 mm)=W_{tube}=3 mm).

This implies that the PCR tube should be at a much closer distance to EEDL to couple 86% of beam power on the fast axis into the tube compared to VCSEL. Thus, EEDL requires more complicated thermal management, as at a closer distance, the heat generated by PCR sample perturbs slope efficiency of EEDL or the poor heat dissipation of EEDL impacts PCR thermocycling. Additionally, even with efficient waste heat removal from both EEDL and tube, the asymmetric EEDL spot size ($W_{\perp}(3.4 \text{ mm})=3 \text{ mm} \text{ vs. } W_{\parallel}(3.4 \text{ mm})=0.6 \text{ mm}$) results in uneven illumination and consequently nonuniform plasmonic heating.

Thus, VCSEL can efficiently and uniformly focus the output beam on the PCR tube with a high coupling efficiency by simply placing VCSEL at a proper distance to the tube without the use of external optics. Finally, as EEDL emits light parallel to their mounting surface/semiconductor

substrate, the substrate should be positioned vertical to the laser mounting, and thereby making EEDL array packaging more complex and costly.

As a result, for our plasmonic thermocycler, VCSELs can be a better choice over EEDLs due to their higher quality of output beam profile and more cost-effective packaging, particularly for the case of laser array, which results in simpler and cheaper optical design, higher coupling efficiency, and uniform photothermal heating.

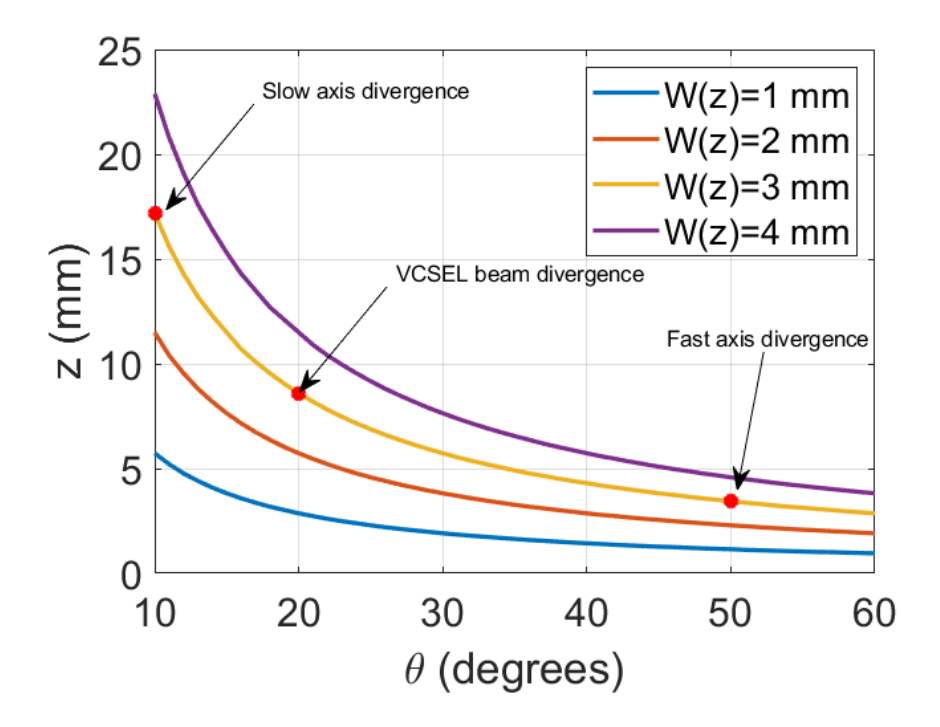


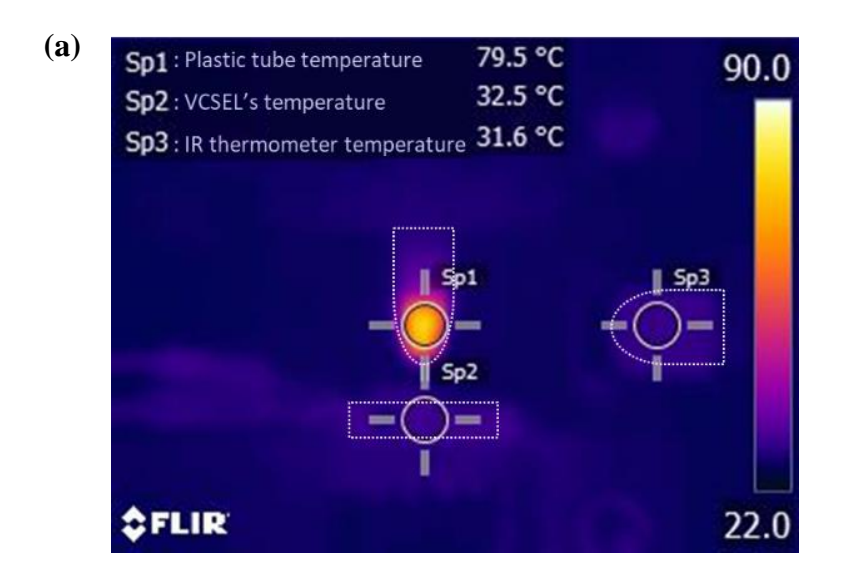
Figure 3.1 Comparison between EEDL-tube and VCSEL-tube distance for optimum beam coupling.

LEDs are another alternative to bulky laser diodes, but their high beam divergence and broad spectral power distribution necessitate using focusing optical elements and high-power LEDs.

Similar to free space VCSEL, fibre-coupled diode laser provides circular and homogenized intensity profile with a symmetric and low divergent beam. The principal advantage of fibre design is the absence of optical alignment and its flexibility in positioning. Therefore, with the help of fibres, the laser source can be placed far from the thermocycling system, and light will be directed easily on the PCR tube. This system with the remotely placed laser source will require less thermal management, as the dissipated heat of the laser source will not impact the temperature-dependent PCR reactions. However, since the minimum required temperature in PCR process is 60 °C, the dissipated heat of a closely placed light source to PCR reaction is negligible in comparison with

the "hot" PCR tube. The thermal images taken from VCSEL-based plasmonic thermocycler show that the maximum temperature increase for VCSEL is 3 °C when the tube's temperature fluctuates between 55 to 80 °C (Figure 3.2). This confirms that heating laser has minimal to zero disturbance to temperature regulation and stability of PCR reaction when it is placed close to PCR reaction. Owing to its small footprint, VCSEL can be placed close to the PCR tube, so that its low-divergence and the circular beam can be coupled into the domed bottom of the PCR tube without the need for focusing lenses. Therefore, this makes free-space VCSELs equally favorable as fibre-coupled lasers in our application.

However, the only factor which makes fibre-coupled lasers less practical for a POC device is the cost due to their packaging particularly for the case of multi-well/channel plasmonic PCR which requires efficient coupling of multiple laser arrays to optical fibres. For example, the cost for an 808 nm fibre-coupled laser diode on Thorlabs ranges from \$827 to \$4,500 depending on packaging (pigtailed or butterfly) with maximum optical power of 250 mW. The cost for an 808 nm 3 W VCSEL is approximately \$20, which can also provide high-quality beam characteristics as fibre-coupled lasers. Thus, VCSEL-based plasmonic thermocycler is simpler and more cost-effective in design compared to the aforementioned light sources.



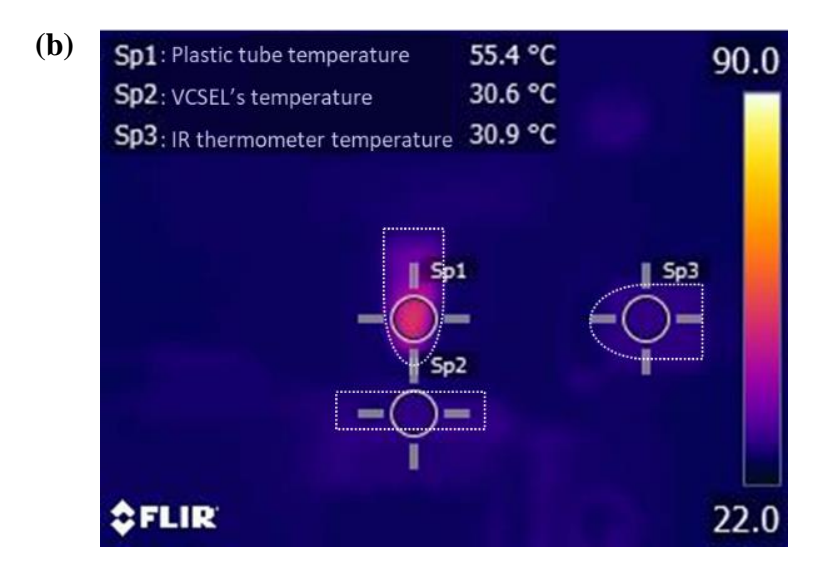


Figure 3.2 Thermal images of VCSEL-based plasmonic thermocycler showing different system components' temperature close to (a) denaturation and (b) annealing stage.

3.2.3 VCSEL-to-tube coupling efficiency

For efficient light-to-heat conversion and consequently high heating rate, the coupling efficiency of VCSEL's optical power into domed bottom of PCR tube should be maximized by calibrating VCSEL-tube separation distance. To fulfill this, Zemax optical design software in non-sequential mode was used to model VCSEL-to-tube beam coupling. The model geometry is such that the cone axis of PCR tube is aligned with optical axis, and the material selected for tube and PCR reaction were polypropylene and water, respectively. In order to use ray-based paraxial gaussian beam propagation, we need to consider that whether the propagation is within or outside Rayleigh range. Considering the nominal wavelength (808 nm) and divergence angle (10 °) provided in its datasheet, the propagation is far outside the Rayleigh range in this model, so the beam width increases linearly with propagation distance. Thus, beam can be modeled as a point source with 808 nm nominal wavelength. In this case, the beam waist is located in VCSEL housing, and the VCSEL output face is where the beam width is equal to VCSEL's emission area (1.1 μ m×1.1 μ m). The 3D layout plot of non-sequential rays traced from the point source to the intensity measurement surface is shown in Figure 3.3.

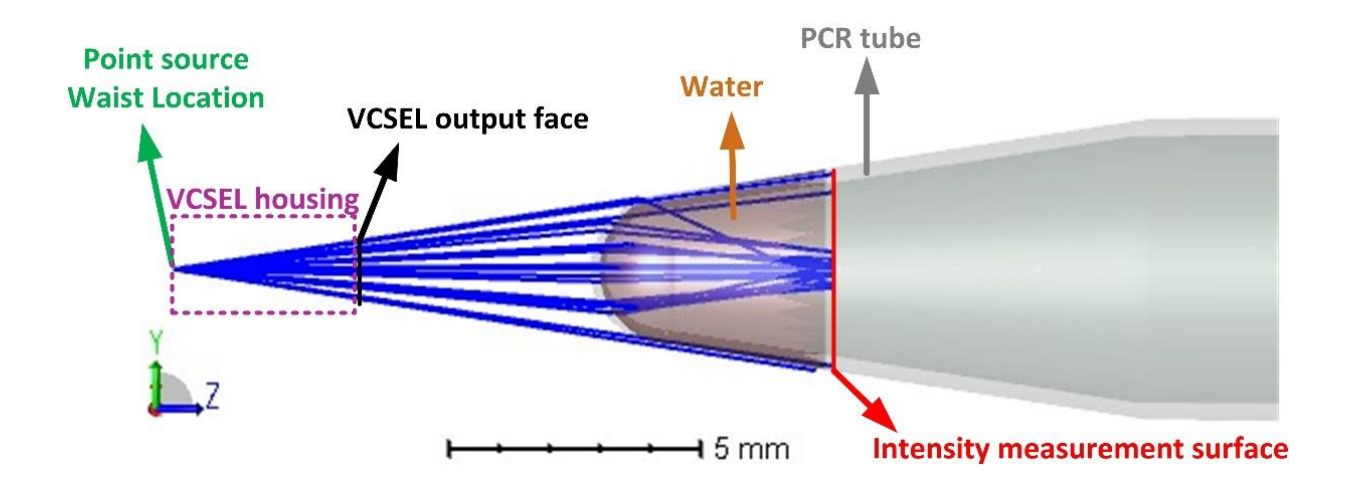
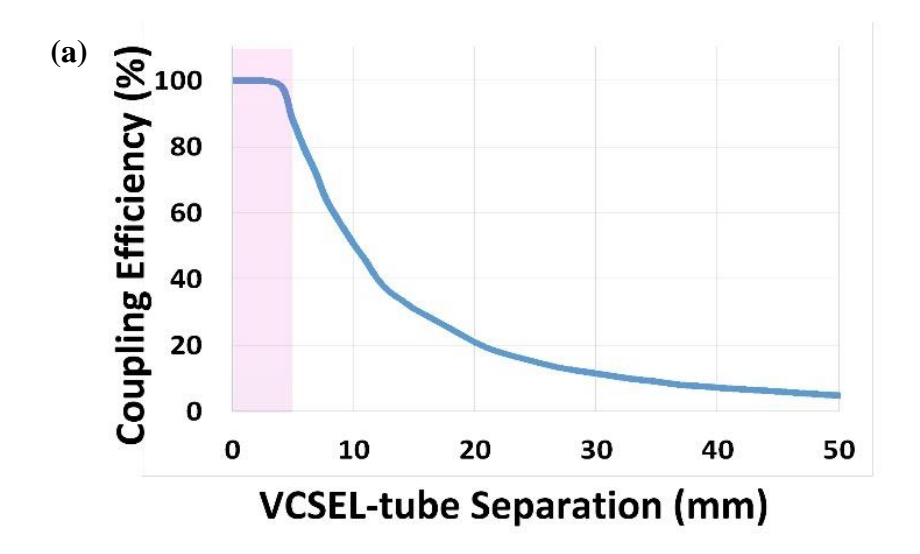
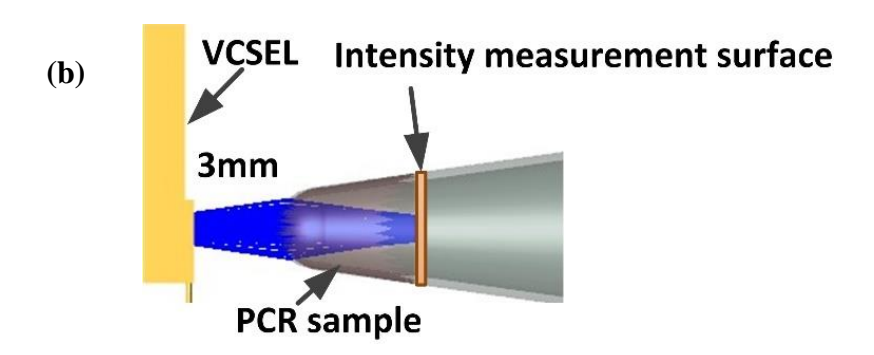


Figure 3.3 Zemax non-sequential model for VCSEL-based plasmonic thermocycler to maximize coupling efficiency.

Next, the distance between VCSEL output face and tube was changed in the model, and the optical power at the intensity measurement surface was calculated. Figure 3.4.a and Figure 3.4.b demonstrate that with VCSEL-tube distance of 5 mm or less (pink region), 89-100% of VCSEL's optical power is coupled into PCR tube. However, VCSEL-tube distance of more than 5 mm leads to significant coupling loss as a result of high beam divergence and laser beam total internal reflection in tube's wall (Figure 3.4.c). After placing VCSEL at the appropriate distance below the tube (\approx 3 mm), the VCSEL-induced photothermal effect was used to increase the sample temperature for thermocycling.





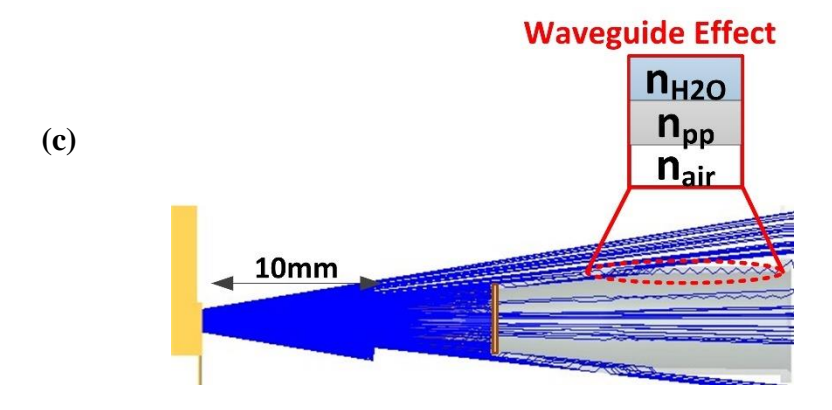


Figure 3.4 Optical simulation for VCSEL-to-tube beam coupling. (a) Calculated coupling efficiency for different VCSEL-tube separation distances based on Zemax optical model. Optical configuration and ray-tracing diagram for VCSEL-tube separation of (b) 3 mm and (c) 10 mm.

3.2.4 Instrument design

Figure 3.5 illustrates the plasmonic thermocycler system setup. PCR tube containing 20 μL of plasmonic PCR reaction was positioned 3 mm above an 808 nm VCSEL (3 W at 3.8 A) purchased from Tyson Technology Co. (Shenzhen, China). LD3000R driver from Thorlabs was used to supply 2.5 A constant current to VCSEL, and thereby VCSEL output optical power of approximately 2 W was obtained. By varying DC voltage applied to current control pin of LD3000R, the VCSEL optical power and subsequently PCR sample temperature was modulated. A 14 V DC brushless cooling fan was positioned above PCR tube. An infrared (IR) pyrometer purchased from Optris GmbH (Berlin, Germany) was placed 10 mm from one side of PCR tube for temperature measurement. The IR pyrometer was calibrated using TS5 fiber optic thermometer from Micronor Inc. (Camarillo, CA). An Arduino Due microcontroller was connected to PWM pin of current source and fan power switch for VCSEL and fan modulation.

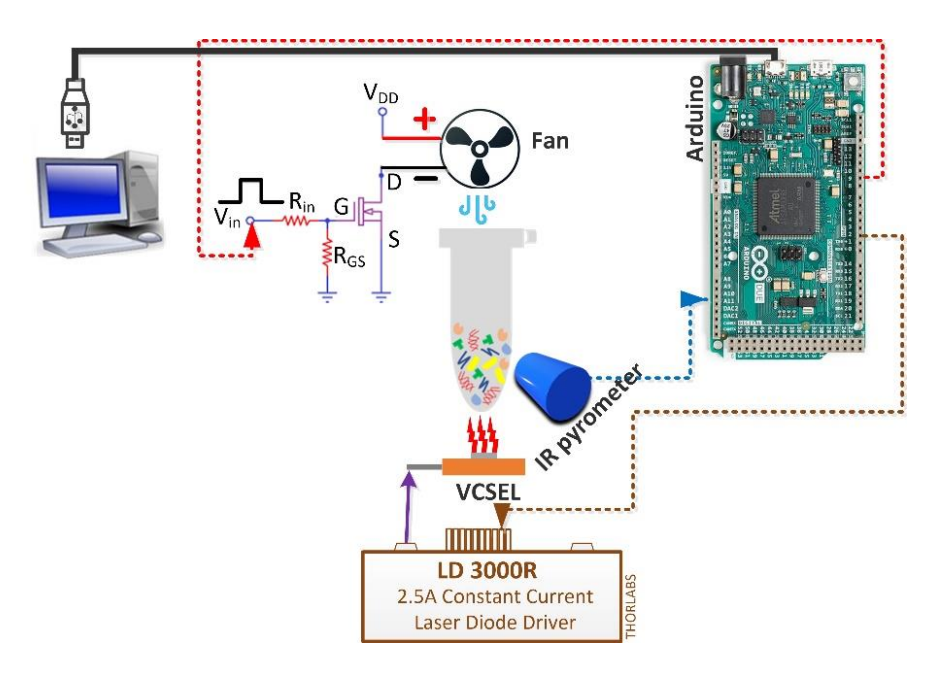


Figure 3.5 Design layout of VCSEL-based plasmonic thermocycler.

3.3 Principle of operation

Temperature regulation is a critical factor governing PCR process. Therefore, the first step is to calibrate IR pyrometer emissivity and transmissivity with a contact temperature probe for valid temperature measurement. Next, PCR set temperatures should be calibrated for the IR pyrometer. As was stated in the previous section, the typical denaturation temperature (T_D) in conventional thermocyclers is 90-95 °C. However, T_D for plasmonic thermocycler is different owing to the following reasons. First, in general, noncontact (IR) temperature measurement has lower spatial and thermal resolution compared to contact thermocouples or nanothermometers (QDs or fluorescent dyes) [206]; as a result, they have intrinsically lower accuracy compared to contact measurements. Second, in micro/nanoscale level, the water shell around AuNR is at much higher temperature than the average bulk temperature measured by macro temperature probes, even for contact thermometers. This phenomenon is more intensified for IR pyrometer, as the temperature is measured from the "cold" surface of PCR tube before PCR tube, PCR solution, and AuNR temperature reach a final equilibrium temperature. Consequently, before thermal equilibrium, the externally measured temperature is at lower temperature compared to internal nanoscale temperature, i.e., thermal lag. One consequence of thermal lag is that hot AuNRs are in contact with temperature sensitive PCR ingredients, potentially causing thermal inactivation of polymerase or thermal damage to other PCR ingredients. As a result, in VCSEL-based plasmonic thermocycler, the externally measured T_D is set lower (85 °C) than typical denaturation temperature to compensate low thermal resolution of noncontact measurement and avoid reagents thermal damage. This is also experimentally investigated in section 0 by exploring the impact of various T_D on PCR efficiency. Other externally measured set temperatures for annealing and elongation stages are 60 and 72 °C, respectively which were calibrated based on maximum PCR yield (section 0). Thus, the plasmonic PCR thermal cycling condition consists of 30-40 cycles of these three set temperatures with hold-times of 1, 5, and 1 s for denaturation, annealing, and elongation steps, respectively.

After placing VCSEL at the appropriate distance below the tube (\approx 3 mm), AuNRs were excited at their plasmon wavelength with a 2 W 808 nm VCSEL. As a result of this excitation, the electron distribution in the AuNRs conduction band is altered, as the electrons undergo a rapid temperature increase. The irradiated/heated electrons deexcitation follows three steps: i) electron-electron scattering within 500 fs, ii) electron-phonon coupling in 2-5 ps, and iii) finally the phonon-phonon interaction with AuNR surrounding medium which dissipates energy of the dipole oscillations in the form of heat to the water shell around AuNR. Considering the AuNR effective radius (r_{eff}) of approximately 9 nm (r_{eff} =($3V/4\pi$)^{1/3}) in our experiment, their total relaxation time (τ) to heat up PCR solution is around 53 ps based on the model of Hu *et al.* (τ =0.64 r_{eff} (nm)²) [130]. The deexcitation of AuNRs in the form of heat energy results in temperature increase which can be calculated by using equation (2.11) presented in chapter 2. To perform PCR thermocycling, the VCSEL is turned on and off to reach denaturation (T_D =85 °C), annealing (T_A =60 °C), and elongation (T_E =72 °C) temperatures (Figure 3.6.a). Fast cooling was obtained by using a fan. During hold-times at each PCR stage, the fan is turned off and temperature is kept constant only by toggling the VCSEL (Figure 3.6.b).

After amplification, the plasmonic PCR efficiency is compared with PCR products obtained from a conventional PCR machine (Eppendorf Mastercycler® Gradient) which is programmed for 40 cycles of 95, 60, and 72 °C with 5 s hold-times for each PCR stage. After PCR process, both plasmonically and conventionally amplified PCR products go through gel electrophoresis and visualization under UV light for PCR efficiency comparison based on band intensities/brightness.

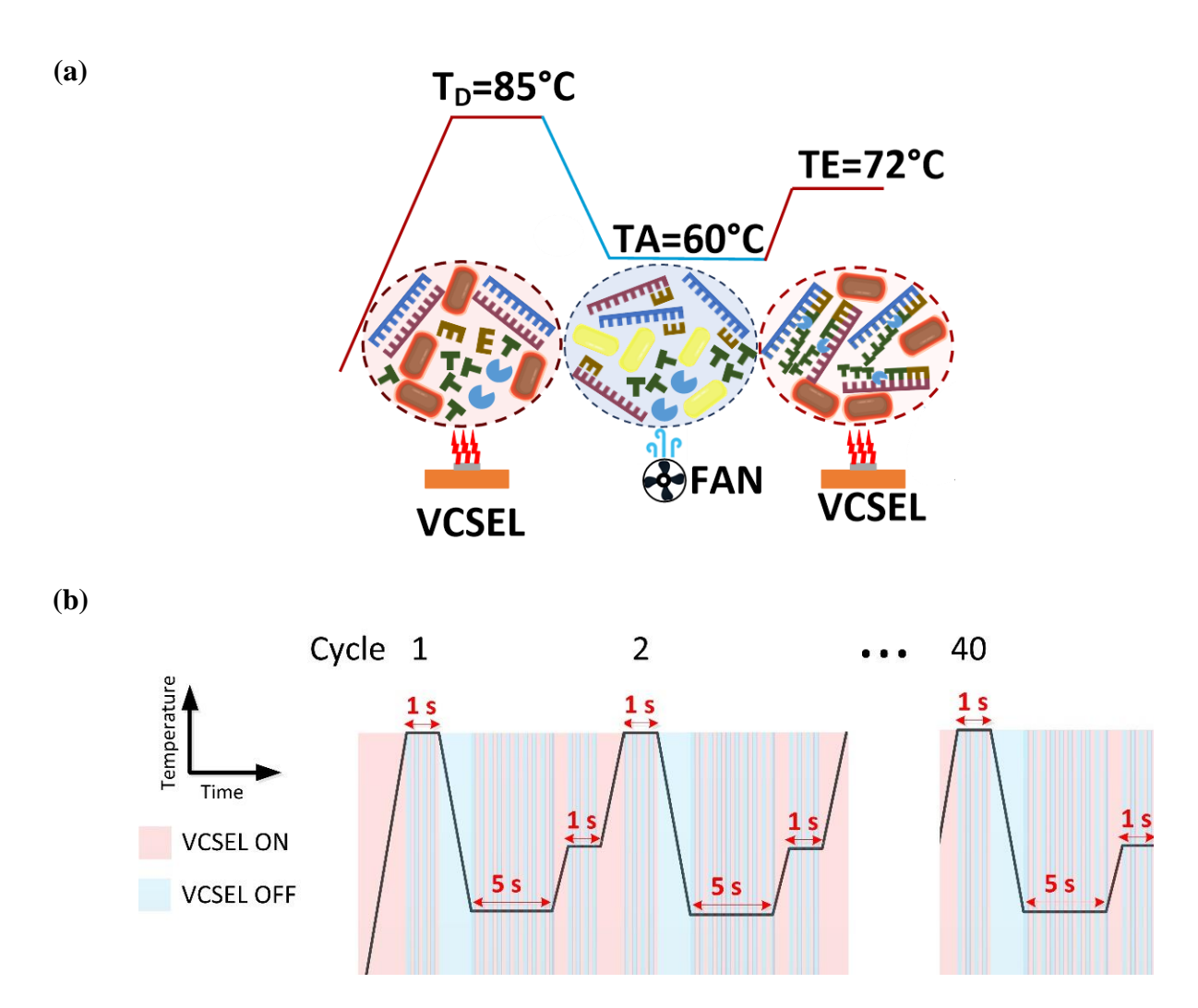


Figure 3.6 (a) Schematic of the VCSEL-based plasmonic thermocycler using suspended AuNRs as a light-to-heat converting medium and (b) conceptual illustration of VCSEL status during thermocycling.

3.4 Experimental results and discussion

3.4.1 DNA amplification in VCSEL-based plasmonic thermocycler

20 μ L PCR reaction containing 10^4 starting copy of *C. Trachomatis* DNA underwent plasmonic amplification with the same set temperatures and hold-times discussed in the previous section. By using 2.5 nM AuNRs final concentration, the total amplification time for 30 cycles was 9.5 min (Figure 3.7.a) with average heating and cooling rate of 6.29 ± 0.14 and $3.3\pm0.077\,^{\circ}$ C. s⁻¹, respectively (Figure 3.7.b). The averages and standard deviations (SD) at each set temperature were derived from the thermocycling curve, and the results were 85.44 ± 0.18 at $85\,^{\circ}$ C, 60.15 ± 0.12

at 60 °C, and 72.1±0.15 at 72 °C, demonstrating the ability of accurate temperature control and high temperature stability obtained from VCSEL-based plasmonic thermocycler.

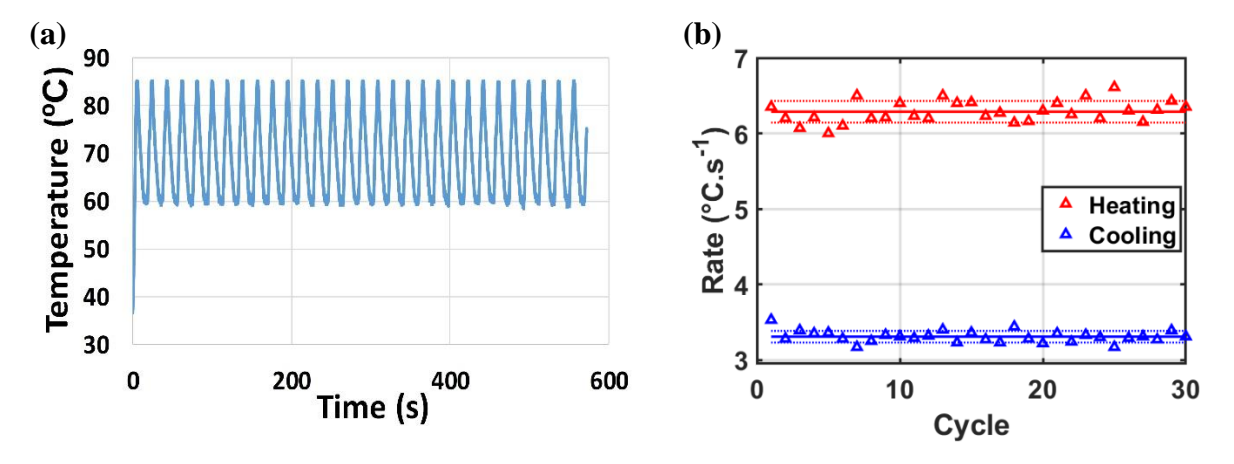


Figure 3.7 (a) An example of temperature profile of 30 thermocycles for successful DNA amplification. (b) Heating and cooling rates obtained from the temperature profile showing the average values (solid lines) with standard deviations (dashed lines).

To compare amplification efficiency of our plasmonic thermocycler with conventional PCR machine, 20 µL PCR solution from the same master mix used for plasmonic amplification went through conventional amplification. PCR products were retrieved from both platforms (plasmonic and conventional) and were visualized by gel electrophoresis. The band intensities on gel image (Figure 3.8) show that VCSEL-based plasmonic thermocycler generates comparable amount of PCR products as conventional PCR machine. Moreover, negative controls (no DNA template and no polymerase) were performed in both platforms to confirm the validity of results.

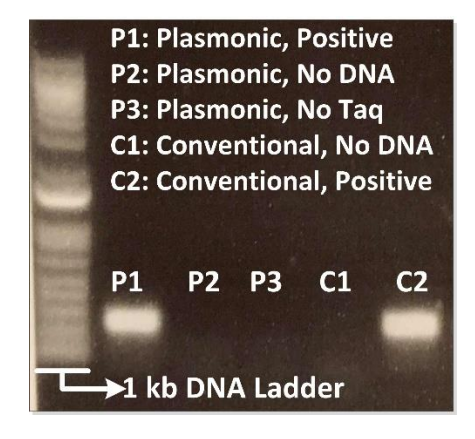


Figure 3.8 Gel electrophoresis image of PCR results. Band intensities obtained from conventional and plasmonic thermocyclers show comparable PCR efficiencies, and negative controls indicate a contamination-free master mix and validity of results.

Additionally, the photothermal efficiency of the VCSEL-based plasmonic thermocycler was calculated using equations (2.1) to (2.3) in chapter 2. Both calculated $\%\eta_{photon \to heat}$ and ramping rates of our plasmonic thermocycler is presented in Table 3.4, and they can be compared with other photonic nanomaterial-assisted PCR devices shown in Table 2.4.

Table 3.4 Summary of VCSEL-based plasmonic thermocycler characteristics.

| Ref. | Light source | P _{in} | λ (nm) | Nanomaterial Type | $[{ m Nanomaterial}]^1$ | V(µL) | $t_{ m cycle}(s)$ | Heating/Cooling rate (°C/s) | $\mathrm{Q}_{\mathrm{cycle}}(\mathrm{j})$ | P(mW) | %nphoton→heat |
|-----------------|--------------|-----------------|--------|----------------------|-------------------------|-------|-------------------|--------------------------------|---|-------|---------------|
| Current work | VCSEL | 2 | 808 | AuNR | 2.5 nM | 20 | 19 | 6.29 /3.3 | 2.34 | 0.52 | 26.32 |

¹Nanomaterial concentration

3.4.2 Study of AuNR robustness in plasmonic PCR reaction

In order to investigate whether AuNRs are robust after prolonged CW VCSEL irradiation in PCR solution, their absorption spectra before and after PCR were compared using UV-vis spectrophotometer (DS-11 Series, DeNovix Inc.) with 10 mm pathlength. To do this, plasmonic positive 20 µL PCR reaction containing different polymerases (Klentaq, KAPA2G, and Phusion) were prepared and underwent both conventional and plasmonic thermocycling. Figure 3.9 shows that AuNRs optical absorption properties remain intact, *i.e.*, no change in absorption peak and no spectral shift, for pre- and post-PCR samples amplified in plasmonic and conventional thermocyclers. Furthermore, PCR results on gel image (Figure 3.9.d) indicate that VCSEL-based plasmonic thermocycler protocol is not polymerase-specific, and despite using different polymerases with varying extension rates, the band intensities exhibit equally efficient DNA amplification in plasmonic and conventional platforms.

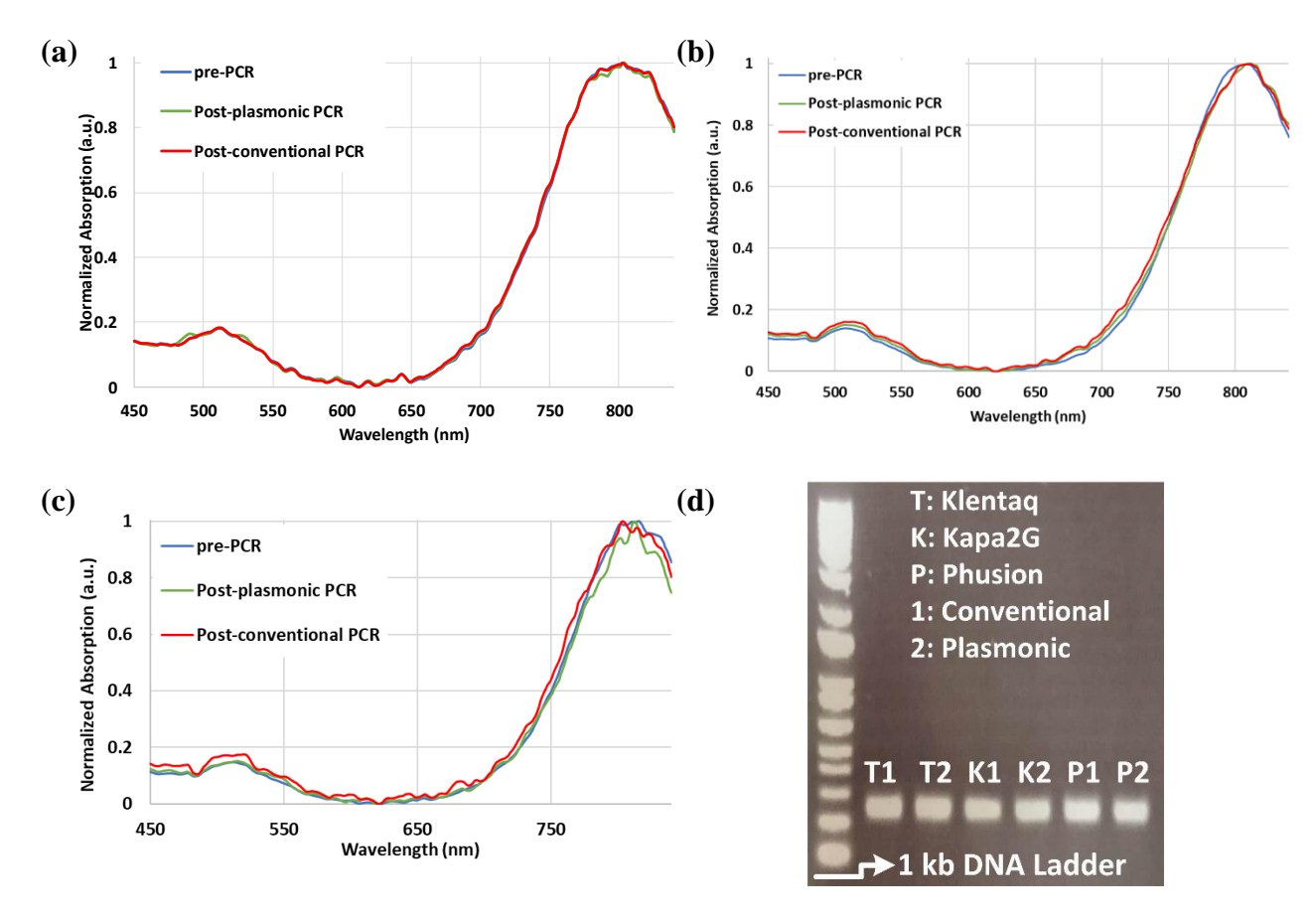


Figure 3.9 Normalized absorption spectra of plasmonic positive PCR reaction before and after PCR with (a) Klentaq, (b) KAPA2G, and (c) Phusion Polymerases. (d) Gel image for plasmonic and conventional DNA amplification using different polymerases, and the results on gel image demonstrate similar amplicon yield.

Additionally, an alternative approach to confirm AuNRs stability is to investigate their size and shape before and after plasmonic amplification by using electron microscopy. To fulfil this, positive and negative PCR samples with Taq polymerase were thermocycled plasmonically. To perform electron microscopy, 4 µL drop of each sample suspension was drop cast onto a 200-mesh Cu TEM grid having carbon support film (Agar Scientific). After 60 s, the excess suspension was wicked off with filter paper and the grid allowed to dry under ambient conditions. The drop-cast samples were then imaged by the FEI Tecnai G2 F20 S/TEM equipped with EDAX Octane T Ultra W/Apollo XLT2 SDD and TEAM EDS Analysis System and Gatan Ultrascan 4000 4k x 4k CCD Camera System Model 895. The proprietary Gatan Digital Micrograph 16-bit images (DM3) were converted to unsigned 8-bit TIFF images. The captured AuNRs in TEM images from pre- and post-PCR samples show that their shape is unaffected (Figure 3.10).

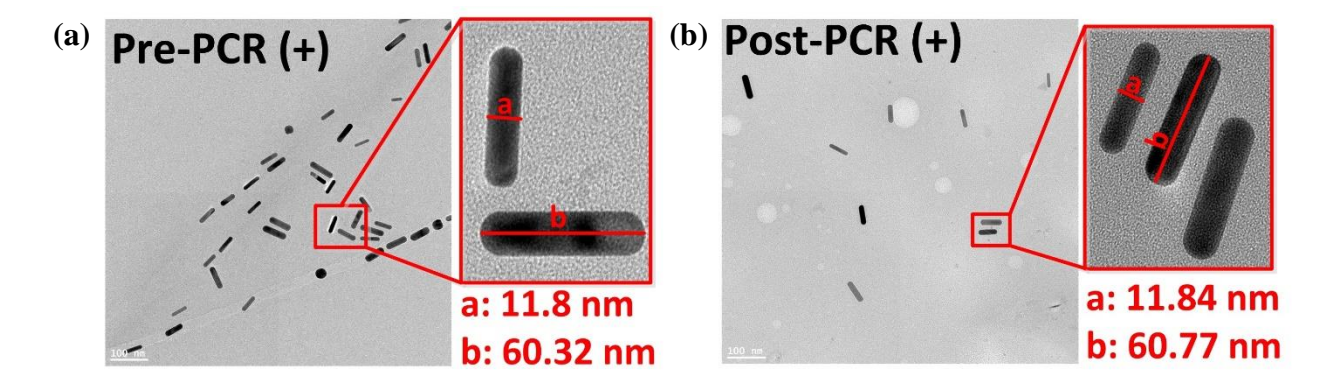


Figure 3.10 An example of close up TEM images captured from AuNRs from (a) pre-PCR and (b) post-PCR samples demonstrating unaltered AuNRs size and morphology.

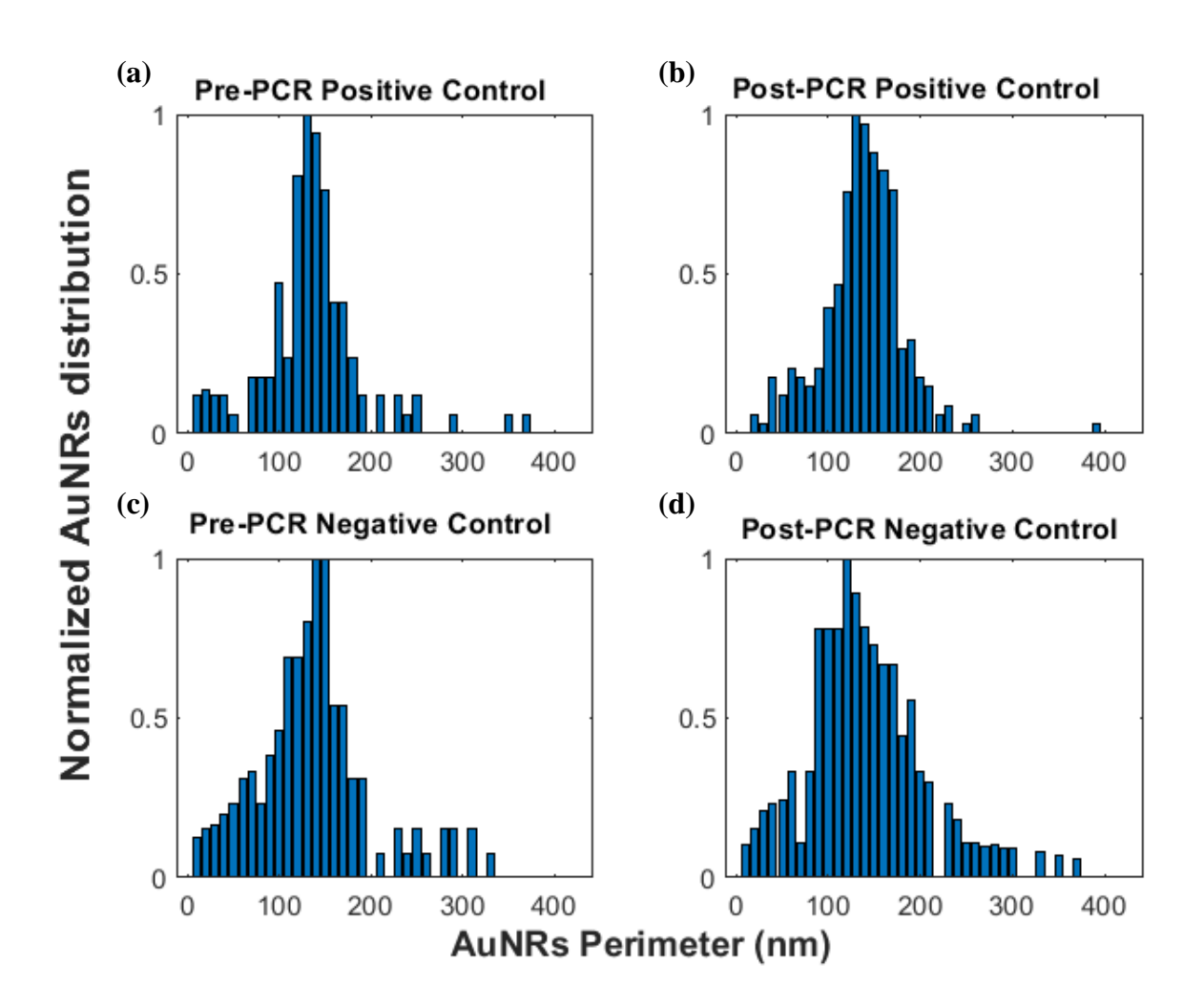
However, in order to understand about possible changes in AuNR's size before and after PCR, the perimeter of captured AuNRs in the TIFF images were calculated using MATLAB Image Processing Toolbox. The y-axis and x-axis in Figure 3.11 represent the normalized distribution of AuNRs' perimeter (P_N) for different controls and AuNRs' perimeters in nanometers, respectively. Dense distribution is observed both for pre- and post PCR of positive and negative controls with AuNRs of perimeters between 100 and 150 nm, while the smaller and bigger AuNRs lie in the left and right tail of the normally distributed perimeter curve (Figure 3.11.a to Figure 3.11.d).

The skewness of the bar graphs is the result of the polydispersity of colloidal AuNRs. The monodispersity of AuNPs depends on factors such as initial quantities of gold, reducing agent(s), and post-synthesis techniques (e.g., centrifugation) during its manufacturing process. Under electron microscopy, it is shown that the colloidal 808 nm AuNRs purchased from Nanopartz have a variety of dimensions resulting in the calculated perimeters ranging from 10 nm to 390 nm. The right skewness of the bar graphs indicates that more AuNRs with perimeters less than 200 nm were formed during fabrication. However, only AuNRs with a perimeter of approximately 140 nm and an AR of 4-4.15 will participate in plasmonic heating (equation (2.9)), as the VCSEL emission spectral BW ranges from 800 nm to 815 nm.

The average of pre- and post-PCR normalized perimeter densities ($P_{N_average}$) were calculated and plotted in Figure 3.11.e and Figure 3.11.f, and two gaussian curves were fitted to $P_{N_average}$ of pre and post-PCR.

Table 3.5 demonstrates the mean, median, and mode of $P_{N_average}$ for pre- and post-PCR samples. The FWHM of $P_{N_average}$ for post-PCR samples were increased by 24 nm indicating possible change in AuNRs' size as a result of thermocycling. However, this change has shown no impact on AuNR's absorption spectra shown in Figure 3.9. Moreover, it should be noted that this change is dependent on the number of AuNRs that we could capture by TEM.

It can be concluded that within the limits of the presented data via electron microscopy, UV-vis spectroscopy, and inhibition-free PCR tests, the AuNRs are sufficiently robust to be utilized in 40 cycles of plasmonic PCR.



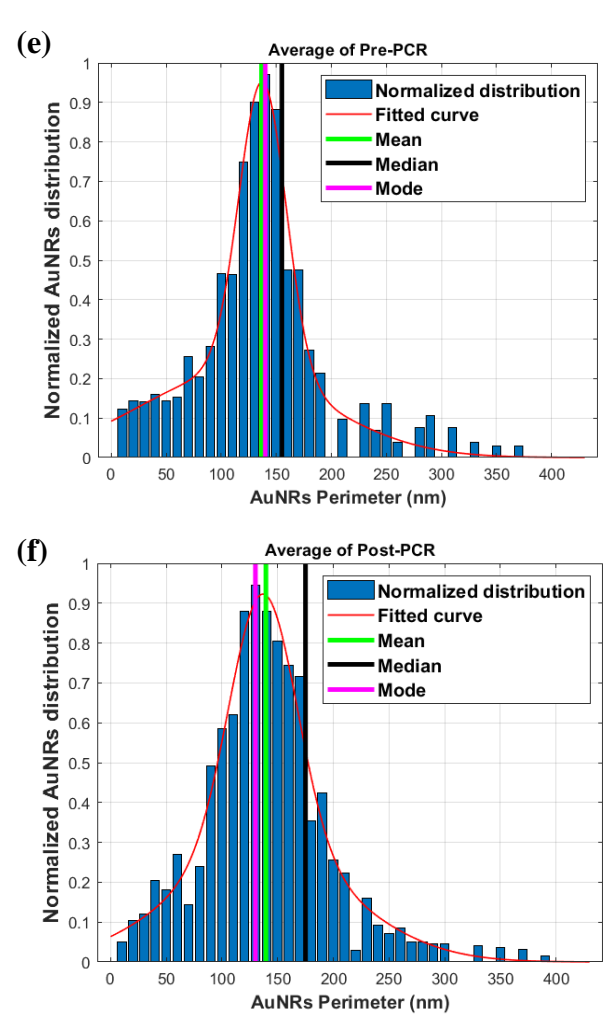


Figure 3.11 Calculated AuNRs' normalized perimeter densities for (a) Pre-PCR positive, (b) Post-PCR positive, (c) Pre-PCR negative, and (d) Post-PCR negative controls. Average of normalized (e) Pre-PCR and (f) post-PCR densities.

Table 3.5 Mean, median, and mode of AuNRs perimeters data set for pre- and post-PCR samples

| | Mean | Median | Mode |
|----------|-----------|--------|--------|
| Pre-PCR | 136.48 nm | 155 nm | 140 nm |
| Post-PCR | 139.41 nm | 175 nm | 130 nm |

3.4.3 Plasmonic PCR protocol optimization

Heating rate enhancement can be accomplished by increasing AuNRs concentration. However, excessive concentration of AuNRs act as a PCR inhibitor due to AuNR's surface interaction with PCR ingredients particularly DNA polymerase, and consequently AuNRs' ability to modulate the

polymerase activity [207]. It has been stated that surface interaction of AuNPs with PCR reagents mediates the PCR yield rather than heat-transfer enhancement [110, 111]. Therefore, it is critical to study the maximum allowed AuNRs concentration for rapid thermocycling without degrading amplification efficiency. Positive PCR samples with final AuNRs concentration of 2.5-29 nM were prepared (Table 3.3) underwent conventional amplification, and PCR results on gel image (Figure 3.12.a) show that excess AuNRs concentration up to 29 nM did not inhibit PCR or lower PCR efficiency. The results here confirm that shorter DNA amplification time (<9.5 min) can be obtained with our plasmonic thermocycler by increasing AuNRs concentration while maintaining the same amplification yield.

The speed of VCSEL-based plasmonic thermocycler depends on other parameters such as air flow rates, PCR set temperatures, and hold-times at each PCR stage. Therefore, these parameters were optimized to obtain faster thermocycling for a POC-ideal PCR device. One key factor in these optimization experiments was to enhance the parameters to a degree without compromising PCR efficiency. To fulfil this, positive PCR samples were prepared from one master mix and underwent plasmonic amplification with various modifications in these parameters (Figure 3.12.b). The gel image demonstrates that PCR failed for shortened annealing hold-times (t_a <5 s), but plasmonic PCR was successful with increased cooling rate (CR) up to 4.1 °C.s⁻¹ and 60 °C annealing temperature (T_A). However, higher cooling rate (CR=5 °C.s⁻¹) demonstrates efficient amplification only for the sample with decreased annealing temperature (T_A =57 °C).

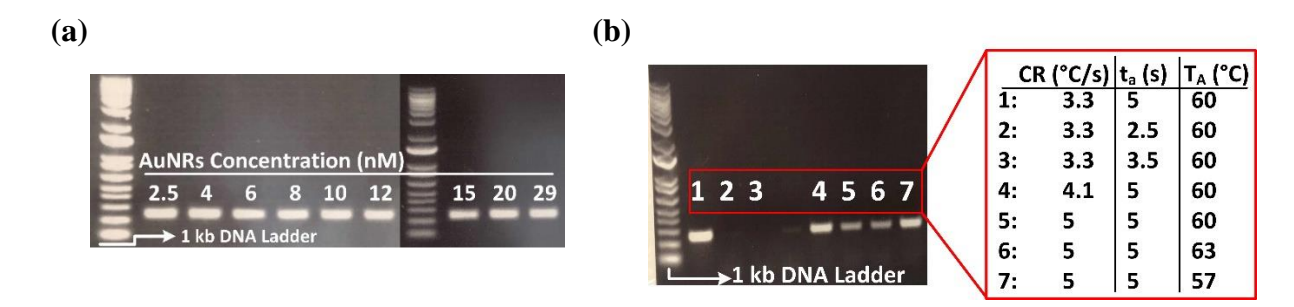


Figure 3.12 (a) Comparison of PCR yield using different AuNRs concentration in conventional thermocycler. The results reveal that AuNRs concentration can be increased up to 29 nM for faster DNA amplification without compromising PCR yield. (b) The gel image shows the impact of different PCR parameters on amplification efficiency. PCR failed for t_a less than 5 s (lane 2 and 3). Successful PCR was obtained with CR of 4.1 °C (lane 4). However, further increase in CR inhibits PCR (lane 5 and 6), and amplicon generation only occurs by lowering T_A (lane 7).

The first explanation to this inconsistent observation is that with 5 °C.s⁻¹ cooling rate and increased annealing temperature (≥ 60 °C), the effective time duration available for primers annealing is shortened, and thereby the annealing stage efficiency is decreased. The second explanation stems from the fact that the plastic tube loses heat faster than hot AuNRs inside PCR reaction (thermal lag), and consequently during sample cooling, IR temperature sensor measures the tube surface temperature which is at lower temperature than PCR solution. That is, before reaching to annealing stage, PCR solution is heated up to the next PCR stage, elongation. To confirm the presence of thermal lag, we used COMSOL Multiphysics to model time-dependent cooling of 20 µL PCR reaction at denaturation temperature. Similar to Zemax model, water was used as PCR reaction material with 85 °C initial temperature. The water is placed in polypropylene PCR tube, covered with 50 µL mineral oil, and enclosed by domed cap (Figure 3.13.a). By using the COMSOL module for heat transfer in solids and fluids, the surface heat transfer coefficient (h₀) was swept from 5 to 40 Wm⁻².K⁻¹ to model free and forced convection cooling. Line A and B were defined on the outer surface and in the center of the tube, respectively. Next, the time-dependent average temperature of line A $(\overline{T}_{line\ A})$ and line B $(\overline{T}_{line\ B})$ were calculated. The aim of this model was to measure the temperature difference between line A and B ($\overline{T}_{line\ B}$ - $\overline{T}_{line\ A}$) while $\overline{T}_{line\ A}$ is at 60 °C (annealing temperature) for different heat transfer coefficient:

$$(\overline{T}_{line B} - \overline{T}_{line A}) | \overline{T}_{line A} = 60 \text{ °C}, \quad 5 \le h_0 \le 40 \text{ Wm}^{-2}.\text{K}^{-1}$$

$$(3.1)$$

The bar graph in Figure 3.13.b shows that by increasing heat transfer coefficient to 40 Wm⁻².K⁻¹ (*i.e.*, cooling rate), $(\overline{T}_{line B} - \overline{T}_{line A}) | \overline{T}_{line A} = 60$ °C is intensified reaching to 6.9 °C. The result here proves the presence of thermal lag, and it also implies that there is a limit to increase CR without hindering temperature-dependent PCR reactions.

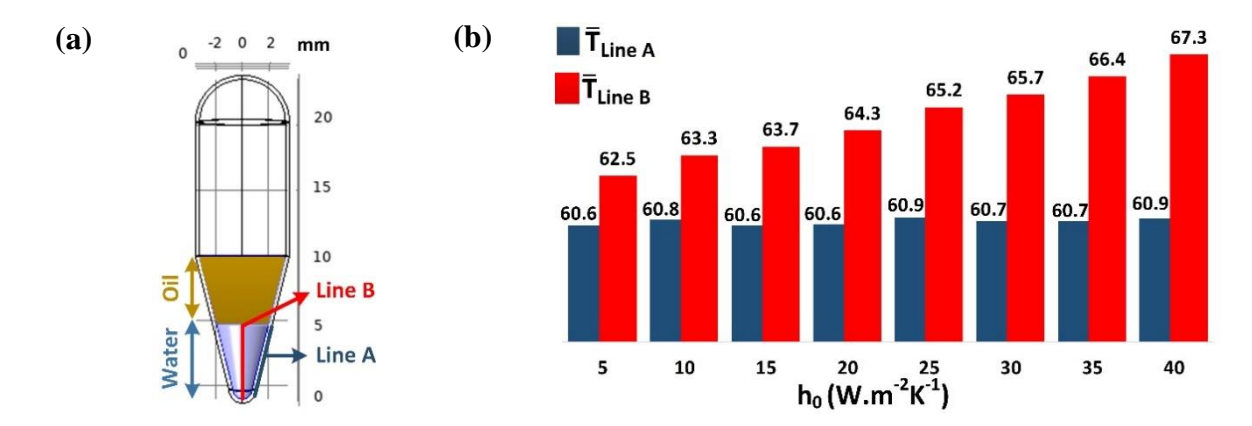


Figure 3.13 COMSOL simulation to obtain time-dependent cooling temperature profiles of the different lines defined in (a) the model geometry of 20 μ L water placed in a 0.2 mL PCR plastic tube. (b) The bar graph shows the impact of increased heat transfer coefficient (h₀) on temperature difference between line A and B (thermal lag).

Additionally, PCR set temperatures optimization is another factor to increase ramping rates and PCR yield. In other words, the lower T_D and the greater T_A result in less temperature difference between PCR stages and subsequently faster thermocycling. Therefore, positive PCR samples went through plasmonic thermocycling with different T_D and T_A , and the impact of various set temperatures on amplicon yield were explored based on the band intensity of samples in gel electrophoresis. Figure 3.14.a and Figure 3.14.b show that plasmonic DNA amplification fails for $T_A \ge 62$ °C and $T_D > 85$ °C. The optimal T_A and T_D are 60 °C and 85 °C which are the highest T_A and the lowest T_D for faster ramping rate giving the brightest band on gel.

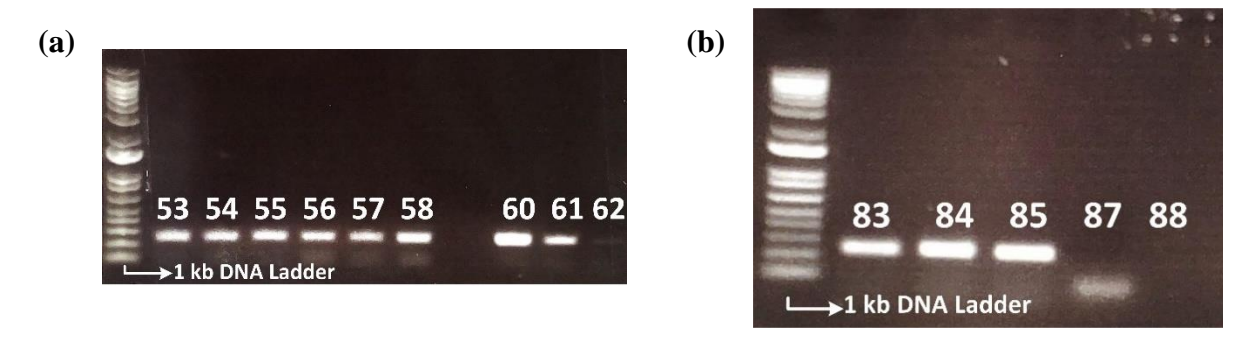


Figure 3.14 Comparison of PCR yield on gel image for different (a) T_A and (b) T_D .

Using PCR-safe set temperatures (83-85, 53-60, and 72°C) and hold-times (1, 5, and 1s), the VCSEL-based plasmonic thermocycler was able to perform more than 80 successful plasmonic PCR tests under different conditions such as different polymerases, cooling rates, and VCSEL position. The failed positive PCR controls were mostly due to unoptimized PCR conditions such

as high denaturation and annealing temperature, short hold-times, extremely fast temperature ramping, or suboptimal reagents concentration.

3.5 Summary

In this chapter, we presented a novel compact rapid thermocycler through plasmonic photothermal heating of AuNRs excited by an 808 nm VCSEL. The small configuration of this thermocycler was achieved *via* a different laser type without sample miniaturization which compromises the convenience in sample loading and the sensitivity in quantification of PCR product. Also, flexibility in positioning the light source close to PCR tube demands no light focusing components resulting in a simpler design than other proposed plasmonic thermocyclers. The amplification of 10^4 copies of *C. Trachomatis* DNA template was carried out in less than 10 min for 30 PCR cycles. The temperature stability during hold-times and reproducibility of successful PCR results indicate the robustness of AuNRs in PCR reaction and reliability of system. The UV-visible spectroscopy of pre- and post-PCR samples confirmed the unaltered optical properties of used AuNRs in our plasmonic thermocycler. Combining this portable, affordable, and low-powered VCSEL-based thermocycler with quantitative amplicon detection method delivers the same sensitivity and specificity of conventional PCR assay to POC diagnostics. The presented work can be further advanced to a multi-well plasmonic PCR on a VCSEL array to conduct multiplexed amplification.

CHAPTER 4

Real-time label-free PCR product detection

4.1 Introduction

Real-time amplicon detection would be an essential feature of in-field PCR testing. Despite all advances in real-time fluorescence- or SPR-based detection methods, they have not yet found their utilization in POC applications. This is due to the fact that they rely on relatively costly and bulky instruments (fluorometer, fluorescence filters, and spectrophotometer) as well as expensive and laborious target-specific probe design. In light of these challenges, in this chapter, the rapid VCSEL-based plasmonic thermocycler was combined with a POC-ideal detection strategy. The quantification of amplicons and determination of a success (amplification) and fail (no amplification) are accomplished by monitoring UV absorption of free nucleotides (dNTPs) in PCR reaction at every cycle. The structure dependency of UV absorption allows us to monitor the consumption of dNTPs for generated amplicons in PCR. The absence of fluorogenic probes and fully relying on optical measurements of one PCR ingredient eliminate false positive incidents due to "misprimed" amplification products, primer dimers, and degraded quencher molecule existing in fluorescent PCR. Also, maintaining the conventional sample volume of 20 µL further enhance the sensitivity and reliability in detection. The proposed real time PCR system would be ideal for POC applications due to its fast amplification, label-free quantification, simple and small configuration, and large reaction volume which leads to more convenience in fluid handling for on-site sample analysis.

4.2 Study Design

Figure 4.1 illustrates the complete amplification and detection system setup. The real-time amplicon detection system consists of a UV LED (Thorlabs, LED260J with ball lens and peak wavelength of 260 nm \pm 5 nm and output optical power of 1 mW at 100 mA injection current) positioned perpendicular to the plane of PCR tube-IR pyrometer. A 2 A BiCMOS constant current

source (STCS2A) from STMicroelectronics was used to drive UV LED with 100 mA, and UV light modulation was executed by connecting PWM dimming pin of STCS2A to Arduino. PDA25K2-GaP photodetector from Thorlabs was used to capture transmitted UV optical power after passing through PCR sample. Finally, the signal of photodetector is collected by an ADS1115 16-bit ADC to improve Arduino resolution and measurement accuracy, and then measured by Arduino's I2C pins.

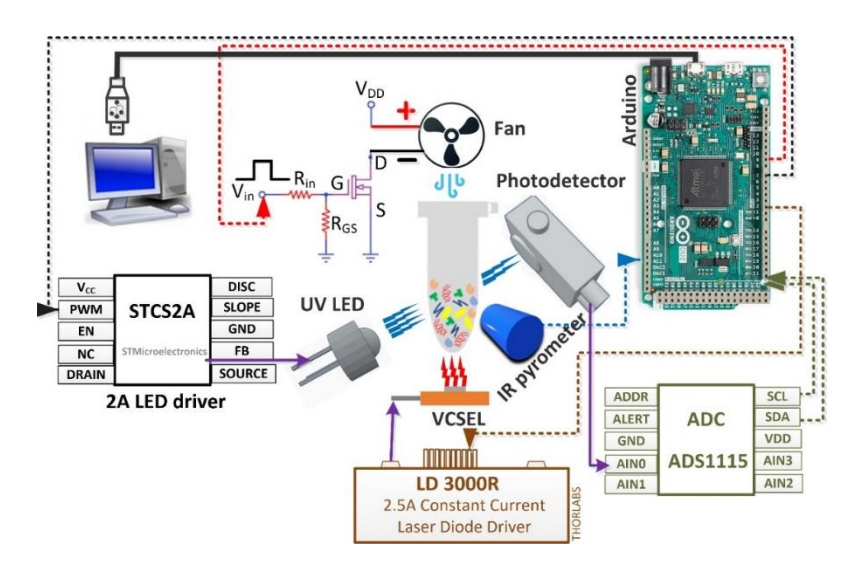


Figure 4.1 Schematic of the VCSEL-based plasmonic thermocycler and real-time UV detection system.

To maximize UV optical power at photodetector (P_{detector}), we performed radiometric analysis in Zemax optical design software in non-sequential mode. The UV LED was modeled as a source radial with 1 mW output optical power (P_{source}), 260 nm nominal wavelength, 3 mm × 3 mm flat rectangular emitting region, and symmetric distribution of rays into a hemisphere. The far field intensity distribution of Thorlabs UV LED, provided in its datasheet, was used to define the relative intensity measured in the far field of the source radial at specific angles. Next, we modeled Thorlabs photodetector with a flat absorbing rectangular detector (2.2 mm × 2.2mm) to store the energy data from non-sequential source rays that strike it. The model geometry is such that the optical axis is perpendicular to cone axis of PCR tube (Figure 4.2.a), and the material selected for tube and PCR reaction were polypropylene and water, respectively. Owing to optical system assembly limitations in practice such as the thickness of optical cage system mounting plates and the thickness of PCR tube holder, the shortest distance to place UV LED and photodetector with respect to PCR tube is 9 mm, and thereby the same distances were considered in the optical model. Furthermore, we considered that the non-sequential rays from source radial were statistically

scattered at ray-surface intercepts. Figure 4.2.b displays the rectangular detector view together with spatially incoherent irradiance at detector. In this figure, the total power indicates that 9.83% of source radial optical power reaches at detector ($\frac{P_{\text{detector}}}{P_{\text{source}}}$ =0.098) with this optical setup. In order to enhance $\frac{P_{\text{detector}}}{P_{\text{source}}}$, two converging lenses were used, and their characteristics were optimized in no-sequential mode for maximum optical power at detector. We found that UV-AR coated double-convex (DCX) lens (EFL: 6 mm and f/#: 1) from Edmund Optics were the best fit for the optimized converging lenses data. Therefore, the first DCX lens was placed between UV LED and PCR tube, and the second lens was placed between tube and photodetector (Figure 4.2.c). The center-to-center separation distance between each lens and PCR tube is 9 mm. Using this optical setup, the $\frac{P_{\text{detector}}}{P_{\text{source}}}$ is 0.127 with an approximately 30% increase in comparison with no-lens setup (Figure 4.2.d). Thus, we used 2-lens system for our real-time plasmonic PCR product detection.

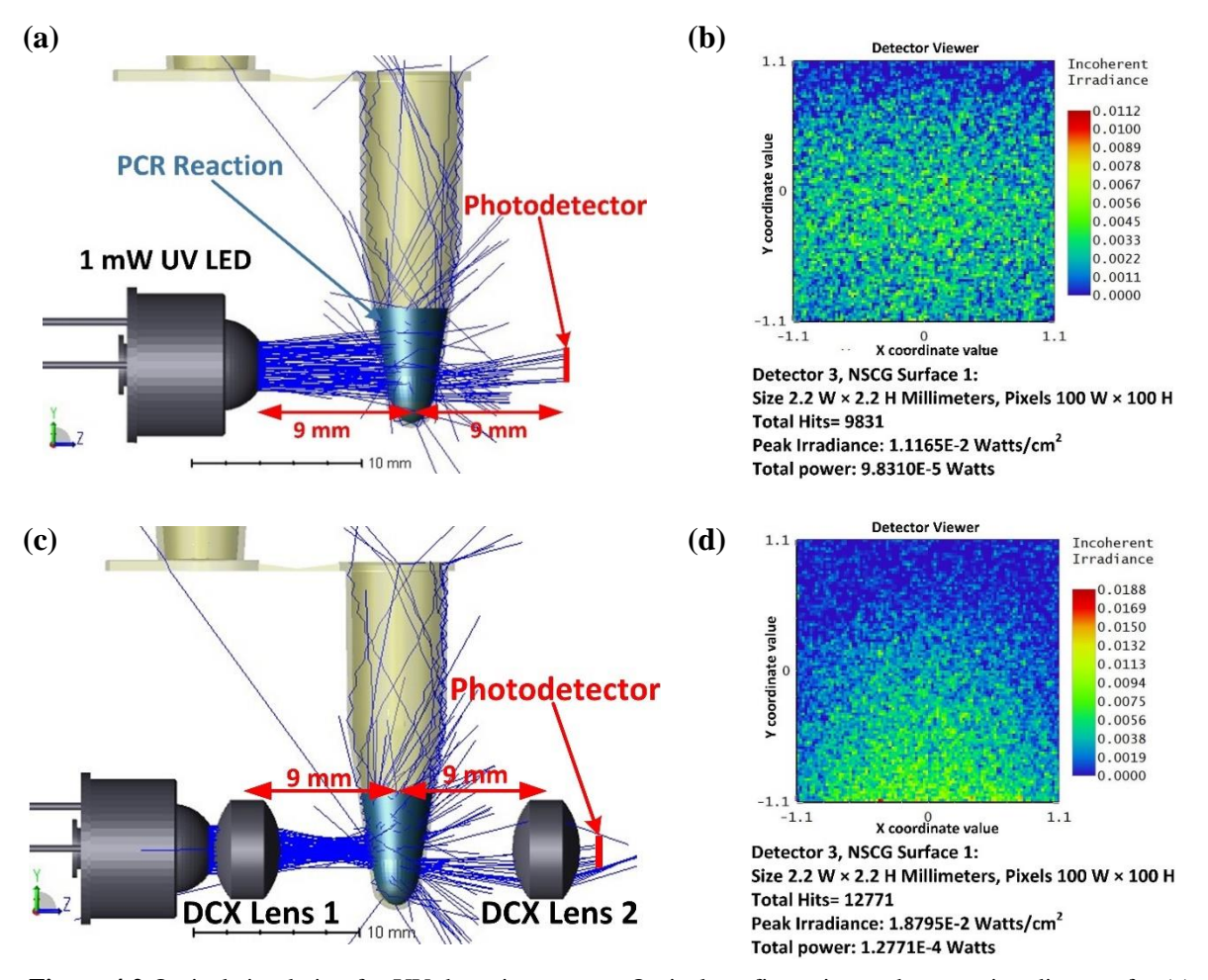


Figure 4.2 Optical simulation for UV detection system. Optical configuration and ray tracing diagram for (a) nolens system and (c) 2-lens system. Detector viewer for (b) no-lens and (d) 2-lens UV detection system.

4.3 Principle of operation

As is shown in Figure 4.3, bases in nucleotides (dNTPs) are either pyrimidines or purines. Both pyrimidines and purines have heterocyclic rings which share around their delocalized electrons. The availability of these electrons makes electron-photon interactions in UV region; therefore, bases in dNTPs are strong UV absorbers [208].

Figure 4.3 Pyrimidines and purines with one and two heterocyclic rings respectively [209].

Figure 4.4.a shows the absorption spectra of four different dNTPs. Although absorbance wavelength maximum is different for each dNTP; they have maximum UV absorbance at 260 nm (A_{260}) after averaging out absorption spectra of four types of dNTPs [210]. If free dNTPs bind together to form ssDNAs, the delocalized electrons are less available to interact with photons due to stacking interactions between dNTPs, and as a result A_{260} drops roughly about 10% going from free nucleotides to ssDNA. The photon-electron interactions are further restricted when dNTPs bind with their complementary bases and form a dsDNA due to hydrogen-bonded base pairs and base pair's hydrophobic characteristic. This leads to an approximately 27% decrease in UV absorption as a result of conformational change from ssDNA to dsDNA, *i.e.*, hyperchromicity.

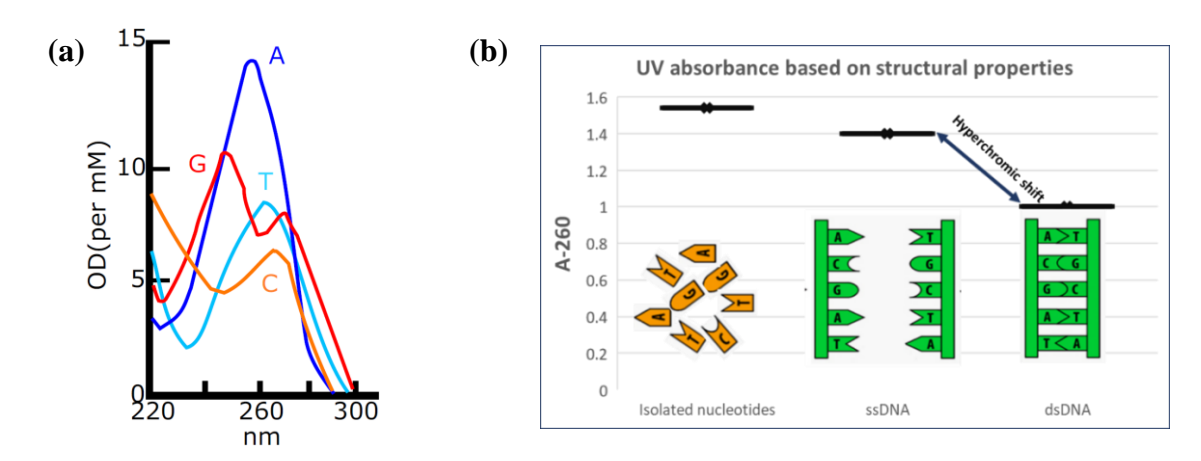


Figure 4.4 (a) Optical density for different dNTPs: adenine (A), thymine (T), guanine (G), and cytosine (C). (b) Change in UV absorbance based on conformational freedom of dNTPs [210].

This drop in UV absorbance as a result of change in dNTPs conformational freedom is the basis of our real-time UV detection. During PCR process, free dNTPs incorporation by polymerase to extend the new DNA strands results in a cycle-by-cycle drop in UV absorption of PCR solution (Figure 4.5).

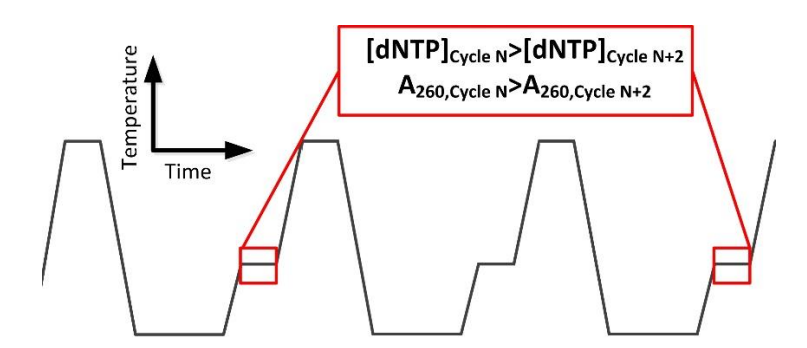


Figure 4.5 Schematic illustration of dNTPs consumption as PCR cycles proceed, and thereby cycle-by-cycle drop in A_{260} . [dNTP] denotes dNTPs concentration.

To monitor UV absorbance variation during thermocycling, the UV LED was turned on for 50 ms at the end of elongation stage of each cycle during plasmonic amplification (Figure 4.6), and the transmitted optical power through PCR reaction was collected by photodetector and plotted against cycles to generate UV amplification curve. To generate normalized UV amplification curve, the UV optical power values (as calculated from the photodetector voltage) were min-max normalized and plotted against cycles. The resulting normalized UV curves are used to determine PCR results and amplicon quantification. Finally, UV detection results are validated by gel electrophoresis.

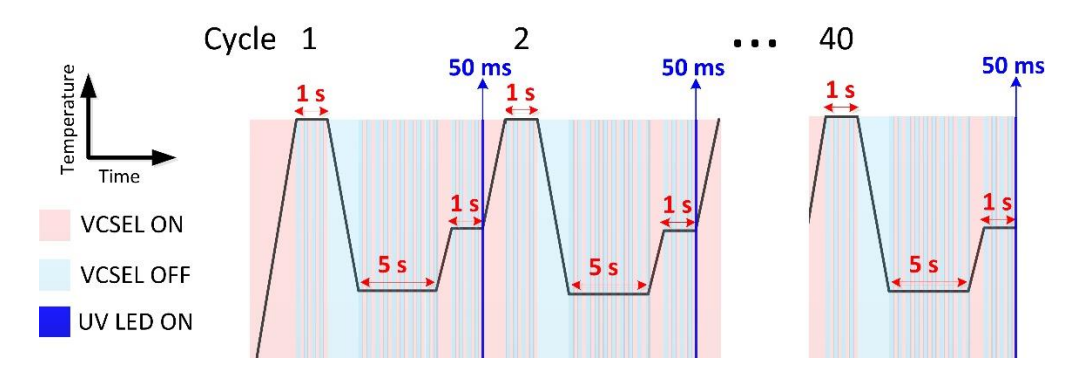


Figure 4.6 Conceptual illustration of the status of VCSEL and UV LED during plasmonic thermocycling.

4.4 Experimental results and discussion

4.4.1 UV absorption and exposure limit of PCR reaction

The contribution of each PCR ingredients to UV absorption is measured using spectrophotometer (DS-11 Series, DeNovix Inc.). Figure 4.7.a shows the UV-vis spectrum of each PCR ingredient with the same final concentration as in positive PCR. It is evident that the dNTPs are the dominant UV absorbers, and 2.5 nM AuNRs and Taq polymerase are about 3 and 5 times less absorptive than dNTPs. The rest of reagents are at least 7 times weaker in absorbing 260 nm light compared to dNTPs. To understand the overall impact of PCR ingredients on UV absorption, a positive PCR sample underwent successful plasmonic PCR amplification, and the UV-vis spectra of pre- and post-PCR samples were compared. Figure 4.7.b shows that 260 nm absorption of pre-PCR sample decreased by approximately 27 % after successful amplification of target DNA.

Furthermore, it is reported that Taq polymerase is highly UV sensitive due to the presence of strong UV absorptive aromatic amino acids (tryptophan, tyrosine, and phenylalanine) [211]. Thus, it is expected that polymerase inactivation can be an outcome of PCR sample's UV overexposure. Moreover, prolonged UV radiation triggers DNA damage by producing a variety of mutagenic and cytotoxic DNA lesions such as cyclobutene pyrimidine dimers and 6-4 photoproducts [212, 213]. Since PCR requires relatively intact DNA strand for DNA synthesis by polymerase, these UV-induced transition mutations in DNA structure result in PCR inhibition or poor PCR efficiency. Hence, it is critical to measure maximum allowed UV exposure time without distorting DNA structure and reducing polymerase activity. To test this, first, positive PCR samples were exposed to 1 mW UV LED for different total duration times from 20 to 320 s. Next, the UV exposed

samples underwent conventional amplification, and finally PCR products were visualized by gel electrophoresis to analyze the impact of different UV light doses on PCR efficiency. In the first set of experiment, Figure 4.7.c shows that 80 s of UV exposure time inhibits PCR. To obtain the precise time duration for UV tolerance limit of plasmonic PCR reaction, the second set of experiments with time duration of 50 to 80 s was examined. Figure 4.7.c shows that a total of 70 s duration of the UV exposure time limit produced a fainter band on the gel. In our real-time amplicon detection procedure, PCR reaction is irradiated for 50 ms per cycle making our method UV-safe for PCR ingredients and its progression.

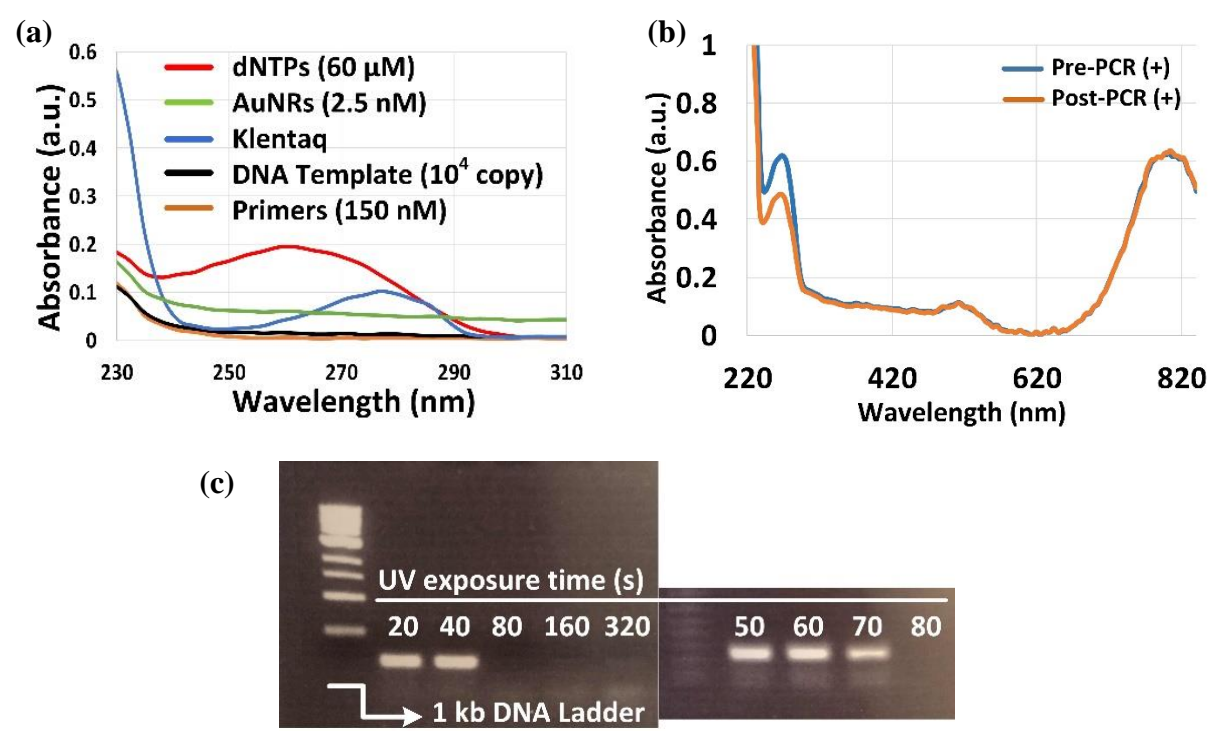


Figure 4.7 (a) Absorption spectra of different PCR reagents with the same concentration as in positive PCR. (b) Absorption spectra of positive PCR reaction before and after plasmonic thermocycling exhibits 260 nm absorption drop as a result of dNTPs conversion to dsDNAs. (c) Gel image of positive PCR samples exposed to 1 mW UV LED irradiation for different UV exposure time durations of 20-320 s and 50-80 s, and their impact on amplicon yield. 70 s UV exposure time shows less amplicon generation/faint band.

4.4.2 Real-time UV monitoring of PCR kinetics

To measure variations in 260 nm absorption during plasmonic amplification, 20 µL positive PCR sample containing 10⁵ copies *C. Trachomatis* DNA was prepared and placed in a two-lens detection system. Sample preparation, plasmonic PCR protocol, and UV detection working principle follow the guidelines presented in Table 3.1, section 3.3 and 4.3 of this thesis, respectively. Figure 4.8 shows the generated UV amplification curve for this experiment. During

fluorescent PCR, 4 phases of PCR kinetics (baseline, exponential, linear, and plateau) appear in different segments of a sigmoidal-shaped amplification curve. Consequently, the same behaviour is expected to occur in UV curve as a result of dNTPs consumption for dsDNAs replication. To explore this, different curves were least square fitted to different segments of UV amplification curve. Figure 4.8 shows that similar to fluorescent PCR, UV curve follows 4 phases of PCR. However, one contradictory observation in UV curve compared to fluorescent real-time curve is the increasing baseline phase. This optical phenomenon conceals the cycle number at which the amplification enters the exponential phase (threshold cycle). As a result, the threshold cycle defined in fluorescent PCR for amplicon quantification is not applicable in UV detection method. Hence, here, we define threshold cycle as the cycle number at which the UV signal rises above exponentially increasing baseline and enters the sigmoid part of UV curve. To determine its value, an exponential and a sigmoid curve are least square fitted to UV signal data of the first and last set of cycles, and their intersection is taken as threshold cycle (C₁).

It is important to note that the optical power at the photodetector ($P_{detector}$) has a maximum of 80 μ W (Figure 4.8). Based on the Zemax optical simulation presented in section 4.2, 128 μ W of UV LED optical power was expected. The experimental results here correspond to our optical simulation, and the difference between experimental and model $P_{detector}$ (128-80=48 μ W) is owing to the fact that in optical model, the optical absorption properties of PCR ingredients were not considered.

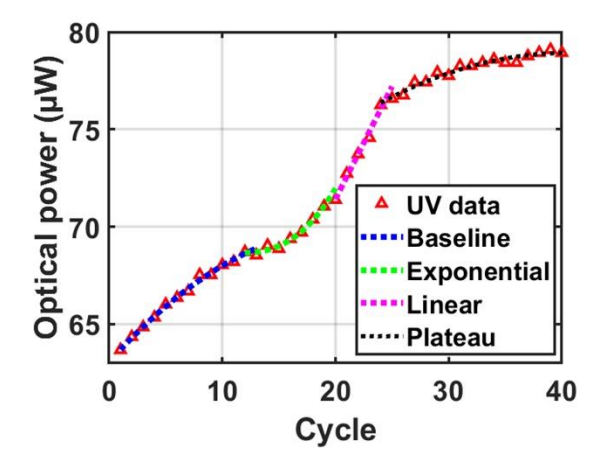


Figure 4.8 The measured UV optical power at photodetector (discrete triangles) is plotted against cycles to generate UV amplification curve. 4 different curves (dashed lines) were least square fitted to experimental values to show 4 phases of PCR kinetics.

4.4.3 PCR results classification based on UV curves shape analysis

In order to investigate the ability of UV detection in classifying PCR results (success or fail), positive PCR control with 10⁴ initial DNA copy number along with different negative controls underwent plasmonic amplification. Figure 4.9.a shows unnormalized UV amplification curves. It is important not to compare UV transmitted optical power values of one experiment to another since UV transmission varies even for the same PCR solution pipetted in different PCR tubes or the same PCR tube with a change of its side facing the UV LED. This is due to changes occurring in pipetting, optical alignment for each experiment, or difference in shape and wall thickness of each side of PCR tube. This implies that for a valid comparison between two different experiments, only UV transmission behaviour throughout 40 cycles should be considered. Thus, UV amplification curves were min-max normalized to clearly analyze/compare their behaviour/shape and extract distinctive features for positive/successful and negative/failed PCR differentiation. Figure 4.9.b shows that different curves were least square fitted to normalized UV data for shape analysis. Normalized UV curve for positive PCR sample is a combination of 2nd degree exponential and a sigmoid curve which intersect at C_t following a sharp increase in UV transmission. However, normalized UV curves for negative controls follow a monotonically increasing 2nd degree exponential function which saturates after C_t. The functions least square fitted to UV data are as follows (where C is cycle number):

$$P_{Positive} = \begin{cases} 0.3e^{0.02 \times C} - 0.4e^{-0.3 \times C} & 1 \le C \le C_t \\ 1.1 & C_t \le C \le 40 \end{cases}$$

$$(4.1)$$

$$P_{\text{Negative}} = \begin{cases} 1.14e^{-0.004 \times C} - 1.2e^{-0.09 \times C} & \text{No primer} \\ 0.54e^{0.009 \times C} - 0.6e^{-0.15 \times C} & \text{No DNA} \\ 1.14e^{-0.002 \times C} - 1.2e^{-0.07 \times C} & \text{No Taq} \end{cases}$$

$$(4.2)$$

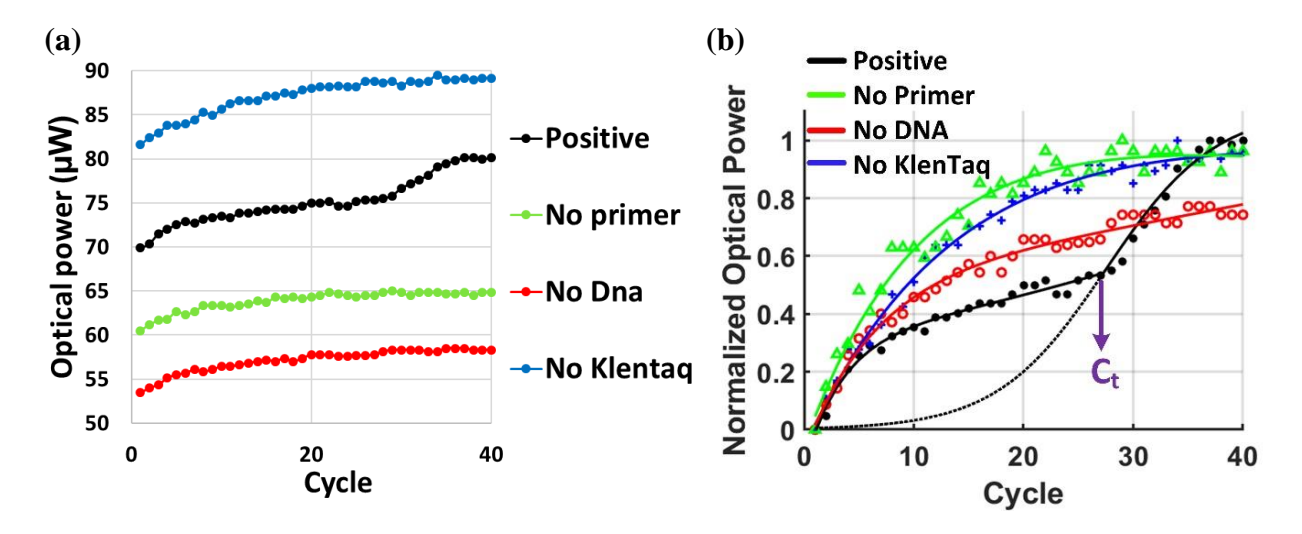


Figure 4.9 (a) UV amplification curves for positive and negative controls. (b) Min-max normalized UV amplification curves for different samples were generated by fitting curves (solid lines) to experimental UV transmission (discrete data points). All amplification curves follow a 2^{nd} degree exponential function throughout 40 cycles except successful PCR (black) with sigmoidal increase at threshold cycle (C_1).

The bar graph in Figure 4.10.a demonstrates that the percentage increase in transmitted optical power from last cycle to C_t ($P_{40}/P_{C_t=27}$) for the successful PCR is at least 9 times greater than P_{40}/P_{27} in negative controls. Therefore, this sigmoidal-shaped increase after C_t in UV amplification curve serves as a signature to differentiate successful and failed PCR results.

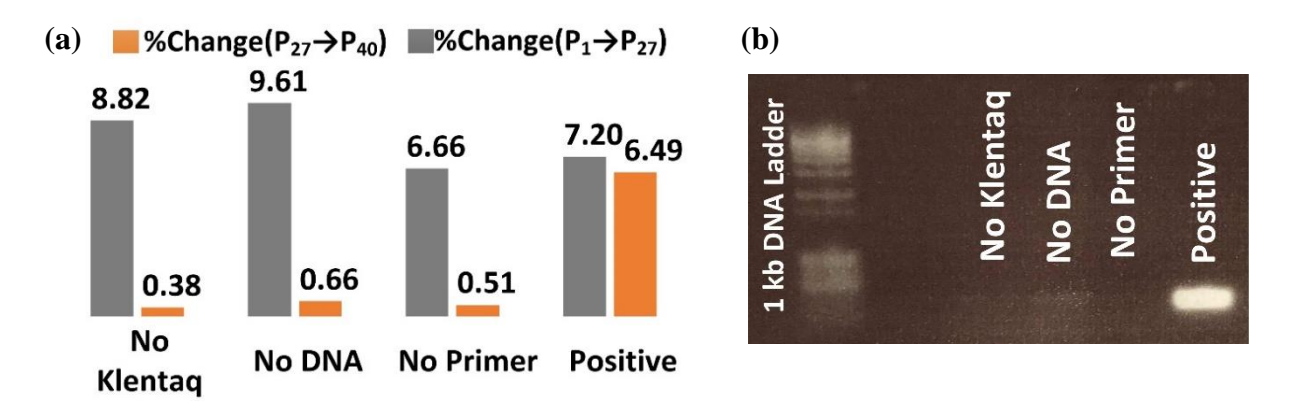
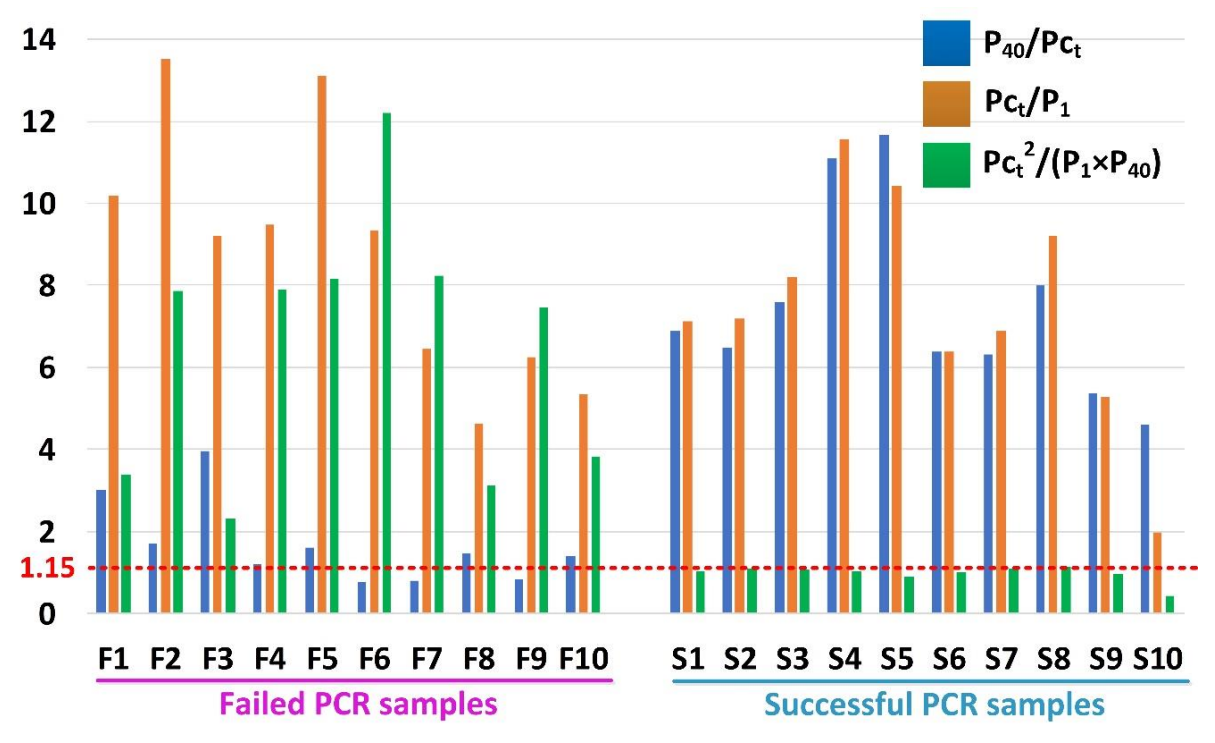


Figure 4.10 (a) Comparison of percentage increase in UV transmission from cycle 1 to C_t (=27) and cycle 27 to 40 for different controls. (b) The gel image confirms the validity of UV results to differentiate successful and failed PCR.

In order to demonstrate the repeatability of our method, we randomly collected UV curves obtained from real-time plasmonic amplification of 20 different PCR samples. These samples were prepared from different master mix solutions and went through plasmonic amplification on different days.

The initial DNA copy numbers of samples are either 10^4 or 10^5 . The samples were positive PCR controls following Klentaq polymerase PCR protocol (Table 3.1). Next, we classified the UV curves obtained from these 20 PCR reactions into two categories of "success" and "fail" based on their results on gel image. Then, P_{40}/P_{C_1} and P_{C_2}/P_1 were calculated for both categories and plotted in Figure 4.11. It should be noted that in this section, the failed PCRs were not negative PCR controls, but rather positive controls which underwent various PCR conditions leading to PCR inhibition or failed PCR. The results in Figure 4.11 shows that for all successful PCR experiments,

 $\frac{P_{C_t}^2}{P_{Ao} \times P_t}$ is less than 1.15 indicating the validity and repeatability of our method.



 $\textbf{Figure 4.11} \ \, \text{The rectangular blue and orange bars represent calculated} \ \, P_{40}/P_{C_t} \ \, \text{and} \ \, P_{C_t}/P_1 \ \, \text{for } 20 \ \, \text{different}$ plasmonic positive PCR samples. The first 10 samples are failed PCR tests with $\frac{P_{C_1}^2}{P_{A0} \times P_1}$ (green bars) greater than 1.15, whereas $\frac{P_{C_1}^2}{P_{Aa} \times P_1}$ is less than or equal to 1.15 for successful PCR tests.

4.4.4 Real-time amplicon quantification

The stock Chlamydia Trachomatis DNA solution with 3.5×10⁵ genome copies.µL⁻¹ were diluted with ddH₂O to obtain 10-fold dilution series of DNA copy numbers. For low DNA copy numbers, we used Poisson distribution to describe the probability of finding x DNA copy numbers in 20 μL sample volume. The probability of random variable X (DNA copy number) takes on the value of x (3.5 < x < 35) after making different dilution series of DNA copy numbers is calculated using the Poisson probability mass function:

$$P(X=x) = \frac{e^{-\lambda} \lambda^x}{x!}$$
 (4.3)

Where x is the number of occurrences, i.e., number of DNA molecules that can be present in the $20 \,\mu\text{L}$ sample, λ is equal to the expected value of X and equals to the mean and variance of random variable X.

The bar graph in Figure 4.12 shows the probability of having different DNA copy numbers for different expected value (λ) of 3.5 and 35 in our 20 μ L PCR reaction.

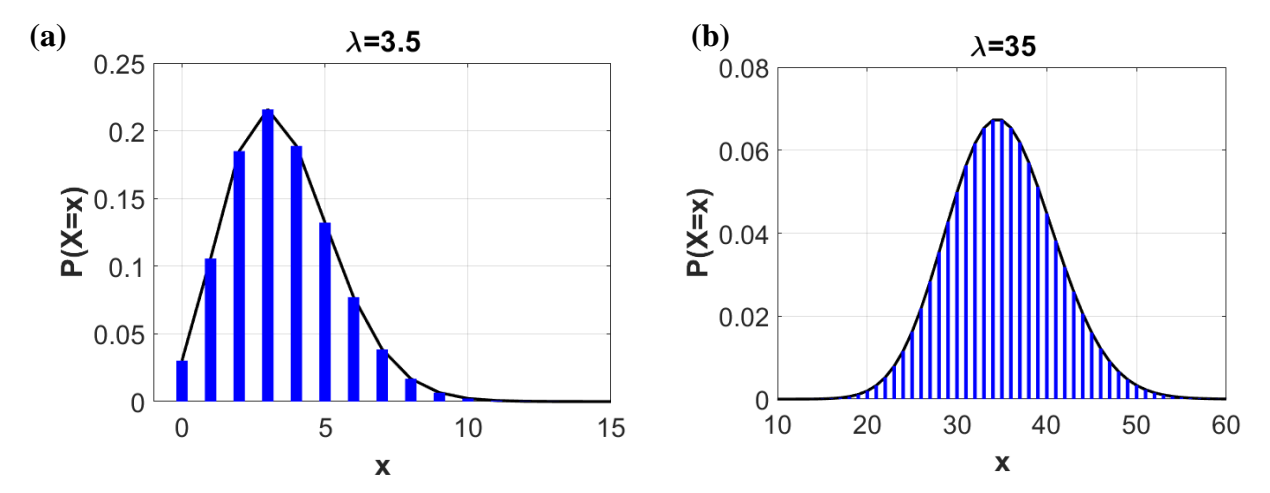


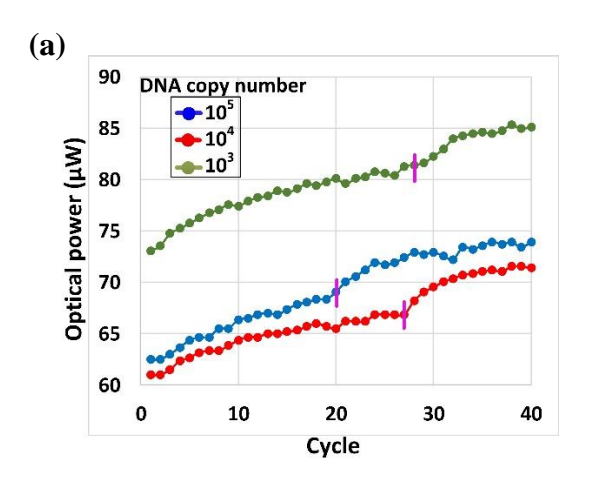
Figure 4.12 Distribution of different DNA copy numbers in 20 μ L sample for (a) λ =3.5 and (b) λ =35.

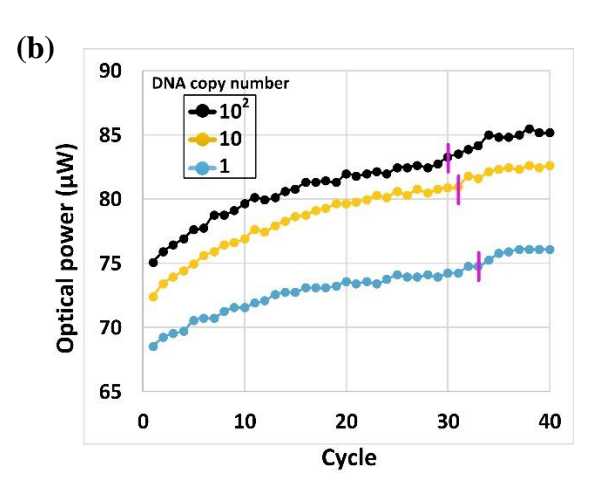
Thus, after diluting the stock solution 10^5 times (λ =3.5), the probability of having at least one DNA copy number in PCR reaction is approximately 96.9%. Similarly, by diluting 10^4 times (λ =35), the chances of having at least 20 DNA copy numbers are approximately 99.6%.

To investigate the ability of real-time UV detection in quantifying DNA concentration, positive PCR reactions with different initial DNA copy numbers ranging from 10^5 through to 10^0 underwent plasmonic amplification and real-time UV monitoring. The resulting normalized UV amplification curves (Figure 4.13.c and Figure 4.13.d) demonstrate that with decreasing DNA template concentration, the fitted sigmoid curve and subsequently the C_t shifts right to higher cycles. The highest obtainable C_t value is 32 per 20 μ L sample volume which corresponds to one

DNA copy amplification. This indicates that our real-time UV system has high sensitivity of detecting amplicons generated by a single target DNA. Based on Table 2.6 in chapter 2, Tran *et al.* reported a LOD of 10⁴ for their UV monitoring system [24]. However, with our 2-lens UV detection system, the LOD is decreased 10⁴ times compared to their work. The reasons for the enhanced detection sensitivity in our UV detection is explained as follows. First, VCSEL-based plasmonic thermocycler is running PCR samples under optimized PCR condition, and the amount of generated amplicons with lower starting DNA copy numbers (<10⁴) in our system is significantly greater. This is evident by comparing the gel image of samples amplified in VCSEL-based thermocycler (Figure 4.13.f) with the gel image of samples amplified in Tran's plasmonic thermocycler (Figure 2.9.b). Second, the SNR is increased in our UV detection system owing to employment of lenses with characteristics optimized in Zemax optical model. Besides, due to our compact system design, the OPL is shortened in our system; thus, higher SNR is achieved leading to lower LOD.

The plot of C_t values against log of starting copy number of DNA target (UV standard curve) can be used for DNA quantity estimation (Figure 4.13.e). Finally, the PCR products were visualized by gel electrophoresis to confirm the validity of UV detection results (Figure 4.13.f). It should be noted that limit of detection in fluorescent PCR assay is defined as the lowest DNA target concentration at which the linear phase does not appear in fluorescence curve, whereas in UV monitoring, the minimum detectable amount of DNA is when the amplification curve appears as a continuous exponential curve with no sigmoidal behaviour towards the end of PCR cycles.





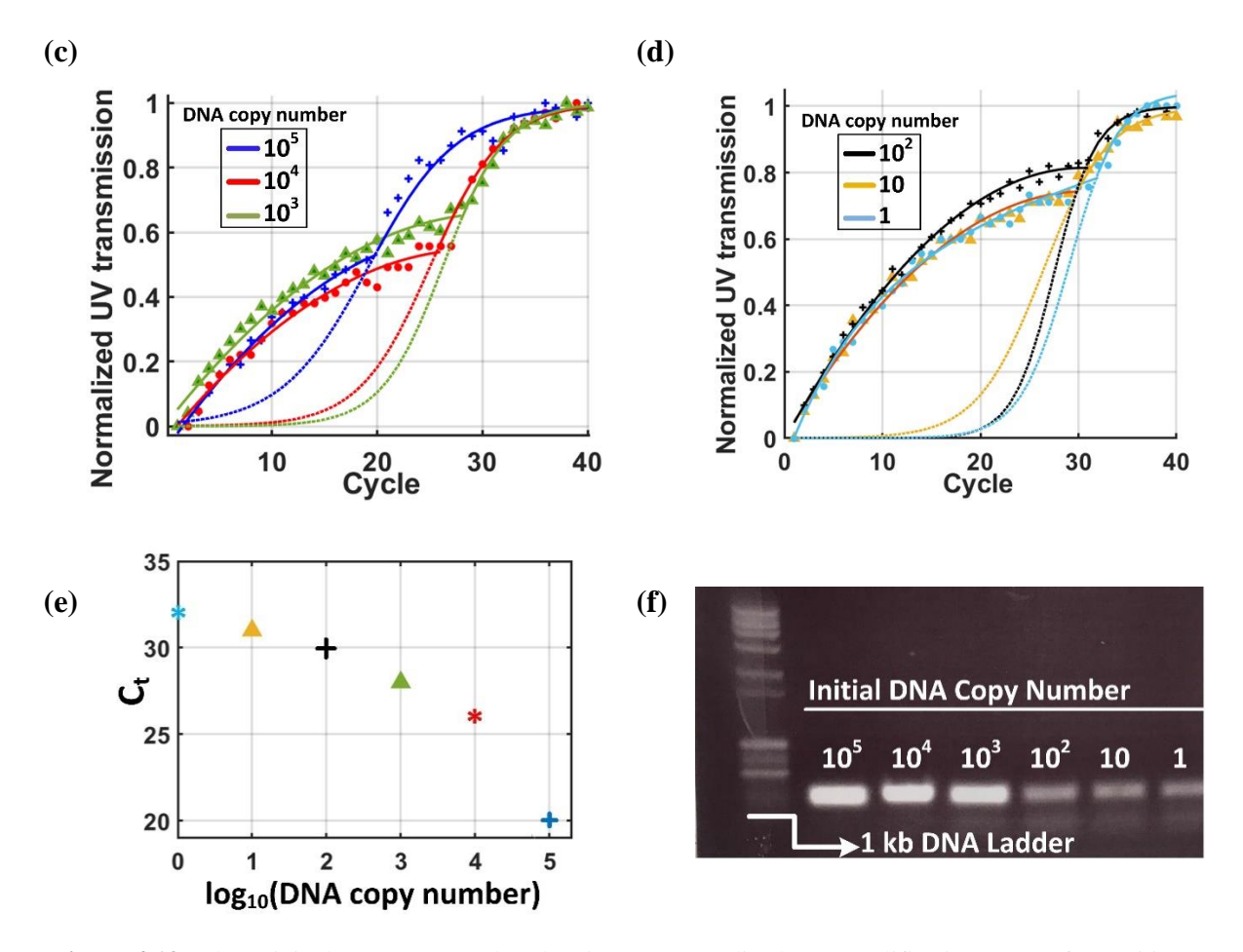


Figure 4.13 (a,b) Original UV curves and (c,d) min-max normalized UV amplification curves for positive PCR samples with initial DNA copy numbers ranging from 10^5 - 10^0 . The C_t shifts right to higher cycles with decreasing target concentration. (e) UV standard curve established between obtained C_t values and log of DNA copy number for real-time amplicon quantification. (f) Gel electrophoresis image of plasmonically amplified samples with different DNA starting concentrations.

In order to measure the repeatability of results, the above experiment was conducted multiple times. That is, five PCR samples with initial DNA concentration of 10⁵ were prepared separately and underwent real-time plasmonic amplification on different days. The UV transmission curves together with their threshold cycles were obtained for these 5 PCR samples, and then the mean and SD of the threshold cycles were calculated. The same procedure was repeated for initial DNA concertation of 10⁴ to 1. Figure 4.14 and Table 4.1. show the mean and SD of threshold cycles for varying starting DNA copy numbers. Also, the number of experiments performed for each DNA copy number is presented.

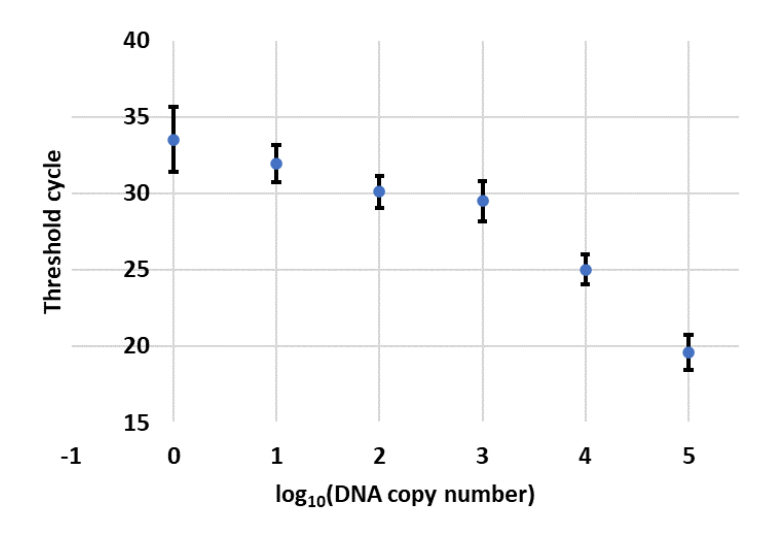


Figure 4.14 UV standard curve showing mean and S.D of obtained threshold cycles.

Table 4.1 Mean and standard deviation of the obtained threshold cycles for different DNA starting copy numbers.

| | Initial DNA concentration | | | | | |
|--------------------|---------------------------|-------|-----------------|------|-------|------|
| [DNA] | 10 ⁵ | 104 | 10 ³ | 100 | 10† | 1‡ |
| No. of experiments | 5 | 5 | 3 | 3 | 3 | 2 |
| Mean | 19.6 | 25.02 | 29.5 | 30.1 | 31.93 | 33.5 |
| Standard deviation | 1.14 | 0.98 | 1.32 | 1.05 | 1.2 | 2.12 |

[DNA]: DNA copy number

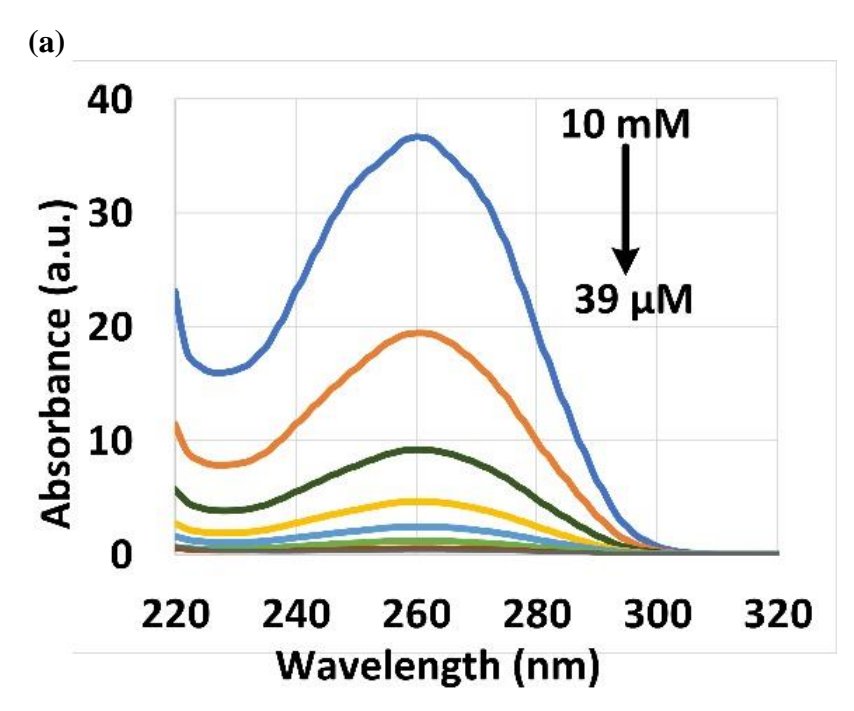
† P(20≤[DNA]≤50)=99.1%

‡P(1≤[DNA]≤9)=96.6%

4.4.5 Limit of detection for dNTPs concentration

It is worth investigating minimum and maximum detectable dNTPs concentration by our UV system. To determine this, 20 μ L of dNTPs solution with 10 mM final concentration was placed in the UV system. In order to eliminate UV transmission variations due to non-specific factors, this experiment was carried out in one PCR tube while maintaining the sample volume at 20 μ L throughout the experiment without changing the tube position or orientation. Next, the UV transmission was measured as the dNTPs concentration was decreased by 2-fold dilution by pipetting out 10 μ L of solution and adding 10 μ L of ddH₂O. The withdrawn 10 μ L sample volume is later went through UV-vis spectroscopy to confirm decreasing dNTPs concentration by probing 260 nm absorption (Figure 4.15.a).

The plot of UV transmission against log of dNTPs concentration (Figure 4.15.b) shows that UV transmission saturates for dNTPs concentration in pink regions, and the maximum detection sensitivity can be achieved provided that dNTPs concentration lies in linear/green region (19.5 μM<dNTPs concentration<625 μM). Based on our plasmonic PCR protocol, dNTPs have a final concertation of 60 μM in 20 μL PCR reaction, and with the assumption of 90% dNTPs consumption in successful PCR, it is anticipated that transmitted optical power moves from point A to B and increases by around 32%. However, this percentage increase should not be expected in real-time UV detection of PCR products. In the above experiment, the concentration of dNTPs was reduced by removing dNTPs from sample, whereas in UV detection, UV transmission increase is due to decrease in conformational freedom of dNTPs not their exhaustion, *i.e.*, their conversion from dissociated free molecules to bounded molecules in DNA structure. Consequently, the generated dsDNAs also contribute to UV absorption resulting in less UV transmission increase (<32%).



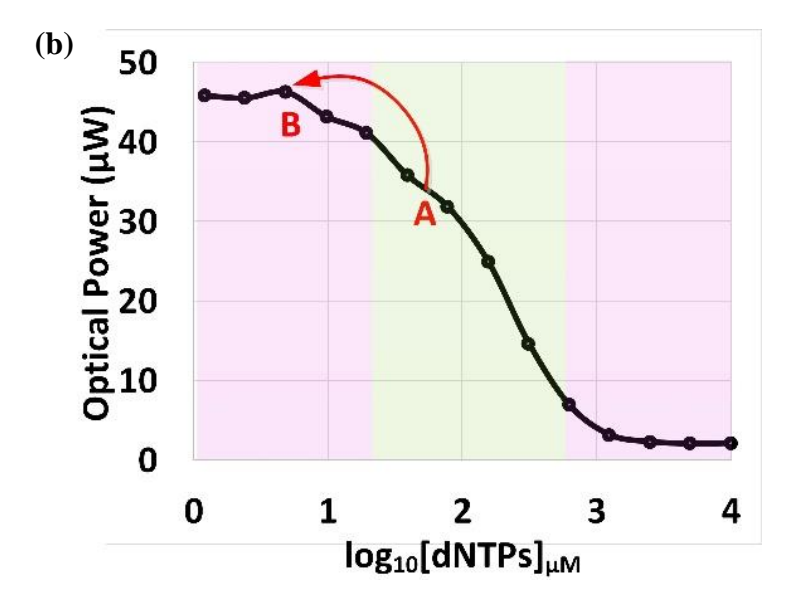


Figure 4.15 (a) UV absorption spectra and (b) UV transmission of solutions containing different dNTPs concentration obtained from spectrophotometer and 2-lens UV detection system, respectively.

4.4.6 Analysis of increasing UV transmission in negative control

As was shown in the previous section, UV transmission increases for failed PCR and in the baseline phase of successful PCR ("false" signal increase). This is owing to the fact that unlike fluorescent PCR, at our probe wavelength (260 nm), the optical absorption property of PCR solution is influenced not only by primary measurand (dNTPs concentration) but also by other PCR ingredients (e.g., polymerase and AuNRs). Accordingly, the detected UV signal is the superposition of the changes in primary and non-primary measurands' physicochemical properties. To confirm this justification, we compared real-time UV curves generated from plasmonic thermocycling of each PCR ingredient separately. AuNRs and each ingredient were diluted with ddH₂O to obtain 20 µL sample volume. The final concertation of reagents is the same as in positive PCR. Figure 4.16.a and Figure 4.16.b show that UV transmission increases only for the sample containing AuNRs and Klentaq polymerase, whereas other ingredients have constant or even decreasing UV transmission throughout 40 cycles. The increasing UV transmission for Taq and AuNRs solution might be owing to greater affinity of Taq polymerase towards AuNRs compared to other PCR ingredients (primer or DNA) which leads to formation of stable Taq-AuNRs complex and consequently changes in UV absorption property of solution [116, 214]. However, the increasing UV signal for "no polymerase" negative control in Figure 4.9 cannot be explained by AuNRs and Taq interaction. Hence, this observation encourages the idea of other existing events

contributing to the emergence of "false" signal increase in UV curve. For instance, the ability of AuNRs to alter primer conformation by partial unfolding the helical structure [215] or high binding affinity of ssDNA to AuNRs [216, 217] are other possible interactions which can change UV absorption property of PCR sample.

Another justification can be found in the exponentially decreasing number of polymerase molecules in the first few cycles before its complete exhaustion or thermal inactivation. Since Taq polymerase is one of the 260 nm-absorbing PCR ingredients, the exponential decline in polymerase concertation leads to UV transmission increase with the same exponential behavior. This is more evident in the baseline phase of UV curve; however, after C_t, dNTPs impact on UV curve is dominant owing to their greater concentration drop and stronger UV absorption property compared to Taq polymerase.

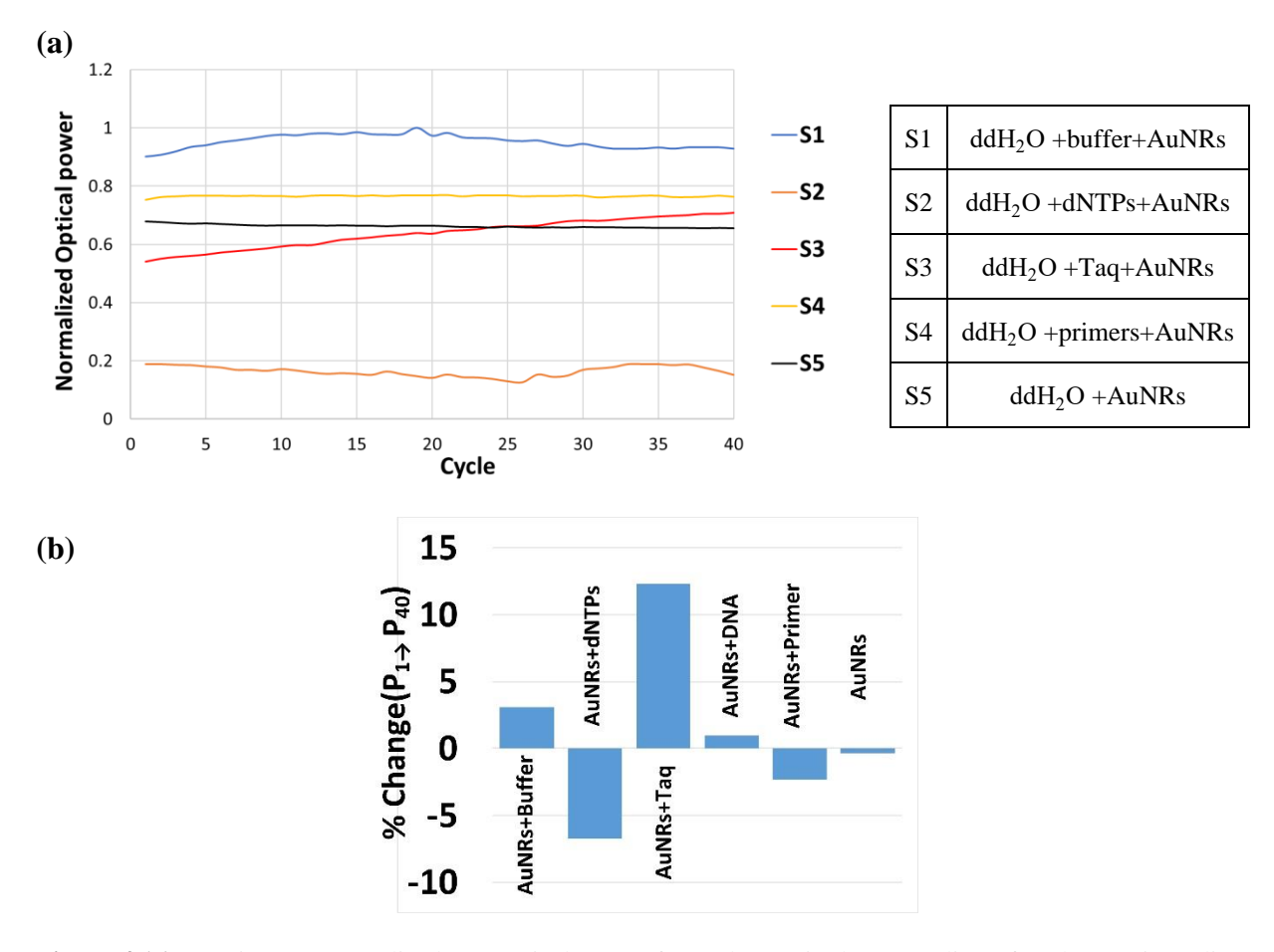


Figure 4.16 (a) Min-max normalized UV optical power from plasmonic thermocycling of each PCR ingredient separately. Only the sample with Klentaq polymerase (S3, red) showed increasing UV transmission throughout 40 cycles. (b) Comparison of percentage change in UV optical power from first to last cycle for different plasmonic solutions containing one PCR ingredient.

4.4.7 Comparison of UV system and qPCR limit of detection

We attempted to compare the detection sensitivity of fluorescent PCR (qPCR) with UV monitoring system. To fulfill this, qPCR experiments were carried out in Applied Biosystems 7500 fast real-time PCR system using a ready-made qPCR kit which provides a blend of polymerase, buffer, and dNTPs. The default setting on qPCR machine has the minimum denaturing, annealing, and elongation hold-times of 30 s, *i.e.*, shorter time intervals are not allowed to be performed on the qPCR software. In contrast to qPCR system, UV monitoring detection provides the flexibility of altering the polymerase type, PCR reagents concentrations, and hold-times. Therefore, accurate comparing of UV detection sensitivity with qPCR is a challenge due to different type of PCR components and their concentrations as well as their PCR running conditions. The UV detection of plasmonically amplified amplicons follows the same protocol explained in the previous sections.

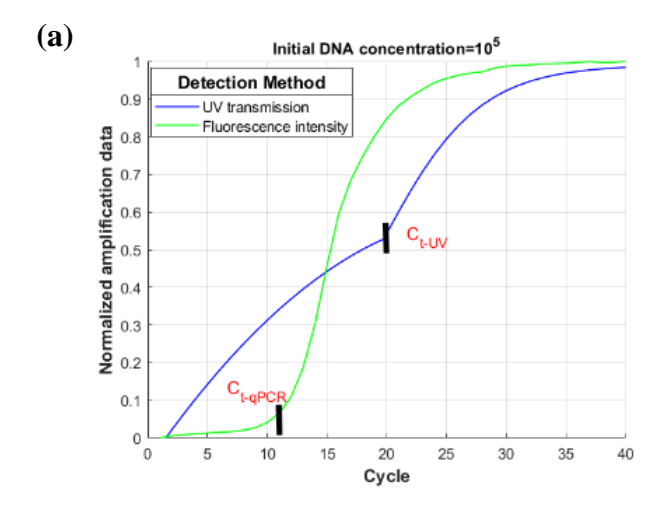
To assess the detection sensitivity of qPCR, different samples containing varying DNA template concentrations of C. Trachomatis DNA were diluted with qPCR master mix/qPCR kit purchased from QIAGEN (Table 4.2), and they underwent conventional amplification in qPCR machine. The threshold cycles of qPCR amplification curves ($C_{t_{qPCR}}$) are compared with the threshold cycles obtained from UV monitoring ($C_{t_{UV}}$) of samples with different initial DNA concentrations (Figure 4.17).

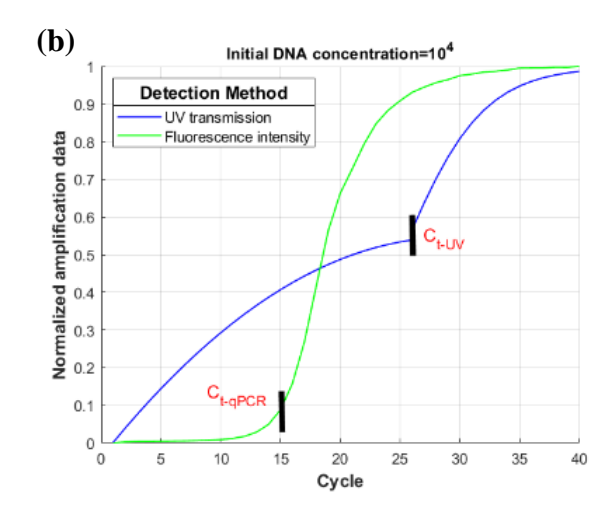
 Table 4.2 Comparison of threshold cycles obtained from UV and fluorescence detection.

| Initial DNA Concentration | $\mathbf{C}_{t_{qPCR}}$ | $\mathbf{C}_{\mathbf{t}_{\mathbf{U}\mathbf{V}}}$ |
|---------------------------|-------------------------|--|
| 10 ⁵ | 12.7 | 20 |
| 10 ⁴ | 15 | 26 |
| 10^{3} | 22.7 | 28 |
| 10 ² | 26 | 30 |
| 10 | 30 | 31 |

The reason for the difference in C_t values between fluorescence and UV detection is explained as follows:

- The varying concentration of dNTPs, polymerase, and buffer in both detection methods influence the amount of amplified DNA as well as threshold cycles.
- The PCR conditions (e.g., hold-times) of both detection methods are different.
- Conventional qPCR thermocyclers complete 40 PCR cycles in approximately an hour. This slow PCR process maximizes each PCR stage efficiency, and thereby the amount of generated amplicons are expected to be higher compared to sub-ten minute plasmonic assay time. Hence, the amplicon reaches detection threshold at earlier cycler/faster for fluorescent PCR in comparison with real-time UV monitoring (*i.e.*, C_{t_{aPCR}} < C_{t_{UV}}).
- In qPCR, the C_t value is defined as a crossing point where fluorescence signal enters the exponential phase. Furthermore, the fluorescence signal is correlated solely to the generation of dsDNA, while UV transmission curve represents the change in UV absorption as result of consumption of UV sensitive PCR components (*e.g.*, dNTPs and Taq). Therefore, the threshold cycle in UV monitoring is observable when the UV transmission increase due to consumption of dNTPs exceeds the transmission increase as a result of exhaustion of Taq polymerase.





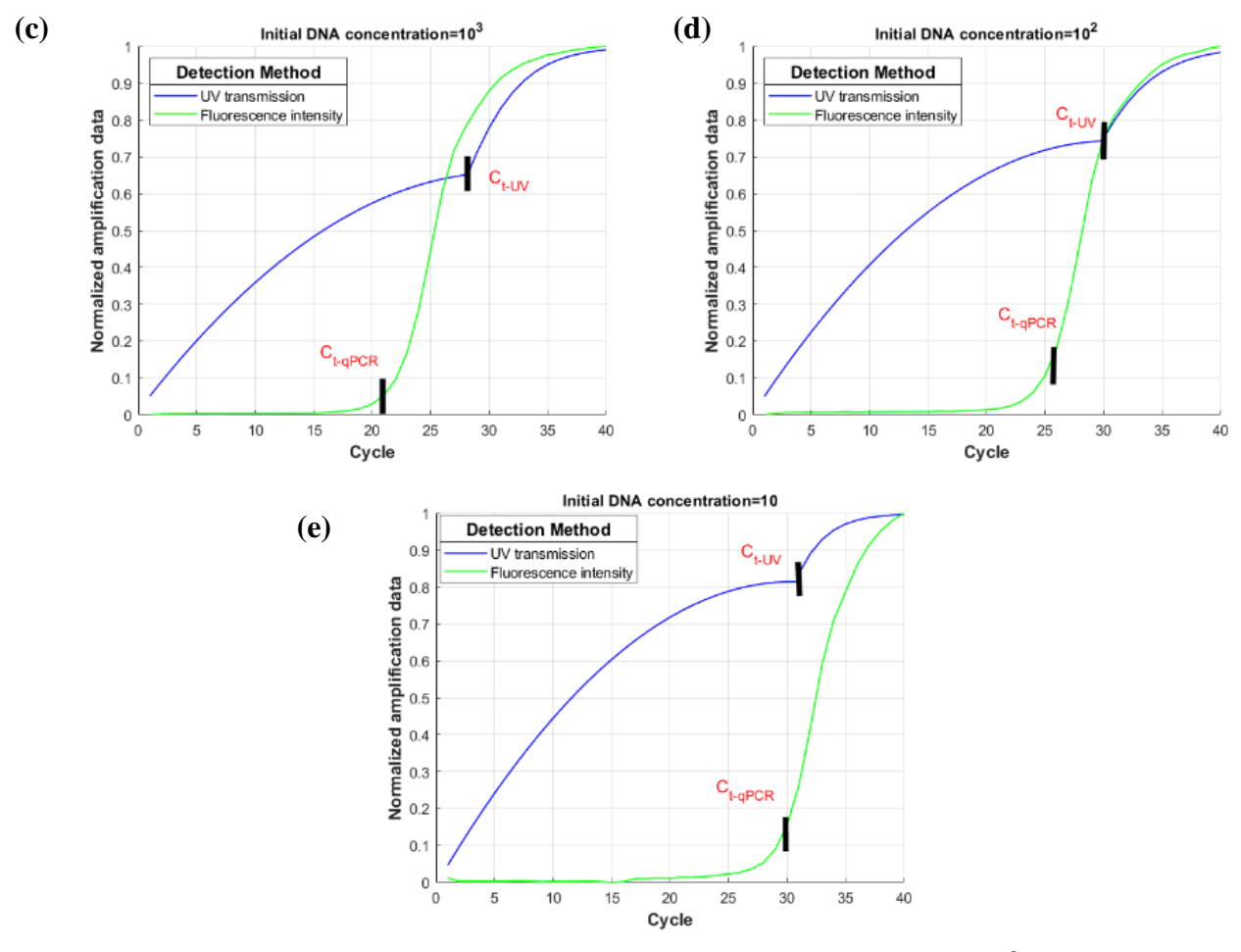


Figure 4.17 Comparison of normalized UV and fluorescent amplification curves using (a) 10^5 , (b) 10^4 , (c) 10^3 , (d) 10^2 , and (e) 10 initial DNA copy numbers.

As a result, a valid comparison between fluorescence and UV detection method can be established when:

- The effect of Taq polymerase on UV transmission is negated.
- The concentration of ingredients in both methods become identical.
- Fluorescence signal is measured with plasmonic amplification of target DNA, *i.e.*, integration of plasmonic thermocycler with fluorescence detection.

4.5 Summary

In this chapter, we demonstrated a miniaturized real-time label-free PCR platform that incorporates plasmonic-driven thermocycling and UV monitoring of dNTPs exhaustion. The total turnaround time for 30 cycles of *Chlamydia Trachomatis* DNA amplification and real-time UV detection in

 $20~\mu L$ sample is 9.5 min which is significantly faster than conventional qPCR machines with typical assay time between 40 to 60 min. Its compact size is derived solely from light-assisted amplification and detection and utilization of different laser type than sample miniaturization techniques. Retaining the conventional sample volume circumvents the suboptimal detection sensitivity found in fluorescent detection microfluidics due to shortened optical path length. The UV amplification curves for positive PCRs demonstrate a sigmoidal-shaped increase at C_t which can be served as a fingerprint to discriminate successful and failed PCRs. Furthermore, we presented a comparison between C_t values of positive transmission curves with different initial DNA concentrations. The result show that our detection system is capable of quantifying PCR products as small as a single DNA copy. The proposed work is a proof-of-principle demonstration of PCR-based optical DNA amplification and detection which offers fast and reliable results in a compact, low-powered, and inexpensive hardware, fundamental requirements for POC testing.

CHAPTER 5

Model-based analysis of real-time UV detection

5.1 Introduction

Real-time polymerase chain reaction, also known as quantitative PCR (qPCR), is used to determine relative quantification of enzymatically amplified double-stranded DNA (dsDNA) fragment carried out in three steps (denaturation, annealing, and elongation) controlled by temperature. In theory, considering the amplification efficiency of 100%, the target grows exponentially as a function of PCR cycles, *i.e.*, the amount of PCR product after n cycles is 2ⁿ times the initial DNA concentration [4, 218]. However, in practice limiting factors such as primer-dimer accumulation, non-uniform temperature regulation, exhaustion of reagents, thermal inactivation of the DNA polymerase decrease efficiency as the PCR cycles progress [219]. The PCR efficiency is instrument dependent and for an acceptable designed qPCR machine, the efficiency should fall above 90% [40].

Many stochastic and mathematical models have been presented to calculate expected efficiency to identify the factors reducing PCR yield. Most models reported an overall PCR performance in which the efficiency of the reaction remains constant throughout all PCR cycles [220-222]. These models are only applicable for the early cycles when the efficiency is nearly constant. Other models have considered the cycle dependency of PCR efficiency by incorporating the melting, annealing, and elongation steps efficiencies into overall efficiency [223, 224]. These models were used in qPCRs to analyze and detect parameters controlling or degrading denaturing, annealing, and extension efficiencies [225, 226]. In this chapter, we use a mathematical model presented by Booth *et al.* to investigate cycle to cycle efficiencies and PCR reagent concentrations of the real-time 260 nm detection plasmonic PCR system [226, 227]. Model calibration based on the captured UV transmission data quantifies PCR parameters such as rates of primer and template annealing as well as polymerase binding. These parameters will help to optimize PCR protocol and ingredient concentrations for faster and more efficient PCR. Furthermore, the calibrated model is used to

study the impact of template/polymerase plasmonic thermal/UV damage and annealing step duration on amplicon generation.

5.2 Model description

In this section, a short review of the mathematical model introduced by Booth *et al.* is presented [226, 227]. This model is based on the following assumptions:

- DNA damage (η_d) and polymerase damage (η_{dE}) are independent of PCR cycles
- Absence of primer-dimer events and primer-template annealing during elongation step
- Constant extension rate
- Irreversible annealing and elongation reactions
- The concentration of forward and reverse primers is equal
- Forward and reverse primers anneal to equal numbers of sense and anti-sense singlestranded DNA (ssDNA) molecules
- Template-primer complexes that are not fully extended during elongation stage are not considered as amplicons; however, they are treated as primers for the following cycle
- All dsDNA molecules are converted to ssDNA during denaturation stage (*i.e.*, denaturation efficiency≈1)
- During each PCR cycle, three reactions take place: i) two ssDNAs bind to form a dsDNA
 (S) with rate k_s, ii) a primer (P) anneals to a ssDNA molecule to form a binary complex
 (B) with rate k_p, and iii) a polymerase molecule (E) anneal to a binary complex to form a ternary complex (C) with rate k_c.

Reaction rates $(k_s, k_p, and k_c)$, PCR protocol parameters (hold-time durations), and initial reagents concentration are among constant parameters of the model shown in Table 5.1. Here, we used the same nomenclature as Booth *et al.* for most of the model parameters.

Table 5.1 Model constant parameters.

| | Constant parameters | Description | Unit |
|-----------------------------------|---|---|------|
| tes | $k_{\rm p}$ | Primer annealing rate | μM/s |
| Reaction rates | k _s | ssDNA annealing rate | μM/s |
| React | k_c, k_c^* | Polymerase annealing rate at annealing and elongation steps | μM/s |
| | $\beta = \frac{k_s}{k_p}$ | Ratio of ssDNA to primer annealing rate | - |
| aturing damage efficiencies | η _d | DNA thermal damage | - |
| Denaturing damage efficiencies | $\eta_{ m dE}$ | Polymerase thermal damage | - |
| PCR protocol | t _a , t _e | Annealing and elongation hold-times/duration | s |
| fic | V | Polymerase extension rate (nucleotide per second) | bp/s |
| -speci tants | $L_{ m DNA}$ | Template length | bp |
| Reagents-specific constants | Template length LDNA Primer length | | bp |
| Re | $L_{\text{ext}} = L_{\text{DNA}} - L_{\text{primer}}$ | Extension length | bp |

The other model parameters are variables indicating PCR reagents concentration at specific PCR stage or PCR cycle (Table 5.2). The variable subscripts clarify the PCR stage and cycle number. The subscript j denotes cycle number, and the subscript a and e indicate the concentration of the PCR reagents at the end of annealing and elongation stages, respectively. For instance, S_j , P_j , and E_j are the concentration of DNA template, primer, and polymerase at the beginning of cycle j, respectively. Also, P_j , a and C_j , e denote the primer and ternary complex concertation at the end annealing and elongation stages of cycle j, respectively. In order to assign the first UV transmission measured at the end of elongation stage of cycle 1 to DNA template concentration at the end of cycle 1 (S_1) , the initial concentrations of reagents are defined with subscript zero, i.e., S_0 , P_0 , and E_0 .

Table 5.2 Model cycle-dependent variables.

| Cycle-dependent variables | Description | Unit |
|---|---|------|
| S ₀ , S _j , S _{j, a} | Initial DNA template concertation, template concertation at the beginning, and at the end of annealing stage of cycle j | M |
| P ₀ , P _j , P _{j, a} | Initial primer concertation, primer concertation at the beginning, and at the end of annealing stage of cycle j | M |
| E_0, E_j | Initial polymerase concertation and polymerase concertation at the beginning of cycle j | М |
| B _{j, a} | Binary complex concertation at the end of annealing stage | M |
| C _{j, c} , C _{j, a} , C _{j, e} | Ternary complex concertation at the cut-off time, end of annealing, and end of elongation stage | M |
| $\gamma_j = \frac{S_j}{P_j}$ | Ratio of template to primer concertation | - |

After solving differential equations governing annealing and extension reactions, the following set of equations can be used to quantify reagents concentrations after annealing and elongation stage of cycle j ($P_{j, a}$, $C_{j, a}$, $B_{j, a}$, and $C_{j, e}$) based on reagents concentration at the beginning of that cycle (S_{j} and P_{j}), PCR protocol (hold-times), and reaction rate constants:

$$P_{j, a} = P_{j} \left(1 + \gamma_{j} (\beta - 1) \left(1 - e^{-k_{p} t_{a} P_{j} (\gamma_{j} (\beta - 1) + 1)^{\frac{1}{1 - \beta}}} \right) \right)^{\frac{1}{1 - \beta}}$$
(5.1)

$$C_{j, a} = E_{j} \left(1 - \frac{(P_{j} - P_{j, a}) - E_{j}}{(P_{j} - P_{j, a}) e^{(((P_{j} - P_{j, a}) - E_{j})k_{c}t_{a}) - E_{j}}} \right)$$
(5.2)

$$B_{i, a} = P_i - P_{i, a} - C_{i, a}$$
 (5.3)

$$C_{j, e} = \frac{\left(E_{j} - C_{j, a}\right) \left(P_{j} - P_{j, a}\right) - B_{j, a} E_{j} e^{\left(\left(\left(P_{j} - P_{j, a}\right) - E_{j}\right) k_{c}^{*} t_{e}\right)}}{\left(E_{i} - C_{i, a}\right) - B_{i, a} e^{\left(\left(\left(P_{j} - P_{j, a}\right) - E_{j}\right) k_{c}^{*} t_{e}\right)}}$$
(5.4)

The calculated reagents concentration at the end annealing and elongation steps are used to quantify the annealing $(\eta_{i,\,a})$, polymerase binding $(\eta_{i,\,E})$, and elongation efficiencies $(\eta_{i,\,e})$:

$$\eta_{j, a} = \frac{(P_j - P_{j, a})}{S_j}$$
 (5.5)

$$\eta_{j, E} = \frac{C_{j, e}}{B_{j, a} + C_{j, a}}$$
 (5.6)

$$\eta_{j, e} = \frac{C_{j, c}}{C_{j, e}} \tag{5.7}$$

Where $\eta_{j,\,a}$ is the fraction of available DNA template that anneal to primers, $\eta_{j,\,E}$ is the fraction of binary complex molecules that bind to polymerase to form ternary complexes by the end of elongation stage, and $\eta_{j,\,e}$ is the fraction of total ternary complexes which are extended to full-length by the end of elongation stage. $C_{j,\,c}$ can be calculated using equation (5.4) by replacing t_e with cut-off time (t_e) which is described as follows:

$$t_{c} = t_{e} - \frac{L_{ext}}{V} \tag{5.8}$$

Where L_{ext} is the remaining length of template after primer annealing that polymerase must extend, and V is the polymerase extension rate (nucleotide per second). Thus, $\frac{L_{ext}}{V}$ is the minimum elongation time needed to fully extend the DNA template, and t_c is the time point after which all available ternary complexes have enough time to extend at full-length.

The multiplication of the three aforementioned efficiencies will give us the overall cycle efficiency (η_i) :

$$\eta_{j} = \eta_{j,a} \eta_{j,E} \eta_{j,e} \tag{5.9}$$

Finally, the number of molecules available for the subsequent cycle (j+1) can be calculated using η_i and DNA/polymerase thermal damage occurring during denaturation stage:

$$S_{j+1} = \eta_d (1 + \eta_i) S_j$$
 (5.10)

$$P_{j+1} = \eta_d (P_j - \eta_i S_j)$$
 (5.11)

$$E_{j+1} = \eta_{dE} E_j \tag{5.12}$$

Where η_d is DNA or primer thermal damage, and η_{dE} is polymerase thermal damage. Since in our real-time amplicon detection method, PCR reaction is exposed to UV light at the end of annealing stage, we should also consider UV damage to DNA (η_{dUV}) and polymerase (η_{dEUV}) ; thus, we modified equation (5.7) and (5.12) as follows:

$$\eta_{j, e} = \eta_{d_{UV}} \frac{C_{j, e}}{C_{j, e}}$$
(5.13)

$$E_{j+1} = \eta_{dE} \eta_{dE_{IIV}} E_j \tag{5.14}$$

The calculated S_{j+1} , P_{j+1} , and E_{j+1} will be used as the initial reagents' concentrations for the equation (5.1) to (5.4), and all other steps will be repeated to quantify reagents concertation for each PCR cycle.

5.3 Model calibration with experimental UV detection results

In this section, the model parameters presented in Table 5.1 and Table 5.2 are classified into two groups with known and unknown values for model calibration. The known parameters consist of PCR protocol, PCR ingredients initial concentration, and template/primer/polymerase characteristics. Table 5.3 demonstrates the experimental values set for known parameters in our real-time UV detection system.

Table 5.3 Known parameters for model calibration.

| Known/Experimental Parameters | Description | Value | Unit |
|--------------------------------|---------------------------------------|----------------------------|------|
| S_0 | Initial DNA concentration/Copy number | 8.3e-9/ 10 ⁵ | μΜ |
| P_0 | Starting Primer Concentration | 0.15 | μΜ |
| E_0 | Initial polymerase concentration | 0.5 | μM |
| V | Polymerase extension rate | 500 | bp/s |
| $L_{ m DNA}$ | Template length | 221 | Bp |
| $L_{ m primer}$ | Primer length | 20 | Bp |
| t _a ,t _e | Annealing and elongation duration | 5, 1 | S |

The unknown parameters are reaction rate constants and template/polymerase damage which will be calibrated based on known parameters and experimental UV transmission curves (Table 5.4). To simplify the calibration process, the polymerase binding rates at annealing (60 °C) and elongation temperatures (72 °C) are considered equal ($k_c = k_c^*$).

Table 5.4 Unknown parameters for model calibration.

| Unknown/Predicted Parameters | Description | Unit |
|------------------------------|---|------|
| k_p | Primer annealing rate | μM/s |
| k _s | ssDNA annealing rate | μM/s |
| k_c, k_c^* | Polymerase annealing rate at annealing and elongation steps | μM/s |
| η_{d} | ssDNA thermal damage | - |
| $\eta_{ m dE}$ | Polymerase thermal damage | - |

Different experiments with varying initial DNA concentrations underwent plasmonic amplification (Table 5.5), and the UV amplification curves (UV transmission vs. cycles, $T_{\text{Experimental}}$) were obtained experimentally. The same experiments were used to calibrate the unknown parameters.

Table 5.5 Experiments for quantifying unknown parameters.

| Experiments No. | Different DNA starting copy number |
|-----------------|------------------------------------|
| 1 | 10^{5} |
| 2 | 10^{4} |
| 3 | 10^{3} |
| 4 | 10^{2} |
| 5 | 10 |
| 6 | 1 |

For each set of predicted unknown parameters, the model calculates DNA concentration per PCR cycle (S_j) , and from DNA concentration, the concentration of consumed free nucleotides (d_j) , is calculated using primer (L_{primer}) and template length (L_{DNA}) difference.

$$d_{i}=S_{i}\times(L_{DNA}-L_{primer})=S_{i}\times(L_{ext})$$
(5.15)

As was stated in section 4.4.1, the PCR reagents with highest 260 nm absorption are nucleotides and Taq polymerase due to their heterocyclic rings and aromatic amino acid network, respectively

[228, 229]. Therefore, in order to calculate the 260 nm transmission of the model (T_{Model}) for the calculated dNTPs (d_j) and Taq concentrations (E_j), the absorbance (A) of varying dNTPs and Taq concentrations were measured experimentally using UV spectrophotometer (DS-11 Series, DeNovix Inc.). Equation (5.16) and (5.17) show linear relation between A and concentration of dNTPs and polymerase.

$$A_{i,d}=3.69\times d_i(mM)+0.125$$
 (5.16)

$$A_{i, E}=1.21\times E_{i}(\mu M)+2.34$$
 (5.17)

Using the superposition of dNTPs and Taq absorbance with respect to optical path length of UV system and the spectrometer ($OPL_{UV \, sys.}$ and $OPL_{Spectrometer}$), the transmission of the model (T_{Model}) is calculated as follows:

$$A_{j, total} = A_{j, d} + A_{j, E}$$
 (5.18)

$$A_{j, UV \text{ system}} = \frac{OPL_{UV \text{ system}}}{OPL_{Spectrometer}} \times A_{j, \text{ total}}$$
(5.19)

$$T_{i, Model} = 10^{-A_{j, UV \text{ system}}}$$

$$(5.20)$$

Next, the calculated transmission (T_{Model}) is normalized and plotted against cycles (j) to generate model/calculated UV curve. Finally, the model is calibrated based on the set of unknown parameters demonstrating the least square error fit between T_{Model} and $T_{Experimental}$. The calibrated unknown parameters are presented in Table 5.6.

Table 5.6 Quantified unknown parameters by least square fitting T_{Model} to $T_{Experimental}$.

| Calculated Parameters | Value |
|-----------------------|-----------|
| k_p | 4.21±0.87 |
| k _s | 4.18±0.86 |
| $k_c = k_c^*$ | 10.34 |
| η_{d} | 1 |
| $\eta_{ m dE}$ | 0.95 |

Figure 5.1 illustrates $T_{Experimental}$ (plus signs) and T_{Model} (solid line) with the calibrated/fitted unknown parameters in Table 5.6 for different initial DNA concentrations.

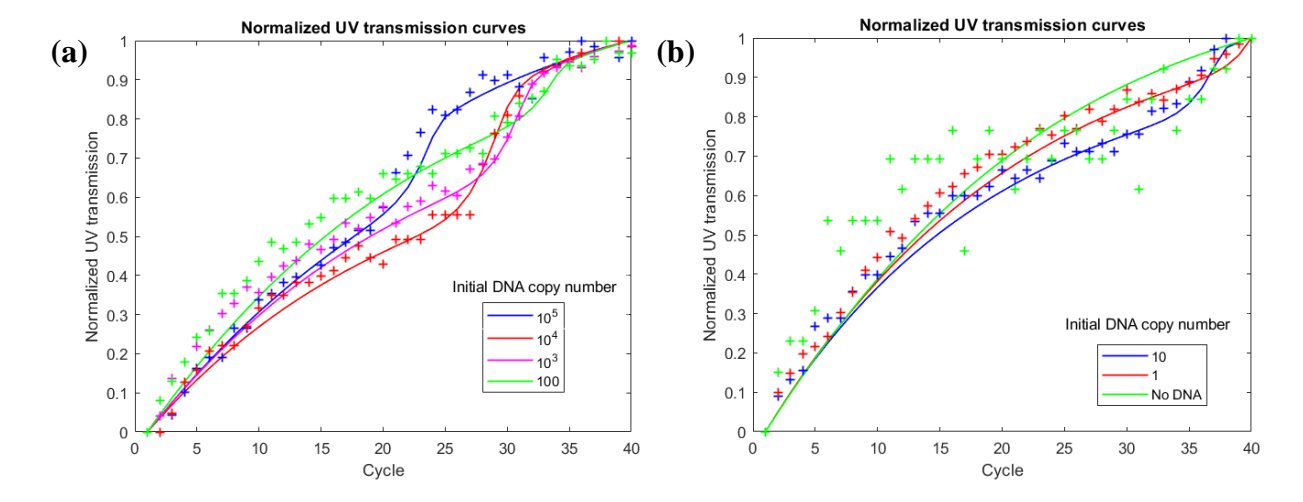


Figure 5.1 Least square fitted T_{Model} (solid lines) to $T_{Experimental}$ (plus signs) to quantify unknown parameters for (a) 10^5 to 100 and (b) 10 to zero initial DNA copy number.

5.4 Results and discussion

5.4.1 Analysis of model parameters on PCR efficiency

Once the model is calibrated, each model parameter can be altered and its impact on amplicon generation can be studied. Moreover, after plasmonic amplification and UV detection, the obtained experimental UV curve can be used to inverse calculate the model to investigate the limiting factor(s) or limiting PCR stage (*i.e.*, denaturation, annealing, and elongation) controlling the PCR yield. Thus, knowing the impact of each parameter on PCR yield or quantifying the limiting factor(s) will help us to optimize and rectify PCR condition for maximum amplicon generation. For all the experiments in this section, the initial DNA copy number of 10⁴ was used, and only one parameter was changed at a time. The rest of the model parameters were kept constant with the values presented in Table 5.3 and Table 5.6.

One of the important parameters to analyze particularly in plasmonic thermocycler is DNA and polymerase thermal damage. Since the source of heat generation is non-radiative decay of localized surface plasmons, the localized hot spots in close proximity of DNA or polymerase molecules result in DNA and polymerase thermal damage.

If we ignore UV damage $(\eta_{d_{UV}} = \eta_{dE_{UV}} = 1)$, by changing η_d and η_{dE} in our calibrated model, their impact on amplicon generation is revealed. Figure 5.2 shows that after threshold cycle (C_t) , dsDNA

generation decreases with increasing thermal damage to DNA and polymerase (*i.e.*, smaller η_d and η_{dE}). However, C_t value is independent of thermal damage to DNA and polymerase during denaturation stage. This implies that thermal damage as a result of high denaturation temperature does not shift C_t , and subsequently the accuracy of amplicon quantification based on C_t is not degraded. Moreover, Figure 5.2.b shows that for polymerase thermal damage of less than 0.89, DNA replication ceases and starts to decrease after cycle 30 due to thermal inactivation of the DNA polymerase. It is important to note that for η_d =0.95, the amount of generated DNA is equal to 3.8 nM; however, with the equal thermal damage to polymerase (η_{dE} = η_d =0.95), 122 nM DNA is generated. It can be concluded that PCR yield diminution is more dependent on cycle-by-cycle DNA thermal damage than polymerase. The result here emphasizes on the importance of denaturation temperature optimization to avoid degrading amplicon yield, which was discussed in section 0 of this thesis.

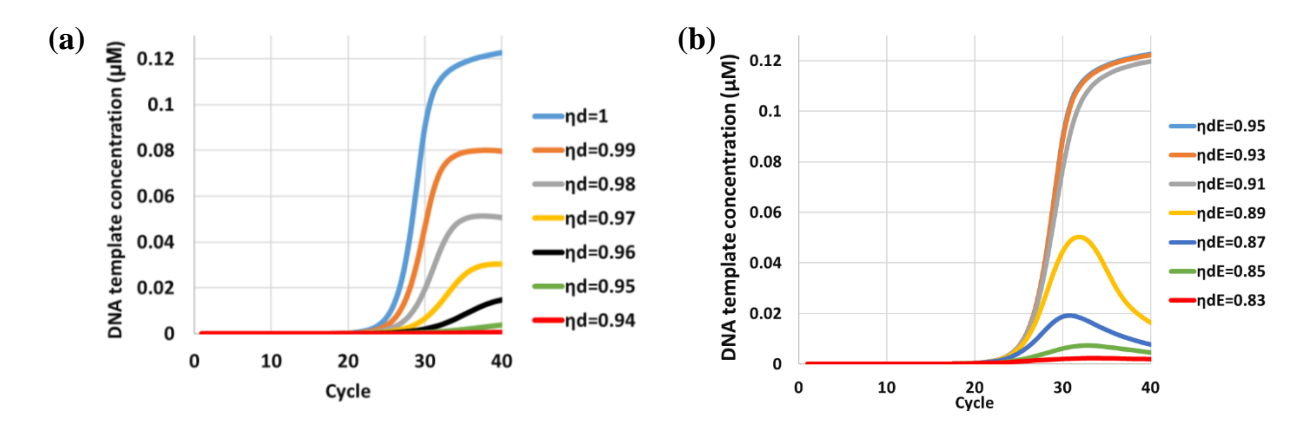


Figure 5.2 (a) DNA and (b) polymerase thermal damage impact on amplificon generation.

The other parameter which impacts the elongation efficiency and subsequently overall PCR efficiency is UV damage to DNA helix $(\eta_{d_{UV}})$ and polymerase $(\eta_{dE_{UV}})$. Figure 5.3.a shows that the UV damage to ternary complexes not only reduces number of generated dsDNAs but also shifts/increases the C_t value. This implies that even samples having identical initial DNA concentration and PCR protocol, but dissimilar UV exposure time show different C_t values, and this reduces the sensitivity in UV amplicon quantification. On the contrary, Figure 5.3.b demonstrates that the impact of $\eta_{dE_{UV}}$ on amplicon generation mimics the same behavior as

polymerase thermal damage (η_{dE}). This is due to the fact that both $\eta_{dE_{UV}}$ and η_{dE} impact polymerase concertation equally based on equation (5.14).

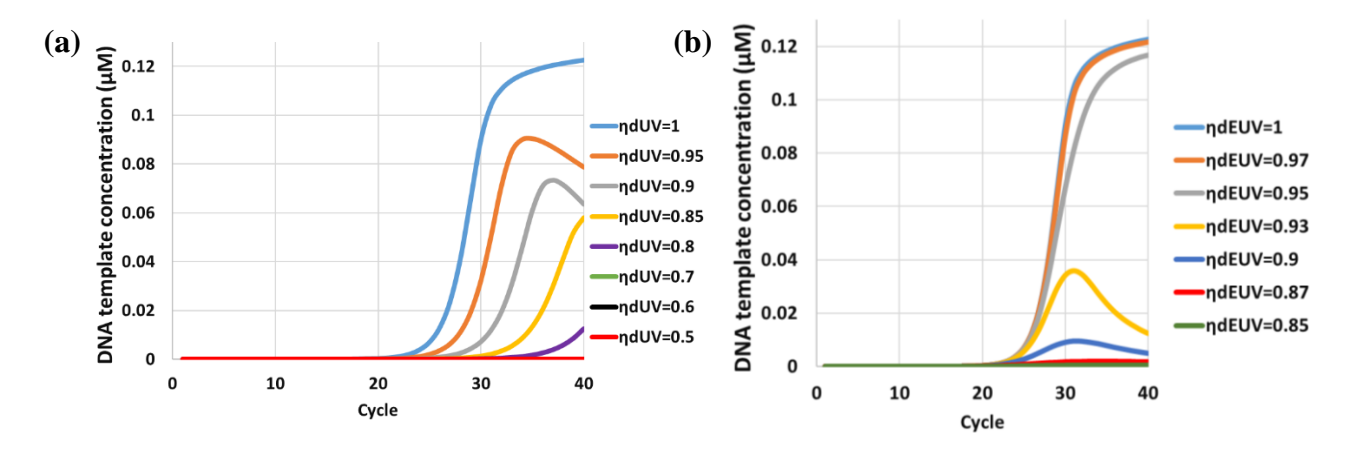


Figure 5.3 (a) DNA and (b) polymerase UV damage impact on amplificon generation.

One advantage of amplifying dsDNA plasmonically is the short amplification time. In our plasmonic PCR procedure, the duration of annealing step (t_a) is 5 times more than the other two PCR steps. Therefore, t_a as the most time-consuming step duration is worthy of study to understand how it governs dsDNA generation. The results in Figure 5.4 indicates that both amplified template concentration and threshold cycle are affected by the amount of time dedicated to primer-template annealing. For time duration less than 3 s, the amplification profile never reaches plateau phase under our plasmonic UV detection system's condition.

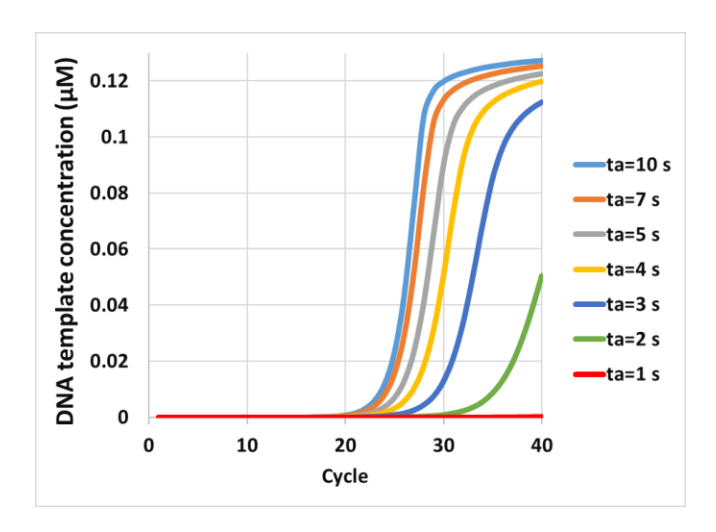


Figure 5.4 Amplification profiles for different t_a.

5.4.2 Minimum detectable threshold cycle

As discussed in section 5.3, only the concentration of Taq polymerase and dNTPs are considered in calculating the model UV absorption and transmission. Figure 5.5 demonstrates how the concentration of these ingredients changes throughout 40 cycles of amplification for 10⁵ DNA copy numbers.

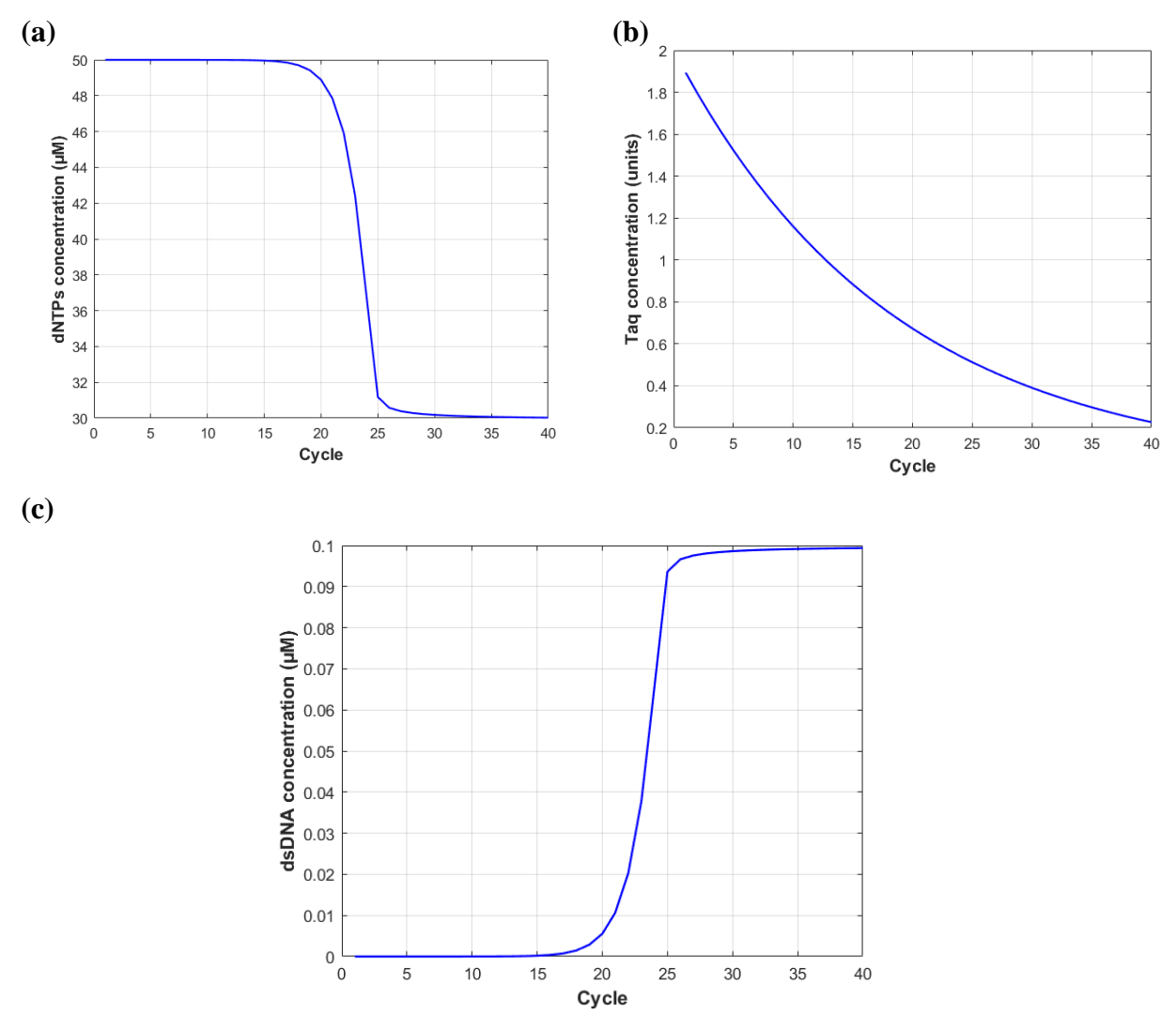


Figure 5.5 The plot of (a) dNTPs, (b) Taq polymerase, and (c) dsDNA concentrations vs. PCR cycles calculated by the model for the initial DNA copy number of 10^5 .

Based on Figure 5.5.c, the model threshold cycle occurs at cycle 16, whereas the experimental UV threshold cycle obtained for 10^5 DNA copy numbers is equal to 19.6 ± 1.14 (section 4.4.4). This discrepancy between the model and experimental C_t value is due to the fact that in our real-time

UV detection, the sum of the UV absorbance of dNTPs and polymerase is monitored, not the dsDNA concentration. Thus, for a correct comparison between model and experimental C_t value, we should refer to the model absorption curves of dNTPs and polymerase which are calculated using equations (5.16) to (5.19). Figure 5.6.a shows that i) the model dNTPs absorption curve demonstrates a similar UV threshold cycle (=20) to what we observed experimentally and ii) the exponential PCR phase or the threshold cycle for dNTPs UV absorption curve shifts to higher cycles compared to dNTPs concentration curve (Figure 5.5.a). The superposition of the dNTPs and polymerase UV absorption is shown in Figure 5.5.c, and finally experimental and model UV transmission curves calculated by equation (5.20) can be compared in Figure 5.5.d.

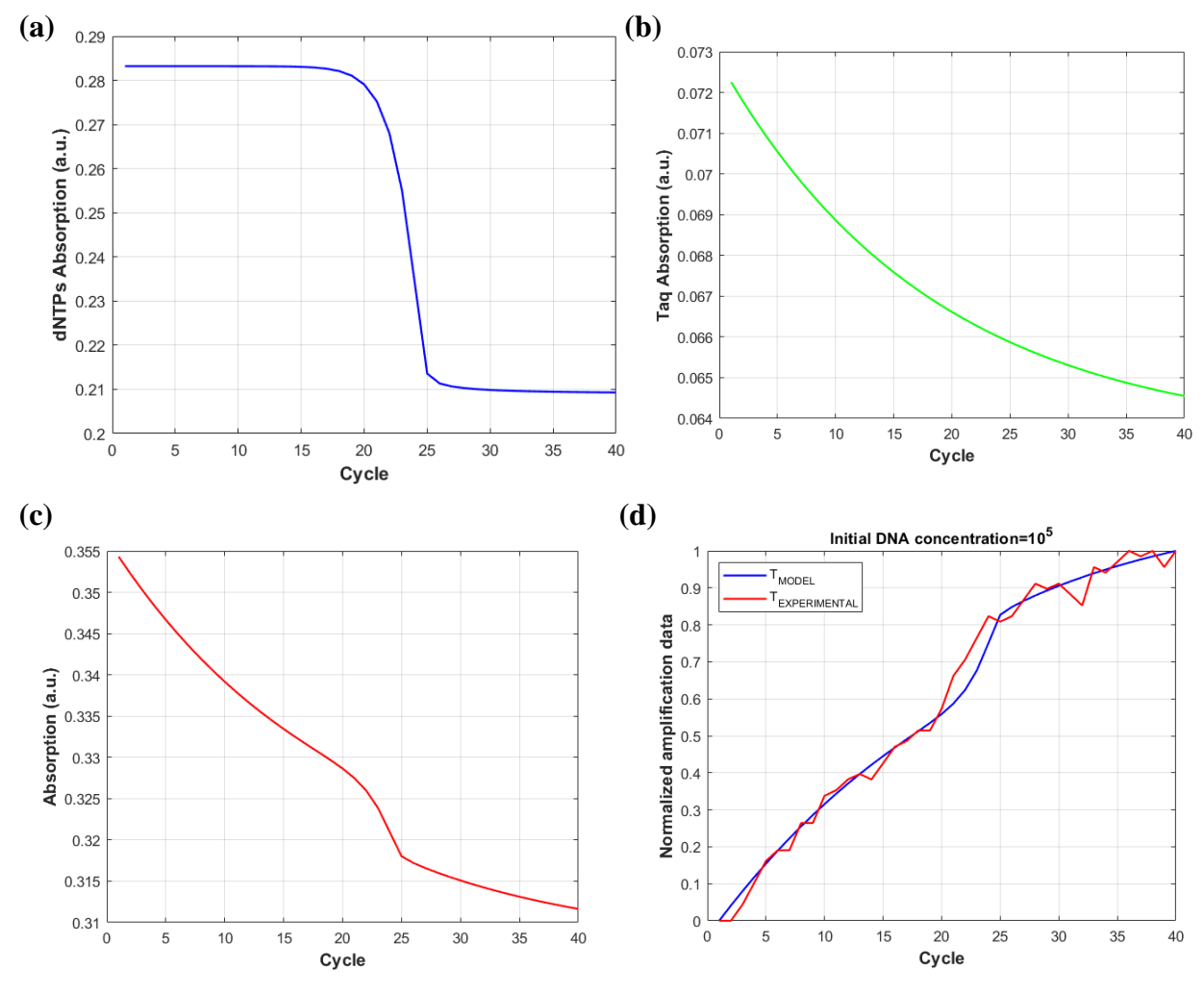


Figure 5.6 The plot of model UV absorption for (a) dNTPs, (b) Taq polymerase, and (c) both Taq and dNTPs as well as (d) UV transmission vs. PCR cycles for the initial DNA copy number of 10⁵.

The results found here imply that dNTPs consumption, i.e., dsDNA generation, enters exponential phase at earlier cycles compared to what we observe in the dNTPs absorption curve or consequently in our experimental UV transmission curve.

Furthermore, due to the identical model and experimental threshold cycles in transmission curves, it can be concluded that the noise power in our detection system is less than the UV transmitted power change as a result of exponential dNTPs consumption. To confirm this finding, the dominant noise in the UV detection system should be calculated. The RMS noise (295 μ V) provided in PDA25K2 photodetector datasheet is used to obtain noise power:

$$P_{rms}(W) = \frac{V_{RMS}}{R(\lambda) \times Transimpedance Gain} = \frac{295 \,\mu\text{V}}{0.037 \frac{A}{W} \times 1.51 \times 10^{5} \frac{v}{A}} = 52.8 \text{ nW}$$
 (5.21)

Where V_{RMS} is the RMS noise voltage, $R(\lambda)$ is the responsivity of the photodetector at a given wavelength (260 nm), and the Transimpedance Gain of the photodetector depends on the gain adjustment by user.

To obtain the amount of dNTPs concentration change ($\Delta[dNTPs]$) for 52.8 nW noise power, we use optical power vs. dNTPs concentration curve presented in Figure 4.15.b. Since the initial concentration of dNTPs (60 μ M) is at point A in the linear region of Figure 4.15.b., $\Delta[dNTPs]$ equivalent to 52.8 nW is calculated as follows:

Slope of the linear region=
$$\frac{52.8 \text{ nW}}{\Delta [\text{dNTPs}]} = 22.36 \rightarrow \Delta [\text{dNTPs}] \approx 1 \text{ } \mu\text{M}$$
 (5.22)

Thus, the real-time UV detection system is not able to optically detect the changes in dNTPs concentration less than 1 μ M (minimum detectable $\Delta[dNTPs]$), i.e., the optical power change equivalent to 1 μ M dNTPs change is equal to noise power. Based on Figure 5.7 calculated by the model, $\Delta[dNTPs]$ is more than minimum detectable $\Delta[dNTPs]$ (\approx 1 μ M) at cycle 20; that is, the transmitted optical power at cycle 20 is above the noise power, and thereby, cycle 20 is the minimum detectable threshold cycle in our UV detection system.

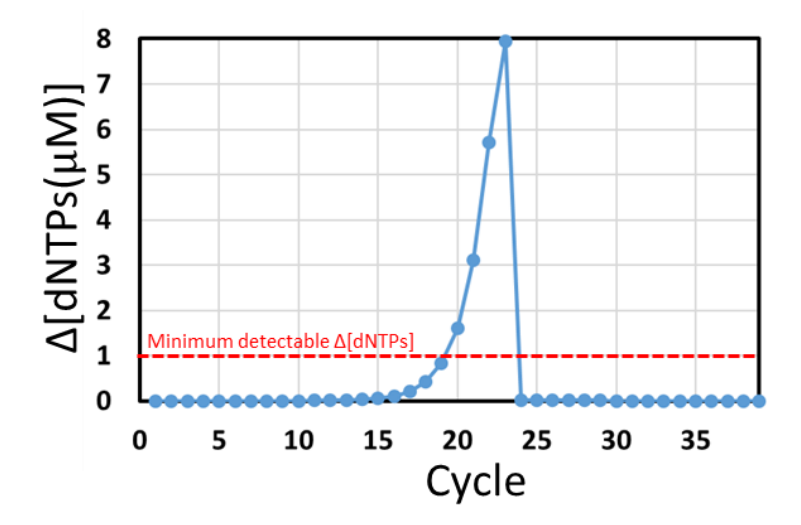


Figure 5.7 dNTPs concentration changes throughout 40 PCR cycles for 10⁵ DNA copy numbers.

5.5 Summary

In this chapter, we briefly described a mathematical model introduced by Booth et al. The calibration of this model by real-time UV detection results helped us to quantify unknown parameters of the plasmonic PCR process such as reaction rate constants as well as template/polymerase denaturing damage. The calibrated model was later used to analyze the impact of PCR conditions and DNA/polymerase thermal/UV damage on PCR efficiency. It was shown that DNA thermal damage is more detrimental to amplicon generation than polymerase thermal and UV damage and even DNA UV damage. Moreover, as the UV damage to the DNA helix increases, the threshold cycle shifts to higher cycle numbers for a fixed initial DNA concentration leading to detection sensitivity loss. The same behavior was observed with shorter annealing hold-time durations, i.e., with a change in annealing hold-time, the threshold cycle is altered. Therefore, by implementing experimental UV transmission to this model, we can understand and quantify the model parameters degrading amplicon generation or sensitivity loss. The results will help to change PCR conditions to maximize amplicon yield and detection sensitivity. Finally, by comparing model and experimental UV curves, it was concluded that the experimental and model threshold cycles are identical which implies that optical power change during the exponential phase of PCR is above noise power. Calculating the UV system noise power showed that exponential consumption of dNTPs is detectable from cycle 20 (minimum detectable threshold cycle) for starting DNA copy number of 10⁵.

CHAPTER 6

Conclusion

6.1 Thesis Summary

The emergence of novel infectious diseases as a result of host shifting is now occurring at unprecedented speed causing dead-end infections, epidemics, or in severe cases pandemics such as the latest infectious agent, severe acute respiratory syndrome coronavirus 2 (SARS-Cov-2). Over the past 300 years, we have been threatened by nine influenza pandemics [230], and in the last 20 years, SARS, MERS, Ebola, avian influenza, swine flu, and COVID-19 has entered the human race [231]. In fact, there exist about 1.7 million other viruses in mammals and water birds which can potentially cause future pandemics [232] with a shorter frequency of occurrence [233]. On the other hand, the medical community has made a great deal of effort to enhance patient safety, prevent disease transmission, and reduce health care costs by timely and accurately detecting these pathogens which are dependent on sensitivity, speed, and cost of diagnostic tools.

Nucleic acid amplification test (NAAT) technique, more commonly called polymerase chain reaction (PCR), is a superior molecular diagnostic technique which surpasses other detection methods in terms of sensitivity and specificity. Despite all of its advantages, this gold-standard molecular diagnostic tool, PCR, is mainly confined to central laboratories due to its bulky size, long assay time, and high-power requirement. These limitations have motivated many researchers to adapt PCR assay for point-of-care (POC) testing to facilitate quick medical decisions and shorten time-to-treatment. One of the major developments in this field was the incorporation of light and optical techniques to make a PCR device that is well-matched to POC requirements.

In the second chapter, the optical PCR thermocyclers, as well as amplicon detectors presented to date, were reviewed extensively, and the hurdles restricting their utilization for POC applications were explained in terms of their speed, photothermal efficiency, size, and detection sensitivity.

In response to these limitations, in the third chapter, a POC-ideal PCR device was presented through photothermal heating of AuNRs excited at their plasmon wavelength by a small-scale VCSEL to achieve rapid thermocycling of large sample volume in a compact system configuration. 30 PCR cycles for plasmonic amplification of *C. Trachomatis* DNA template was accomplished in less than 10 min. The excellent temperature stability and reproducibility of successful PCR results indicated the reliability of the system and robustness of AuNRs within our application. The AuNRs stability was studied by observing their unaltered size, morphology, and absorption spectra using electron microscopy and UV-vis spectroscopy. Finally, the impact of faster heating/cooling rates, as well as different PCR set temperature on amplicon yield, were investigated.

In chapter 4, for the first time, we integrated a real-time fluorophore-free quantitative amplicon detection method into a miniature plasmonic thermocycler with one DNA copy detection sensitivity. The real-time amplicon detection is based on monitoring cycle-by-cycle UV absorption drop in a successful PCR as a result of dNTP-to-dsDNAs conversion. The transmitted UV optical power through PCR reaction from a UV LED was measured at every cycle, and the generated UV amplification curves exhibit distinctive shapes to differentiate PCR results and quantify amplicons. Furthermore, the safe UV exposure limit, contribution of PCR ingredients to 260 nm absorption, detection sensitivity, and the increasing UV transmission phenomenon in baseline phase and negative controls were studied.

In chapter 5, we used a mathematical model to quantify plasmonic PCR reaction rates and the amount of UV/thermal damage to PCR ingredients by implementing UV amplification curves into the model. Using this model, we showed the impact of different PCR conditions on the overall PCR efficiency. That is, each PCR experiment can be analyzed by applying the real-time UV curve to the calibrated model, and by inverse calculating the model, we can understand the impact of each PCR parameter on the shape of the resulting UV curve. Consequently, PCR conditions can be optimized based on these results for maximum amplicon yield.

The research aims stated in chapter 1 are accomplished by presenting:

1. Successful amplification of 221 bp *C. Trachomatis* DNA template in VCSEL-based plasmonic thermocycler with comparable amplification efficiency as conventional PCR machine (chapter 3).

2. Real-time label-free quantification of PCR products via measuring UV transmittance at every PCR cycle (chapter 4). A LOD of one DNA copy number in a $20\,\mu\text{L}$ plasmonic PCR sample was achieved with a 96.6% chance of having one to nine DNA copy numbers in the sample.

The research aims were realized through the following research objectives:

- 1. Maximizing photothermal efficiency through modeling VCSEL-to-tube beam coupling (section 3.2.3).
- 2. Maximizing PCR efficiency through heat transfer modeling and experimental investigation of different PCR conditions such as set temperatures, hold-times, cooling rate, and AuNRs concentration (section 0).
- 3. Signal-to-noise ratio enhancement through the development of an optical model for the UV detection system (section 4.2).
- 4. Real-time amplicon quantification and PCR result classification through analyzing UV amplification curves (section4.4.34.4.4).
- 5. Studying the impact of PCR condition and UV/thermal damage on PCR overall efficiency through calibrating a mathematical model to our experimental UV transmission data (section 5.4).

The other research objectives of this thesis require further investigation which is presented as follows:

- 1. Validating our methodology and testing the device performance by using different target DNAs and polymerases.
- 2. Further assessment of the repeatability of our amplification and detection methodologies.

The proposed work is the first proof-of-concept demonstration realizing plasmonic amplification and UV detection in a single platform. Thus, more improvements are required to make our device ideal for POC testing, e.g., integrating plasmonic DNA extraction, plasmonic amplification, and UV detection in a single fully automated workflow.

The following features required for POC testing are met by our plasmonic and real-time label-free PCR device:

- Run-to-run cross-contamination and specific fabrication of AuNPs and PCR chamber are precluded due to employing commercially available disposable AuNRs and conventional PCR plastic tubes.
- 2. The portability of the presented system is due to hardware miniaturization; not sample volume; therefore, abundant sample volume (20 μL) enables a lower limit of detection due to increased OPL and any other post-PCR sample analysis.
- 3. Not being reliant on target-specific probes, our real-time detection strategy is universal, simple, and cost-effective only dependent on the change in dNTPs concentration.
- 4. Mathematical model analysis of real-time UV detection enables reagents concentration and PCR protocol optimization to maximize PCR efficiency.

6.2 Applications and implications of the POC-ideal real-time label-free VCSEL-based plasmonic thermocycler

The use of PCR in infectious disease diagnosis has led to rapid therapeutic interventions and improving patients' clinical outcomes. However, the current standing of PCR devices with respect to their speed and practicality in both centralized and decentralized environments results in the loss of thousands of lives and billions of dollars as a result of unsuccessful outbreak containment such as Ebola [234]. The risk of emergence of new infectious diseases and the re-emergence of old ones causing epidemic or pandemic outbreaks necessitate developing miniature, fast, easy-to-operate, and cost-effective PCR devices allowing nucleic acid analysis (NA) performed by unskilled personnel at the point of care with lab-quality results.

In order to perform NA, the following analytical steps should be performed [235]: 1) sample preparation, *i.e.*, DNA extraction from blood, urine, saliva, or swab, 2) target-specific probe design and addition to PCR sample, 3) DNA amplification by PCR, 4) preparatory steps for detection such as incubation and heating for amplicon denaturation, and 5) PCR product detection. The presence of step 2 depends on the amplicon detection method. From POC point of view, these five steps should be integrated into a PCR device in a fully automated fashion. Thanks to the developments achieved in real-time PCR devices such as SPR- and fluorescence-based detection techniques, steps 3 to 5 merged into one single step. However, the laborious and costly labeling procedure (step 2) particularly for nanoprobes with their surface functionalization by target-specific bioreceptors needs to be performed by skilled technicians and specialized instruments in

centralized laboratories. Our proposed real-time label-free UV detection technique, on the contrary, skips the 2nd step leading to a simple, fast, and universal assay for any DNA target detection. This implies that our PCR device has only one more step, *i.e.*, sample preparation step integration, to be a fully automated POC device with "one-pot" and "sample-in-result-out" assay format in a miniature optical system. The comparison between one-step and conventional NA is illustrated in Figure 6.1.

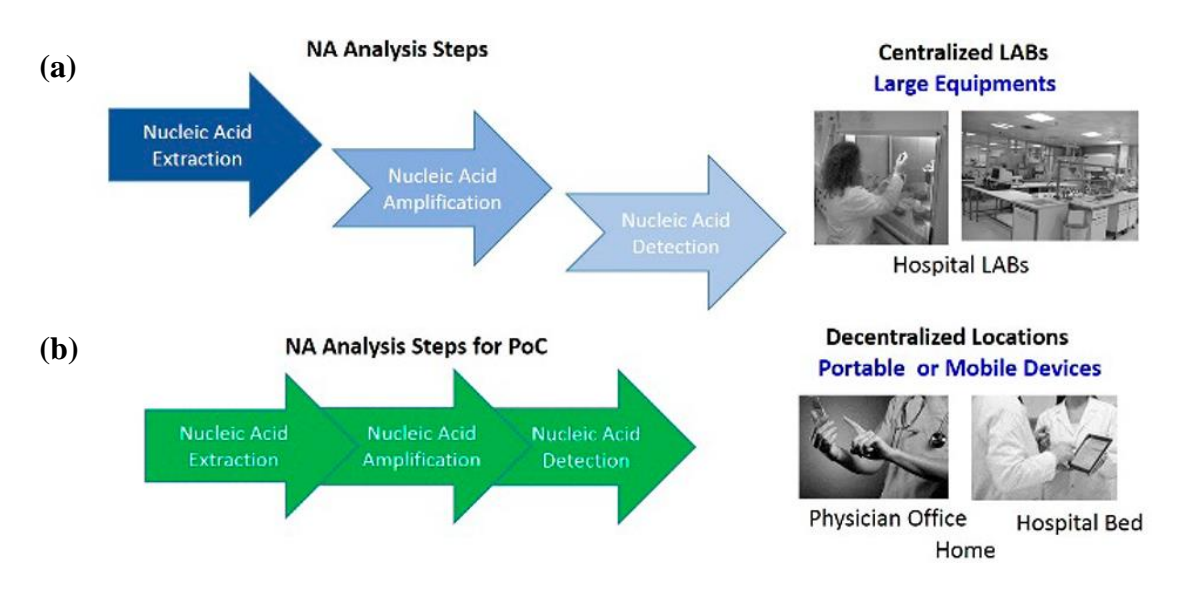


Figure 6.1 Schematic illustration of NA analysis steps carried out in (a) current laboratories and (b) POC format. Reprinted from Ref. [235], Copyright (2017), with permission from American Chemical Society.

The significance of the proposed rapid plasmonic thermocycler can be further realized by observing the current pandemic situation in Canada. As of September 2020, the daily COVID-19 PCR tests per thousand people is averagely 1.5 [236]. Based on the report by public health Ontario, 60% of COVID-19 PCR results are completed within 24 hours and 80% are completed within 48 hours [237]. Considering that the laboratory is equipped with fast and modern qPCR machine, the time duration dedicated to performing qPCR should be around 1.5 h. On the other hand, with a one-step/one-pot VCSEL-based plasmonic thermocycler, the test duration is 9.5 min for 20 μ L sample volume. The POC capability of this plasmonic thermocycler can provide instant availability of results at test centers eliminating the additional steps for transporting samples to laboratories and results verification by technicians. This implies that the number of daily COVID-19 PCR tests per thousand people can at least increase up to 14.2 (1.5 test/thousand people× $\frac{1.5 \text{ h}}{9.5 \text{ min}}$). It should be pointed out that this comparison is valid provided that our real-time plasmonic

thermocycler is upgraded to a multi-channel PCR device by using VCSEL, LED, and photodiode arrays. This is owing to the fact that conventional qPCR machines perform multiplex amplification and detection on at least 96 PCR samples. Multiplexing the proposed work is commercially viable thanks to the well-established optoelectronic industry for the mass production of laser diodes and photodiodes. It is also noteworthy that the plasmonic assay time can be further shortened by decreasing sample volume or increasing AuNRs concentration.

Additionally, the speed of NA is not only reliant on the device automation/speed but also on the total assay cost. For instance, owing to the high cost of qPCR machines, they are unavailable in some health centers of U.S.; thus, the turnaround time for qPCR COVID-19 testing takes an additional time of one day or more for sample transportation to laboratory and relaying the test result to the healthcare provider and patient [238]. It should be noted that the test cost takes into account the costs associated with instrumentation (e.g., thermocycler, detector, pipettes, PCR pot/tube), assay reagents (e.g., nanoprobes), working hours, and workers' level of skill required for testing. The real-time VCSEL-based plasmonic thermocycler costs approximately one thousand dollars which is significantly cheaper than commercially available PCR devices. The most expensive components are the IR thermometer, UV LED, and photodetector, and the rest of the components, namely the VCSEL, fan, and electronics cost less than 100 CAD per component. The PCR reaction is placed in the conventional Eppendorf PCR tubes without the need for fabrication of particular tubes or pipettes. In terms of reagents, the only additive other than PCR ingredients is inexpensive disposable AuNRs. Furthermore, the short assay time and its automation require less user-intervention making our device more affordable and user-friendly compared to qPCR machines.

6.3 Future work and potential improvements

The following recommendations are towards further improvement of this POC-ideal real-time VCSEL-based plasmonic thermocycler:

 Although PCR assay is highly specific due to enzymatic amplification of specific target sequence, the specificity of the proposed work for amplification and detection of various target DNAs should be further investigated. As a case in point, target DNAs with different

- bp sequences and lengths can be studied to analyze the plasmonic amplification efficiency and detection sensitivity of our real-time plasmonic thermocycler.
- Enhancing UV detection sensitivity by offsetting UV transmission increase due to Taq polymerase consumption, so that exponential phase of amplification curve is detectable similar to fluorescent PCR. This results in higher detection sensitivity, as the sharp increase in UV signal at threshold cycle due to dNTPs consumption is not masked by polymerase concentration reduction.
- Development of a VCSEL-based plasmonic thermocycler integrated with fluorescence detection for a valid comparison between detection sensitivity of UV monitoring and florescence detection method.
- Employment of fluorescence thermometry instead of IR temperature measurement. The advantages of fluorescence thermometers are mainly their fast response, high spatial/thermal resolution, and sensitivity. With fluorescent thermometry, more accurate temperature measurement can be achieved since in contrast to IR pyrometer, i) they do not rely on the emissivity of the material where the temperature is to be measured, and ii) the temperature is measured within PCR reaction. As was stated in sections 3.3 and 0, the presence of thermal lag degrades the temperature accuracy measured by IR pyrometers.
- Exploring the impact of other types of polymerases on UV transmission curve. This will help to further clarify the reason behind the increasing UV signal in the baseline phase and negative PCR control.
- Performing many more experiments in our real-time VCSEL-based plasmonic thermocycler to further asses the detection sensitivity and repeatability.
- Comparison between experimental UV amplification curve and model generated amplification curve for different PCR parameters and conditions, *i.e.*, experimental validation of the numerical model.
- Model enhancement to differentiate PCR byproducts (primer-dimers) from amplified DNAs based on their UV transmission curves.
- Upgrading the detection system by incorporating another amplicon monitoring strategy apart from UV detection. This will add a validation layer to improve the accuracy of UV results. For the 2nd detection method:

- The AuNRs used for photothermal heating of PCR solution can be functionalized with oligos complementary to target DNA sequence. By performing aPCR, the amplified sequence of interest (ssDNAs) crosslinks with functionalized AuNRs, and thereby a color change is observed as a result of successful amplification of target DNA (colorimetric detection).
- Target DNA can be amplified with thiolated primers, so that thiol group is added to amplicon and crosslinks with AuNR via thiol-gold interaction, and consequently, the color of PCR solution changes for successful PCR (colorimetric detection).
- O By using AuNRs with higher magnitude zeta potentials, AuNRs undergo salt-induced aggregation and color change for failed PCR; however, aPCR-amplified ssDNAs protect them against salt-induced aggregation, and thereby no color change for successful aPCR (colorimetric detection). The addition of colorimetric assay as an end-point amplicon detection method is beneficial for POC diagnostic circumstances where a simple yes/no answer is needed.
- O Cost-efficient intercalating dyes can be used for fluorescence detection. The fluorescence excitation and emission band should not overlap with the wavelength range of UV photodetector. Also, fluorescence photodetector should have minimal/zero responsivity in UV range. Another simple way is to use an optical filter for each detection method.
- Integrating sample preparation step (DNA extraction), DNA amplification, and detection into a single step. VCSEL-induced photothermal effect of AuNRs can be used to lyse the cells through a heat shock, and after DNA release in solution, the 40 cycles of plasmonic amplification and UV detection are executed. The optimal time duration and temperature for plasmonic cell lysis should be experimented. Also, since the sample reaction is opaque owing to the presence of other non-PCR ingredients, UV signal loss is expected, and signal enhancing approaches should be employed.
- The simplicity in design due to the optical nature of amplification and detection enables us
 to upgrade our PCR device to a high throughput multiplex PCR assay by using VCSEL,
 UV LED, and photodiode arrays bringing all benchtop PCR machine capabilities outside
 of central laboratories to field testing.

- [1] M. Urdea *et al.*, "Requirements for high impact diagnostics in the developing world," *Nature*, vol. 444, no. Suppl 1, pp. 73-9, 2006.
- [2] V. Pribul and T. Woolley, "Point of care testing," *Surgery (Oxford),* vol. 31, no. 2, pp. 84-86, 2013, doi: 10.1016/j.mpsur.2012.12.002.
- [3] "PRODUCT OVERVIEW: Reaction size guidelines for qPCR." Takara Bio Inc. https://www.takarabio.com/learning-centers/real-time-pcr/reaction-size-guidelines-for-qpcr (accessed 2020-08-23.
- [4] P. Boisseau, P. Houdy, M. Lahmani, and S. European Materials Research, *Nanoscience : nanobiotechnology and nanobiology*, Berlin ;: Springer, 2009.
- [5] J. Trauba and C. Wittwer, "Microfluidic Extreme PCR: <1 Minute DNA Amplification in a Thin Film Disposable," *Journal of Biomedical Science and Engineering*, vol. 10, pp. 219-231, 2017.
- [6] C. D. Ahrberg, A. Manz, and B. G. Chung, "Polymerase chain reaction in microfluidic devices," *Lab on a Chip,* vol. 16, no. 20, pp. 3866-3884, 2016, doi: 10.1039/c6lc00984k.
- [7] P. C. H. Li, Fundamentals of microfluidics and lab on a chip for biological analysis and discovery, Boca Raton, FL: CRC Press/Taylor & Francis, 2010.
- [8] C. K. Fredrickson and Z. H. Fan, "Macro-to-micro interfaces for microfluidic devices," *Lab on a Chip,* vol. 4, no. 6, pp. 526-533, 2004, doi: 10.1039/b410720a.
- [9] Y. Ouyang *et al.*, "A disposable laser print-cut-laminate polyester microchip for multiplexed PCR via infra-red-mediated thermal control," *Analytica Chimica Acta*, vol. 901, pp. 59-67, 2015, doi: 10.1016/j.aca.2015.09.042.
- [10] C. J. Easley, J. M. Karlinsey, and J. P. Landers, "On-chip pressure injection for integration of infrared-mediated DNA amplification with electrophoretic separation," *Lab on a Chip,* vol. 6, no. 5, pp. 601-610, 2006, doi: 10.1039/b600039h.
- [11] A. F. Hühmer and J. P. Landers, "Noncontact infrared-mediated thermocycling for effective polymerase chain reaction amplification of DNA in nanoliter volumes," *Analytical chemistry*, vol. 72, no. 21, pp. 5507-12, 2000.
- [12] P. J. R. Roche *et al.*, "Real time plasmonic qPCR: how fast is ultra-fast? 30 cycles in 54 seconds," *The Analyst*, vol. 142, no. 10, pp. 1746-1755, 2017, doi: 10.1039/c7an00304h.
- [13] P. J. R. Roche *et al.*, "Demonstration of a plasmonic thermocycler for the amplification of human androgen receptor DNA," *The Analyst*, vol. 137, no. 19, p. 4475, 2012, doi: 10.1039/c2an35692a.
- [14] J. H. Son *et al.*, "Ultrafast photonic PCR," *Light: Science & Applications*, vol. 4, no. 7, p. e280, 2015, doi: 10.1038/lsa.2015.53.
- [15] J. H. Son *et al.*, "Rapid Optical Cavity PCR," *Advanced Healthcare Materials*, vol. 5, no. 1, pp. 167-174, 2016, doi: 10.1002/adhm.201500708.

- [16] J. H. Lee *et al.*, "Plasmonic Photothermal Gold Bipyramid Nanoreactors for Ultrafast Real-Time Bioassays," *Journal of the American Chemical Society,* vol. 139, no. 24, pp. 8054-8057, 2017, doi: 10.1021/jacs.7b01779.
- [17] Y. Liu *et al.*, "On-chip quantitative PCR using integrated real-time detection by capillary electrophoresis," *ELECTROPHORESIS*, vol. 37, no. 3, pp. 545-552, 2016, doi: 10.1002/elps.201500298.
- [18] L. Zhu *et al.*, "Rapid identification of H5 avian influenza virus in chicken throat swab specimens using microfluidic real-time RT-PCR," *Analytical Methods*, vol. 6, no. 8, p. 2628, 2014, doi: 10.1039/c3ay42126k.
- [19] E. Y. Kim, J. Stanton, R. A. Vega, K. J. Kunstman, C. A. Mirkin, and S. M. Wolinsky, "A real-time PCR-based method for determining the surface coverage of thiol-capped oligonucleotides bound onto gold nanoparticles," *Nucleic acids research*, vol. 34, no. 7, p. e54, 2006.
- [20] H. M. Hiep, K. Kerman, T. Endo, M. Saito, and E. Tamiya, "Nanostructured biochip for label-free and real-time optical detection of polymerase chain reaction," *Analytica Chimica Acta*, vol. 661, no. 1, pp. 111-116, 2010, doi: 10.1016/j.aca.2009.12.006.
- J. Pollet, K. P. F. Janssen, K. Knez, and J. Lammertyn, "Real-Time Monitoring of Solid-Phase PCR Using Fiber-Optic SPR," *Small*, vol. 7, no. 8, pp. 1003-1006, 2011, doi: 10.1002/smll.201001984.
- [22] D. Daems, K. Knez, F. Delport, D. Spasic, and J. Lammertyn, "Real-time PCR melting analysis with fiber optic SPR enables multiplex DNA identification of bacteria," *The Analyst*, vol. 141, no. 6, pp. 1906-11, 2016, doi: 10.1039/c5an02342d.
- [23] D. Devin, P. Bernd, D. Filip, R. Tony, L. Jeroen, and S. Dragana, "Identification and Quantification of Celery Allergens Using Fiber Optic Surface Plasmon Resonance PCR," *Sensors*, vol. 17, no. 8, doi: 10.3390/s17081754.
- [24] N. A. M. Tran, "Universal point of care biosensor using ultrafast plasmonic polymerase chain reaction," McGill University Libraries, [Montreal], 2019. [Online]. Available: http://digitool.Library.McGill.CA/R/?func=dbin-jump-full&object_id=168418
- [25] J. Lederberg, D. A. Relman, and T. Institute of Medicine . Forum on Microbial, *Microbial evolution and co-adaptation : a tribute to the life and scientific legacies of Joshua Lederberg : workshop summary*, Washington, D.C.: National Academies Press, 2009.
- [26] W. H. Frost, "Statistics of Influenza Morbidity: With Special Reference to Certain Factors in Case Incidence and Case Fatality," *Public Health Reports (1896-1970)*, vol. 35, no. 11, pp. 584-597, 1920.
- [27] F. M. S. Burnet and E. Clark, *Influenza*; a survey of the last 50 years in the light of modern work on the virus of epidemic influenza, by F.M. Burnet and Ellen Clark (Walter and Eliza Hall Institute of Medical Research, Melbourne. no. 4. Monographs;). Melbourne: Macmillan (in English), 1942.
- [28] W. A. Adedeji, "THE TREASURE CALLED ANTIBIOTICS," *Annals of Ibadan postgraduate medicine,* vol. 14, no. 2, pp. 56-57, 2016.
- [29] B. Greenwood, "The contribution of vaccination to global health: past, present and future," *Philosophical transactions of the Royal Society of London. Series B, Biological sciences,* vol. 369, no. 1645, p. 20130433, 2014, doi: 10.1098/rstb.2013.0433.

[30] C. R. Parrish *et al.*, "Cross-species virus transmission and the emergence of new epidemic diseases," *Microbiology and molecular biology reviews : MMBR*, vol. 72, no. 3, pp. 457-70, 2008, doi: 10.1128/MMBR.00004-08.

- [31] L. Sang Hee, C. Ill Hwan, J. Byeong Chul, and L. Chang-Ro, "Strategies to Minimize Antibiotic Resistance," *International Journal of Environmental Research and Public Health*, vol. 10, no. 9, pp. 4274-4305doi: 10.3390/ijerph10094274.
- [32] E. A. Nelson *et al.*, "Concordance in diabetic foot ulcer infection," *BMJ Open*, vol. 3, no. 1, doi: 10.1136/bmjopen-2012-002370.
- [33] R. P. Peters, M. A. van Agtmael, S. A. Danner, P. H. Savelkoul, and C. M. Vandenbroucke-Grauls, "New developments in the diagnosis of bloodstream infections," *The Lancet. Infectious diseases*, vol. 4, no. 12, pp. 751-60, 2004.
- [34] I. M. Mackay, "Real-time PCR in the microbiology laboratory," *Clinical Microbiology and Infection,* vol. 10, no. 3, pp. 190-212, 2004, doi: 10.1111/j.1198-743X.2004.00722.x.
- [35] F. J. Loge, D. E. Thompson, and D. R. Call, "PCR detection of specific pathogens in water: a risk-based analysis," *Environmental science & technology*, vol. 36, no. 12, pp. 2754-9, 2002.
- [36] K. Mullis, F. Faloona, S. Scharf, R. Saiki, G. Horn, and H. Erlich, "Specific enzymatic amplification of DNA in vitro: the polymerase chain reaction," *Cold Spring Harbor symposia on quantitative biology*, vol. 51, no. Pt 1, pp. 263-73, 1986.
- [37] J. M. Berg, J. L. Tymoczko, and L. Stryer, *Biochemistry*, 7th ed. ed. New York: W.H. Freeman (in English), 2012.
- [38] W. Rychlik, W. J. Spencer, and R. E. Rhoads, "Optimization of the annealing temperature for DNA amplification in vitro," *Nucleic acids research*, vol. 18, no. 21, pp. 6409-12, 1990.
- [39] T. C. Lorenz, "Polymerase chain reaction: basic protocol plus troubleshooting and optimization strategies," *Journal of visualized experiments : JoVE,* no. 63, p. e3998, 2012, doi: 10.3791/3998.
- [40] D. Svec, A. Tichopad, V. Novosadova, M. W. Pfaffl, and M. Kubista, "How good is a PCR efficiency estimate: Recommendations for precise and robust qPCR efficiency assessments," *Biomolecular detection and quantification*, vol. 3, pp. 9-16, 2015, doi: 10.1016/j.bdq.2015.01.005.
- [41] J. Talapko, I. Škrlec, T. Alebić, M. Jukić, and A. Včev, "Malaria: The Past and the Present," *Microorganisms*, vol. 7, no. 6, 2019, doi: 10.3390/microorganisms7060179.
- [42] "Malaria." World Health Organization. https://www.who.int/news-room/facts-in-pictures/detail/malaria (accessed 2020-10-11.
- [43] F. Mahmud. "Bangladesh scientists create \$3 kit. Can it help detect COVID-19?" AL JAZEERA NEWS. https://www.aljazeera.com/news/2020/03/bangladesh-scientists-create-3-kit-detect-covid-19-200323035631025.html (accessed.
- [44] I. M. D. William F. Marshall. "How do COVID-19 antibody tests differ from diagnostic tests?" Mayoclinic. https://www.mayoclinic.org/diseases-conditions/coronavirus/expert-answers/covid-antibody-tests/faq-20484429 (accessed.
- [45] C. T. Wittwer, G. C. Fillmore, and D. J. Garling, "Minimizing the time required for DNA amplification by efficient heat transfer to small samples," *Analytical biochemistry*, vol. 186, no. 2, pp. 328-31, 1990.

- [46] J. S. Farrar and C. T. Wittwer, "Extreme PCR: efficient and specific DNA amplification in 15-60 seconds," *Clinical chemistry*, vol. 61, no. 1, pp. 145-53, 2015, doi: 10.1373/clinchem.2014.228304.
- [47] A. St John and C. P. Price, "Existing and Emerging Technologies for Point-of-Care Testing," *The Clinical biochemist. Reviews*, vol. 35, no. 3, pp. 155-67, 2014.
- [48] C. Zhang and D. Xing, "Miniaturized PCR chips for nucleic acid amplification and analysis: latest advances and future trends," *Nucleic Acids Research*, vol. 35, no. 13, pp. 4223-4237doi: 10.1093/nar/gkm389.
- [49] E. Nunez-Bajo *et al.*, "Disposable silicon-based all-in-one micro-qPCR for rapid on-site detection of pathogens," *Nature Communications*, vol. 11, no. 1, 2020, doi: 10.1038/s41467-020-19911-6.
- [50] S. Battaglia, S. Petralia, N. Vicario, D. Cirillo, and S. Conoci, "An innovative silicon-chip for sensitive real time PCR improvement in pathogen detection," *The Analyst*, vol. 144, no. 7, pp. 2353-2358, 2019, doi: 10.1039/c9an00006b.
- [51] "QuantStudio™ 3D Digital PCR." ThermoFisher SCIENTIFIC. https://www.thermofisher.com/ (accessed 18 April, 2021, 2021).
- [52] D. Moschou *et al.*, "All-plastic, low-power, disposable, continuous-flow PCR chip with integrated microheaters for rapid DNA amplification," *Sensors & Actuators: B. Chemical*, vol. 199, pp. 470-478, 2014, doi: 10.1016/j.snb.2014.04.007.
- [53] D. P. Manage *et al.*, "On-chip PCR amplification of genomic and viral templates in unprocessed whole blood," *Microfluidics and Nanofluidics*, vol. 10, no. 3, pp. 697-702, 2011, doi: 10.1007/s10404-010-0702-4.
- [54] S. Furutani, H. Nagai, Y. Takamura, Y. Aoyama, and I. Kubo, "Detection of expressed gene in isolated single cells in microchambers by a novel hot cell-direct RT-PCR method," *The Analyst*, vol. 137, no. 13, pp. 2951-7, 2012, doi: 10.1039/c2an15866c.
- [55] P. Liu, X. Li, S. A. Greenspoon, J. R. Scherer, and R. A. Mathies, "Integrated DNA purification, PCR, sample cleanup, and capillary electrophoresis microchip for forensic human identification," *Lab on a Chip*, vol. 11, no. 6, pp. 1041-1048, 2011.
- [56] D. S. Lee *et al.*, "Bulk-micromachined submicroliter-volume PCR chip with very rapid thermal response and low power consumption," *Lab on a chip*, vol. 4, no. 4, pp. 401-7, 2004.
- [57] J. P. Ferrance *et al.*, "Developments toward a complete micro-total analysis system for Duchenne muscular dystrophy diagnosis," *Analytica Chimica Acta*, vol. 500, no. 1, pp. 223-236, 2003, doi: 10.1016/j.aca.2003.08.067.
- [58] D. J. Marchiarullo, A. H. Sklavounos, K. Oh, B. L. Poe, N. S. Barker, and J. P. Landers, "Low-power microwave-mediated heating for microchip-based PCR," *Lab on a Chip,* vol. 13, no. 17, p. 3417, 2013, doi: 10.1039/c3lc50461a.
- [59] J. Chiou, P. Matsudaira, A. Sonin, and D. Ehrlich, "A closed-cycle capillary polymerase chain reaction machine," *Analytical chemistry*, vol. 73, no. 9, pp. 2018-21, 2001.
- [60] A. Harandi and T. Farquhar, "A microfluidic device providing continuous-flow polymerase chain reaction heating and cooling," *Journal of micromechanics and microengineering : structures, devices, and systems.,* vol. 24, no. 11, p. 115009, 2014.

[61] L. Jiang, M. Mancuso, Z. Lu, G. Akar, E. Cesarman, and D. Erickson, "Solar thermal polymerase chain reaction for smartphone-assisted molecular diagnostics," *Scientific reports,* vol. 4, p. 4137, 2014, doi: 10.1038/srep04137.

- [62] J. J. Chen, M. H. Liao, K. T. Li, and C. M. Shen, "One-heater flow-through polymerase chain reaction device by heat pipes cooling," *Biomicrofluidics*, vol. 9, no. 1, p. 014107, 2015, doi: 10.1063/1.4906505.
- [63] B. Miao *et al.*, "Centrifugal Microfluidic System for Nucleic Acid Amplification and Detection," *Sensors (Basel, Switzerland)*, vol. 15, no. 11, pp. 27954-68, 2015, doi: 10.3390/s151127954.
- [64] H. Tachibana, M. Saito, K. Tsuji, K. Yamanaka, L. Q. Hoa, and E. Tamiya, "Self-propelled continuous-flow PCR in capillary-driven microfluidic device: Microfluidic behavior and DNA amplification," *Sensors & Actuators: B. Chemical*, vol. 206, pp. 303-310, 2015, doi: 10.1016/j.snb.2014.09.004.
- [65] Y. Sun, Y. C. Kwok, and N. T. Nguyen, "A circular ferrofluid driven microchip for rapid polymerase chain reaction," *Lab on a Chip,* vol. 7, no. 8, pp. 1012-1017, 2007.
- [66] C. Zhang, J. Xu, W. Ma, and W. Zheng, "PCR microfluidic devices for DNA amplification," *Biotechnology Advances*, vol. 24, no. 3, pp. 243-284, 2006, doi: 10.1016/j.biotechadv.2005.10.002.
- [67] P. A. Auroux, Y. Koc, A. deMello, A. Manz, and P. J. R. Day, "Miniaturised nucleic acid analysis," *Lab on a Chip,* vol. 4, no. 6, pp. 534-546, 2004.
- [68] R. P. Oda *et al.*, "Infrared-Mediated Thermocycling for Ultrafast Polymerase Chain Reaction Amplification of DNA," *Analytical Chemistry*, vol. 70, no. 20, pp. 4361-4368, 1998, doi: 10.1021/ac980452i.
- [69] L. N. Sanford and C. T. Wittwer, "Monitoring temperature with fluorescence during real-time PCR and melting analysis," *Analytical biochemistry*, vol. 434, no. 1, pp. 26-33, 2013, doi: 10.1016/j.ab.2012.10.037.
- [70] Kebes. "Electromagnetic absorption by water." English Wikipedia. https://en.wikipedia.org/wiki/Electromagnetic absorption by water (accessed 2020-12-01.
- [71] M. G. Roper, C. J. Easley, L. A. Legendre, J. A. Humphrey, and J. P. Landers, "Infrared temperature control system for a completely noncontact polymerase chain reaction in microfluidic chips," *Analytical chemistry*, vol. 79, no. 4, pp. 1294-300, 2007.
- [72] Y. Yu, B. Li, C. A. Baker, X. Zhang, and M. G. Roper, "Quantitative polymerase chain reaction using infrared heating on a microfluidic chip," *Analytical Chemistry*, vol. 84, no. 6, pp. 2825-2829, 2012, doi: 10.1021/ac203307h.
- [73] B. C. Giordano, J. Ferrance, S. Swedberg, A. F. R. Hühmer, and J. P. Landers, "Polymerase Chain Reaction in Polymeric Microchips: DNA Amplification in Less Than 240 Seconds," *Analytical Biochemistry*, vol. 291, no. 1, pp. 124-132, 2001, doi: 10.1006/abio.2000.4974.
- [74] L. A. Legendre, J. M. Bienvenue, M. G. Roper, J. P. Ferrance, and J. P. Landers, "A simple, valveless microfluidic sample preparation device for extraction and amplification of DNA from nanoliter-volume samples," *Analytical chemistry*, vol. 78, no. 5, pp. 1444-51, 2006.
- [75] J. J. Chen and I. Hsiang Hsieh, "Using an IR lamp to perform DNA amplifications on an oscillatory thermocycler," *Applied Thermal Engineering*, vol. 106, pp. 1-12, 2016, doi: 10.1016/j.applthermaleng.2016.05.184.

- [76] J. A. Lounsbury *et al.*, "From sample to PCR product in under 45 minutes: a polymeric integrated microdevice for clinical and forensic DNA analysis," *Lab on a Chip*, vol. 13, no. 7, p. 1384, 2013, doi: 10.1039/c3lc41326h.
- [77] C. Ke, H. Berney, A. Mathewson, and M. M. Sheehan, "Rapid amplification for the detection of Mycobacterium tuberculosis using a non-contact heating method in a silicon microreactor based thermal cycler," *Sensors and actuators. B, Chemical.*, vol. 102, no. 2, p. 308, 2005.
- [78] C. J. Easley, J. M. Karlinsey, and J. P. Landers, "On-chip pressure injection for integration of infrared-mediated DNA amplification with electrophoretic separation," *Lab on a chip,* vol. 6, no. 5, pp. 601-10, 2006.
- [79] A. M. Schrell and M. G. Roper, "Frequency-encoded laser-induced fluorescence for multiplexed detection in infrared-mediated quantitative PCR," *The Analyst*, vol. 139, no. 11, pp. 2695-701, 2014, doi: 10.1039/c3an02334f.
- [80] N. Pavel, Z. Chunyan, P. Juergen, O. Sharon, and Z. Lang, "Ultra fast miniaturized real-time PCR: 40 cycles in less than six minutes," *Nucleic Acids Research*, vol. 34, no. 11, pp. e77-e77doi: 10.1093/nar/gkl416.
- [81] D. C. Saunders, C. R. Phaneuf, and C. R. Forest, "Plug-and-play, infrared, laser-mediated PCR in a microfluidic chip," *Biomedical Microdevices*, vol. 14, no. 2, pp. 427-433, 2012.
- [82] S. Y. Teh, R. Lin, L. H. Hung, and A. P. Lee, "Droplet microfluidics," *Lab on a chip,* vol. 8, no. 2, pp. 198-220, 2008, doi: 10.1039/b715524g.
- [83] K. T. Kotz, Y. Gu, and G. W. Faris, "Optically addressed droplet-based protein assay," *Journal of the American Chemical Society*, vol. 127, no. 16, pp. 5736-7, 2005.
- [84] H. Terazono, A. Hattori, H. Takei, K. Takeda, and K. Yasuda, "Development of 1480 nm photothermal high-speed real-time polymerase chain reaction system for rapid nucleotide recognition," *Japanese Journal of Applied Physics, Part 1: Regular Papers and Short Notes and Review Papers*, vol. 47, no. 6 PART 2, pp. 5212-5216, 2008, doi: 10.1143/JJAP.47.5212.
- [85] H. Kim, S. Vishniakou, and G. W. Faris, "Petri dish PCR: laser-heated reactions in nanoliter droplet arrays," *Lab on a Chip,* vol. 9, no. 9, pp. 1230-1235, 2009.
- [86] H. Kim, S. Dixit, C. J. Green, and G. W. Faris, "Nanodroplet real-time PCR system with laser assisted heating," *Optics express*, vol. 17, no. 1, pp. 218-27, 2009.
- [87] K. Hettiarachchi, H. Kim, and G. W. Faris, "Optical manipulation and control of real-time PCR in cell encapsulating microdroplets by IR laser," *Microfluidics and Nanofluidics*, vol. 13, no. 6, pp. 967-975, 2012, doi: 10.1007/s10404-012-1016-5.
- [88] H. A. Druett, "Equilibrium Temperature of a Small Sphere suspended in Air and exposed to Solar Radiation," *Nature*, vol. 201, no. 4919, p. 611, 1964, doi: 10.1038/201611a0.
- [89] H. S. Bachmann, W. Siffert, and U. H. Frey, "Successful amplification of extremely GC-rich promoter regions using a novel 'slowdown PCR' technique," *Pharmacogenetics*, vol. 13, no. 12, pp. 759-66, 2003.
- [90] M. A. Khan, "A Review on NanoPCR: History, Mechanism and Applications," *Journal of Nanoscience and Nanotechnology*, vol. 18, 12/01 2018, doi: 10.1166/jnn.2018.16390.

[91] N. Baskaran, R. P. Kandpal, A. K. Bhargava, M. W. Glynn, A. Bale, and S. M. Weissman, "Uniform amplification of a mixture of deoxyribonucleic acids with varying GC content," *Genome research*, vol. 6, no. 7, pp. 633-8, 1996.

- [92] W. A. Rees, T. D. Yager, J. Korte, and P. H. Von Hippel, "Betaine can eliminate the base pair composition dependence of DNA melting," *Biochemistry*, vol. 32, no. 1, pp. 137-144, 1993/01/12 1993, doi: 10.1021/bi00052a019.
- [93] E. Chevet, G. Lemaître, and M. D. Katinka, "Low concentrations of tetramethylammonium chloride increase yield and specificity of PCR," *Nucleic acids research*, vol. 23, no. 16, pp. 3343-4, 1995.
- [94] G. Sarkar, S. Kapelner, and S. S. Sommer, "Formamide can dramatically improve the specificity of PCR," *Nucleic acids research*, vol. 18, no. 24, p. 7465, 1990.
- [95] K. Varadaraj and D. M. Skinner, "Denaturants or cosolvents improve the specificity of PCR amplification of a G + C-rich DNA using genetically engineered DNA polymerases," *Gene*, vol. 140, no. 1, pp. 1-5, 1994, doi: 10.1016/0378-1119(94)90723-4.
- [96] H. Su-Hua *et al.*, "Gold nanoparticle-based RT-PCR and real-time quantitative RT-PCR assays for detection of Japanese encephalitis virus," *Nanotechnology*, vol. 19, no. 40, 2008, doi: 10.1088/0957-4484/19/40/405101.
- [97] C. Shen, W. Yang, Q. Ji, H. Maki, A. Dong, and Z. Zhang, "NanoPCR observation: different levels of DNA replication fidelity in nanoparticle-enhanced polymerase chain reactions," *Nanotechnology*, vol. 20, no. 45, p. 455103, 2009, doi: 10.1088/0957-4484/20/45/455103.
- [98] M. W. Ryan, N. Sara, D. D. Bridget, and J. S. Letha, "The effect of DNA-dispersed single-walled carbon nanotubes on the polymerase chain reaction," *PLoS ONE*, vol. 9, no. 4, doi: 10.1371/journal.pone.0094117.
- [99] L. Wang *et al.*, "Effects of Quantum Dots in Polymerase Chain Reaction," *The Journal of Physical Chemistry B,* vol. 113, no. 21, pp. 7637-7641, 2009/05/28 2009, doi: 10.1021/jp902404y.
- [100] J. Jia, L. Sun, N. Hu, G. Huang, and J. Weng, "Graphene Enhances the Specificity of the Polymerase Chain Reaction," *Small*, vol. 8, no. 13, pp. 2011-2015, 2012, doi: 10.1002/smll.201200139.
- [101] R. Abdul Khaliq *et al.*, "Enhancement in the efficiency of polymerase chain reaction by TiO₂ nanoparticles: crucial role of enhanced thermal conductivity," *Nanotechnology*, vol. 21, no. 25, 2010, doi: 10.1088/0957-4484/21/25/255704.
- [102] W. Tong *et al.*, "Enhancing the specificity and efficiency of polymerase chain reaction using polyethyleneimine-based derivatives and hybrid nanocomposites," *International Journal of Nanomedicine*, vol. 7, pp. 1069-1078, 2012, doi: 10.2147/IJN.S28947.
- [103] M. Yuce, H. Kurt, V. R. S. S. Mokkapati, and H. Budak, "Employment of nanomaterials in polymerase chain reaction: insight into the impacts and putative operating mechanisms of nanoadditives in PCR," *RSC Adv.*, vol. 4, no. 69, pp. 36800-36814, 2014, doi: 10.1039/C4RA06144F.
- [104] H. Li *et al.*, "Nanoparticle PCR: Nanogold-Assisted PCR with Enhanced Specificity," *Angewandte Chemie*, vol. 117, no. 32, pp. 5230-5233, 2005, doi: 10.1002/ange.200500403.
- [105] L. Min, L. Yu-Cheng, W. Chao-Chin, and L. Hsiao-Sheng, "Enhancing the efficiency of a PCR using gold nanoparticles," *Nucleic Acids Research*, vol. 33, no. 21, pp. e184-e184doi: 10.1093/nar/gni183.

- [106] S. Wang *et al.*, "Enhancement of thermal conductivity in water-based nanofluids employing TiO₂/reduced graphene oxide composites," *Journal of Materials Science*, vol. 51, no. 22, pp. 10104-10115, 2016, doi: 10.1007/s10853-016-0239-3.
- [107] A. Amiri *et al.*, "Heat transfer enhancement of water-based highly crumpled few-layer graphene nanofluids," *RSC Advances*, vol. 6, no. 107, pp. 105508-105527, 2016, doi: 10.1039/C6RA22365F.
- [108] W. Yu and H. Xie, "A review on nanofluids: Preparation, stability mechanisms, and applications," *Journal of Nanomaterials*, vol. 2012, 2012, doi: 10.1155/2012/435873.
- [109] S. A. Angayarkanni and J. Philip, "Review on thermal properties of nanofluids: Recent developments," *Advances in colloid and interface science,* vol. 225, pp. 146-76, 2015, doi: 10.1016/j.cis.2015.08.014.
- [110] B. V. Vu, D. Litvinov, and R. C. Willson, "Gold Nanoparticle Effects in Polymerase Chain Reaction: Favoring of Smaller Products by Polymerase Adsorption," *Analytical Chemistry*, vol. 80, no. 14, pp. 5462-5467, 2008/07/01 2008, doi: 10.1021/ac8000258.
- [111] S. Mandal, M. Hossain, T. Muruganandan, G. S. Kumar, and K. Chaudhuri, "Gold nanoparticles alter Taq DNA polymerase activity during polymerase chain reaction," *RSC Advances*, vol. 3, no. 43, pp. 20793-20799, 2013, doi: 10.1039/c3ra41882k.
- [112] W. Yang, X. Li, J. Sun, and Z. Shao, "Enhanced PCR amplification of GC-rich DNA templates by gold nanoparticles," *ACS applied materials & interfaces*, vol. 5, no. 22, pp. 11520-4, 2013, doi: 10.1021/am4040448.
- [113] L. P. Sun *et al.*, "Interaction of gold nanoparticles with Pfu DNA polymerase and effect on polymerase chain reaction," *IET nanobiotechnology*, vol. 5, no. 1, pp. 20-4, 2011, doi: 10.1049/iet-nbt.2010.0009.
- [114] S. Xu and M. Yao, "NanoPCR detection of bacterial aerosols," *Journal of Aerosol Science*, vol. 65, pp. 1-9, 2013, doi: 10.1016/j.jaerosci.2013.06.005.
- [115] A. L. Haber, K. R. Griffiths, A. s. K. Jamting, and K. R. Emslie, "Addition of gold nanoparticles to real-time PCR: effect on PCR profile and SYBR Green I fluorescence," *Analytical and Bioanalytical Chemistry*, vol. 392, no. 5, pp. 887-896, 2008, doi: 10.1007/s00216-008-2358-4.
- [116] L. Mi, H. Zhu, X. Zhang, J. Hu, and C. Fan, "Mechanism of the interaction between Au nanoparticles and polymerase in nanoparticle PCR," *Chinese Science Bulletin*, vol. 52, no. 17, pp. 2345-2349, 2007, doi: 10.1007/s11434-007-0327-5.
- [117] S. Enoch and N. Bonod, *Plasmonics: from basics to advanced topics*, Berlin ;: Springer, 2012.
- [118] S. Link and M. El-Sayed, "Shape and size dependence of radiative, non-radiative and photothermal properties of gold nanocrystals," *International Reviews in Physical Chemistry*, vol. 19, no. 3, pp. 409-453, 2000.
- [119] S. A. Maier, *Plasmonics : fundamentals and applications*, New York: Springer, 2007.
- [120] P. K. Jain and M. A. El-Sayed, "Noble Metal Nanoparticle Pairs: Effect of Medium for Enhanced Nanosensing," *NANO LETTERS*, vol. 8, no. 12, pp. 4347-4352, 2008.
- [121] P. K. Jain, K. S. Lee, I. H. El-Sayed, and M. A. El-Sayed, "Calculated absorption and scattering properties of gold nanoparticles of different size, shape, and composition: applications in biological imaging and biomedicine," *The journal of physical chemistry. B,* vol. 110, no. 14, pp. 7238-48, 2006.

[122] K. Park, S. Biswas, S. Kanel, D. Nepal, and R. A. Vaia, "Engineering the Optical Properties of Gold Nanorods: Independent Tuning of Surface Plasmon Energy, Extinction Coefficient, and Scattering Cross Section," *The Journal of Physical Chemistry C,* vol. 118, no. 11, pp. 5918-5926, 2014, doi: 10.1021/jp5013279.

- [123] Y. Tian, S. Qiang, and L. Wang, "Gold Nanomaterials for Imaging-Guided Near-Infrared in vivo Cancer Therapy," *Frontiers in bioengineering and biotechnology*, vol. 7, p. 398, 2019, doi: 10.3389/fbioe.2019.00398.
- [124] S. Link and M. A. El-Sayed, "Simulation of the Optical Absorption Spectra of Gold Nanorods as a Function of Their Aspect Ratio and the Effect of the Medium Dielectric Constant," *The Journal of Physical Chemistry B*, vol. 109, no. 20, pp. 10531-10532, 2005, doi: 10.1021/jp058091f.
- [125] D. Thompson, "Michael Faraday's recognition of ruby gold: the birth of modern nanotechnology: His 1857 lecture to the royal society in London," *Gold Bulletin*, vol. 40, no. 4, pp. 267-269, 2007, doi: 10.1007/BF03215598.
- [126] J. A. Creighton and D. G. Eadon, "Ultraviolet–visible absorption spectra of the colloidal metallic elements," *J. Chem. Soc., Faraday Trans.*, vol. 87, no. 24, pp. 3881-3891, 1991, doi: 10.1039/FT9918703881.
- [127] P. J. Roche *et al.*, "Demonstration of a plasmonic thermocycler for the amplification of human androgen receptor DNA," *The Analyst*, vol. 137, no. 19, pp. 4475-81, 2012, doi: 10.1039/c2an35692a.
- [128] H. Aldewachi, T. Chalati, M. N. Woodroofe, N. Bricklebank, B. Sharrack, and P. Gardiner, "Gold nanoparticle-based colorimetric biosensors," *Nanoscale*, vol. 10, no. 1, pp. 18-33, 2017, doi: 10.1039/c7nr06367a.
- [129] V. K. Pustovalov, "Light-to-heat conversion and heating of single nanoparticles, their assemblies, and the surrounding medium under laser pulses," *RSC Advances*, vol. 6, no. 84, pp. 81266-81289, 2016, doi: 10.1039/C6RA11130K.
- [130] M. Hu and G. V. Hartland, "Heat Dissipation for Au Particles in Aqueous Solution: Relaxation Time versus Size," *The journal of physical chemistry. B, Condensed matter, materials, surfaces, interfaces & biophysical.*, vol. 106, no. 28, p. 7029, 2002.
- [131] D. K. Roper, W. Ahn, and M. Hoepfner, "Microscale Heat Transfer Transduced by Surface Plasmon Resonant Gold Nanoparticles," *The journal of physical chemistry. C, Nanomaterials and interfaces,* vol. 111, no. 9, pp. 3636-3641, 2007.
- [132] H. H. Richardson, M. T. Carlson, P. J. Tandler, P. Hernandez, and A. O. Govorov, "Experimental and theoretical studies of light-to-heat conversion and collective heating effects in metal nanoparticle solutions," *Nano letters*, vol. 9, no. 3, pp. 1139-46, 2009, doi: 10.1021/nl8036905.
- [133] G. Uchehara, A. Kirk, M. Trifiro, M. Paliouras, and P. Mohammadyousef, *Real time label-free monitoring of plasmonic polymerase chain reaction products* (SPIE Smart Structures + Nondestructive Evaluation). SPIE, 2019.
- [134] M. Tran, M. Paliouras, P. Mohammadyousef, M. Trifiro, and A. G. Kirk, "Real-time fluorophore-free optical monitoring of ultrafast DNA amplification for qPCR," presented at the 2nd European Biosensor Symposium 2019, EBS2019, Florence, Italy, 2019.

- [135] J. H. Son *et al.*, "Ultrafast photonic PCR," *Light: Science and Applications*, vol. 4, no. 7, 2015, doi: 10.1038/lsa.2015.53.
- [136] J. R. G. Navarro *et al.*, "Plasmonic bipyramids for fluorescence enhancement and protection against photobleaching," *Nanoscale*, vol. 6, no. 10, p. 5138, 2014, doi: 10.1039/c3nr06425e.
- [137] T.-J. Li *et al.*, "Handheld energy-efficient magneto-optical real-time quantitative PCR device for target DNA enrichment and quantification," *NPG Asia Materials*, vol. 8, no. 6, p. e277, 2016, doi: 10.1038/am.2016.70.
- [138] W. Liu, M. Zhang, X. Liu, A. Sharma, and X. Ding, "A Point-of-Need infrared mediated PCR platform with compatible lateral flow strip for HPV detection," *Biosensors and Bioelectronics*, vol. 96, pp. 213-219, 2017, doi: 10.1016/j.bios.2017.04.047.
- [139] H. Hung Ji *et al.*, "Light Energy Conversion Surface with Gold Dendritic Nanoforests/Si Chip for Plasmonic Polymerase Chain Reaction," *Sensors*, vol. 20, no. 5, doi: 10.3390/s20051293.
- [140] F. B. Myers and L. P. Lee, "Innovations in optical microfluidic technologies for point-of-care diagnostics," *Lab on a chip,* vol. 8, no. 12, pp. 2015-31, 2008, doi: 10.1039/b812343h.
- [141] A. Pierik *et al.*, "Real time quantitative amplification detection on a microarray : towards high multiplex quantitative PCR," *Lab on a Chip*, vol. 12, no. 10, p. 18997, 2012.
- [142] V. K. Rajendran, P. Bakthavathsalam, P. L. Bergquist, and A. Sunna, "Smartphone detection of antibiotic resistance using convective PCR and a lateral flow assay," *Sensors & Actuators: B. Chemical*, vol. 298, 2019, doi: 10.1016/j.snb.2019.126849.
- [143] M. P. M. Tran, P. Mohammadyousef, M. Trifiro, and A. G. Kirk, "Real-time fluorophore-free optical monitoring of ultrafast DNA amplification for qPCR," *2nd European Biosensor Symposium 2019, EBS2019*, 2019.
- [144] B. L. Fernández-Carballo *et al.*, "Low-cost, real-time, continuous flow PCR system for pathogen detection," *Biomedical Microdevices : BioMEMS and Biomedical Nanotechnology*, vol. 18, no. 2, pp. 1-10, 2016, doi: 10.1007/s10544-016-0060-4.
- [145] J. Wu, Y. Huang, X. Bian, D. Li, Q. Cheng, and S. Ding, "Biosensing of BCR/ABL fusion gene using an intensity-interrogation surface plasmon resonance imaging system," *Optics Communications*, vol. 377, pp. 24-32, 2016, doi: 10.1016/j.optcom.2016.05.035.
- [146] D. Yao *et al.*, "Surface plasmon field-enhanced fluorescence spectroscopy in PCR product analysis by peptide nucleic acid probes," *Nucleic acids research*, vol. 32, no. 22, p. e177, 2004.
- [147] D. van Lierop, K. Faulds, and D. Graham, "Separation free DNA detection using surface enhanced Raman scattering," *Analytical chemistry*, vol. 83, no. 15, pp. 5817-21, 2011, doi: 10.1021/ac200514e.
- [148] F. Li, F. Li, G. Yang, Z. P. Aguilar, W. Lai, and H. Xu, "Asymmetric polymerase chain assay combined with propidium monoazide treatment and unmodified gold nanoparticles for colorimetric detection of viable emetic Bacillus cereus in milk," *Sensors & Actuators: B. Chemical: Part 2*, vol. 255, no. Part 2, pp. 1455-1461, 2018, doi: 10.1016/j.snb.2017.08.154.
- [149] P. Valentini and P. P. Pompa, "A Universal Polymerase Chain Reaction Developer," *Angewandte Chemie International Edition*, vol. 55, no. 6, pp. 2157-2160, 2016, doi: 10.1002/anie.201511010.

[150] H. Deng *et al.*, "Gold nanoparticles with asymmetric polymerase chain reaction for colorimetric detection of DNA sequence," *Analytical chemistry*, vol. 84, no. 3, pp. 1253-8, 2012, doi: 10.1021/ac201713t.

- [151] X. Chen *et al.*, "Development of a rapid and sensitive quantum dot-based immunochromatographic strip by double labeling PCR products for detection of Staphylococcus aureus in food," *Food Control*, vol. 46, pp. 225–232, 12/01 2014, doi: 10.1016/j.foodcont.2014.04.044.
- [152] D. Chen *et al.*, "An integrated, self-contained microfluidic cassette for isolation, amplification, and detection of nucleic acids," (in eng), *Biomed Microdevices*, vol. 12, no. 4, pp. 705-19, Aug 2010, doi: 10.1007/s10544-010-9423-4.
- [153] D. K. Kim *et al.*, "Label-free DNA biosensor based on localized surface plasmon resonance coupled with interferometry," *Analytical chemistry*, vol. 79, no. 5, pp. 1855-64, 2007.
- [154] P. M. Kalligosfyri, A. Sevastou, I. K. Kyriakou, S. S. Tragoulias, D. P. Kalogianni, and T. K. Christopoulos, "Smartphone-based chemiluminometric hybridization assays and quantitative competitive polymerase chain reaction," *Analytica Chimica Acta*, vol. 1088, pp. 123-130, 2019, doi: 10.1016/j.aca.2019.08.051.
- [155] O. C. Estalilla, L. J. Medeiros, J. T. Manning, and R. Luthra, "5' → 3' Exonuclease-Based Real-Time PCR Assays for Detecting the t(14;18)(q32;21): A Survey of 162 Malignant Lymphomas and Reactive Specimens," *Modern Pathology*, vol. 13, no. 6, pp. 661-666, 2000, doi: 10.1038/modpathol.3880116.
- [156] A. S. Biebricher, I. Heller, R. F. H. Roijmans, T. P. Hoekstra, E. J. G. Peterman, and G. J. L. Wuite, "The impact of DNA intercalators on DNA and DNA-processing enzymes elucidated through force-dependent binding kinetics," *Nature Communications*, vol. 6, no. 1, 2015, doi: 10.1038/ncomms8304.
- [157] G. S. Makowski, *Advances in clinical chemistry. Volume 71*, Amsterdam: Academic Press, 2015. [Online]. Available: http://www.sciencedirect.com/science/book/9780128022566.
- [158] M. Gerami-Nejad, J. Berman, and C. A. Gale, "Cassettes for PCR-mediated construction of green, yellow, and cyan fluorescent protein fusions in <i>Candida albicans</i>," *Yeast*, vol. 18, no. 9, pp. 859-864, 2001, doi: 10.1002/yea.738.
- [159] I. Vanden Bempt, V. Vanhentenrijk, M. Drijkoningen, I. Wlodarska, P. Vandenberghe, and C. De Wolf-Peeters, "Real-time reverse transcription-PCR and fluorescence in-situ hybridization are complementary to understand the mechanisms involved in HER-2/neu overexpression in human breast carcinomas," *Histopathology*, vol. 46, no. 4, pp. 431-441, 2005.
- [160] P. Liu, T. S. Seo, N. Beyor, K. J. Shin, J. R. Scherer, and R. A. Mathies, "Integrated portable polymerase chain reaction-capillary electrophoresis microsystem for rapid forensic short tandem repeat typing," *Analytical chemistry*, vol. 79, no. 5, pp. 1881-9, 2007.
- [161] D. Liu *et al.*, "Analysis of multiplex PCR fragments with PMMA microchip," *Talanta*, vol. 68, no. 3, pp. 616-622, 2006, doi: 10.1016/j.talanta.2005.04.064.
- [162] J. Wu, X. Liu, L. Wang, L. Dong, and Q. Pu, "An economical fluorescence detector for lab-on-a-chip devices with a light emitting photodiode and a low-cost avalanche photodiode," *The Analyst*, vol. 137, no. 2, pp. 519-25, 2012, doi: 10.1039/c1an15867h.

- [163] K. Miyaki, Y. Guo, T. Shimosaka, T. Nakagama, H. Nakajima, and K. Uchiyama, "Fabrication of an integrated PDMS microchip incorporating an LED-induced fluorescence device," *Analytical and Bioanalytical Chemistry*, vol. 382, no. 3, pp. 810-816, 2005, doi: 10.1007/s00216-004-3015-1.
- [164] "The Molecular Probes Handbook: Fluorescence Fundamentals." Thermo Fisher Scientific. https://www.thermofisher.com/ (accessed 2020-09-07.
- [165] V. E. C. F. Brian Herman, Joseph R. Lakowicz, Douglas B. Murphy, Kenneth R. Spring, Michael W. Davidson. "Fluorescence Microscopy." https://micro.magnet.fsu.edu/ (accessed 2020-09-25.
- [166] C. J. Easley *et al.*, "A fully integrated microfluidic genetic analysis system with sample-in-answer-out capability," *Proceedings of the National Academy of Sciences of the United States of America.*, vol. 103, no. 51, p. 19272, 2006.
- [167] A. C. Hatch, T. Ray, K. Lintecum, and C. Youngbull, "Continuous flow real-time PCR device using multi-channel fluorescence excitation and detection," *Lab Chip,* vol. 14, no. 3, pp. 562-568, 2014, doi: 10.1039/C3LC51236C.
- [168] S. Bhuckory, "Quantum dots and upconverting nanoparticles: Bioconjugation and time-resolved multiplexed FRET spectroscopy for cancer diagnostics," 2016.
- [169] J. R. Lakowicz, *Principles of fluorescence spectroscopy*, 3rd ed. ed. New York: Springer (in English), 2006.
- [170] "Molecular Probes™ Handbook, Introduction to Fluorescence Techniques." Invitrogen by ThermoFisher

 Scientific.

 https://www.thermofisher.com/content/dam/LifeTech/global/technical-reference-library/Molecular%20Probes%20Handbook/chapter-pdfs/Intro-to-Fluorescence.pdf (accessed 2020-11-11.
- [171] U. Resch-Genger, M. Grabolle, S. Cavaliere-Jaricot, R. Nitschke, and T. Nann, "Quantum dots versus organic dyes as fluorescent labels," *Nature methods,* vol. 5, no. 9, pp. 763-75, 2008, doi: 10.1038/nmeth.1248.
- [172] J. i. Homola and J. Dostálek, Surface plasmon resonance based sensors, Berlin ;: Springer, 2006.
- [173] Y. Li, Plasmonic optics: theory and applications, Bellingham, Washington: SPIE Press, 2017.
- [174] S. Sawata, E. Kai, K. Ikebukuro, T. Iida, T. Honda, and I. Karube, "Application of peptide nucleic acid to the direct detection of deoxyribonucleic acid amplified by polymerase chain reaction," *Biosensors and Bioelectronics*, vol. 14, no. 4, pp. 397-404, 1999, doi: 10.1016/S0956-5663(99)00018-4.
- [175] J. N. Anker, W. P. Hall, O. Lyandres, N. C. Shah, J. Zhao, and R. P. Van Duyne, "Biosensing with plasmonic nanosensors," *Nature materials*, vol. 7, no. 6, pp. 442-53, 2008, doi: 10.1038/nmat2162.
- [176] J.-F. Li, C.-Y. Li, and R. F. Aroca, "Plasmon-enhanced fluorescence spectroscopy," *Chemical Society Reviews*, vol. 46, no. 13, pp. 3962-3979, 2017, doi: 10.1039/c7cs00169j.
- [177] K. Vasilev, W. Knoll, and M. Kreiter, "Fluorescence intensities of chromophores in front of a thin metal film," *The Journal of chemical physics,* vol. 120, no. 7, pp. 3439-45, 2004.
- [178] G. P. Acuna, F. M. Möller, P. Holzmeister, S. Beater, B. Lalkens, and P. Tinnefeld, "Fluorescence Enhancement at Docking Sites of DNA-Directed Self-Assembled Nanoantennas," *Science*, vol. 338, no. 6106, pp. 506-510, 2012.

[179] J. R. Lakowicz *et al.*, "Advances in Surface-Enhanced Fluorescence," *Journal of Fluorescence*, vol. 14, no. 4, pp. 425-441, 2004, doi: 10.1023/B:JOFL.0000031824.48401.5c.

- [180] B. C. Ferrari and P. L. Bergquist, "Quantum Dots as alternatives to organic fluorophores for Cryptosporidium detection using conventional flow cytometry and specific monoclonal antibodies: lessons learned," *Cytometry. Part A: the journal of the International Society for Analytical Cytology*, vol. 71, no. 4, pp. 265-71, 2007.
- [181] Z. S. Pillai and P. V. Kamat, "What Factors Control the Size and Shape of Silver Nanoparticles in the Citrate Ion Reduction Method?," *The Journal of Physical Chemistry B,* vol. 108, no. 3, pp. 945-951, 2004, doi: 10.1021/jp037018r.
- [182] J. A. Dieringer, R. B. Lettan, 2nd, K. A. Scheidt, and R. P. Van Duyne, "A frequency domain existence proof of single-molecule surface-enhanced Raman spectroscopy," *Journal of the American Chemical Society*, vol. 129, no. 51, pp. 16249-56, 2007.
- [183] E. C. Le Ru, M. Meyer, and P. G. Etchegoin, "Proof of single-molecule sensitivity in surface enhanced Raman scattering (SERS) by means of a two-analyte technique," *The journal of physical chemistry. B,* vol. 110, no. 4, pp. 1944-8, 2006.
- [184] K. Kneipp, M. Moskovits, and H. Kneipp, *Surface-enhanced raman scattering : physics and applications*, Berlin ;: Springer, 2006.
- [185] R. J. Stokes, A. Macaskill, P. J. Lundahl, W. E. Smith, K. Faulds, and D. Graham, "Quantitative Enhanced Raman Scattering of Labeled DNA from Gold and Silver Nanoparticles," *Small*, vol. 3, no. 9, pp. 1593-1601, 2007, doi: 10.1002/smll.200600662.
- [186] P. L. White *et al.*, "Evaluation of a commercially developed semiautomated PCR-surface-enhanced raman scattering assay for diagnosis of invasive fungal disease," *Journal of clinical microbiology*, vol. 52, no. 10, pp. 3536-43, 2014, doi: 10.1128/JCM.01135-14.
- [187] S. M. Restaino and I. M. White, "Real-time multiplexed PCR using surface enhanced Raman spectroscopy in a thermoplastic chip," *Lab on a chip,* vol. 18, no. 5, pp. 832-839, 2018, doi: 10.1039/c7lc01227f.
- [188] J. S. Lee, M. S. Han, and C. A. Mirkin, "Colorimetric detection of mercuric ion (Hg2+) in aqueous media using DNA-functionalized gold nanoparticles," *Angewandte Chemie (International ed. in English)*, vol. 46, no. 22, pp. 4093-6, 2007.
- [189] L. Tang and J. Li, "Plasmon-Based Colorimetric Nanosensors for Ultrasensitive Molecular Diagnostics," *ACS sensors*, vol. 2, no. 7, pp. 857-875, 2017, doi: 10.1021/acssensors.7b00282.
- [190] Y. L. Jung, C. Jung, H. Parab, T. Li, and H. G. Park, "Direct colorimetric diagnosis of pathogen infections by utilizing thiol-labeled PCR primers and unmodified gold nanoparticles," *Biosensors & bioelectronics*, vol. 25, no. 8, pp. 1941-6, 2010, doi: 10.1016/j.bios.2010.01.010.
- [191] C. Miao, L. Feng, Z. Yan, and W. Qiangbin, "One-pot polymerase chain reaction with gold nanoparticles for rapid and ultrasensitive DNA detection," *Nano Research*, vol. 3, no. 8, pp. 557-563doi: 10.1007/s12274-010-0016-6.
- [192] M. Zourob, S. Elwary, and A. Turner, *Principles of bacterial detection : biosensors, recognition receptors, and microsystems*, New York: Springer, 2008.
- [193] A. Ymeti *et al.*, "Fast, ultrasensitive virus detection using a Young interferometer sensor," *Nano Letters*, vol. 7, no. 2, p. 394, 2007.

- [194] L. Ali, M. U. Mohammed, M. Khan, A. H. B. Yousuf, and M. H. Chowdhury, "High-Quality Optical Ring Resonator-Based Biosensor for Cancer Detection," *IEEE sensors journal.*, vol. 20, no. 4, pp. 1867-1875, 2020.
- [195] N. T. Georgios, "A study on refractive index sensors based on optical micro-ring resonators," *Photonic Sensors*, vol. 7, no. 3, pp. 217-225doi: 10.1007/s13320-017-0418-0.
- [196] M. S. Murib, D. Martens, and P. Bienstman, "Label-free real-time optical monitoring of DNA hybridization using SiN Mach–Zehnder interferometer-based integrated biosensing platform," *Journal of Biomedical Optics*, vol. 23, no. 12, p. 127002, 2018. [Online]. Available: https://doi.org/10.1117/1.JBO.23.12.127002.
- [197] M. C. Cardenosa-Rubio, R. M. Graybill, and R. C. Bailey, "Combining asymmetric PCR-based enzymatic amplification with silicon photonic microring resonators for the detection of IncRNAs from low input human RNA samples," *The Analyst*, vol. 143, no. 5, pp. 1210-1216, 2018, doi: 10.1039/c7an02045g.
- [198] R. M. Graybill, M. C. Cardenosa-Rubio, H. Yang, M. D. Johnson, and R. C. Bailey, "Multiplexed microRNA Expression Profiling by Combined Asymmetric PCR and Label-Free Detection using Silicon Photonic Sensor Arrays," *Analytical methods : advancing methods and applications,* vol. 10, no. 14, pp. 1618-1623, 2018, doi: 10.1039/C8AY00190A.
- [199] P. Rabiei, "Calculation of losses in micro-ring resonators with arbitrary refractive index or shape profile and its applications," *Journal of Lightwave Technology,* vol. 23, no. 3, pp. 1295-1301, 2005, doi: 10.1109/JLT.2004.841437.
- [200] S. Neethirajan, V. Ragavan K, X. Weng, and R. Chand, "Biosensors for Sustainable Food Engineering: Challenges and Perspectives," *Biosensors*, vol. 8, p. 23, 03/12 2018, doi: 10.3390/bios8010023.
- [201] A. Karabchevsky, A. Mosayyebi, and A. V. Kavokin, "Tuning the chemiluminescence of a luminol flow using plasmonic nanoparticles," *Light, science & applications*, vol. 5, no. 11, p. e16164, 2016, doi: 10.1038/lsa.2016.164.
- [202] D. L. Wiedbrauk and D. H. Farkas, *Molecular methods for virus detection*, San Diego: Academic Press, 1995.
- [203] O. S. Wolfbeis, Fluorescence Spectroscopy: New Methods and Applications, Berlin, Heidelberg: Springer Berlin Heidelberg, 1993. [Online]. Available: https://doi.org/10.1007/978-3-642-77372-3.
- [204] S. Li, Y. Gu, Y. Lyu, Y. Jiang, and P. Liu, "Integrated Graphene Oxide Purification-Lateral Flow Test Strips (iGOP-LFTS) for Direct Detection of PCR Products with Enhanced Sensitivity and Specificity," *Analytical chemistry*, vol. 89, no. 22, pp. 12137-12144, 2017, doi: 10.1021/acs.analchem.7b02769.
- [205] S. Gilbert *et al.*, "Increased sample volume and use of quantitative reverse-transcription PCR can improve prediction of liver-to-blood inoculum size in controlled human malaria infection studies," *Malaria Journal*, vol. 14, no. 1, pp. 1-9doi: 10.1186/s12936-015-0541-6.
- [206] F. Yang, N. Yang, X. Huo, and S. Xu, "Thermal sensing in fluid at the micro-nano-scales," *Biomicrofluidics*, vol. 12, no. 4, p. 041501, 2018, doi: 10.1063/1.5037421.
- [207] L. Mi, H. Zhu, X. Zhang, J. hu, and C. Fan, "Mechanism of the interaction between Au nanoparticles and polymerase in nanoparticle PCR," *Chinese Science Bulletin*, vol. 52, pp. 2345-2349, 09/01 2007, doi: 10.1007/s11434-007-0327-5.

[208] H. Lodish et al., "Molecular Cell Biology, 3.0," Clinical chemistry., vol. 43, no. 4, p. 701, 1997.

- [209] "28.1 Nucleotides and Nucleic Acids," ed, 2020.
- [210] M. R. Hicks, J. Kowałski, and A. Rodger, "LD spectroscopy of natural and synthetic biomaterials," *Chemical Society reviews*, vol. 39, no. 9, pp. 3380-93, 2010, doi: 10.1039/b912917k.
- [211] C. Hazra, T. Samanta, and V. Mahalingam, "A resonance energy transfer approach for the selective detection of aromatic amino acids," *J. Mater. Chem. C*, vol. 2, no. 47, pp. 10157-10163, 2014, doi: 10.1039/C4TC01954G.
- [212] H. Yokoyama and R. Mizutani, "Structural biology of DNA (6-4) photoproducts formed by ultraviolet radiation and interactions with their binding proteins," *International journal of molecular sciences*, vol. 15, no. 11, pp. 20321-38, 2014, doi: 10.3390/ijms151120321.
- [213] T. Douki, A. von Koschembahr, and J. Cadet, "Insight in DNA Repair of UV-induced Pyrimidine Dimers by Chromatographic Methods," *Photochemistry and photobiology,* vol. 93, no. 1, pp. 207-215, 2017, doi: 10.1111/php.12685.
- [214] H.-P. Zhu, L.-J. Mi, S.-M. Chen, W.-F. Wang, and S.-D. Yao, "Study on the Interaction of Colloidal Gold with Taq DNA Polymerase," *Chinese Journal of Chemistry*, vol. 25, no. 9, pp. 1233-1237, 2007, doi: 10.1002/cjoc.200790229.
- [215] S. Mandal, M. Hossain, T. Muruganandan, G. S. Kumar, and K. Chaudhuri, "Gold nanoparticles alter Taq DNA polymerase activity during polymerase chain reaction," *RSC Advances*, vol. 3, no. 43, p. 20793, 2013, doi: 10.1039/c3ra41882k.
- [216] J. M. Carnerero, A. Jimenez-Ruiz, P. M. Castillo, and R. Prado-Gotor, "Covalent and Non-Covalent DNA-Gold-Nanoparticle Interactions: New Avenues of Research," *Chemphyschem : a European journal of chemical physics and physical chemistry,* vol. 18, no. 1, pp. 17-33, 2017, doi: 10.1002/cphc.201601077.
- [217] Y. N. Tan, K. H. Lee, and X. Su, "Study of single-stranded DNA binding protein-nucleic acids interactions using unmodified gold nanoparticles and its application for detection of single nucleotide polymorphisms," *Analytical chemistry*, vol. 83, no. 11, pp. 4251-7, 2011, doi: 10.1021/ac200525a.
- [218] Q. Phenix-Lan, S. Martin, and B. Eric, "dPCR: A Technology Review," *Sensors*, vol. 18, no. 4, doi: 10.3390/s18041271.
- [219] J. Linda and H. Johannes, "Challenging the proposed causes of the PCR plateau phase," *Biomolecular Detection and Quantification*, vol. 17, doi: 10.1016/j.bdq.2019.100082.
- [220] G. Stolovitzky and G. Cecchi, "Efficiency of DNA Replication in the Polymerase Chain Reaction," *Proceedings of the National Academy of Sciences of the United States of America*, vol. 93, no. 23, pp. 12947-12952, 1996.
- [221] P. Jagers and F. Klebaner, "Random variation and concentration effects in PCR," *Journal of Theoretical Biology,* vol. 224, no. 3, pp. 299-304, 2003, doi: 10.1016/S0022-5193(03)00166-8.
- [222] M. W. Pfaffl, "A new mathematical model for relative quantification in real-time RT-PCR," *Nucleic acids research,* vol. 29, no. 9, p. e45, 2001.

- [223] W. Liu and D. A. Saint, "Validation of a quantitative method for real time PCR kinetics," *Biochemical and Biophysical Research Communications,* vol. 294, no. 2, pp. 347-353, 2002, doi: 10.1016/S0006-291X(02)00478-3.
- [224] A. E. Platts, G. D. Johnson, A. K. Linnemann, and S. A. Krawetz, "Real-time PCR quantification using a variable reaction efficiency model," *Analytical biochemistry*, vol. 380, no. 2, pp. 315-22, 2008, doi: 10.1016/j.ab.2008.05.048.
- [225] A. Hassibi, H. Kakavand, and T. Lee, "A stochastic model and simulation algorithm for polymerase chain reaction (PCR) systems," *Proc. of IEEE Workshop on Genomics Signal Processing and Statistics*, 01/01 2004.
- [226] T. M. Louw, C. S. Booth, E. Pienaar, J. R. TerMaat, S. E. Whitney, and H. J. Viljoen, "Experimental validation of a fundamental model for PCR efficiency," *Chemical Engineering Science*, vol. 66, no. 8, pp. 1783-1789, 2011, doi: 10.1016/j.ces.2011.01.029.
- [227] C. S. Booth, E. Pienaar, J. R. Termaat, S. E. Whitney, T. M. Louw, and H. J. Viljoen, "Efficiency of the polymerase chain reaction," *Chemical Engineering Science*, vol. 65, no. 17, pp. 4996-5006, 2010, doi: 10.1016/j.ces.2010.05.046.
- [228] B. C. Pang and B. K. Cheung, "One-step generation of degraded DNA by UV irradiation," *Analytical biochemistry*, vol. 360, no. 1, pp. 163-5, 2007.
- [229] L. C. Burgess and J. O. Hall, "UV light irradiation of plastic reaction tubes inhibits PCR," (in eng), *Biotechniques*, vol. 27, no. 2, pp. 252, 254-4, 256, Aug 1999, doi: 10.2144/99272bm07.
- [230] P. M. Sandman. "A severe pandemic is not overdue it's not when but if." CIDRAP. www.cidrap.umn.edu (accessed.
- [231] V. Gill. "Coronavirus: This is not the last pandemic." Science correspondent, BBC News. www.bbc.com (accessed.
- [232] J. Dalton. "Coronavirus: Pandemics will be worse and more frequent unless we stop exploiting Earth and animals, top scientists warn." Independent. Independent.co.uk (accessed.
- [233] C. Burdeau. "Scientists Expect More Pandemics in Age of Globalization, Climate Change & Assault on Nature." Courthouse news. www.courthousenews.com (accessed.
- [234] C. E. Coltart, B. Lindsey, I. Ghinai, A. M. Johnson, and D. L. Heymann, "The Ebola outbreak, 2013-2016: old lessons for new epidemics," *Philosophical transactions of the Royal Society of London. Series B, Biological sciences*, vol. 372, no. 1721, 2017, doi: 10.1098/rstb.2016.0297.
- [235] S. Petralia and S. Conoci, "PCR Technologies for Point of Care Testing: Progress and Perspectives," *ACS sensors*, vol. 2, no. 7, pp. 876-891, 2017, doi: 10.1021/acssensors.7b00299.
- [236] J. Hasell *et al.*, "A cross-country database of COVID-19 testing," *Scientific data*, vol. 7, no. 1, p. 345, 2020, doi: 10.1038/s41597-020-00688-8.
- [237] "Coronavirus Disease 2019 (COVID-19) PCR." Public Health Ontario. www.publichealthontario.ca (accessed.
- [238] "TESTING FAQ, These FAQs provide answers to some of the most frequently asked questions on COVID-19." Johns Hopkins UNIVERSITY. https://coronavirus.jhu.edu/about (accessed 2020-08-29.